

**POLYTECHNIQUE MONTRÉAL**

affiliée à l'Université de Montréal

**Spray drying  $\text{LiFePO}_4$  nanoparticle suspensions and scale-up**

**MARCO GIULIO RIGAMONTI**

Département de génie chimique

Thèse présentée en vue de l'obtention du diplôme de *Philosophiæ Doctor*  
Génie chimique

Mai 2019

**POLYTECHNIQUE MONTRÉAL**

affiliée à l'Université de Montréal

Cette thèse intitulée :

**Spray drying  $\text{LiFePO}_4$  nanoparticle suspensions and scale-up**

présentée par **Marco Giulio RIGAMONTI**

en vue de l'obtention du diplôme de *Philosophiæ Doctor*  
a été dûment acceptée par le jury d'examen constitué de :

**Paul STUART**, président

**Gregory PATIENCE**, membre et directeur de recherche

**David VIDAL**, membre

**Nasser ASHGRIZ**, membre externe

## DEDICATION

*To my family,  
for always being there for me,  
no matter what.*

*Dedicato alla mia famiglia,  
mamma, papà, zii e nonni,  
per essere sempre presenti,  
vi voglio bene.*



*In loving memory of Dario Cardarelli; painter, architect, loving granpa.  
Shaping spaces towards functionality and beauty.*

## ACKNOWLEDGEMENTS

The author recognizes the support of Natural Science, Engineering Research Council of Canada and the Canadian Foundation for Innovation through the Automotive Partnership Canada program and our industrial partner Johnson-Matthey Battery Materials. The author appreciates the collaboration of Dr. Pierre Sauriol (Polytechnique Montreal) and Dr. Delin Li, Dr. Wojciech Kasprzak, (and colleagues) of CanmetMATERIALS for generating the pilot scale melt-synthesized LFP ingots used for this study.

The author would also like to thank Prof. Gregory Patience, for always striving me to improve and giving me the means of connecting with the world's best research scientists. Prof. Daria Boffito, for collaborating with her research team and extend my knowledge to ultrasonication, heterogeneous catalysis and photocatalysis. Prof. Francesco Gatti, whom I can always rely upon. Stefano and Minerva Lucini, you are awesome! Dr. Davide Carnevali, Dr. Nooshin Saadatkah, Dr. Marta Stucchi, Dr. Federico Galli, Dr. Hayat Khan, Dr. Jaber Darabi: wonderful people, excellent scientists, magnificent friends. Yu-Xiang Song, Simone Casagrande, Marc Chavalle: my exceptionally competent interns, it was a pleasure to work with you. To my friends and colleagues, whose future shine bright as their path. I always felt good among you, and I hope to continue this way.

*Voor een awesome meisje.*

*Ik zit nu enkele maanden achter op mijn werk,  
maar je bezorgde me de beste tijd van mijn leven.*

*The most disappointing concept I learned in chemical engineering  
was always assuming steady state...*

*because life is not.*

*Marco*

## RÉSUMÉ

Les voitures électriques ont le potentiel de définir le nouvel horizon du transport routier à venir, dont la seule contrainte est le système de stockage d'énergie. C/LiFePO<sub>4</sub> (C/LFP) est un matériau cathodique prometteur pour les batteries aux ions lithium: car il est peu coûteux, non-flammable, et stable. Dans le cadre du projet avec "Automotive Partnership Canada", l'École Polytechnique et l'Université de Montréal ont mis au point un processus de synthèse par fusion pour réduire le prix de production de LiFePO<sub>4</sub> (LFP), de 20 \$/kg à moins de 5 \$/kg. Pour atteindre cet objectif, le processus implique la production de nanoparticules de LFP suspendues dans l'eau, (distribution granulométrique, PSD médian 200 nm) à partir du broyage d'un lingot obtenu par une synthèse en fusion. Une source de carbone est ajoutée lors du broyage (<10 %). Ensuite, l'eau est éliminée par séchage par pulvérisation (jusqu'à 99 %) et la poudre est chauffée dans un four (700 °C pendant 4 h) pour convertir la source de carbone dans une couche de 1 nm à 3 nm de graphite électriquement conductrice, qui recouvre les nanoparticules d'LFP, qui ne conduisent pas d'électricité.

L'élimination des solvants à partir des suspensions solides de nanoparticules demande la même diligence que le séchage des ingrédients pharmaceutiques. Sécher et pyrolyser la suspension simultanément, à la fois donnera un morceau de céramique frittée. Si la suspension de nanoparticules d'LFP sèche dans un four conventionnel, le matériel s'oxyde, s'agglomère et perd de porosité et de surface spécifique. Le séchage par pulvérisation préserve ces propriétés car les temps de contact sont de l'ordre de quelques secondes; de plus, les gouttelettes atomisées sont petites (5 µm à 20 µm) et bien dispersées. Après, un four pyrolyse le précurseur de carbone, sans altérer la structure mésoporeuse interne ni les microparticules de poudre. Le matériel est ensuite imprégné d'électrolyte et appliqué en couche mince dans une batterie. Nous concevons les séchages par atomisation à l'échelle de laboratoire (0.12 m) et pilote avec une unité de diamètre 0.8 m permettant d'évaluer la faisabilité du processus. Nous séchons par atomisation l'LFP avec des précurseurs organiques (lactose et PVA) afin de recouvrir de manière homogène la structure mésoporeuse de la poudre et créer une cage de carbone qui entoure les nanoparticules. Les tests de capacité sur la batterie permettent de déterminer quelle source de carbone recouvre mieux le matériau après la pyrolyse et démontre que la cage en carbone prolonge la durée de vie de la batterie et sa vitesse de décharge.

## ABSTRACT

As fossil fuels become less attractive for powering vehicles, electric cars have the potential to define the new skyline for future road transportation. C/LiFePO<sub>4</sub> (C/LFP) is a promising cathode material for such batteries: inexpensive, non-flammable and stable. As part of the “Automotive Partnership Canada” project, Polytechnique and Université de Montreal developed a melt-synthesis process for LiFePO<sub>4</sub> (LFP), aiming to cut its price from 20 \$/kg to less than 5 \$/kg. To reach this target the process involves grinding an ingot from a melt synthesis batch, to nanosized-particles by means of a wet media mill (particle size distribution, PSD median 200 nm). A carbon source is added during milling (<10%). Then water is removed by spray drying (up to 99%) and the powder is heated in a furnace (700 °C for 4 h) to pyrolyze the carbon source into a 1 nm to 3 nm electrically conductive layer.

Removing solvent from nanoparticle solid suspensions requires the same diligence as drying pharmaceutical ingredients. Simultaneously drying and pyrolyzing the suspension will produce a sintered ceramic chunk. LFP nanoparticle suspensions in water oxidize, agglomerate and lose surface area when drying in a furnace. Spray drying preserves those properties because contact times are on the order of seconds; furthermore, the atomized droplets ensure particles are small (5 μm to 20 μm) and dispersed. A furnace pyrolyzes the carbon precursor, but does not sinter the internal mesoporous structure or sinter the micro-sized powder particles. The material is then impregnated with the electrolyte and applied as a 60 μm thin layer on a cathode sheet of the Li-ion battery. Scale-up from a 0.12 m to a 0.8 m diameter unit determines the process’ feasibility. We spray dry the LFP suspension with the organic precursors (lactose and PVA) to homogeneously coat the LFP mesoporous structure and create a carbon-cage that surrounds the nanoparticles. Battery capacity tests assess which organic source better coats the material after pyrolysis and demonstrate that the carbon-cage extends the battery’s life and discharge rate.

## TABLE OF CONTENTS

DEDICATION . . . . .	iii
ACKNOWLEDGEMENTS . . . . .	iv
RÉSUMÉ . . . . .	v
ABSTRACT . . . . .	vi
TABLE OF CONTENTS . . . . .	vii
LIST OF TABLES . . . . .	xi
LIST OF FIGURES . . . . .	xiii
LIST OF SYMBOLS AND ACRONYMS . . . . .	xxii
LIST OF APPENDICES . . . . .	xxiii
CHAPTER 1 INTRODUCTION . . . . .	1
1.1 Definitions and basic concepts . . . . .	3
1.2 Open problems . . . . .	5
1.3 General research objectives . . . . .	7
1.4 Specific objectives . . . . .	7
1.4.1 Identification of the optimal spray drying conditions . . . . .	8
1.4.2 Deriving an empirical model for bulk density . . . . .	8
1.4.3 Conceive scale-up criteria based on testing in the pilot and laboratory scale dryer, investigate interactions with carbon precursors and elec- trochemical battery tests . . . . .	8
CHAPTER 2 LITERATURE REVIEW . . . . .	10
2.1 Spray drying . . . . .	10
2.2 Scale-up . . . . .	13
2.3 Carbon coating . . . . .	15
2.4 Surfactant . . . . .	17
2.5 Nozzles . . . . .	17
2.5.1 Pressure jet . . . . .	17

2.5.2	Dual fluid . . . . .	18
2.5.3	Effervescent . . . . .	18
2.5.4	Ultrasound . . . . .	18
2.5.5	Rotary atomizers . . . . .	19
CHAPTER 3 METHODOLOGY . . . . .		20
3.1	Laboratory and pilot spray dryers . . . . .	20
3.2	Experimental - laboratory-scale . . . . .	22
3.2.1	Micronization . . . . .	22
3.2.2	Spray Drying . . . . .	22
3.3	Experimental - pilot-scale . . . . .	23
3.3.1	Nanoparticle suspension preparation . . . . .	23
3.3.2	Spray drying . . . . .	24
3.3.3	Calcination and electrochemical tests . . . . .	25
3.3.4	Reagents and Characterization . . . . .	25
CHAPTER 4 ARTICLE 1 - INFLUENCE OF ATOMIZATION CONDITIONS ON SPRAY DRYING LITHIUM IRON PHOSPHATE NANOPARTICLE SUSPENSIONS		28
4.1	Abstract . . . . .	28
4.2	Introduction . . . . .	28
4.3	Experimental . . . . .	30
4.3.1	Micronization . . . . .	30
4.3.2	Spray Drying . . . . .	31
4.3.3	Material Characterization . . . . .	32
4.4	Results and discussion . . . . .	34
4.4.1	Powder Formation . . . . .	35
4.4.2	Particle Size Distribution . . . . .	36
4.4.3	Residual Moisture (Drying Efficiency) . . . . .	37
4.4.4	Yield . . . . .	38
4.4.5	Powder Bulk Density and Flowability . . . . .	38
4.4.6	Mercury Porosimeter . . . . .	39
4.4.7	Nitrogen Physisorption . . . . .	40
4.4.8	X-ray Diffraction . . . . .	42
4.5	Conclusions . . . . .	43
4.6	Acknowledgments . . . . .	44
CHAPTER 5 ARTICLE 2 - $\text{LiFePO}_4$ SPRAY DRYING SCALE-UP AND BINDERS		



FOR IMPROVED CYCLABILITY . . . . .	45
5.1 Abstract . . . . .	45
5.2 Introduction . . . . .	46
5.3 Experimental section . . . . .	47
5.3.1 Nanoparticle suspension preparation . . . . .	47
5.3.2 Spray drying . . . . .	48
5.3.3 Calcination and electrochemical tests . . . . .	49
5.3.4 Reagents and Characterization . . . . .	49
5.4 Results and discussion . . . . .	51
5.4.1 LFP characterization and elemental analysis . . . . .	51
5.4.2 Particle size and powder morphology . . . . .	54
5.4.3 Pyrolysis and carbon layer . . . . .	55
5.4.4 N <sub>2</sub> physisorption porosimetry . . . . .	57
5.4.5 Rheology of the nanoparticles suspension . . . . .	59
5.4.6 Ultrasonication . . . . .	64
5.4.7 Carbon coat chemical analysis . . . . .	65
5.4.8 Electrochemical tests . . . . .	67
5.5 Conclusions . . . . .	71
CHAPTER 6 GENERAL DISCUSSION . . . . .	73
6.1 Powder formation: atomization and drying . . . . .	74
6.2 Suspension density, Nozzle' spray cone angle and infra-red investigation of the nozzle temperature . . . . .	78
6.2.1 Materials and methods . . . . .	78
6.2.2 Slurry density . . . . .	78
6.2.3 IR and nozzle temperature . . . . .	79
6.2.4 Spray cone angle . . . . .	83
6.3 Experimental design and results on the pilot spray dryer . . . . .	85
6.4 Article highlights and scientific contribution as author . . . . .	91
6.4.1 INFLUENCE OF ATOMIZATION CONDITIONS ON SPRAY DRY- ING LITHIUM IRON PHOSPHATE NANOPARTICLE SUSPENSIONS	91
6.4.2 LiFePO <sub>4</sub> SPRAY DRYING SCALE-UP AND BINDERS FOR IM- PROVED CYCLABILITY . . . . .	91
6.4.3 EXPERIMENTAL METHODS IN CHEMICAL ENGINEERING: NU- CLEAR MAGNETIC RESONANCE . . . . .	93
6.5 Article highlights and scientific contribution as co-author . . . . .	94

6.5.1	Spray dried $\text{SiO}_2$ $\text{WO}_3/\text{TiO}_2$ and $\text{SiO}_2$ vanadium pyrophosphate core-shell catalysts . . . . .	94
6.5.2	Spray dried $\text{TiO}_2/\text{WO}_3$ heterostructure for photocatalytic applications with residual activity in the dark . . . . .	95
6.5.3	Water treatment: Mn- $\text{TiO}_2$ synthesized by ultrasound with increased aromatics adsorption . . . . .	98
6.5.4	Ultrasound assisted wet stirred media mill of high concentration $\text{LiFePO}_4$ and catalysts . . . . .	101
6.5.5	Gas-phase fructose conversion to furfural in a microfluidized bed reactor	102
6.5.6	Platinum doped $\text{WO}_3/\text{TiO}_2$ catalyst. . . . .	106
6.5.7	Levulinic acid upgrade to succinic acid with hydrogen peroxide . . . . .	114
6.5.8	Enhanced photocatalytic activity of Pt- $\text{TiO}_2/\text{WO}_3$ hybrid material with energy storage ability . . . . .	116
6.5.9	Ultrasonic intensification to produce diester biolubricants . . . . .	121
6.5.10	Influence of frequency and amplitude on the mucus viscoelasticity of the novel mechano-acoustic frequencer <sup>TM</sup> . . . . .	124
6.5.11	$\text{LiFePO}_4$ synthesis via ultrasound assisted mechanochemistry . . . . .	127
CHAPTER 7 CONCLUSION . . . . .		131
7.1	Summary of work . . . . .	131
7.2	Limitations . . . . .	132
7.3	Future Research . . . . .	133
REFERENCES . . . . .		134
APPENDICES . . . . .		158

## LIST OF TABLES

Table 3.1	Two-fluid, external mixing, air blast atomizer, with bores in $\mu\text{m}$ and a non-protruding tip. . . . .	20
Table 4.1	Two-fluid, external mixing, air blast atomizers; bores in $\mu\text{m}$ ; when assembled the tip is non-protruding. . . . .	32
Table 4.2	Particle size distribution: (a) measured $D_{4,3}$ arithmetic mean diameter $\bar{x}$ and standard deviation $s$ , (b) log-normal, (c) Weibull and (d) skew normal distribution models, regressed by minimization of the residual sum of squares over non-zero measured values. . . . .	37
Table 4.3	BET surface area by nitrogen physisorption ( $\pm 2\%$ ), $\phi$ pore volume for pores smaller than 92 nm, $D'_{[4,3]m}$ , $D''_{[4,3]m}$ primary and secondary particle mode, $T_{in}$ , $T_{out}$ inlet outlet drying temperature, $\omega$ solid mass fraction, $u_g$ atomizing gas velocity, $\Delta_{H_2O}$ residual water (water lost during degassing). . . . .	37
Table 5.1	Spray dried powders from LFP suspensions with additives in water, all slurries include the Tween-20 surfactant. PSD: secondary particle size mode and (distribution at one standard deviation). Carbon: total carbon relative to bone dry LFP powder ( $CI_{n=3}^{95\%}$ ). $S_a$ : specific surface area ( $CI_{n=3}^{95\%}$ ), $V_{\text{pore}}$ : pore volume ( $CI_{n=3}^{95\%} < 0.01 \text{ cm}^3 \text{ g}^{-1}$ ) and porosity $\varphi$ . Average crystallite size considering the 3 most intense peaks (Scherrer equation), and $\gamma\text{-Li}_3\text{PO}_4$ composition (Retveld refinement). “Py”: pyrolyzed powders. “US”: ultrasonicated suspension. . . . .	53
Table 5.2	Rheology of LFP suspensions; the apparent viscosity ( $\mu$ , $\pm 0.05 \text{ mPa}\cdot\text{s}$ ) increases with: increasing solid mass fraction ( $\omega_{\text{LFP}}$ ) and increasing PVA binder content ( $\omega_{\text{PVA}}$ ), while $\mu$ decreases with increasing temperature ( $T$ ) and increasing shear rates ( $\dot{\gamma}_{sr}$ ). “US”: ultrasonicated suspension. . . . .	62
Table 5.3	XPS elemental composition (atomic $\pm 0.2\%$ ). . . . .	65
Table 5.4	Identification of functional groups and their at. % obtained from high resolution XPS spectra, fitting of the C1s (top) and O1s peaks (bottom). Raman intensity ratio between carbon’s D and G bands (bottom, last column). . . . .	66
Table 6.1	Experimental design and results of the pilot spray dryer (1/5). . . . .	86
Table 6.2	Experimental design and results of the pilot spray dryer (2/5). . . . .	87

Table 6.3	Experimental design and results of the pilot spray dryer (3/5). . . . .	88
Table 6.4	Experimental design and results of the pilot spray dryer (4/5). . . . .	89
Table 6.5	Experimental design and results of the pilot spray dryer (5/5). . . . .	90
Table 6.6	N <sub>2</sub> physisorption data. . . . .	97
Table 6.7	AMO's degradation regressed zero and second order kinetic constants.	98
Table 6.8	BET surface area by nitrogen physisorption, results are within $\pm 3\%$ (95% confidence interval), $\phi$ pore volume, $\Delta_{dV(d)}$ BJH $dV(d)$ mesopore median, <i>coke</i> carbon content (0.05% precision, 95% confidence interval).	105
Table 6.9	$D$ crystallite size (standard deviation among Pt signals); Riet.Pt Rietveld refinement of the Pt phase, the complementary fraction was anatase TiO <sub>2</sub> ; BET surface area by nitrogen physisorption, results are within $\pm 3\%$ ( $n = 3$ , 95% confidence interval C.I.); $\phi$ pore volume (C.I. $\pm 8 \times 10^{-5} \text{ cm}^3 \text{ g}^{-1}$ ); $\Delta_{dS(d)}$ $dS(d)$ characteristic pore median (ads. BJH for mesopore and QSDFT for micro); $V-t$ micropore area.	108
Table 6.10	Table of N <sub>2</sub> physisorption data. . . . .	120
Table 6.11	Initial DOE regression. . . . .	125
Table 6.12	Refined DOE regression. . . . .	126

## LIST OF FIGURES

Figure 1.1	Crystal structures that intercalate lithium ion.[1] (a) Olivine $\text{LiFePO}_4$ confines $\text{Li}^+$ through a tunnel-like structure, this nearly close-packed hexagonal array of oxides centers provides little free volume for $\text{Li}^+$ to diffuse. The layered structure of $\text{LiCoO}_2$ (b) and $\text{TiS}_2$ (c) is more open and lets $\text{Li}^+$ to migrate bidimensionally. . . . .	6
Figure 2.1	Schematic representation of particle morphologies. a) Layered with central core. b) Layered with central void. c) Solid foam, closed cell. d) Solid foam, open cell. e) Particle with embedded nanoparticles. f) Composite shell. g) Irregular, with external voids and internal concentration gradients.[2] . . . . .	11
Figure 2.2	Summary of the behaviors according to the nanoparticle interactions, which determine the shell permeability and consequently the Darcy pressure.[3] . . . . .	12
Figure 2.3	Buckling time as a function of ionic strength. The experimental data measured for drying droplets of zirconia suspensions (circles) are well described by the model. The photographs show the grains obtained after full drying for different initial ionic strengths of the suspension, corresponding to different initial states (fully dispersed or suspension of fractal aggregates).[3] . . . . .	12
Figure 2.4	Modeling droplet size distribution, temperature profiles, relative humidity, and cyclone efficiency give a better basis for spray-drying scale up, instead of trial-and-error approaches.[4] . . . . .	13
Figure 2.5	Control volume and transport terms for the spray dryer energy balance.[5]	14
Figure 2.6	Illustration of the preparation process and the microscale structure of triple carbon coated $\text{LiFePO}_4$ composite.[6] . . . . .	16
Figure 3.1	Schematic of the Yamato GB-22 spray dryer, co-current mode. . . . .	21
Figure 3.2	GEA Mobile minor spray dryer setup. . . . .	21
Figure 3.3	Typical particle size distribution and model fit for the feed material. . . . .	22
Figure 3.4	Yamato GB-22 spray dryer, co-current mode.[7] . . . . .	23
Figure 4.1	Crystal structures that intercalate lithium ion.[1] . . . . .	29
Figure 4.2	Typical particle size distribution and model fit for the feed material. . . . .	31
Figure 4.3	Yamato GB-22 spray dryer, co-current mode.[7] . . . . .	32

Figure 4.4	Semi-spherical secondary particles. The image shows both doughnut shape and spherical particles but all of the particles are toroidal. Close-up: When holes face the SEM detector, the doughnut-shape morphology is evident. . . . .	34
Figure 4.5	Poor atomization conditions creates semi-spherical and fragmented material. The lack of carbon coating makes the non electrically conductive LFP surface look glassy. . . . .	35
Figure 4.6	$T_{inlet}$ 200°C, atomization velocity 140 m s <sup>-1</sup> , nozzle n.4, mass fraction 0.32 g g <sup>-1</sup> . . . . .	36
Figure 4.7	Nozzle n.4, same batch feed material, at a mass fraction of 0.32 g g <sup>-1</sup> at different inlet temperatures. The bars represent the PSD standard deviation. . . . .	36
Figure 4.8	Data from different experimental conditions correlate with respect drying temperature and atomization gas velocities. . . . .	38
Figure 4.9	Each column represents a different batch of milled material with respect solid loading and primary particle size. Particle density is invariant, but secondary particle size influences the flowability. . . . .	39
Figure 4.10	Mercury porosimeter curves for sample n. 2, on the abscissa, the calculated pore diameter from pressure, using the Washburn equation, assuming cylindrical pores. . . . .	40
Figure 4.11	Sample n.2 isotherms, STP at 0°C and 101 kPa . . . . .	41
Figure 4.12	BJH adsorption dVolume(diameter) at different inlet temperatures and secondary particle sizes. . . . .	42
Figure 4.13	Theta-2-theta acquisition at 50 kV and 40 mA, using a Cu anode, Gonio mode, CuK $\alpha$ sideband removed. . . . .	43
Figure 5.1	GEA Mobile minor spray dryer setup. The recovery yield averages 80%: 10% of the material coats the chamber and another 10% escapes the cyclone. . . . .	48
Figure 5.2	The spray dried LFP (red, bottom) presents broad peaks; calcination improves crystallinity and the sample diffracts three times more (black, top). Diffraction patterns between samples are the same (Table 5.1). Top-right insert: # LiFePO <sub>4</sub> , * Li <sub>3</sub> PO <sub>4</sub> . . . . .	52

Figure 5.3	The primary particles suspended in water agglomerate to secondary particles during spray drying. The resulting powder is homogeneous and different samplings makes minimal deviations. However sampling the suspension leads to greater uncertainty, due to instrument resolution and irregular particle shape. Error bars for a $CI_{n=5}^{95\%}$ . . . . .	54
Figure 5.4	Particle morphology by SEM: “a” to “d” belong to the spray dried neat LFP suspension (adding lactose does not change the texture). However calcination of LFP powders without carbon precursor sinters the primary particles together “g” and “h”, but not the secondary: “e” and “f”. Lactose prevents sintering and the powder remains nanostructured: “i” to l”. Adding PVA changes the morphology of the spray dried material, creating submicron rods: “m” to “o”. Calcination of this material breaks some particles, revealing that they are hollow “p”.	56
Figure 5.5	Carbon coat morphology by TEM after pyrolysis: lactose decomposes into a thin layer of semi-graphitic carbon (arrows, 1 nm to 3 nm, “a”), coating the primary LFP particles “b”. The addition of PVA superimposes over the thin layer of lactose a grid-like carbon structure interconnecting the primary particles (circled, “c”). Ultrasonication depolymerizes PVA into a short-chain polymer so the carbon grid is now smaller “d”. . . . .	56
Figure 5.6	$N_2$ adsorption-desorption isotherms at 77 K, STP at 0 °C and 1 atm. .	57
Figure 5.7	Comparison between BJH (top) and NLDFIT (bottom) pore size distribution methods. Spray dried powders with (red, black green) or without carbon precursors (blue) shows similar pore morphology in the meso-macro pore region 5 nm to 300 nm. Calcination pyrolyzes the carbon precursors and partially sinters the LFP primary particles (open symbols). . . . .	58
Figure 5.8	The shear increasing isotherms at 25.0 °C (upward triangles) overtop the shear decreasing curves (downward triangles). Viscosity increases with the solid mass fraction of LFP in water (blue, red, black). The addition of less than 7 % lactose does not modify the rheology of the material; while PVA increases the viscosity of the slurry (green). Error bars for a $CI_{n=3}^{95\%}$ . . . . .	60

Figure 5.9	Eq. 5.6 model regression for 415 data points at different solid concentrations, increasing shear rates, temperatures and binder loadings. Most deviations come from low instrument sensitivity at low torque (when $\mu < 3 \text{ mPa}\cdot\text{s}$ ) and low shear rate ( $\dot{\gamma}_{sr} < 50 \text{ s}^{-1}$ ). . . . .	63
Figure 5.10	(a) XPS spectra for the different carbon coating and control sample, and high resolution spectra of C1s (b) and O1s (c) for LFP-LP-Py. (d) Raman spectra, the vertical bars are the $CI_{n=3}^{95\%}$ for each material. The small peak at $950 \text{ cm}^{-1}$ correlates with the stretching modes of $\text{PO}_4^{3-}$ . . . . .	65
Figure 5.11	Preliminary test of cyclability at 0.1C discharge rate. PVA creates larger secondary particles, and a material with poor cyclability. Adding PVA and lactose stabilizes the trend, despite the same particle size. Smaller particles improve the discharge capacity. . . . .	67
Figure 5.12	Cyclability at 1C discharge rate, and 0.1C for the neat LFP and the colloidal silica. Error bars represent 1 standard deviation, $n=2$ . Adding PVA significantly improves the cyclability of the battery vs. the lactose based material ( $p < 0.02$ ). . . . .	68
Figure 5.13	Normalized cyclability at 1C discharge rate (one every 10 cycles is conducted at 0.1C and not shown on the graph for simplicity). Lactose-PVA confer greater stability, the coin-cell battery would retain 80% of the initial capacity after 1700 cycles (vs. lactose: 1100 cycles). Ultrasonication shortens the PVA's chain length and induce instability in the trend. . . . .	69
Figure 5.14	Rate performance (bottom-left axes, symbols) and Galvanostatic curves (top-right). The addition of high-Mw PVA (black lines and upward triangles) creates an extended carbon grid that better distributes the electric charge across the LFP nanoparticles, improving the discharge capacity. . . . .	70
Figure 5.15	Discharge curves at increasing C-rates. An extended carbon-grid (solid line) dissipates the charge more efficiently at high C-rates with respect to a shorter carbon-grid (dashed) or no grid (dotted). . . . .	71
Figure 6.1	Three models describe the measured particle size distribution: the skew-normal distribution has the best fit ( $R^2 > 99\%$ ). . . . .	74
Figure 6.2	Nozzle n.4, same batch feed material, at concentration of 0.32 wt./wt. The bars represent the particle size distribution's standard deviation. . . . .	75
Figure 6.3	Bars represents the measured spray dried particles' standard deviation, not all are reported. . . . .	77



Figure 6.4	The slow evaporation rate allows to identify the spray pattern. Temperature (in °C) is displayed on the right, with a color-coding gradient.	79
Figure 6.5	Temperature (in °C) is displayed on the right, with a color-coding gradient. . . . .	80
Figure 6.6	Low liquid flows reach higher temperatures as they heat up flowing through the nozzle. Temperature (in °C) is displayed on the right, with a color-coding gradient. . . . .	81
Figure 6.7	At 180 mL min <sup>-1</sup> the liquid contact time inside the nozzle decreases to 4 s, decreasing also the specific heat flow from the hot metal. Temperature (in °C) is displayed on the right, with a color-coding gradient. .	81
Figure 6.8	The “fog” inside the chamber demonstrates that the particles dry at the wet bulb temperature and do not overheat. Temperature (in °C) is displayed on the right, with a color-coding gradient. . . . .	82
Figure 6.9	Error bars for a $CI_{n=3}^{95\%}$ , the difference between the two groups is statistically significant regarding temperature ( $p < 0.05$ , two-tail $t$ -test), but not regarding the liquid flowrate. Data in the transition zone are not regressed. . . . .	83
Figure 6.10	Nozzle and top portion of the chamber. . . . .	84
Figure 6.11	Nitrogen adsorption-desorption isotherms of the calcined control and hybrid powders.[8] . . . . .	96
Figure 6.12	Correlation between US power and adsorption kinetic constant for Amoxicillin. . . . .	99
Figure 6.13	Experimental and regressed data validation. . . . .	100
Figure 6.14	Milling vanadyl pyrophosphate over time. The particle size distribution assume a bimodal trend and most material remains above 1 μm in size without ultrasound (a). Ultrasound milling speeds-up the process, achieving mostly submicron primary particles (b). . . . .	101
Figure 6.15	All fresh catalysts with loading <5% express the same trend as the bare support. Higher loading and used catalysts have occluded pores that decrease the amount of N <sub>2</sub> adsorbed. . . . .	103
Figure 6.16	The pore fraction below 10 nm is filled as the WO <sub>3</sub> loading and coke formation increases. . . . .	104
Figure 6.17	Pore volume and specific surface area model fitting. . . . .	104

Figure 6.18	Stacked spectra recorded with the same conditions and smoothed with an 11 points cubic function, Cu- $k\alpha$ sidebands were removed: coke deposits on the used sample reduced the signal to noise ratio. Four sharp Pt signals ( $39.6^\circ$ , $46.0^\circ$ , $67.4^\circ$ , $81.2^\circ$ ) and their respective planes [hkl] have been identified. The remaining peaks belong to the Titania support (anatase).[8] . . . . .	109
Figure 6.19	Fresh 1.5 % Pt over $\text{WO}_3/\text{TiO}_2$ particles. The LABE detector enhanced the signal from heavy elements and the Pt crystals appeared as bright white spots.[9] . . . . .	110
Figure 6.20	Fresh 1.5 % Pt over $\text{WO}_3/\text{TiO}_2$ particles. The metallic platinum crystals appeared as multi-facets prisms. Considering their sizes (submicron), the crystallite size of 88 nm (XRD) and the crystal structure of metallic Pt (cubic), we could conclude that each crystal was composed of several crystallites. . . . .	111
Figure 6.21	Used “t12” catalyst’s surface. Shiny “metallic-lookalike” coke chunks were dispersed around the spherical catalyst particles after mechanical breakage. Some particles broke as well. . . . .	111
Figure 6.22	SEM and EDS mapping of the used “t12” catalyst’s surface. Carbon (C, red) partially covered the surface and suppressed the underlying elements’ signals. Oxygen (O, blue) was predominant were titanium was also present (Ti, yellow), less were carbon was present and absent were platinum was present (Pt, violet). Tungsten (W, green) was homogeneously distributed along with titanium. . . . .	112
Figure 6.23	Catalyst particle size distribution in logarithmic scale. Coke deposits broadened the peak and increased the average. . . . .	112
Figure 6.24	The fresh catalyst was mesoporous and after reaction resulted microporous. In the latter, the adsorption rapidly grows to plateau ( $P/P_0$ 0.0005-0.1) and the type 4 hysteresis remained open. This is often associated to narrow slit micropores. . . . .	113
Figure 6.25	Correlation between catalyst loading and selectivity.[10] . . . . .	114
Figure 6.26	Interaction of the $\text{H}_2\text{WO}_4$ catalyst with the levulinic acid substrate. This octagonal adduct enhances the formation of methyl succinate.[10]	115
Figure 6.27	$\text{N}_2$ physisorption isotherms at different catalyst loadings (0.7 mm I.D. nozzle). The lack of hysteresis superimposes the adsorption and desorption isotherms. 0.8 % Pt maximize adsorption. . . . .	117

Figure 6.28	Porosity and SSA for the two set of spray drying conditions, with regression and 95 % confidence bands. . . . .	118
Figure 6.29	The Pt-W-Ti composite formulation creates a network of micropores that dictates the high SSA (0.7 mm I.D. nozzle). Meso- and macropores contribute for 5-10 % of the total SSA, invariant with the Pt loading.	119
Figure 6.30	Pareto chart of standardized effect. Response variable: FFA concentration at 1 h (red) and 3 h (black). 2.3 is the value above which the variable (T = temperature, P = ultrasound power and Xj = alcohol/FFA molar ratio) has a significative effect ( $\alpha = 0.1$ ) . . . . .	121
Figure 6.31	Viscosity of biolubricants vs T and logarithmic regression and extrapolation up to 100 °C. . . . .	122
Figure 6.32	Mucus becomes less viscous at high shear rates. . . . .	124
Figure 6.33	Work of adhesion (mN/m) response surface when the mucin fraction reaches 4 %. A saddle contour identifies the areas where WA is minimum (cold colours): lowest frequency with highest salt concentration and high frequency with no salt. . . . .	126
Figure 6.34	Type IV(a) isotherms, glucose arranges the material in plate-like particles (blue and red) while cellulose and lignin create a bottle-neck network (green). . . . .	128
Figure 6.35	Pore size distribution: when the material has two sharp peaks around 2 nm and 4 nm, it exhibits higher EC performances. . . . .	129
Figure 6.36	Pore volume contour plot: the aberrant data (sample 215) has been excluded. . . . .	130
Figure A.1	On the left an old ('80) FT-NMR Spectrometer; a pneumatic arm lowers the sample between the 80 MHz resistive magnets. An RF pulse generator activates the test sample in the center of a static magnetic field (N-S) and an RF receiver measures the fluctuations. The recorded spectrum (FID, free induction decay) sums multiple scans into a sinusoid that decays exponentially with time. A Fourier-Transform of the FID identifies the dominant frequencies that belongs to atoms in the molecule. . . . .	160

- Figure A.2 The  $^1\text{H}$  spectrum for a derivative of 6-methylhept-6-en-2-one in  $\text{CDCl}_3$ , recorded at 400 MHz at rt.[11] The signal from “A” has three peaks (t: triplet) and its integration gives an area that is normalized to 1.0 (in green, one proton). Each peak has a distinctive chemical shift (blue) and their distance (in Hz) measure the  $J$ -coupling constant (violet). The “ $J$ -tree” (violet) is a representation of the Pascal’s triangle: a rule that correlates the shape of the NMR signal with the number of vicinal protons. “A” couples with the two protons in “G” and creates a triplet. “B”, “C”, “E”, “F” and “H” are all singlets (s), meaning that close to them there are no protons available. “E”, “F” and “H” belong to the methyl groups, as their area integral is three times the one from “A”. Between them “E” in the most deshielded group: the electron cloud is displaced towards the double bond, so the peak appears at high chemical shifts. Unlike in the methyl group, where all three protons are chemically equivalent, the protons bonded to a  $\text{sp}^2$  carbon are not. Therefore “B” and “C” appear as two distinctive singlets as none of them correlates with a vicinal proton, with an integral of one. “D” follows the same rule as “A”, but the integral is double as it has two protons. “G” has also two protons, but it also has a more complex coupling: on the left it couples with one proton from “A” and on the right with two protons from “D”. Because the two couplings have different  $J$ -constants (14.3 and 6.6 Hz), the doublet (d) from “A” splits the triplet from “D” in two branches. Following the Pascal’s triangle rule, this shape (dt) appears with five peaks, as the two branches in the center overlap and increase in intensity. . . . . 163
- Figure A.3 NMR bibliometric network:[12, 13] the size of the keyword is proportional to the number of occurrences (from 80 to 640). The distance between keywords shows how two topics closely relate each other. The number of links was limited in order to elucidate the main connections between different areas. . . . . 166

Figure A.4	On the left: non-spinning samples' peaks appear broader (blue). A spinning sample sharpens the peaks and allow multiplicity detection, but creates secondary peaks —sidebands— equally spaced (3 Hz, which corresponds to the rotational sample's rate) from the main peak (red). On the right: a poorly shimmed and phased 100 MHz proton spectrum (blue) and a 400 MHz one (red). On the latter each peak is symmetrical (good shim and phase) and the stronger magnet resolve the multiplicity (dddd) for the two exocyclic doublebond's protons ( $H^a$ and $H^{a'}$ ). . . .	171
Figure A.5	$^{13}C$ spectra of a solution of an organic compound in $(CD_3)_2SO$ , recorded at 100 MHz in J-MOD, to separate primary and tertiary carbons (top peaks) from secondary and quaternary ones (bottom). From bottom to top after: 2 (red), 4 (yellow), 8 (green), 16 (cyan), 32 (blue) and 256 scans (violet), the $s/n$ increases from 13, 19, 27, 35, 52 to 150 (top peak). . . . .	173
Figure B.1	LEI detector: spray dried spherical VPO secondary particles, in detail the primary particles composing the aggregates. LABE detector: in detail the detector can better visualize the vanadyl primary particle in respect to the silica coating. . . . .	176
Figure B.2	EDS spectrum (left), note how vanadium is not detected since is coated with a layer of silica. EDS mapping (right) of a spray dried core-shell VPO catalyst, the external silica shell (red), covers the bulk vanadyl pyrophosphate salt (green). . . . .	177
Figure B.3	SEM (a) and TEM (a') of VPO precursor. . . . .	178
Figure C.1	Sketch of the wet media mill, reducing the size of the primary particle from 27 $\mu m$ to 200 nm took 4 h for a batch of 50 kg. . . . .	190
Figure C.2	Model regression for estimating the carbon contribution of each precursor. . . . .	190
Figure C.3	High-resolution spectra of C1s and O1s of the pyrolyzed samples: LFP-L-Py with lactose (a-b), LFP-LPU-Py with lactose, PVA and ultrasonicated (c-d) and LFP-neat-Py calcined with no carbon precursor (e-f). . . . .	191

**LIST OF SYMBOLS AND ACRONYMS**

C/LFP	Carbon coated Lithium Iron Phosphate, C/LiFePO <sub>4</sub>
EG	Exfoliated Graphene flakes
GO	Graphene Oxides sheets
LFP	Lithium Iron Phosphate, LiFePO <sub>4</sub>
LIB	Lithium Ion Battery
LMO	Lithium metal oxide
PSD	Particle Size Distribution
VPP	Vanadyl Pyrophosphate, (VO) <sub>2</sub> P <sub>2</sub> O <sub>7</sub>

**LIST OF APPENDICES**

Appendix A	ARTICLE 3 - EXPERIMENTAL METHODS IN CHEMICAL ENGINEERING: NUCLEAR MAGNETIC RESONANCE . . . . .	158
Appendix B	Additional scientific contribution as co-author . . . . .	175
Appendix C	CHAPTER 5 - SUPPLEMENTARY INFORMATION . . . . .	190
Appendix D	MILESTONES . . . . .	192

## CHAPTER 1 INTRODUCTION

The obnoxious beauty of fossil fuels is due to their ability of disposing of their energy quickly, on-demand and to store it in small volumes due to its high energy density. Renewable energy sources instead, are fundamentally discontinuous. Therefore these centuries global effort, to reduce carbon emission and to switch to renewable energy sources, is mostly focused to create an efficient and economic energy storage system. Bloomberg's "New energy finance" report forecast that by 2050, 50 % of the global electric generation will be met by wind and solar, with an 11.5 trillion dollar investment in new power generation. This investment will be accompanied by 0.5 trillion dollar in new battery capacity. Indeed, energy storage is the missing piece of the puzzle for renewable energies. Energy storage becomes particularly important when looking at transportation vehicles, for example gasoline and diesel vehicles pollute and require more and more sophisticated systems to decompose the exhaust pollutants to CO<sub>2</sub>. In fact, Europe will ban diesel car sales by 2020, due to their unacceptable pollution standards. On the other hand, electric cars, are more expensive to purchase, although the cost is primarily related to the battery pack. A gasoline car is more expensive to manufacture compared to an electric car without its "battery", the gasoline car has also more mechanical components, requires more maintenance and fluids to operate. In collaboration with Université de Montréal and CANMET materials, we developed a new process to make inexpensive cathode materials for Li-ion batteries for automotive applications. In 2010 the cost of a Li-ion battery pack was 1000 USD kWh<sup>-1</sup>, in 2014 500 USD kWh<sup>-1</sup>, and in 2018 dropped to 200 USD kWh<sup>-1</sup>. In a battery the most expensive component is the cathode material, which represents 20 % of the total cost. In the melt-synthesis process we prepare ingots of LiFePO<sub>4</sub> with inexpensive ore-grade substrates.[14] The ingots from the melt are ground with a jaw crusher, roller grinder and ultimately with a wet media mill, to reach a nanoparticle solid suspension in water,[15] as a 200 nm particle size enhance the performance and cyclability of the battery.[16] Controlling the primary particle size (200 nm) is critical to achieve a high flow of Li-ions during the charge/discharge of the battery. Unlike other cathode materials, LiFePO<sub>4</sub> has a mono dimensional tunnel-like crystalline structure, in which the Li-ions intercalate. This limits the diffusivity of the Li-ion inside the material and to achieve fast charging and discharging properties, a small primary particle generates a high specific surface area and therefore, a high Li-ion flow. To achieve that, we have to grind the material to the nanoparticle size and a suitable instrument is a wet media mill, which creates a nanoparticle suspension in water. But, removing solvent from nanoparticle solid suspension requires the same diligence as drying pharmaceutical ingredients. LiFePO<sub>4</sub>



nanoparticles suspension in water oxidize, sinter and  $\text{Li}_3\text{PO}_4$  segregates on the surface when they dry in a furnace. Spray drying preserves the material properties because contact times are on the orders of seconds; furthermore, the atomized droplets ensure particles are small and dispersed. This PhD thesis regards spray drying this LFP nanoparticle suspension into a bone dry dust and testing their performance once assembled in a battery. However, the  $\text{LiFePO}_4$  material also suffers from poor electrical conductivity, to resolve this issue we spray dry the mixture with organic binders dissolved in the suspension. Spray drying coats the primary particles with the organic binders, it aggregates the nanoparticles in a micron sized secondary particle and removes the solvent. Finally pyrolysis converts the carbon precursors into conductive carbon, which improves the electric conductivity of the active material. The pyrolyzed powder is then mixed with the electrolyte, homogenized in a tube roller, painted on an aluminum current collector and assembled in a coin cell battery for testing.

## 1.1 Definitions and basic concepts

Li-ion batteries (LIB) are rechargeable accumulators where, during discharge, electrons flow from the negative electrode to the positive one through an external electrical circuit, while the lithium ions close the internal circuit by diffusing from the anode to the cathode within the cell unit. Anode (graphite,  $C_6$ ) and cathode (LFP,  $LiFePO_4$ ) are separated by a semi-permeable mesoporous polyethylene membrane, that allows only  $Li^+$  to pass through (good ionic conductivity) but avoids electrons to flow directly across (avoid an internal short circuit). LIB have the peculiar characteristic in which anode and cathode intercalates  $Li^+$ . The liquid electrolyte solvates the  $Li^+$  and allows its diffusion through the cell, withstanding severe redox conditions without decomposition.[17] To increase the medium conductivity; salts ( $LiPF_6$ ,  $LiBF_4$  or  $LiClO_4$ ) are added to the organic solvent (ethylene carbonate, dimethyl carbonate, or diethyl carbonate).[18]

In  $LiFePO_4$ , the lithium atom has a positive +1 charge, the iron +2 and the phosphate group balances with a -3 charge. When  $Li^+$  deintercalates, the cathode material becomes  $FePO_4$ , with  $Fe^{3+}$ . [19] During discharge  $Li^+$  deintercalates from the higher redox potential graphite anode:



$Li^+$  diffuse through the membrane and reaches the cathode, then  $Li^+$  ion intercalates the  $Fe^{3+}PO_4^{3-}$ , which gets reduced to  $Fe^{2+}$ :



The reaction is reversible by imposing an external electromotive force during the charge process.[20]

The C-rate is the rate at which a battery discharges relative to its maximum capacity. At 1C the battery discharges in 1 h, at 0.1C in 10 h and at 2C in 30 min, for automotive purposes the average C-rate is 0.5C-1C, with peaks of 10C during acceleration. High C-rates are more demanding and stress the battery more and represent transportation applications best.

The capacity of a battery (Ah for a specific C-rate) is the coulometric capacity, the total Amp-hours available when the battery is discharged at a certain discharge current (specified as a C-rate) from 100 percent state-of-charge to the cut-off voltage. Capacity is calculated by multiplying the discharge current (in Amps) by the discharge time (in hours) and decreases

with increasing C-rate.

The cyclability of a battery is the number of cycle of charge-discharge the battery experiences before it fails to meet specific performance criteria.

## 1.2 Open problems

Lithium-ion batteries power our life: cellphones and computers count in billions of units, all with a lithium-ion battery inside. Technology aims to scale-up batteries to the automotive industry and stationary energy storage systems.[21] Towards this goal, batteries having high efficiency, long-life and low-cost are the best choices to effectively transition to electric vehicles and decrease our dependency on fossil fuels; while electric storage units create a flexible and reliable grid system smoothing-out the fluctuating supply from renewable sources.[22] The cathode represents the bottle-neck of this technology, as its capacity is one order of magnitude lower than the graphite anode.  $\text{LiCoO}_2$ , at  $273 \text{ mA h g}^{-1}$ , is the cathode of choice for electric vehicles, but is costly and has safety and environmental issues.[23]  $\text{LiFePO}_4$  has a lower capacity ( $170 \text{ mA h g}^{-1}$ ) but costs less, is thermally stable, and its precursors are environmentally benign.[24, 25] Lithium-sulfur cells with a glass solid-state electrolyte promise to be the next generation batteries, but despite their outstanding cycle life (above 15000), and improved capacity (reaching  $500 \text{ mA h g}^{-1}$ ) this technology is still young and is unknown whether it will be industrially scalable and cost-effective.[26] Commercial  $\text{LiFePO}_4$  batteries discharging at 2.5C-rate maintain their temperature below  $55^\circ\text{C}$  and in case of short-circuit would not sustain a thermal-runaway and ignite.[27, 28] On the other hand,  $\text{LiFePO}_4$  material has a poor electrical conductivity and slow  $\text{Li}^+$  diffusivity in the crystalline matrix. The addition of carbon black[29] and coating with a carbon layer or metal oxide increases the electrical conductivity[30, 31] while doping it with cations improve the  $\text{Li}^+$  diffusivity.[32] Carbon nanotubes (CNT) demonstrated high power output and excellent cycling performance in a  $\text{ZnFe}_2\text{O}_4\text{-C/LiFePO}_4\text{-CNT}$  battery, but only at a laboratory scale (10000 cycles at 10C, retained 85% of the initial capacity).[33] Other laboratory scale innovations improve the wettability by nanostructuring the material: a greater specific surface area puts more material in contact with the electrolyte, which increases  $\text{Li}^+$  flow rate across the cathode while nanoparticles shortens the diffusion path and lowers the mass transfer resistance across the material.[34] Moreover, flame-spray pyrolysis demonstrated the importance of controlling the size of the powder also at a micron-scale level.[35] Coupling  $\text{LiFePO}_4$  with iodine modifies the redox cycle and improves the energy density[36] and different carbon precursors lead to a better conductive carbon layer.[37]

It is important to stress that in the optic of sustainable development, new materials, processes and products have to be sustainable. A patented melt-synthesis process[38] cuts the costs of raw material manufacturing by an order of magnitude, the melt-synthesized LFP achieves an optimal elemental dispersion and crystal structure[39] and it can potentially recycle the spent material at the end of its life. A melt-synthesis process can recover the inorganic

salt components of the cathode, burn-off the carbon and plastic components of the battery casing and separator, thus allowing battery's recycling of the main components. The melt-synthesis process requires then to grind the melted ingots to nanometric particles:  $\text{Li}^+$  flow increases six orders of magnitude by reducing the particle size from micron to nano size while creating a mesoporous structure: both specific power and cyclability improve.[40] In fact, lithium ion diffusivity through the olivine crystal matrix of LFP is low compared to the more open structures of  $\text{LiMnO}_2$ ,  $\text{LiCoO}_2$  and  $\text{TiS}_2$  (Figure 4.1) and varies from  $10^{-11} \text{ m}^2 \text{ s}^{-1}$  to  $10^{-18} \text{ m}^2 \text{ s}^{-1}$ . [41] LFP electrical conductivity is also low at  $10^{-7} \Omega^{-1} \text{ m}^{-1}$ .

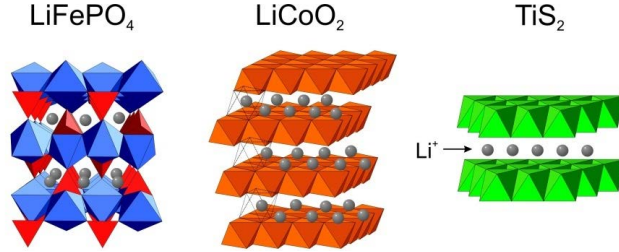


Figure 1.1 Crystal structures that intercalate lithium ion.[1] (a) Olivine  $\text{LiFePO}_4$  confines  $\text{Li}^+$  through a tunnel-like structure, this nearly close-packed hexagonal array of oxides centers provides little free volume for  $\text{Li}^+$  to diffuse. The layered structure of  $\text{LiCoO}_2$  (b) and  $\text{TiS}_2$  (c) is more open and lets  $\text{Li}^+$  to migrate bidimensionally.

We solve those shortcomings by reducing the LFP powders to the submicron and nano particle range,[42] and coating with a 2 nm electron-conductive carbon layer.[43, 1] Lithium ion diffuses through the olivine crystal structure of  $\text{LiFePO}_4$  to the electrolyte medium faster when the specific surface area of the material is increased.

There are several commercial processes to synthesize the nano-structured cathode material for Li-ion batteries: sol-gel process, electrochemical synthesis, solution co-precipitation, hydrothermal synthesis, and flame-spray pyrolysis.[44] All these methods involve processing large quantities of solvent with solid mass fractions ranging from 10% to 70%. Drying is a critical step and controlling the temperature during the process is important to maintain the desired material morphology.[45] Removing solvent in furnaces changes the nano-structure, oxidizes the surface, agglomerates the particles, occludes the pores and change the crystal structure.[46] Drying in fluidized bed dryers is a discontinuous process divided in multiple drying and comminution steps, each lasting 10 min to 60 min: as the powder dries, it agglomerates. Therefore the resulting granules need to be reduced in size between each step to be able to control the residual moisture of the final material.[47] Spouted bed dryers have 10 to 15 times the drying rate of a conventional spray dryers but only fluidize big particles ( $>200 \mu\text{m}$ ). [48] Plasma-spraying is a novel technology for delivering nanometric ( $<30 \text{ nm}$ )

dried particles,[49] but the cost for this technology discourages any industrial scale up for LFP. It is also unclear if it is possible to maintain the olivine crystal structure during the plasma process. Spray drying is a robust technology used in the pharmaceutical, food and catalyst industries to dry solutions or suspensions economically and quickly (0.1 s to 60 s) at low temperatures (60 °C to 200 °C), preventing degradation and achieving a fine granule size (2  $\mu\text{m}$  to 300  $\mu\text{m}$ ).

We demonstrate the scale-up feasibility for spray drying melt-synthesized  $\text{LiFePO}_4$  and organic precursors that self-assemble into a carbon cage, which increases the cathode cyclability, similarly to carbon nanotubes.[50] Melt-cast processes reduce the reactant cost by 40 %, starting from lower-grade purity precursors, but still yield a pure, crystalline material.[51, 52] In our process, a furnace produces LFP ingots. Subsequently, a jaw crusher, a roller grinder and a wet media mill reduce the size of the material to the nanoscale in water. Organic precursors are mixed and spray drying desiccates the suspension. In the process, a two-fluid nozzle atomizes the suspension with compressed air. The hot air dries the microscopic droplets (from 1  $\mu\text{m}$  to 100  $\mu\text{m}$ ), and the suspended nanoparticles (primary particles, facing sizes ranging from 0.07  $\mu\text{m}$  to 0.2  $\mu\text{m}$ ) agglomerate into a porous, spherical or doughnut-shaped, secondary particles (from 5  $\mu\text{m}$  to 50  $\mu\text{m}$ ) which forms the powder that is collected from the unit. The resulting porous powder is then calcined to pyrolyze the organic precursor to semi-graphitic carbon which enhances the electrical conductivity of the material. Finally, we established the electrochemical quality of the LFP/C active cathode material using coin-cell batteries.

### 1.3 General research objectives

Identify spray dry conditions to dry  $\text{LiFePO}_4$  nanoparticle's suspensions that maximize the bulk density, while maintaining high surface area, porosity and optimal electrical properties, including different carbon precursors.

### 1.4 Specific objectives

We aim to identify the optimal spray drying conditions and correlate the main factor of spray drying (temperature, atomization pressure, drying air flow, feed flow, solid loading, feed composition and particle size) with yield, residual moisture, secondary particle size and morphology, porosity and density. We want to establish on the laboratory unit, the scale-up criteria and use them on the pilot unit to investigate how carbon precursors and secondary particle size affect the electrochemical property of the cathode in a battery.

### 1.4.1 Identification of the optimal spray drying conditions

As inlet temperature augments, the drying thermal efficiency increases. However excessive temperature and residence time oxidize the material to Fe(III). At the laboratory scale, we ramp up temperature to 200 °C (in the pilot, up to 350 °C), to identify the optimal drying conditions. We investigate the effect of temperature, feed concentration, atomization and primary particle size over the response variables: secondary particle size distribution, bulk density, residual moisture, surface area and porosity. Higher temperatures increase the mesoporosity, increasing the surface area. A faster drying rate leaves less time for particle agglomeration. Moisture level decreases as the heat flux is more intense and particles dried at a higher temperature will be bigger as the drying air density decreases. We will assess if the drying conditions oxidize the surface of the material with XRD. SEM will give us the microscopic material morphology and EDS mapping the phase segregation (in case drying segregates two or more phases or the melting process created a different material). A laser scattering diffractometer assesses the particle size distribution. Surface area, porosity and residual moisture are measured using a nitrogen physisorption instrument.

### 1.4.2 Deriving an empirical model for bulk density

Higher temperatures increase the powder mesoporosity (a microscopic property), but the bulk density of the powder is mostly affected by macroporosity (a macroscopic property). We established that the material porosity increases as the feed solid concentration decreases. A less concentrated material increases the amount of steam leaving the drying particle, thus pushing the primary particles away to create discharge channels for the leaving vapors. Also, smaller secondary particles increase the cohesive force, allowing less powder to compact during bulk and tapped density measurement.

### 1.4.3 Conceive scale-up criteria based on testing in the pilot and laboratory scale dryer, investigate interactions with carbon precursors and electrochemical battery tests

Spray drying creates a mesoporous powder that promotes wettability. The addition to the suspension of lactose and high-Mw polyvinyl alcohol (PVA) and pyrolysis creates a carbon grid that interconnects the cathode nanoparticles, imparting better capacity (LiFePO<sub>4</sub>/C: 161 mA h g<sup>-1</sup> at 0.1C-rate), discharge rate (flat plateau with 135 mA h g<sup>-1</sup> at 10C), and cyclability (88% capacity retention after 950 cycles at 1C). Spray dried particle size affects battery stability; PVA increases the suspension's viscosity and alters the powder morphol-

ogy, from spherical to hollow particles. A model describes the rheology of the non-Newtonian ternary system: water-LFP-PVA, for shear and temperature variation. We investigate the calcination mechanism by measuring the carbon content and chemical composition of the pyrolyzed species by XPS and Raman. Carbon precursors prevent sintering of the nanoparticles but lactose gasifies 50% of the carbon. The PVA carbon grid imparts microporosity and we correlate the SEM and TEM powder's morphology with  $N_2$  physisorption porosimetry. Ultrasonication of the LFP-organic precursors suspension leads to the fragmentation of the PVA chain, which is detrimental for the final cathode material.



## CHAPTER 2 LITERATURE REVIEW

Researchers use spray drying as a tool to desiccate materials and form particles, without investigating the effect of particle size, density, porosity, morphology on the material properties. Spray drying scale-up is mainly carried-out based on experimental know-how and a list of carbon precursors gives a starting point for achieving an optimal electron-conductive carbon layer after pyrolysis. Moreover, the choice of the appropriate nozzle and surfactants impact on the atomization of the suspension during drying.

### 2.1 Spray drying

The process of milling, spray drying and powder's pyrolysis has already been reported in literature (called WSC: Wet milling, Spray drying, Carbothermal reduction).[53] The researchers mill the salt precursors to a  $<100$  nm suspension, spray dry the material maintaining a mesoporous structure forming  $5\ \mu\text{m}$  to  $10\ \mu\text{m}$  aggregates, then synthesize the cathode material and carbon coat it with starch simultaneously at the carbothermal reduction step — solid state reaction at  $650\ ^\circ\text{C}$  for 8.5 h. Our methodology envisages ore-grade materials, thus is economically more appealing. Controlling the primary particle size distribution is crucial to reach the desired electrochemical properties. As milling progresses, the material comminutes. Batches of different milling times — and different PSDs — have, however, counterintuitive properties. After spray drying each batch material with the same conditions, a battery capacity test demonstrates that the process is nonlinear.[54] Specific surface area and battery capacity are maximized at 2.5 h of milling, with a  $D_{50}$  primary particle of 110 nm. After, the assembled battery performance decreases. It is unknown however, if different drying conditions enhance the smaller particles' rheological suspension.

Spray drying a suspension instead of a solution achieves better results.[55] Three different drying methods are reported to make LFP/C, including particle morphology analysis and elemental distribution. Directly spray drying a solution of the precursor salts resulted in phase segregation that could not be resolved during annealing. Two different crystalline products lead to no energy storage property. Gelification of the starting solution intimately mixed the components, leading to pure LFP/C product during annealing. However poor specific surface area leads to poor battery performance. Spray drying the sol-gel material creates a mesoporous structure with higher surface area and battery capacity. To avoid thin-shell particles from spray drying a solution, a sol-gel process precipitates the molecules into nano-sized primary particles that then agglomerate into a micro-sized network. This

forms an homogeneous mesoporous structure upon spray drying.[56] Another paper reports the effect of pH over the stability of a nanoparticle suspension. Breaking the isoelectric point and letting the nanoparticles flocculate together (pH 8) avoid blow-holes and improve the density of the material, thus maximizing the battery's energy density.[57] Supercritical synthesis of 80 nm LFP crystals starting from salt precursors and subsequent spray drying to 60  $\mu\text{m}$  particles, created a material with poor electrical properties.[58] The material surface area is undisclosed as well as the spray drying conditions, in fact, 2  $\mu\text{m}$  to 10  $\mu\text{m}$  spray dried particles would maximize the battery's performance, by exposing high surface for  $\text{Li}^+$  flow.[6] Particle engineering of pharmaceutical ingredients via spray drying is an intense field of research that has already established several criteria and dimensionless numbers to describe the process. The definition of the dimensionless Peclet number discriminates between particle morphologies (Figure 2.1).[2]

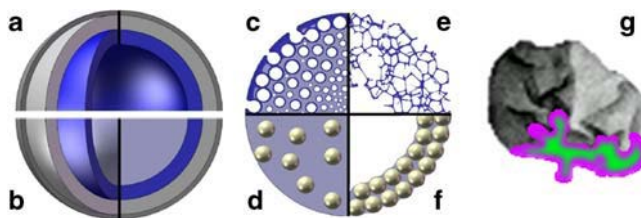


Figure 2.1 Schematic representation of particle morphologies. a) Layered with central core. b) Layered with central void. c) Solid foam, closed cell. d) Solid foam, open cell. e) Particle with embedded nanoparticles. f) Composite shell. g) Irregular, with external voids and internal concentration gradients.[2]

Each particle morphology is examined — doughnut, hollow-shell, deflated balloon, homogeneous isotropic shrinkage (Figure 2.2) — and a drying mechanism is associate for each phenomena. For  $Pe < 1$  we have isotropic shrinkage to a dense spherical particle. For  $Pe > 10$  the dried particle resembles a deflated balloon. The effect of nanoparticle interaction (Figure 2.3) and shell permeability are introduced to model the drying mechanism .[3]

The spray of a solution of salt precursors in water gives a thin-shell dried particle. Wet milling overcomes the material inherent low particle density, while forming a compact dense spray dried particle.[59] However, the methodology is unrepeatable due to the lack of the experimental conditions. The initial particle morphology could have been engineered from the beginning to obtain a void-less material by changing the drying rate or the pH of the solution. There is no information regarding the drying step, and again all effort has been put in the precursors choice and battery testing, rather than the powder technology. An alloy of  $2\text{LiFePO}_4\text{Li}_3\text{V}_2(\text{PO}_4)_3$  is prepared by wet ball milling and spray drying, along with additives for carbon coating.[60] No information nor references regarding the methodology are

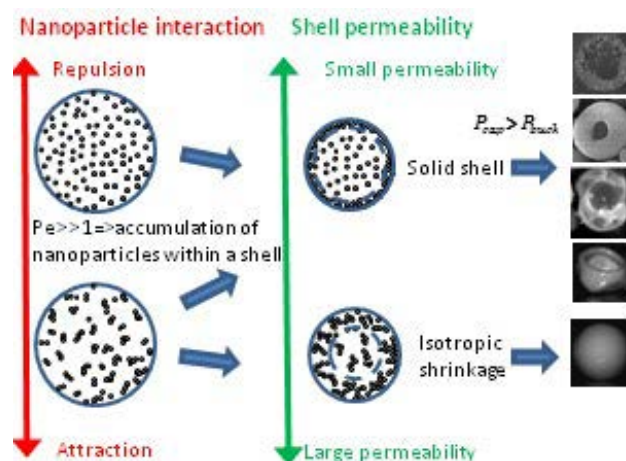


Figure 2.2 Summary of the behaviors according to the nanoparticle interactions, which determine the shell permeability and consequently the Darcy pressure.[3]

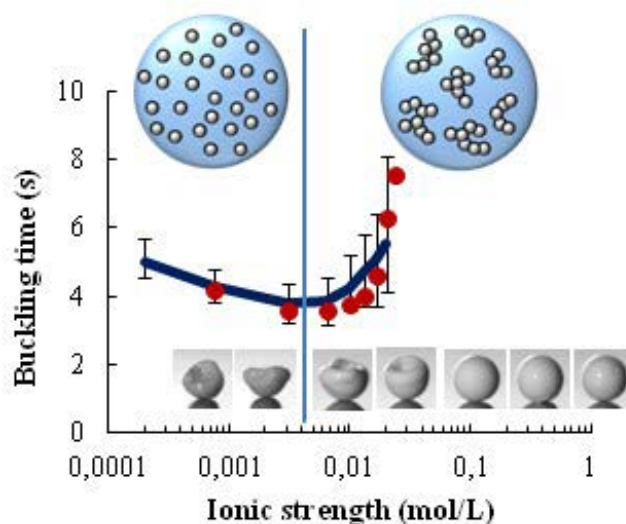


Figure 2.3 Buckling time as a function of ionic strength. The experimental data measured for drying droplets of zirconia suspensions (circles) are well described by the model. The photographs show the grains obtained after full drying for different initial ionic strengths of the suspension, corresponding to different initial states (fully dispersed or suspension of fractal aggregates).[3]

disclosed, the focus is only on the novel cathode material and its testing. On the other hand, spray drying of APIs is well described in literature. A Monte-Carlo stochastic approach is used to model the impact of the feed material's different particle sizes on the dried material.[5] The crystallization time, versus the time required to dry the solid into an amorphous state, plays a role in defining the particle morphology during spray drying.[61] Indeed LFP is

insoluble in water, at pH 6.5, but in acidic conditions LFP is partially soluble which alters the viscosity of the feed material. The importance of drying rate for achieving a dense, compact spray dried particle relies on the spray dryer dimensions.[62] A bigger spray dryer unit allows more contact time for the drying particle, thus allowing the suspended particles to compact more and achieve a superior attrition resistance material. Lower inlet temperatures — lower drying rates — allows the suspended nanoparticles to compact into a less porous dried material.

## 2.2 Scale-up

The scale-up of spray drying has been mainly carried-out based on experimental experience (Figure 2.4).[4] The whole process depends on the feed properties, equipment dimensions and design. However, some theoretical engineering models approaches can be found in the literature.[63]

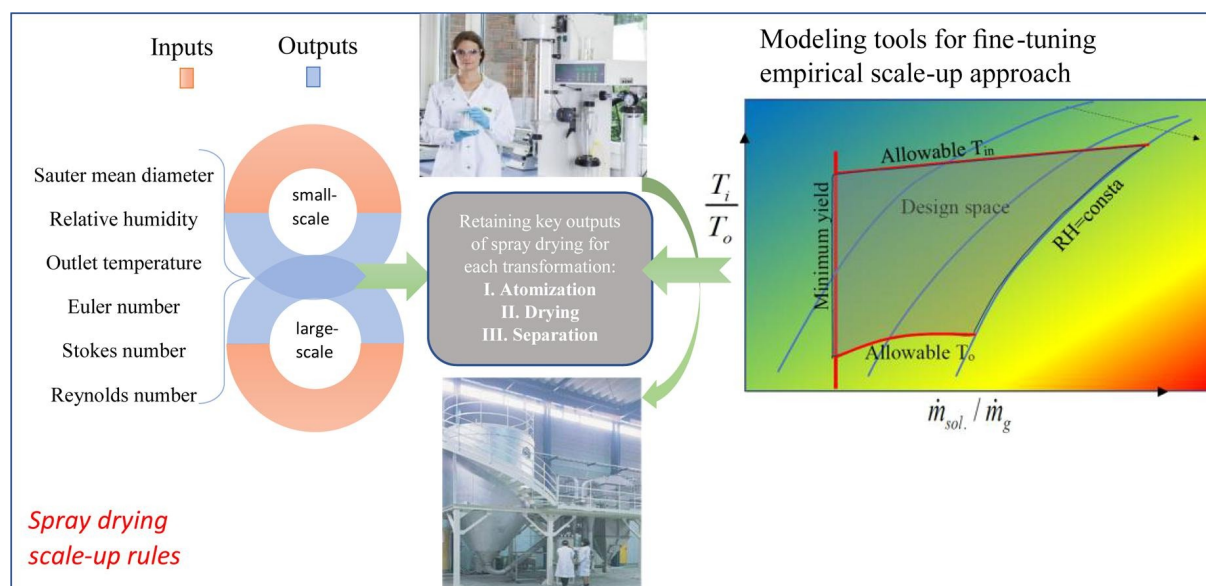


Figure 2.4 Modeling droplet size distribution, temperature profiles, relative humidity, and cyclone efficiency give a better basis for spray-drying scale up, instead of trial-and-error approaches.[4]

The humidity of the air leaving the drying chamber is a critical control parameter. Thermodynamic calculations estimate the humidity of the exhaust air for a particular set of temperature, pressure, flow and heat loss conditions. However, this methodology was incapable to predict particle and powder related characteristics (particle size and moisture level in the particle).[64]

Further investigations looked for the ability to produce identical powders, in different scale instruments, by matching the droplet size distribution atomized. However, the methodology was unsuccessfully implemented, because the differences in droplet temperature and contact time were ignored as the scale of the instrument changes.[65]

A methodology that takes advantage of thermodynamics calculations, droplet drying kinetics simulations, particle formation, computational fluid dynamic and atomization principles give an alternative to traditional empirical spray-drying process development methods.[66]

Spray-dryer scale-up presents some advantages when scaling suspensions feed materials. The atomization process gives a more uniform droplets size distributions and the drying rate is slower, the possibility to work in different fluid-dynamic regimes around the droplet (pure diffusion to laminar), controls the density of the powder.[67] However, the need for more feed material poses critical evaluations over the choice of liquids' volumes. Spray-drying small volumes of suspensions lead to uncertainty at the beginning and at the end of the spray, as the material mixes with the air or pure solvents and solid loading drops. The internal fluid dynamic of the drying air changes to a turbulent regime, as the internal chamber diameter increases. The more complex design and faster air flows increase the attrition of the dried material with the piping, leading to particle fracture.[68]

A thermodynamic model predicts outlet temperature and powder's residual moisture content during the spray drying process and Monte-Carlo simulation analyzes the effects of the aerodynamic size of the droplets. These modeling techniques allows to order the relative importance of the process variables and aids in understanding the drying unit operation (Figure 2.5).[5]

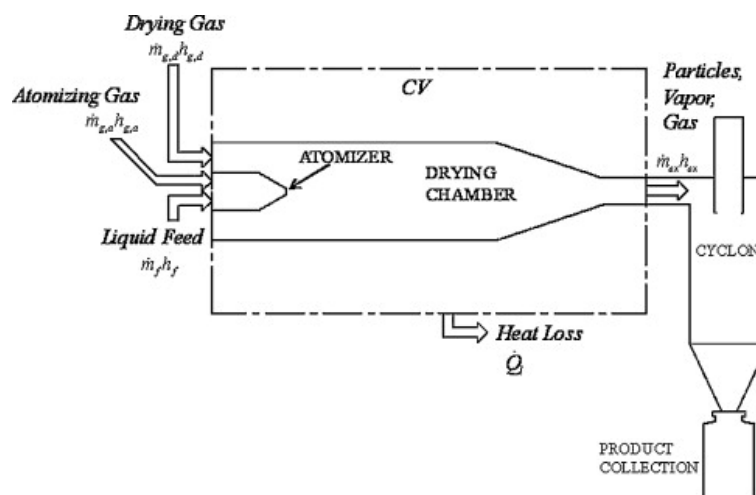


Figure 2.5 Control volume and transport terms for the spray dryer energy balance.[5]

The biggest challenge in spray dryer scale-up is the formation of the same particle size and structure with respect to the laboratory unit, and therefore the same powder properties. The numerous interacting mechanisms that happen across all length scales make standard process scale-up approaches, (like dimensional analysis), of limited use in a spray dryer. There is no linear correlation between the mechanisms and associated dimensionless groups, even if the geometry of the instrument is preserved. A starting point in process scale-up is to recognize the scale-independent process factors that are necessary to achieve the desired particle properties. Ideally, one would match the following important parameters across the different scales:

- Feed properties and feed solid content.
- Atomized droplet size distribution
- The droplet drying rate.
- The (if present) desired particle to droplet collisions which form agglomerates.
- Avoid wall contacts and build-up.

However, in most cases it is not possible to conciliate all factors and differences are seen in particle size, morphology, and product residual moisture content, due to differences in tower design at different scales.[68]

On the laboratory scale, dilute feeds tend to be sprayed due to small-scale pump performance in achieving a good pressure drop during atomization. The particle size is also small due to the low residence times available for drying at the laboratory scale ( $< 1$  s), pilot scale towers have shorter residence times (20 s) and on the production scale ( $> 40$  s). Laboratory scale spray dryers are typically equipped with two-fluid nozzles which make small droplets whereas large scale spray dryers use pressure nozzles that create larger droplets and therefore larger particles. Adjusting the feed composition can lead to variation in product quality and heat loss from the dryer walls and yield varies between the scales. Yields on small scale spray dryers are generally below 70 % due to a large fraction of fine particles lost in the cyclone or filters and the formation of wall deposits. The latter phenomena happens due to incomplete drying of the droplets and changes the product properties and texture.[67]

### 2.3 Carbon coating

A three-component carbon precursor forms a hierarchical conductive architecture as high-performance cathode for Li-ion batteries after spray drying a precursor solution ( $160 \text{ mA h g}^{-1}$

at 1C) (Figure 2.6).[6] However the methodology is unrepeatable due to the lack of the experimental conditions related to the spray drying step.

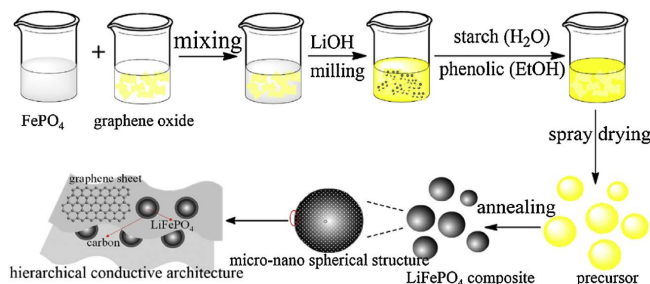


Figure 2.6 Illustration of the preparation process and the microscale structure of triple carbon coated  $\text{LiFePO}_4$  composite.[6]

Doped graphene oxide sheets (GO) achieve superior battery performance, with respect to traditional graphene (anode). In this process researchers spray dry GO and doping salts together and provide some information regarding the drying mechanism but the main aspects — surface area vs. drying rate or temperature, particle density — remain undisclosed.[69] Exfoliated graphene flakes (EG) were synthesized, imparting superior properties with respect to a commercial grade LFP/C (25% better capacity vs. commercial grade LFP/C).[70] This technology can be applied to our situation since we want to impart electrical conductivity to a pre-synthesized LFP and the EG nano-sheets can effectively coat our primary particles. However, spray drying remains a poorly reported step in literature. The authors prepare a novel formulation for carbon coating the LFP, spray dry it and test the assembled battery performance.[71] They use chemicals to reduce the graphene particle size (to undisclosed size). Due to the lack of spray drying informations and methodology, it is unknown whether the battery performance can be attributed to the novel formulation or drying conditions. It is relevant to experiment whenever is possible to grind the graphene along with LFP during the wet ball milling, spray dry it and test the material properties. This would eliminate the pyrolysis step during manufacture, to limit costs and particle sintering. The PSD of spray dried  $\text{LiFePO}_4$  increases during the pyrolysis step for the carbon coating, as the particles sinter together. An increase in the carbon content limits the sinter growth. An excess of carbon limits the  $\text{Li}^+$  diffusion, blocks the pores and lowers the amount of LFP in the battery. Pyrolysis at  $600^\circ\text{C}$  for 10 h with a 4% remaining carbon, optimizes the battery capacity.[72] Another methodology to limit particle sintering is to increase the porosity. Mesoporosity increases surface area for  $\text{Li}^+$  intercalation, but macroporosity wastes space as it creates a low density particle. Hollow morphology is a result of too rapid drying rates[73] as a result,  $\text{Li}^+$  takes more time to diffuse.[74] With an hollow structure the material loses 20% of the

capacity by increasing the discharge current C-rate from 0.2C to 1C. Commercial batteries have 5 % loss.

Cycling stability is also known to be dependent on the synthesis conditions, and pouch-cells batteries would demonstrate the material performance in more realistic conditions. In fact, there are several mechanisms related to capacity loss of coin-cells batteries over cycling, including loss of Li due to side reactions, dendrite formation,[75] materials dissolution,[14] acidic side reactions,[76] and losing active materials due to particle cracking.[77, 78] In order to conclude which ones are involved, further post-mortem characterization would be necessary. A pouch-cell tests more active material (grams) and is assembled in a machine, with a standardized procedure; pouch-cells are also one of the main standards in industry for cell-pack assembly.

## 2.4 Surfactant

Nanoparticle suspensions tend to agglomerate and sediment overtime. To counteract this phenomena, a surfactant stabilizes the system, coating each solid particle at the interface. The resulting dipole moment polarizes the surface with the same charge and repels each particle by electrostatic repulsion.[79] The choice of surfactant is particularly important at the micronization stage, in fact a suitable formulation has been developed using 0.8 % Tween-20<sup>®</sup>. [15] During the atomization stage in spray drying, the surfactant reduces the surface tension of water, creating smaller droplets.

## 2.5 Nozzles

All Li-ion batteries are built using the thin-film application: the gap between the electrodes is generally 200  $\mu\text{m}$  to 400  $\mu\text{m}$ . [80] The thickness of the cathode is 60  $\mu\text{m}$ . [81] This aspect demands the formulation of a dried particle as small as possible, to maximize packing efficiency.

### 2.5.1 Pressure jet

The jet forms from a single fluid nozzle where the suspension is heavily compressed and forced through a tiny orifice. The difference in pressure sets the liquid in motion at high speed, while the impact with the surrounding air, breaks the jet into finer and finer droplets.[82] Although it is the least expensive to operate (by eliminating the need of compressed air for atomization), it requires a huge pressure to achieve a fine droplet atomization (1000 bar for a 20  $\mu\text{m}$  droplet). Therefore, this nozzle is impractical for laboratory use, but is best suited



for commercial operation, especially for our shear thinning LFP suspension where viscosity drops to 11 mPa s (water-like).

### 2.5.2 Dual fluid

The liquid is slightly compressed ( $<2$  bar), to overcome the pressure drop inside the nozzle and pass through an orifice, exiting at  $<1$  m s<sup>-1</sup>. From an outer adjacent annulus, compressed atomizing air leaves the tip of the nozzle at 1 bar and 300 m s<sup>-1</sup>, entraining the liquid jet and nebulizing it with a turbulent fluid dynamic.[82] This versatile airblast, external mixing atomizer achieves a wide distribution of droplet sizes ranging from 10  $\mu$ m to 1000  $\mu$ m by changing the atomization pressure. Higher pressure speeds-up the gas, imparting more kinetic energy blasting the liquid stream and shattering it into smaller droplets.

### 2.5.3 Effervescent

This has the same design as a dual fluid nozzle, but mixing happens in an internal chamber. As the liquid flows in the nozzle chamber, it is filled with tiny bubbles under pressure. As both fluids leave the chamber through an orifice, the pressure drop expands the gas bubbles, nebulizing the continuous phase. Compared to the dual fluid nozzle, it can achieve the same performance for small droplet atomization but using less atomizing air — less compression gas costs — (ALR Air to Liquid mass Ratio for a 10  $\mu$ m droplet with an effervescent nozzle is 0.5 and 3 with a dual fluid nozzle).[83]

### 2.5.4 Ultrasound

It is a single fluid nozzle where the tip is coupled with a sonicator. A Lecher GmbH atomizer that operates at 50 kHz to 70 kHz and atomizes up to 50 mL min<sup>-1</sup> of water creates 20  $\mu$ m to 100  $\mu$ m droplets. Macroscopically there are no atomization benefits with respect to a simpler and less expensive design. Moreover, this nozzle cannot be exposed to a hot environment, thus limiting its application. We already demonstrated that high drying temperature deagglomerates the primary particle in the suspension and leave a dried material more porous with more surface area (Chapter 4). We hypothesize that an ultrasound device can achieve the same effect at lower drying temperatures. But this is at the expense of the drying process efficiency.

### **2.5.5 Rotary atomizers**

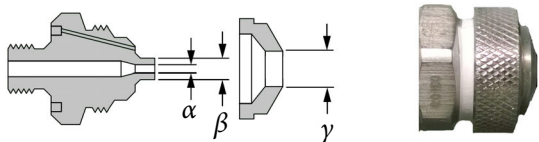
A rotor spins a hollow disk where the suspension passes through. The centrifugal force sets the fluid in motion radially. It is a mechanical device, and breakdown and clogging renders this device unsuitable. Especially, nozzle clogging at the laboratory scale is a serious concern and cleaning these devices is time consuming. Lastly, radial atomization is incompatible with a tall cone-shaped spray dryer chamber: the radial mean free path is much lower than the axial used by pressure/dual fluid nozzles.

## CHAPTER 3 METHODOLOGY

### 3.1 Laboratory and pilot spray dryers

The Yamato GB-22 laboratory-scale spray dryer consists of a 12 cm I.D. by 58 cm tall glass drying chamber. Drying air and atomizing air are preheated at 50 °C to 200 °C and flow at 0.45 m<sup>3</sup> min<sup>-1</sup>, contacting the liquid spray co-currently from top to bottom. It possesses a set of stainless steel two-fluid nozzles (Table 4.1), 0.406 mm to 1.530 mm inner diameter for the slurry and 1.626 mm to 3.060 mm outer annulus for the atomizing air, capable of achieving different droplet size distributions.

Table 3.1 Two-fluid, external mixing, air blast atomizer, with bores in  $\mu\text{m}$  and a non-protruding tip.



Nozzle bore:	$n_1$	$n_{1A}$	$n_2$	$n_{2A}$	$n_3$	$n_{3A}$	$n_4$
$\alpha$	406	406	508	508	711	711	1530
$\beta$	1270	1270	1270	1270	1270	1270	2550
$\gamma$	1626	1778	1626	1778	1626	1778	3060

A peristaltic-pump feeds the slurry at 5 mL min<sup>-1</sup> to 15 mL min<sup>-1</sup>, while a pressure regulator from 0.2 bar to 1.5 bar sets the gas velocity for the atomizing air, leaving the nozzle and nebulizing the liquid (after calibration using a rotameter and data regression). The feed slurry is gently stirred at 2 Hz at room temperature, mixing the suspension while avoiding air incorporation. Finally a cyclone separates the dried powders from the gas stream. Assuming Stokes law regime for a single 1600 kg m<sup>-3</sup> dense particle, the cyclone has a cut diameter of 2.7  $\mu\text{m}$  at 50 % separation efficiency. We start feeding material after reaching 30 min of steady state conditions with water.

We spray dried the feed material with a GEA Niro Mobile Minor<sup>TM</sup>-PSR pilot-scale spray dryer, with an internal chamber diameter of 0.8 m and 0.8 m chamber height, a 60° cone shapes the bottom of the chamber (Fig. 5.1). A 11 kW electrical coil heated 90 kg h<sup>-1</sup> of drying air at 350(2) °C (confidence interval), which flowed co-currently with the spray, leaving the bottom of the chamber at 125(2) °C. We chose a two-fluid nozzle, with 0.7 mm I.D. for the liquid and an annulus of 3.1 mm I.D. and 5.0 mm O.D. for the atomizing air, based on laboratory-scale tests of flowability of LFP suspensions through a bore restriction.[7, 84]

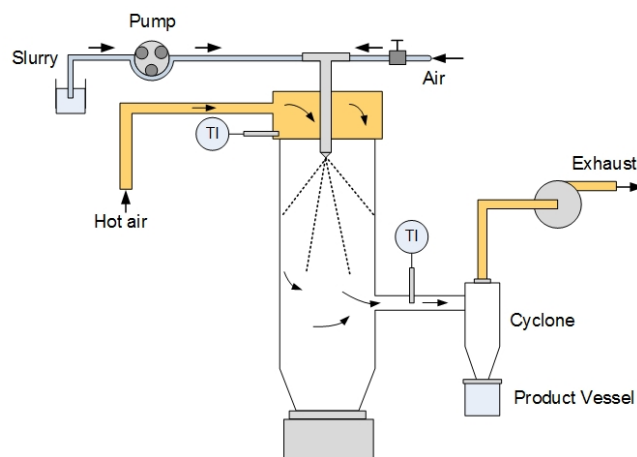


Figure 3.1 Schematic of the Yamato GB-22 spray dryer, co-current mode.

Compressed air at 0.25 MPa to 0.40 MPa fed the nozzle while a peristaltic pump fed the suspension at flow rates between  $130 \text{ mL min}^{-1}$  to  $180 \text{ mL min}^{-1}$ , creating a fine mist. A cyclone separated the resulting powder, with a 50% cut-off efficiency for  $0.7 \mu\text{m}$ ,  $1600 \text{ kg m}^{-3}$  secondary particles. Before feeding the suspension, we reached thermal steady state with an equivalent volumetric flow of water (up to  $90 \text{ mL min}^{-1}$ ) during 2 h.

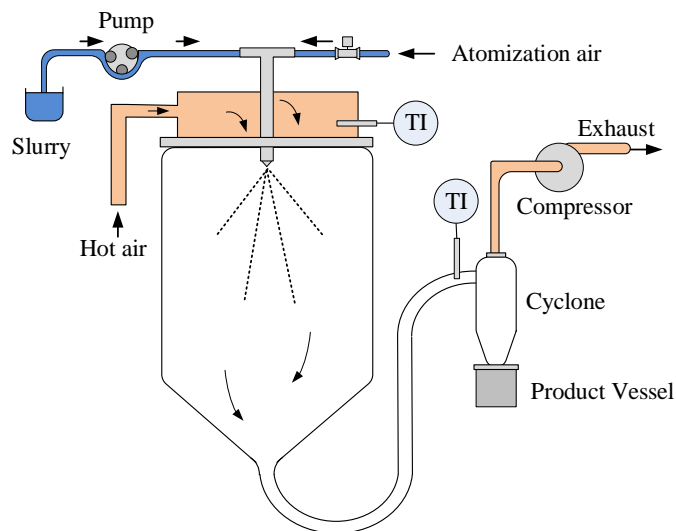


Figure 3.2 GEA Mobile minor spray dryer setup.

## 3.2 Experimental - laboratory-scale

### 3.2.1 Micronization

A jaw crusher (Fritsch Pulverisette, model 1, Type II) pulverized 20 cm LFP ingots, from a melt synthesis process,[14] to less than 1 mm.[15] Subsequently a roller grinder (MPE Chicago 6F, granulizer) with a 50  $\mu\text{m}$  gap reduced the particle size to 25  $\mu\text{m}$ . Finally, a wet media mill (NETZSCH, Minifer) ground the powder to a water suspension of 200 nm median particle size distribution (Figure 4.2). The wet milling chamber was filled to 80 % of the design capacity (60 % of chamber volume capacity) with yttria-stabilized zirconia beads ranging from 0.3 mm to 0.4 mm. We fed the instrument with 292 mL of water, along with Tween-20 surfactant (0.8 % mass/mass of LFP) to increase the stability of the suspension.[85] We slowly poured LFP powder to reach the desired mass fraction: 6 % up to 60 % (mass of LFP/mass of suspension). The grinding chamber rotated at 60 Hz and a pump recirculated the mixture at 360 mL min<sup>-1</sup>. Within 30 min of milling, the primary particle size distribution median reached 200 nm.[86]

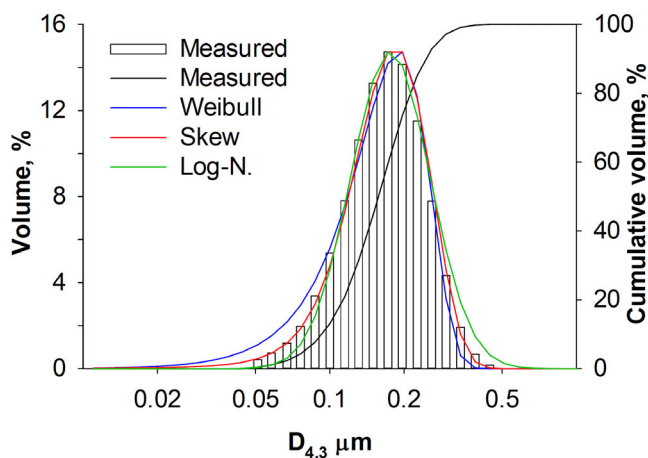


Figure 3.3 Typical particle size distribution and model fit for the feed material.

### 3.2.2 Spray Drying

To avoid nanoparticle agglomeration, we hand-shaked the feed material and used an ultrasound probe VCX500 (Sonics & Materials, Inc.) for 3 min to disperse the material.[87] We spray dried the suspension with a Yamato GB-22 laboratory-scale spray dryer, with a 0.12 m internal diameter by 0.58 m tall glass chamber (Figure 4.3). An electrical coil heated both atomizing and drying air from 50 °C to 200 °C, while an internal flowmeter regulated the drying air to 0.45 m<sup>3</sup> min<sup>-1</sup>. The air and suspension were fed co-currently, from top to bottom. We

tested seven stainless steel two-fluid nozzles (Table 4.1) ranging from 0.406 mm to 1.530 mm inner diameter for the liquid and 1.626 mm to 3.060 mm outer annulus for the atomizing air. Pressure, air and liquid flow, drying air temperature and nozzle geometry affects the resulting spray nebulization.[88] A peristaltic pump fed the suspension at flow rates of  $5 \text{ mL min}^{-1}$  to  $15 \text{ mL min}^{-1}$ . A pressure regulator from 0.02 MPa to 0.15 MPa ensured that the atomizing air dispersed the suspension into a fine mist. We calibrated the pressure to the atomizing airflow with a rotameter and regressed the data to calculate the gas velocity. A magnetic stirrer maintained the solid suspended in a 250 mL flask at ambient temperature. A cyclone separated the powder from the gas stream leaving the drying chamber: assuming Stokes law regime, the cyclone's cut diameter is  $2.7 \mu\text{m}$  at 50 % separation efficiency for a  $1600 \text{ kg m}^{-3}$  particle density. Feeding the suspension began 30 min after reaching thermal steady state with an equivalent volumetric flow of water.[7]

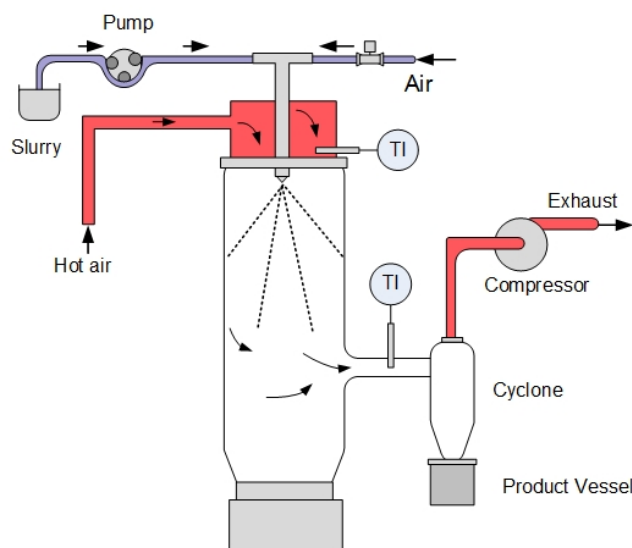


Figure 3.4 Yamato GB-22 spray dryer, co-current mode.[7]

### 3.3 Experimental - pilot-scale

#### 3.3.1 Nanoparticle suspension preparation

An induction furnace at  $1100^\circ\text{C}$  melted and synthesized  $\text{LiFePO}_4$  in a graphite crucible. Starting from:  $\text{LiH}_2\text{PO}_4$ ,  $\text{P}_2\text{O}_5$ ,  $\text{Li}_2\text{CO}_3$  and iron ore concentrate ( $>99\%$   $\text{Fe}_2\text{O}_3$  with  $\text{SiO}_2$  impurity) with a Li/Fe/P: 1.03/1/1.03 stoichiometry.[14, 89, 90] The batch we used derived from a re-melt synthesis of previous runs, casting 50 kg of LFP into 200 mm ingots.[91] LFP is the dry solid fraction of our feed material, comprised of 97.8%  $\text{LiFePO}_4$  and 2.2%  $\gamma$ -

$\text{Li}_3\text{PO}_4$  ( $\pm 0.4\%$   $CI_{n=6}^{95\%}$ , by AAS and XRD;  $CI_{n=i}^{95\%}$ : 95% confidence interval estimate, with a two-tail  $t$ -test for a sample number  $n$ ). A Pulverisette 1 model II, Fritsch jaw crusher ground the ingots to 1 mm to 3 mm gravel, processing  $13 \text{ kg h}^{-1}$  of material. A roller grinder (MPE 6F granulizer, Chicago) further reduced the particle size distribution (PSD) to  $d_{v,50}$  of  $27 \mu\text{m}$  and  $d_{v,99}$  of  $200 \mu\text{m}$ ; treating  $2 \text{ kg h}^{-1}$  of material at 10% feeding rate. A wet media mill (NETZSCH - LMZ 4) ground the powder, equipped with a 0.1 mm mesh filter and loaded with 3.2 L of 0.68 mm yttria-stabilized zirconia beads, which filled 75% of the total volume of the grinding chamber. Pilot and commercial grinding chambers are made of ceramic rather than stainless steel to minimize iron contamination. We filled the apparatus with 25 L of deionized water and we loaded 25 kg of LFP, with a 0.008 mass ratio of Tween-20 surfactant, in the mixing tank. We scaled-up the process using our previous laboratory practice,[15] and we added LFP progressively at a rate slow enough to avoid plugging the mesh filters ( $20 \text{ kg h}^{-1}$ ). A cooling system pumped water at  $15^\circ\text{C}$  around the grinding chamber and mixing tank (ESI Fig. 1S).<sup>†</sup> We sampled the slurry at the outlet of the grinding chamber every 15 min and immediately analyzed by laser scattering to avoid agglomeration. We operated the wet media mill until the PSD median reached 200 nm.

### 3.3.2 Spray drying

Despite the Tween-20 surfactant, the suspended primary particles tend to settle when stored for weeks. A mechanical mixer homogenized the slurry periodically and an aliquot of material was weighed and ultrasonicated for 15 min before each experiment to de-agglomerate the nanoparticles.[87] For standard feed materials, we added binders (lactose, polyvinyl alcohol solution or colloidal silica, 1% to 7%) and mechanically stirred the suspension for an additional 15 min. For ultrasonicated slurries (US), we added the binders while stirring and ultrasonicated for 15 min. We spray dried the feed material with a GEA Niro Mobile Minor<sup>TM</sup>-PSR pilot-scale spray dryer (0.8 m I.D. x 0.6 m height /  $60^\circ$  cone chamber Fig. 5.1). A 11 kW electrical coil heated  $90 \text{ kg h}^{-1}$  of drying air at  $350(2)^\circ\text{C}$ , which flowed co-currently with the spray, leaving the bottom of the chamber at  $125(2)^\circ\text{C}$ . We chose a two-fluid nozzle, with 0.7 mm I.D. for the liquid and 3.1 mm I.D. 5.0 mm O.D. for the atomizing air, based on laboratory-scale tests of flowability of LFP suspensions through a bore restriction.[7, 84] Compressed air at 0.25 MPa to 0.40 MPa fed the nozzle while a peristaltic pump fed the suspension at flow rates between  $130 \text{ mL min}^{-1}$  to  $180 \text{ mL min}^{-1}$ , creating a fine mist. A cyclone separated the resulting powder, with a 50% cut-off efficiency for  $0.7 \mu\text{m}$ ,  $1600 \text{ kg m}^{-3}$  secondary particles. Before feeding the suspension, we reached thermal steady state with an equivalent volumetric flow of water (up to  $90 \text{ mL min}^{-1}$ ) during 2 h.

### 3.3.3 Calcination and electrochemical tests

We loaded 2 g of spray dried powder into an alumina crucible, and inserted it in a tube furnace flushed with a  $N_2$  atmosphere. We let the powder outgas at  $100^\circ C$  for 2 h and we increased the temperature to  $700^\circ C$  for 2 h to calcine the material. The electrode of carbon coated LFP was prepared by mixing the pyrolyzed active material ( $LiFePO_4/C$ , 500 mg), with carbon black C65 as conductive additive, and polyvinylidene fluoride (PVDF) at a weight ratio of 84:9:7 in N-methyl-2-pyrrolidone (NMP) solvent. The mixture was then shaken in a Turbula 3D mixer for 20 min, and homogenized in a tube roller overnight with 5 mm by 6 mm cylindrical beads. The uniform slurry was spread onto a piece of aluminum foil current collector using the doctor blade technique. The electrode dried in a vacuum oven at  $80^\circ C$  overnight. Disc-shaped electrodes with a loading of  $1.8(1) \text{ mg cm}^{-2}$ , and a thickness of  $24 \mu\text{m}$ , were cut and assembled in coin cells (2032) in an argon filled glove box. A lithium metal foil was used as the negative electrode,  $LiFePO_4/C$  as positive one, Celgard 2400 as the separator, and 1 M  $LiPF_6$  in ethylene carbonate-dimethyl carbonate (weight ratio of 1:2) solvent as the electrolyte. The electrochemical tests were performed on the cells at  $30^\circ C$  on a Arbin BT2000 electrochemical station with cut-off voltages of 2.2 V and 4.0 V vs  $Li^+/Li$  at 0.1C-rate for galvanostatic cycling and at different current rates for power performance determination.

Given the lengthy process of calcination, battery assembly and testing (a single electrochemical test could take up to several weeks, for example 10 cycles at 0.1C last 1 week) we were allotted a limited number of slots for testing, thus limiting the amount of factors to test and repetitions.

### 3.3.4 Reagents and Characterization

D(+)-lactose monohydrate (>98 % Sigma-Aldrich). LUDOX<sup>®</sup> SM colloidal silica (30 % suspension in water, Sigma-Aldrich). Polyvinyl alcohol (PVA) with a weight average  $M_w$  146,000-186,000  $\text{g mol}^{-1}$  was purchased from Sigma-Aldrich, and dissolved in boiling deionised water forming a 5 % solution. An X-ray diffractometer (XRD, BRUKER D8) recorded the diffractogram of the spray dried powder in a stepwise scan of the gonio axis ( $10^\circ$  to  $80^\circ$   $2\theta$ ,  $0.02^\circ$  stepwise), with a copper anode at 40 kV and 40 mA. The HighScore Plus software stripped the K-Alpha sidebands and refined the spectra using the Crystallography Open Database (COD) database:  $LiFePO_4$  orthorhombic Pnma, ref. 96-400-1849;  $Li_3PO_4$  orthorhombic Pnma, ref. 96-901-2822, and JCPDS card:  $LiFePO_4$  01-070-6684;  $Li_3PO_4$  00-015-0760. We solubilized 20 mg of spray dried powder in 5 mL of  $6 \text{ mol L}^{-1}$  HCl (HPLC grade). Once completely dissolved, we diluted the solution in 1 L of deionized water (reaching



pH 1.5). An atomic absorption spectrometer (AAS, PerkinElmer AAnalyst 200) measured the absolute concentration of  $\text{Li}^+$  and  $\text{Fe}^{3+}$  in the solution (*wt/vol*), using the manufacturer procedure (N0225001 Rev.C). A laser diffractometer (LA-950 Horiba) measured the PSD, from 30 nm to 3 mm, using the Mie algorithm, reporting the volume moment mean diameter (DeBroukere mean)  $D_{4,3}$ , and one standard deviation as the square root of the variance in the distribution:

$$D_{4,3} = \frac{\sum d_i^4 \cdot N_i}{\sum d_i^3 \cdot N_i} \quad (3.1)$$

where  $N_i$  is the number of particles with the corresponding diameter  $d_i$ . Ultrasonication and stirring dispersed the slurry in water, while only stirring dispersed the spray dried powders during analysis. A refractive index of  $1.68 + 0.1i$  for LFP and 1.333 for water minimized below 0.1 the R and Chi fitting scores.[86] We measured the tapped density  $\rho_t$ , following the ASTM B527 procedure, by pouring the powder in a graduated volumetric cylinder and hand-tapping until no further variation of volume could be observed. A field emission scanning electron microscope (SEM, FE-SEM-JEOL JSM-7600F) equipped with an energy dispersive X-ray detector (EDS) acquired the images of the powder at 2 kV with the SEI detector. A transmission electron microscope (TEM, JEOL JEM-2100F) recorded the images of the pyrolyzed material at 200 kV in bright field imaging mode. A CS elemental analyzer (LECO CS744) measured the elemental carbon weight fractions in our powders, after spray drying and after pyrolysis. The value has been corrected in terms of dried material ( $wt_C/wt_{LFP}$  %) without the residual moisture. A Quantachrome Autosorb-1 measured the  $\text{N}_2$  physisorption isotherms at 77 K. The powder was degassed at 200 °C, under vacuum, for 12 h and weighed with an Entris224-1S balance ( $\pm 0.2$  mg). We regressed the total specific surface area ( $SSA$ ), over the best linear range, with the Brunauer-Emmett-Teller (BET) equation ( $P/P_0$ : 0.07-0.20,  $C$  constant 60-200). The Barrett-Joyner-Hallender (BJH) method estimates the pore size distribution for the mesoporous material (desorption branch,  $P/P_0$ : 0.2-0.995, excluding the cavitation-induced artifact at  $P/P_0$ : 0.45, 4 nm). As comparison, the NLDFT method for siliceous materials with cylindrical pores, calculates the pore size distribution including the micropore region for the spray dried powders ( $P/P_0$ : 0-0.98 equilibrium adsorption-desorption). While pyrolyzed powders that have a carbon coat, use the NLDFT kernel for carbonaceous materials with cylindrical pores (same, up to 0.95).[92] The  $V - t$  method regresses the specific surface area, characteristic pore size and volume for the microporous fraction over the best linear range (DeBoer thickness). The total pore volume is evaluated at  $P/P_0$ : 0.995, which accounts for pores smaller than 300 nm in diameter.[8] The intra-primary-particle void fraction (porosity  $\varphi$ , %) was calculated from the skeletal density of the material (LFP:  $\rho_{sk} = 3.57 \text{ g cm}^{-3}$ ) and the measured pore volume ( $PV$ ,  $\text{cm}^3 \text{ g}^{-1}$ ) (Eq. 5.2). While the apparent particle density  $\rho_p$ ,  $\text{g cm}^{-3}$  with Eq. 5.3.

$$\varphi = \frac{PV}{PV + \frac{1}{\rho_{sk}}} \quad (3.2)$$

$$\rho_p = \frac{\rho_{sk}}{1 + PV\rho_{sk}} \quad (3.3)$$

A HAAKE<sup>TM</sup> Viscotester<sup>TM</sup> iQ Air rheometer (Thermo Scientific<sup>TM</sup>) equipped with a CC27 coaxial cylinder double gap geometry (3.00(5) mL volume) and an external water/glycol temperature controller (polystat<sup>®</sup> Cole-Parmer<sup>®</sup>  $-10.0(1)^\circ\text{C}$  to  $80.0(1)^\circ\text{C}$ ) recorded the apparent viscosity of the LFP suspensions while increasing and decreasing stepwise the shear rate ( $50\text{ s}^{-1}$  to  $4000\text{ s}^{-1}$  range, after pre-shearing at  $10\text{ s}^{-1}$  for 3 min). A VCX 500, Sonics & Materials, Inc. powered a 20 mm diameter ultrasonic horn at 500 W, resonating at 20 kHz and 40% amplitude. The horn was immersed half-way in a magnetically stirred beaker, and the actual power delivered to a 0.6 L suspension was  $40\text{ W L}^{-1}$ , calibrated with a calorimetric procedure.[93] An X-ray photoelectron spectrometer (XPS, VG ESCALAB 3 MkII) analyzed the carbon coating of our LFP powders.[8] A Mg  $K\alpha$  source at 15 kV gathered the spectra over a  $<10\text{ nm}$  material thickness, reporting carbon and oxygen bonding information. We acquired the Raman spectra on 3 different spots per sample, with a Renishaw inVia Microscope, a 50x objective lens, 30 s exposure time,  $600\text{ lines mm}^{-1}$  optical grating, giving a spectral resolution of  $3\text{ cm}^{-1}$ . The 514.5 nm laser was reduced in power (to 10%, 2.5 mW) to avoid damaging the carbon coat and irradiated the powder in a  $7\text{ }\mu\text{m}^2$  area.

## CHAPTER 4 ARTICLE 1 - INFLUENCE OF ATOMIZATION CONDITIONS ON SPRAY DRYING LITHIUM IRON PHOSPHATE NANOPARTICLE SUSPENSIONS

Marco G. Rigamonti,<sup>a</sup> Yu-Xiang Song,<sup>a</sup> He Li,<sup>a</sup> Nooshin Saadatkhah,<sup>a</sup> Pierre Sauriol,<sup>a</sup> Gregory S. Patience<sup>a</sup>

Published in 2018, in the *Canadian Journal of Chemical Engineering*. [84]

### 4.1 Abstract

Removing solvents from nanoparticle solid suspensions requires the same diligence as drying pharmaceutical ingredients.  $\text{LiFePO}_4$  nanoparticles suspension in water oxidize, sinter and  $\text{Li}_3\text{PO}_4$  segregates on the surface when they dry in a furnace. Spray drying preserves the material properties because contact times are on the orders of seconds; furthermore, the atomized droplets ensure particles are small ( $5\ \mu\text{m}$  to  $20\ \mu\text{m}$ ) and dispersed. A Yamato GA-32 (120 mm inner diameter) spray dried in co-current flow a nanoparticle suspension of  $\text{LiFePO}_4$  in water, with a solid content up to 60%. Atomization gas velocities of  $140\ \text{m s}^{-1}$  to  $350\ \text{m s}^{-1}$  agglomerated the nanomaterial into spherical particles that ranged from  $3\ \mu\text{m}$  to  $10\ \mu\text{m}$ . The particle diameters ranged from  $10\ \mu\text{m}$  to  $20\ \mu\text{m}$  at atomization velocities of  $50\ \text{m s}^{-1}$  to  $140\ \text{m s}^{-1}$ . At this condition, yield was lower because the semi-dried particles adhere on the wall. At ( $150\ ^\circ\text{C}$  to  $200\ ^\circ\text{C}$ ) the surface area reached  $26\ \text{m}^2\ \text{g}^{-1}$  while from ( $50\ ^\circ\text{C}$  to  $100\ ^\circ\text{C}$ ) it varied from  $14\ \text{m}^2\ \text{g}^{-1}$  to  $20\ \text{m}^2\ \text{g}^{-1}$ . The trend for mesoporosity versus spray drying temperature is the same as for surface area: pore volumes are higher ( $0.18\ \text{cm}^3\ \text{g}^{-1}$ ) above  $200\ ^\circ\text{C}$  and 20% lower below  $200\ ^\circ\text{C}$ . Drying temperature modifies drying speed; low temperatures compact the powders more than high temperature which results in lower surface area and porosity.

### 4.2 Introduction

Li-ion batteries (LIB) dominate the market for portable electronic devices, power tools and automotives. Even though the fire hazard for  $\text{LiCoO}_2$  is greater than for  $\text{LiFePO}_4$ , its capacity is higher— $273\ \text{mA h g}^{-1}$  versus  $170\ \text{mA h g}^{-1}$  (theoretical)—so it is the material of choice for

---

<sup>a</sup> Department of Chemical Engineering, Polytechnique Montréal, C.P. 6079, Succ. CV Montréal, H3C 3A7, Québec, Canada.

car batteries. Nickel metal hydride (NiMH) batteries monopolize hybrid electric vehicles (HEV) with marginal incursion of LIB in high-end HEVs. The cathode material is the most expensive LIB component[94] at 60 \$/kWh and it also dictates overall battery performance (voltage, capacity, power, energy, cyclability, safety).  $\text{LiFePO}_4$  (LFP) cathodes offer a good compromise between price and performance.[40] It delivers near its theoretical capacity,[95, 96, 97] while its low cell voltage (3.0 V to 3.3 V vs. graphitic anodes) limits side reactions with the electrolyte.[19] Oxide-based metal cathode materials (and their delithiated counterparts) release  $\text{O}_2$  above 150 °C unlike LFP, which releases  $\text{O}_2$  above 700 °C.[28] Commercial LFP batteries do not exceed 55 °C while discharging at 2.5C-rate.[27] Consequently, LFP batteries are intrinsically safer than  $\text{LiCoO}_2$  or  $\text{LiMnO}_2$ . However, lithium ion diffusivity through the olivine crystal matrix of LFP is low compared to the more open structures of  $\text{LiMnO}_2$ ,  $\text{LiCoO}_2$  and  $\text{TiS}_2$  varying from  $10^{-11} \text{ m}^2 \text{ s}^{-1}$  to  $10^{-18} \text{ m}^2 \text{ s}^{-1}$ .[41] Olivine  $\text{LiFePO}_4$  confines  $\text{Li}^+$  through a tunnel-like structure, this nearly close-packed hexagonal array of oxide centers provides little free volume for  $\text{Li}^+$  to diffuse. The layered structure in  $\text{LiCoO}_2$  and  $\text{TiS}_2$  is more open and let  $\text{Li}^+$  migrate bidimensionally (Figure 4.1).

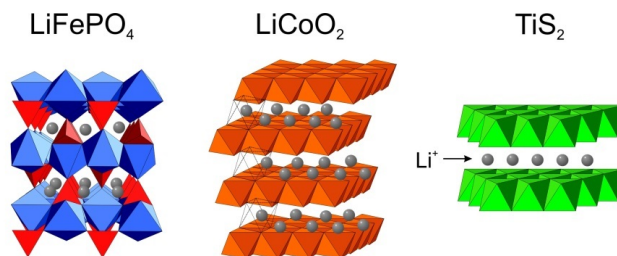


Figure 4.1 Crystal structures that intercalate lithium ion.[1]

These shortcomings are commonly addressed by micronizing LFP powders to the submicron and nanoparticle range[42] and coating it with an electron-conductive carbon layer to improve LFP's low electrical conductivity ( $10^{-7} \Omega^{-1} \text{ m}^{-1}$ ).[43, 1]  $\text{Li}^+$  diffusivity increases by six orders of magnitude by reducing the particle size from micron to nanosize, while maintaining a mesoporous structure: both specific power and cyclability improve.[40] Lithium ion diffuses through the olivine crystal structure of  $\text{LiFePO}_4$  to the electrolyte medium faster when the specific surface area of the material is increased.

Processes to produce LFP materials include: melt synthesis followed by comminution and wet media milling; sol-gel process; electrochemical synthesis; solution co-precipitation; hydrothermal synthesis; and flame-spray pyrolysis.[44] All these methods involve processing solvent, with solid mass fractions ranging from 10 % to 70 %. Drying is a critical step and controlling the temperature during the process is crucial to maintain the desired material

morphology.[45] Removing water in furnaces changes the morphology, the crystal structure, oxidizes the surface in the presence of air and  $\text{Li}_3\text{PO}_4$  segregates on the surface of the nanoparticle, reducing LFP's energy density.[98] Furnace process also sinter the nanoparticles into chunks, losing the ability to control the secondary particle size and introducing an additional grinding step afterwards.[99] Drying in fluidized beds is a discontinuous process divided in several drying and comminution steps, each lasting 10 min to 60 min: as the powder dries, it agglomerates. The resulting granules need to be reduced in size between each step to be able to control the residual moisture of the final material.[47] Spouted bed dryers have 10 to 15 times the drying rate of a conventional spray dryer but only fluidize big particles ( $>200\ \mu\text{m}$ ).[48] Plasma-spraying is a novel technology for delivering nanometric ( $<30\ \text{nm}$ ) dried particles.[49] But the cost for this technology discourage any industrial scale up for LFP, as well as unclear if it is possible to maintain the olivine crystal structure during the plasma process. Spray drying is a robust technology used in the pharmaceutical, food and catalyst industries to dry solutions or suspensions economically and quickly (0.1 s to 60 s) at low temperatures ( $60\ ^\circ\text{C}$  to  $200\ ^\circ\text{C}$ ), preventing degradation and achieving a fine granule size ( $2\ \mu\text{m}$  to  $300\ \mu\text{m}$ ). A dual-fluid nozzle atomizes a feed solution or suspension at pressures of 0.015 MPa to 0.2 MPa. A stream of hot air flows co- or counter-currently in respect to the liquid; the solvent (water in most cases) evaporates while the particles shrink. Droplets less than  $10\ \mu\text{m}$  dry within a few milliseconds.[61] We investigate whether spray drying preserves the optimal primary particle size distribution ( $200\ \text{nm}$ ),[16] and agglomerates this material in a mesoporous  $10\ \mu\text{m}$  secondary particle, which allow  $\text{Li}^+$  diffusivity in the battery and limit the material's degradation during drying.[98] We also provide a laboratory scale correlation for surface area and powder characteristics with respect to spray drying conditions, assessing preliminary boundaries for future scale-up.

## 4.3 Experimental

### 4.3.1 Micronization

A jaw crusher (Fritsch Pulverisette, model 1, Type II) pulverized 20 cm LFP ingots, from a melt synthesis process,[14] to less than 1 mm.[15] Subsequently a roller grinder (MPE Chicago 6F, granulizer) with a  $50\ \mu\text{m}$  gap reduced the particle size to  $25\ \mu\text{m}$ . Finally, a wet media mill (NETZSCH, Minifer) ground the powder to a water suspension of 200 nm median particle size distribution (Figure 4.2). The wet milling chamber was filled to 80 % of the design capacity (60 % of chamber volume capacity) with yttria-stabilized zirconia beads ranging from 0.3 mm to 0.4 mm. We fed the instrument with 292 mL of water, along with Tween-20 surfactant (0.8 % mass/mass of LFP) to increase the stability of the suspension.[85] We slowly

poured LFP powder to reach the desired mass fraction: 6% up to 60% (mass of LFP/mass of suspension). The grinding chamber rotated at 60 Hz and a pump recirculated the mixture at  $360 \text{ mL min}^{-1}$ . Within 30 min of milling, the primary particle size distribution median reached 200 nm.[86]

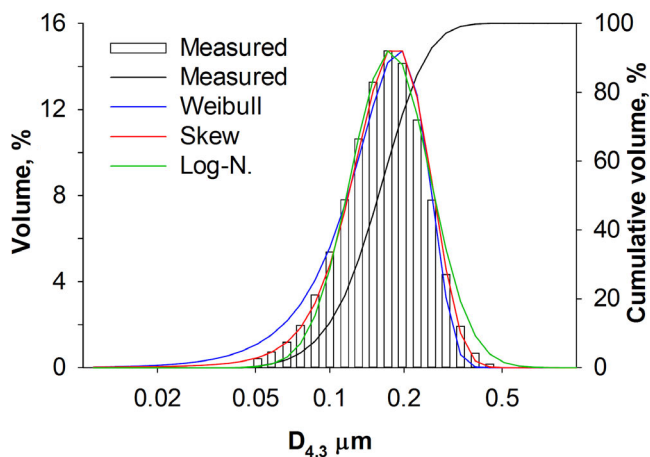


Figure 4.2 Typical particle size distribution and model fit for the feed material.

### 4.3.2 Spray Drying

To avoid nanoparticle agglomeration, we hand-shaked the feed material and used an ultrasound probe VCX500 (Sonics & Materials, Inc.) for 3 min to disperse the material.[87] We spray dried the suspension with a Yamato GB-22 laboratory-scale spray dryer, with a 0.12 m internal diameter by 0.58 m tall glass chamber (Figure 4.3). An electrical coil heated both atomizing and drying air from  $50 \text{ }^\circ\text{C}$  to  $200 \text{ }^\circ\text{C}$ , while an internal flowmeter regulated the drying air to  $0.45 \text{ m}^3 \text{ min}^{-1}$ . The air and suspension were fed co-currently, from top to bottom. We tested seven stainless steel two-fluid nozzles (Table 4.1) ranging from 0.406 mm to 1.530 mm inner diameter for the liquid and 1.626 mm to 3.060 mm outer annulus for the atomizing air. Pressure, air and liquid flow, drying air temperature and nozzle geometry affects the resulting spray nebulization.[88] A peristaltic pump fed the suspension at flow rates of  $5 \text{ mL min}^{-1}$  to  $15 \text{ mL min}^{-1}$ . A pressure regulator from 0.02 MPa to 0.15 MPa ensured that the atomizing air dispersed the suspension into a fine mist. We calibrated the pressure to the atomizing airflow with a rotameter and regressed the data to calculate the gas velocity. A magnetic stirrer maintained the solid suspended in a 250 mL flask at ambient temperature. A cyclone separated the powder from the gas stream leaving the drying chamber: assuming Stokes law regime, the cyclone's cut diameter is  $2.7 \text{ }\mu\text{m}$  at 50% separation efficiency for a  $1600 \text{ kg m}^{-3}$  particle density. Feeding the suspension began 30 min after reaching thermal steady state

with an equivalent volumetric flow of water.[7]

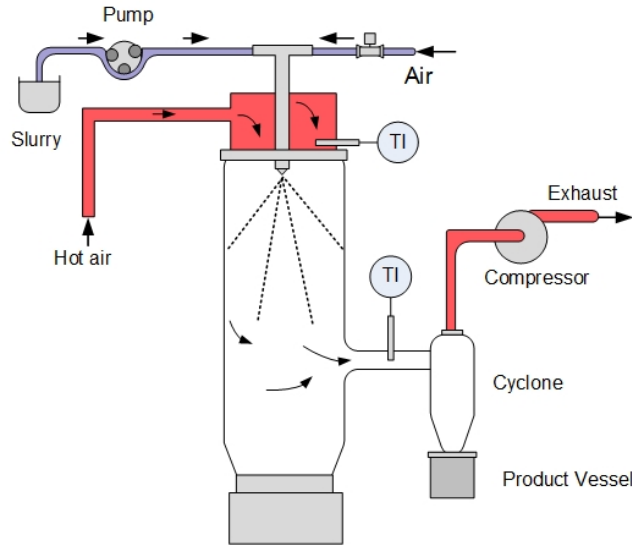


Figure 4.3 Yamato GB-22 spray dryer, co-current mode.[7]

Table 4.1 Two-fluid, external mixing, air blast atomizers; bores in  $\mu\text{m}$ ; when assembled the tip is non-protruding.

Nozzle bore:	$n_1$	$n_{1A}$	$n_2$	$n_{2A}$	$n_3$	$n_{3A}$	$n_4$
$\alpha$	406	406	508	508	711	711	1530
$\beta$	1270	1270	1270	1270	1270	1270	2550
$\gamma$	1626	1778	1626	1778	1626	1778	3060

### 4.3.3 Material Characterization

A Scott volumeter measured the bulk density of the spray dried powder, with and without tapping, reporting the Hausner ratio. We calculated the suspension density  $\rho_{mix}$  from the liquid densities of water and the surfactant, the theoretical skeletal density of LFP[100] ( $3570 \text{ kg m}^{-3}$ ) and the mass fraction  $x_i$  for each component  $i$ .

$$\rho_{mix} = \left( \sum_{i=1}^n \frac{x_i}{\rho_i} \right)^{-1} \quad (4.1)$$

LFP suspensions are non-Newtonian shear thinning fluids.[101] The apparent viscosity measured with a rotational rheometer (Physica, MCR 501) at a solid mass fraction of 30 % with 0.8 % surfactant changed with the shear rate. It was 22 mPa s at a shear rate representative of the suspension feeding tube, while it decreased below 11 mPa s at the shear rates found at the tip of the atomization nozzle.[15]

An optical contact angle instrument (Dataphysics, OCA 15EC) measured the suspension's surface tension using the pendant drop method. Our measurements (33 mN m<sup>-1</sup> to 40 mN m<sup>-1</sup>) agree with the literature (36 mN m<sup>-1</sup>).[102] The surface tension is unaffected by submicron particles.[103]

An LA-950 Horiba laser diffractometer measured the particle size distribution (PSD), using the Mie algorithm, after dispersing our suspension in water with an ultrasound probe, reporting the volume moment mean diameter  $D_{4,3}$  for the primary particles:

$$D_{4,3} = \frac{\sum d_i^4 \cdot N_i}{\sum d_i^3 \cdot N_i} \quad (4.2)$$

where  $N_i$  is the number of particles with the corresponding diameter  $d_i$ . For the dried secondary particles an internal mixer dispersed the material in water. The PSD analysis takes one minute to equilibrate to steady state: the product does not agglomerate/deagglomerate during a 10 min test. The Mie theory applies for both the primary and the spray dried spherical particles, with a refractive index for LFP of  $1.68 + 0.1i$ , and for water of 1.333 (R and Chi parameter below 0.1).[104, 105]

A field emission scanning electron microscope (FE-SEM-JEOL JSM-7600F) acquired the images of the powder at 2 kV and confirmed the particle size distribution from the LA-950 diffractometer.

An X-ray diffractometer (Philips X'PERT) generated the diffractogram of the dried powder to determine if the spray drying conditions oxidized the LFP (forming Fe<sub>2</sub>O<sub>3</sub> and Li<sub>3</sub>Fe<sub>2</sub>(PO<sub>4</sub>)<sub>3</sub>).

A Quantachrome Autosorb-1 measured the N<sub>2</sub> physisorption at 77 K on a dried, degassed sample. Orr and Dallevale[106] proposed a general formula to estimate the time  $\theta$  (in hours) required to degas a sample at a given temperature T (in °C) under vacuum.

$$\theta = 1.44 \times 10^5 T^{-1.77} \quad (4.3)$$

200 °C requires 12 h. The weight change on the degassed sample estimated the residual water content of the spray dried powder. The Barrett-Joyner-Hallender (BJH) theory estimates the pore size distribution (adsorption branch,  $P/P_0$  0.15-0.995); the total pore volume is



evaluated at  $P/P_0$  0.98; and the Brunauer-Emmett-Teller (BET) theory estimates the specific surface area ( $P/P_0$  0.05-0.25,  $C$  constant 60-80).

A Quantachrome Poremaster PM 33-12 mercury porosimeter generated the intrusion and extrusion curves, over a dried degassed sample, up to 228 MPa. This consent to measure down to a 6 nm cylindrical pore, using the Washburn equation (mercury surface tension  $0.480 \text{ N m}^{-1}$  with  $140^\circ$  contact angle). The penetrometer constant was calibrated the same month with a  $0.5 \text{ cm}^3$  cell stem.

#### 4.4 Results and discussion

During atomization, the relative velocity between the atomizing air and the droplet set the droplet surface in motion. This momentum transfer within the globule creates a toroidal recirculation of suspended LFP nanoparticles ( $\mu = 11 \text{ mPa s}$  viscosity). Surface tension also contributes to this effect, because it increases with lower liquid temperatures (located on the drop impact section with air). This cause a hydrodynamic effect on the droplet surface, enhanced by the presence of the surfactant.[107] As the toroidal droplet dries, the slurry assembly shrinks and forms a semi-spherical doughnut-shaped secondary particle (Figure 4.4).[108]

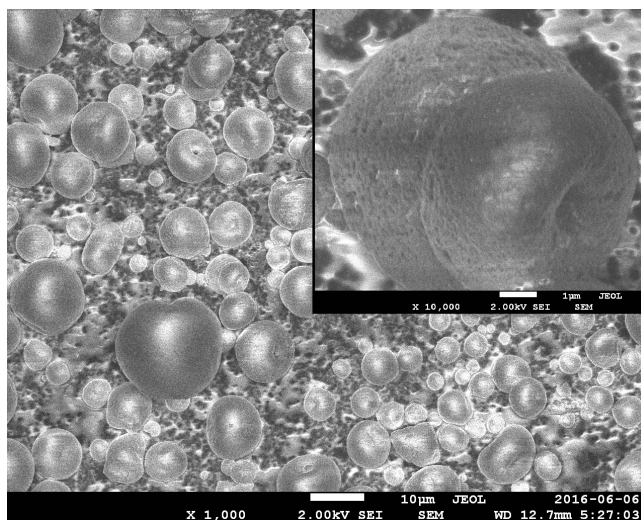


Figure 4.4 Semi-spherical secondary particles. The image shows both doughnut shape and spherical particles but all of the particles are toroidal. Close-up: When holes face the SEM detector, the doughnut-shape morphology is evident.

When the atomization and drying conditions are poor (atomizing gas velocity  $<140 \text{ m s}^{-1}$ , inlet temperature  $<100^\circ \text{C}$ ), droplets coat the internal walls of the spray dryer. They form

agglomerates, which detach as chunks that collect with the powder (Figure 4.5). Air in the spray dryer oxidizes the wall build-up because of the longer residence time and high temperature, which is detrimental to the powders' electrochemical properties.

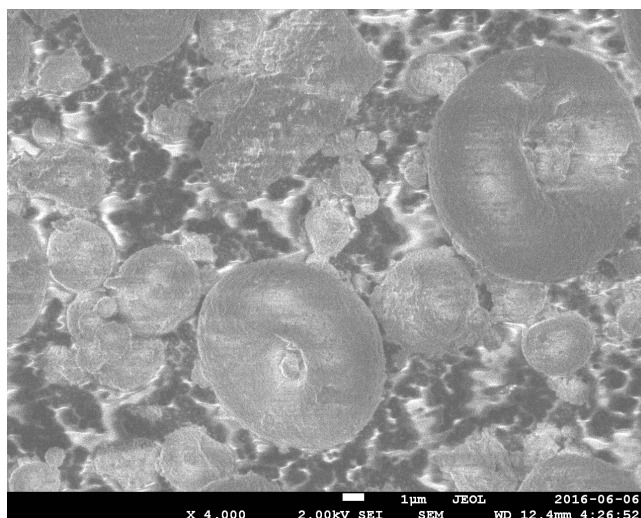


Figure 4.5 Poor atomization conditions creates semi-spherical and fragmented material. The lack of carbon coating makes the non electrically conductive LFP surface look glassy.

#### 4.4.1 Powder Formation

Atomization and drying define the powder formation mechanics. Air atomizes the slurry and blasts the fluid through the nozzle at  $50 \text{ m s}^{-1}$  to  $330 \text{ m s}^{-1}$ . The pump contribution to the initial liquid velocity is negligible ( $<2 \text{ m s}^{-1}$ ). The kinetic energy of the air shatters the liquid jet into filaments that then form droplets. The turbulent nature of the atomization process and velocity gradient inside the jet creates a distribution of filament dimensions and thus droplet sizes that dry to give the final particle size distribution (Figure 4.6).

For gas velocities less than  $140 \text{ m s}^{-1}$ , the droplet size are too large to dry in the chamber and thus coat the internal walls. Smaller particles follow the air streamlines more closely than larger particles because of their lower momentum and so yield of these are higher. The resulting PSD is still monomodal but reflects an atomization condition in which only the smaller droplets dry. For example, drying fails when atomizing at  $53 \text{ m s}^{-1}$ , with an insufficient drying air temperature of  $100^\circ\text{C}$  (Figure 4.7). For such small drying chamber, the biggest particle mode obtainable without a binding agent[7] was  $16 \mu\text{m}$  with a yield of 14%. Increasing the atomization gas velocity allows more kinetic energy to break more liquid surface and obtain smaller droplets. Higher inlet temperatures however, decrease the drying gas density, forming bigger droplets.

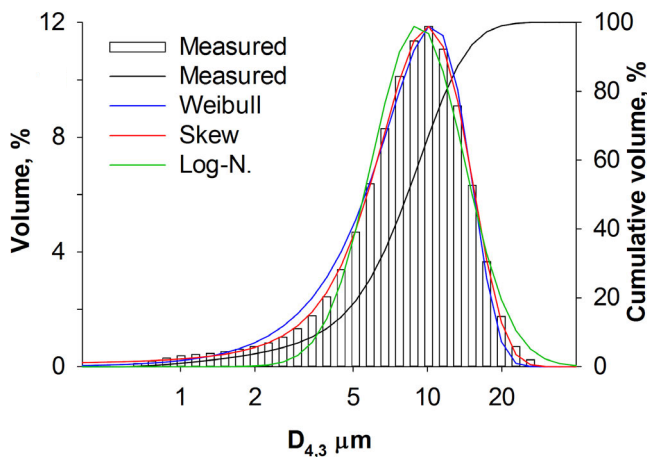


Figure 4.6  $T_{inlet}$  200 °C, atomization velocity 140  $\text{m s}^{-1}$ , nozzle n.4, mass fraction 0.32  $\text{g g}^{-1}$

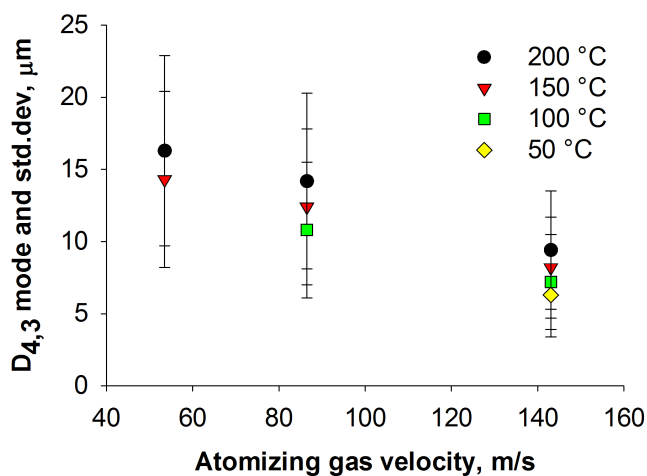


Figure 4.7 Nozzle n.4, same batch feed material, at a mass fraction of 0.32  $\text{g g}^{-1}$  at different inlet temperatures. The bars represent the PSD standard deviation.

#### 4.4.2 Particle Size Distribution

Both the milled and spray dried materials  $D_{4,3}$  PSDs, exhibit nonsymmetrical distributions (Figure 4.6).[109] We noticed also that all distributions become broader when spray drying particles with a larger diameter: the ratio of the measured standard deviation to the particle size distribution mode remains constant ( $const. = 0.4$ ). The 2-parameters log-normal probability density function ( $\alpha, \beta$ ) and the Rosin-Rammler (Weibull) distribution ( $\gamma, \delta$ ) account for >97% of the variance in the data,  $R^2$ .[82] While the three parameters skew normal distribution ( $\epsilon, \zeta, skew$ ) correlates >99%,  $R^2$  (Table 4.2).[110] A two parameters skew normal distribution, ( $skew = 1.8$ ) keeps  $R^2$  above 98%.

Table 4.2 Particle size distribution: (a) measured  $D_{4,3}$  arithmetic mean diameter  $\bar{x}$  and standard deviation  $s$ , (b) log-normal, (c) Weibull and (d) skew normal distribution models, regressed by minimization of the residual sum of squares over non-zero measured values.

	(a)		(b)			(c)			(d)			
	$\bar{x}$ , $\mu\text{m}$	$s$ , $\mu\text{m}$	$\alpha$	$\beta$	$R^2$ , %	$\gamma$	$\delta$	$R^2$ , %	$\epsilon$	$\zeta$	$skew$	$R^2$ , %
slurry	0.16	0.060	-1.6	0.37	98.3	3.5	0.21	97.3	0.18	0.075	1.9	99.1
1	8.6	4.1	2.4	0.43	97.7	3.0	12	99.0	9.3	5.2	1.9	99.9
2	15	6.6	2.9	0.36	96.8	3.6	20	98.5	16	7.7	1.5	99.7
3	7.7	3.5	2.3	0.44	98.2	3.1	10	97.5	7.5	4.5	1.5	99.2
4	7.4	3.3	2.2	0.42	98.5	3.1	9.9	98.1	7.9	4.1	2.0	99.7
5	6.5	2.9	2.1	0.42	98.9	3.1	8.7	97.8	7.0	3.5	2.1	99.6

#### 4.4.3 Residual Moisture (Drying Efficiency)

Heat and mass transfer resistance in porous materials inhibit solvent evaporation rates. Residual water,  $\Delta_{H_2O}$ , increases with decreasing residence time and drying temperatures. The Yamato spray dryer was incapable of removing more than 99% of the water from the LFP and typically  $1\% < \Delta_{H_2O} < 10\%$  (Table 6.8). A power law model accounts for 88% of the variance in the  $\Delta_{H_2O}$ , with  $\beta_0 = 9500$  and three factors: it is proportional to the secondary particle mode ( $D''_{[4,3]m}$ ,  $\mu\text{m}$ ) over the primary particle mode ( $D'_{[4,3]m}$ ,  $\mu\text{m}$ ), and inversely proportional to the square of the inlet temperature (K) (Equation 4.4):

Table 4.3 BET surface area by nitrogen physisorption ( $\pm 2\%$ ),  $\phi$  pore volume for pores smaller than 92 nm,  $D'_{[4,3]m}$ ,  $D''_{[4,3]m}$  primary and secondary particle mode,  $T_{in}$ ,  $T_{out}$  inlet outlet drying temperature,  $\omega$  solid mass fraction,  $u_g$  atomizing gas velocity,  $\Delta_{H_2O}$  residual water (water lost during degassing).

	BET $\text{m}^2 \text{g}^{-1}$	$\phi$ $\text{cm}^3 \text{g}^{-1}$	$D'_{[4,3]m}$ nm	$D''_{[4,3]m}$ $\mu\text{m}$	$T_{in}$ $^{\circ}\text{C}$	$T_{out}$ $^{\circ}\text{C}$	$\omega$ wt./wt.	$u_g$ $\text{m s}^{-1}$	$\Delta_{H_2O}$ %
1	26.4	0.17	81	9.4	200	114	0.32	140	5.8
1r	26.2	0.17	81	9.4	200	114	0.32	140	5.8
2	23.3	0.17	81	16.3	200	118	0.32	55	8.9
3	22.7	0.15	81	8.2	150	89	0.32	140	4.9
4	22.4	0.15	81	7.2	100	58	0.32	140	6.6
5	21.8	0.14	81	6.3	50	36	0.32	140	6.4
5r	22.1	0.14	81	6.3	50	36	0.32	140	6.4
6	23.3	0.14	140	6.2	200	129	0.27	250	3.0
7	21.3	0.15	160	3.6	200	66	0.06	330	0.9
8	14.5	0.09	240	6.3	150	98	0.60	330	2.1

$$\Delta_{H_2O} = \frac{\beta_0 D''_{[4,3]m}}{T_{in}^2 D'_{[4,3]m}} \quad (4.4)$$

Higher temperatures increase the heat transfer from the hot air to the particle bulk, de-

creasing the residual moisture for the same contact time. On the other hand, the ratio of the mode of the secondary particle over the primary, represents the tortuosity of the powder's internal channels. Tortuosity increase the mass transfer resistance of steam leaving the material. Large secondary particles dry slower, because in a sphere the surface to volume ratio decreases with the diameter ( $6/d$ ). While the small primary particles increase the sample specific surface area, *i.e.* the residence time that the steam molecules have to travel throughout the porous material.

#### 4.4.4 Yield

Yield is the ratio between the collected spray dried powder mass (including any remaining water) and the mass of LFP in the feed slurry. Yields greater than 70% indicate well achieved spray drying conditions (Figure 4.8). It increases with atomizing gas velocities above  $150 \text{ m s}^{-1}$  and drying temperatures above  $150^\circ\text{C}$ . However, temperatures above  $150^\circ\text{C}$  in synergy with feed flow below  $3 \text{ mL min}^{-1}$  clog the nozzle, creating a solid crust on the tip. This situation is more compelling for small bore nozzles (from  $n_1$  to  $n_{2A}$ ) (Table 4.1). Solid mass fraction does not affect the yield.

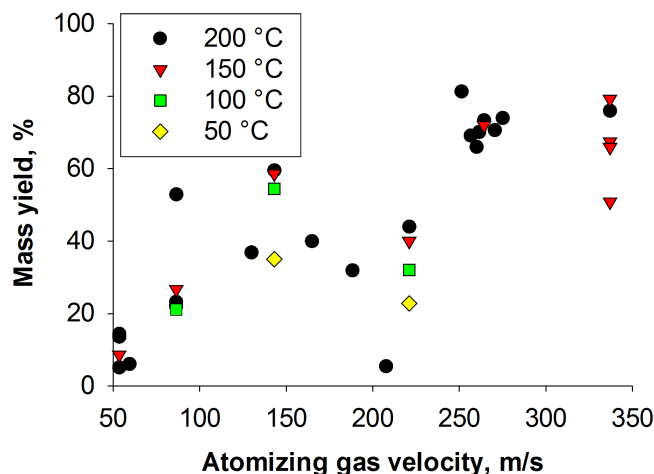


Figure 4.8 Data from different experimental conditions correlate with respect drying temperature and atomization gas velocities.

#### 4.4.5 Powder Bulk Density and Flowability

These fine LFP spray dried particles (mode  $<16 \mu\text{m}$ ) are cohesive,[111] resulting in a loosely compacted material with a bulk density much lower than the skeletal density. The Hausner ratio was between 1.4 and 1.6 for all samples, indicating poor flowability,[112] invariant with

respect to the drying conditions. The powder does not flow through a 10 mm bore hopper unless vibrated. The bulk density of the powder increases with the solid suspension mass fraction ( $\omega$ , wt./wt.) and the secondary particle mode ( $D''_{[4,3]m}$ ,  $\mu\text{m}$ ) (Figure 4.9). A high water-content slurry increases the amount of steam leaving the drying particle, thus pushing the primary particles away to create discharge channels for the leaving vapors. Also, smaller secondary particles increase the cohesive force, allowing less powder to compact in the Scott volumeter (Table 6.8). A two parameters model is proposed to describe this trend (Equation 4.5). The regressed bulk density  $\rho_B$  ( $\text{kg m}^{-3}$ ) accounts for 67% of the variance in the data ( $R^2$ ), when  $\beta_0 = 450$ ,  $\beta_1 = 220$ . Atomization and drying conditions are insensitive.

$$\rho_B = \beta_0 + \beta_1 \omega \left( D''_{[4,3]m} \right)^{0.33} \quad (4.5)$$

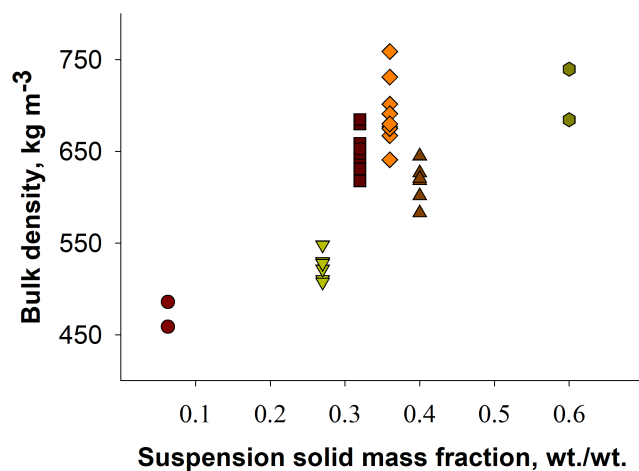


Figure 4.9 Each column represents a different batch of milled material with respect solid loading and primary particle size. Particle density is invariant, but secondary particle size influences the flowability.

#### 4.4.6 Mercury Porosimeter

We tested two samples that gave good yield (>70%) and were dried at extreme temperatures (200 °C and 100 °C). Since the volume intrusion curves for samples 2 and 5 were similar, a third analysis was not justified (Figure 4.10). The first slope accounts for inter-particle filling and plateaus at 300 nm. The second is the intra-particle filling, measuring down to the instrument limit of 6 nm. The inter-particle porosity for samples 1 and 4 is 30% and 32%, this is consistent with the mathematical void fraction of packed spheres. Intra-particle porosity adds an additional 30% and 28% to the total pore volume. Surface area is 21 m<sup>2</sup> g<sup>-1</sup>

and  $20 \text{ m}^2 \text{ g}^{-1}$ , while intra-particle pore volume is  $0.270 \text{ cm}^3 \text{ g}^{-1}$  and  $0.268 \text{ cm}^3 \text{ g}^{-1}$ , which is mostly distributed between 10 nm to 150 nm, with a peak at 70 nm. Nitrogen physisorption validates the same pore volumes for pores smaller than 330 nm, while the surface area is slightly higher ( $26.4 \text{ m}^2 \text{ g}^{-1}$  and  $21.8 \text{ m}^2 \text{ g}^{-1}$ ), meaning the presence of a meso and microporous structure. Tortuosity (1.55) is the same for both samples, as well as the throat to pore ratio (0.080). Permeability (accounting for tortuosity effect) is instead  $0.026 \text{ nm}^2$  and  $0.032 \text{ nm}^2$ , respectively. Interestingly, skeletal density at fill pressure is  $2800 \text{ kg m}^{-3}$  (sample 2) and  $2500 \text{ kg m}^{-3}$  (sample 5), while LFP material should be  $3570 \text{ kg m}^{-3}$ . This discrepancy can be attributed to the raw material preparation, or the presence of closed pores. Evaluating the density at the beginning of the second slope, give a particle density of  $1600 \text{ kg m}^{-3}$  and  $1500 \text{ kg m}^{-3}$ .

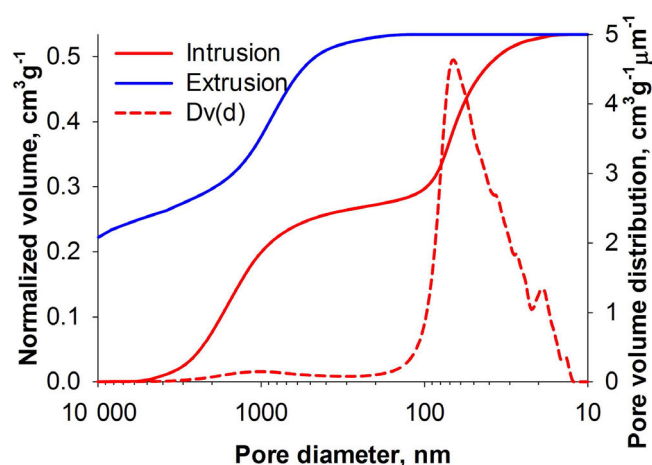


Figure 4.10 Mercury porosimeter curves for sample n. 2, on the abscissa, the calculated pore diameter from pressure, using the Washburn equation, assuming cylindrical pores.

#### 4.4.7 Nitrogen Physisorption

Nitrogen adsorption/desorption isotherms are similar for all the samples analyzed, with a type II isotherm and an H1 hysteresis loop (Figure 4.11).[113]

Type H1 is often associated with porous materials consisting of well-defined cylindrical-like pore channels or agglomerates of compacts of approximately uniform spheres.[114] The lack of plateau over a range of high  $P/P_0$  indicates incomplete pore filling. In fact, the mercury porosimeter analysis revealed the presence of a macroporous structure, while the nitrogen physisorption can only measure micro and mesoporous materials.[115] BJH volume pore size distribution over the adsorption branch shows two sharp peaks around 2 to 3 nm and 4 to 5 nm and one broad between 5 to 200 nm. The two sharp peaks are invariant, as part of

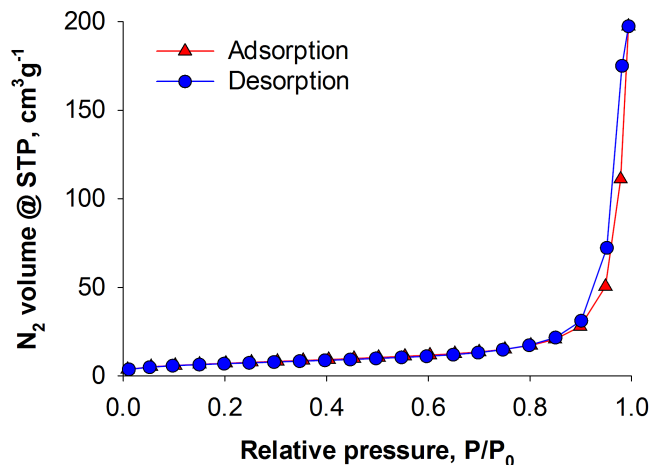


Figure 4.11 Sample n.2 isotherms, STP at 0 °C and 101 kPa

a LFP's morphological properties.[116] The broad peak decrease in intensity as the drying temperature decreases (Figure 4.12), suggesting that higher drying temperatures increase the drying rate, steam generation in the particle, channel formation and, therefore, the mesoporosity of the material. This porosity change in respect with the time-temperature history in the spray dryer is also found in other studies where spray drying the same material in bigger drying chambers allowed to decrease the drying rate, therefore achieving a more compact secondary particle with higher bulk density.[62] The specific surface area ( $SSA$ ,  $\text{m}^2 \text{g}^{-1}$ ) increases linearly with the total pore volume ( $\phi$ ,  $\text{cm}^3 \text{g}^{-1}$ ) for pores smaller than 92 nm (Table 6.8).

$$SSA = \beta_0 + \beta_1 \phi \quad (4.6)$$

The regressed value accounts for 91 % of the variance in the data ( $R^2$ ), when  $\beta_0 = 4.4$ ,  $\beta_1 = 120$ . This is an indication that the primary particle, grinded after melt synthesis, is non porous. Porosity arises when these primary particles overlay and compact. In fact higher drying temperatures help create a more mesoporous material. In these conditions the primary particles do not perfectly overlay and expose more surface area. Moreover, the laser scattering measure on the primary particle size distribution, estimates a surface area which accounts between 70 % to 90 % of the BET measured surface area of the dried material (assuming a nonporous and spherical particle with a density of  $2700 \text{ kg m}^{-3}$ ). Drying at 200 °C optimizes the surface area. Working at 250 °C does not seem beneficial, as we reach the same surface area. A 20 % smaller primary particle mode, leads a gain of 55 % more surface area, which is consistent to previously reported papers.[117] Secondary particle dimensions moderately



influence the BET surface area. A 75 % bigger particle mode will decrease the surface area by 10 %.

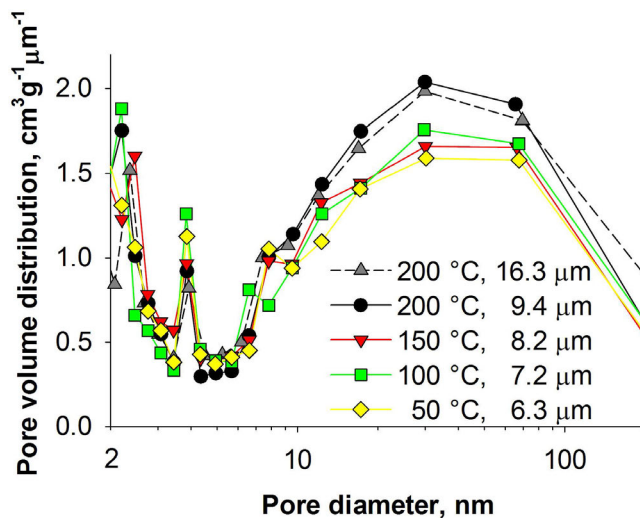


Figure 4.12 BJH adsorption  $dVolume(diameter)$  at different inlet temperatures and secondary particle sizes.

To estimate the specific surface area of a spray dried suspension of LFP ( $SSA$ ,  $m^2 g^{-1}$ ), we created a two-parameters model to regress the primary particle mode ( $D'_{[4,3]m}$ , nm), the secondary particle mode ( $D''_{[4,3]m}$ ,  $\mu m$ ), and the inlet temperature ( $T_{in}$ ,  $^{\circ}C$ ) (Equation 4.7). The regressed surface area accounts for 85 % of the variance in the data,  $R^2$  (Table 6.8), when  $\beta_0 = 24.8$  and  $\beta_1 = -0.104$ .

$$SSA = \beta_0 + \beta_1 \frac{D'_{[4,3]m}{}^3}{D''_{[4,3]m} T_{in}^2} \quad (4.7)$$

#### 4.4.8 X-ray Diffraction

We performed XRD to exclude the presence of contaminants in the final product, arising from overoxidation of the material at high drying temperatures and phase segregation:  $Fe^{3+}$ :  $Li_3Fe_2(PO_4)_3$ , at  $27.5^{\circ} 2\theta$ , [118] and  $\beta$ - $Li_3PO_4$ , at  $34.0^{\circ} 2\theta$ . [119] We tested the material dried at  $100^{\circ}C$  and  $350^{\circ}C$  (a pilot 0.8 m I.D. GEA mobile minor spray dryer, with the purpose of comparing diffraction pattern of powders dried at temperatures above the limit of our laboratory scale instrument). The gas contact time for the Yamato spray drier is 0.5 s, while the GEA spray dryer reaches 14 s. For both cases, the outlet temperature was sought to be  $110^{\circ}C$ , and no contaminants were detected (Figure 6.18,  $T_{in}$ :  $350^{\circ}C$ ). We calculated a

crystallite diameter of 30 nm using the XRD peak at  $2\theta = 17^\circ$  ( $\text{LiFePO}_4$  (200), diffraction peak) by the Scherrer equation.

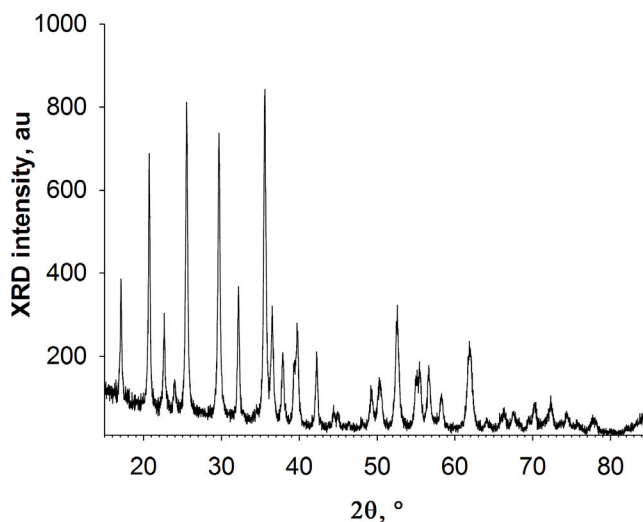


Figure 4.13 Theta-2-theta acquisition at 50 kV and 40 mA, using a Cu anode, Gonio mode,  $\text{CuK}\alpha$  sideband removed.

## 4.5 Conclusions

All spray drying conditions creates semi-spherical doughnut-shaped secondary particles. A two parameters skew normal distribution fits the experimental PSD better than the log-normal and the Weibull distribution, with a skew value of 1.8 ( $R^2 > 98\%$ ).

The nozzle  $n_2$  yields the best (liquid bore 508  $\mu\text{m}$ ), atomizing the feed material into ultimately a fine narrow powder (mode  $6 \pm 3$   $\mu\text{m}$ ), but LFP suspension clogs more frequently this small bore nozzle. Nozzle  $n_4$  does not clog (liquid bore 1530  $\mu\text{m}$ ) and creates larger particles with a wider distribution (mode  $9 \pm 4$   $\mu\text{m}$ ). The distribution's standard deviation is linearly proportional (40%) with respect to the PSD mode.

High temperature and atomization velocity (200  $^\circ\text{C}$ ,  $>250$   $\text{m s}^{-1}$ ) increase the yield ( $>70\%$ ). Higher solid content in the slurry increases the final bulk density of the powder, up to 750  $\text{kg m}^{-3}$  at 60% loading. But fine material (mode  $<16$   $\mu\text{m}$ ), have poor flowability (Hausner ratio 1.5).

Spray dried sample porosity is distributed mainly in the macroporous region, in particular the pore mode diameter has the same order of magnitude as the primary particle. The surface area derived from the PSD (assuming spherical particles) is proportional and within 80% with respect to the BET surface area, indicating that melt-synthesized LFP is non-porous.

The secondary particles however, possess a mesoporous structure that increases in volume by 10%, when the drying temperature is increased from 100 °C to 200 °C. Which suggests that slower drying rates (at lower temperatures) form a more compact material.

Operating at 200 °C maximizes the surface area ( $26.4 \text{ m}^2 \text{ g}^{-1}$ ). Also 20% smaller primary particle mode, leads a gain of 55% more surface area.

#### **4.6 Acknowledgments**

The authors recognize the support of Natural Science, Engineering Research Council of Canada and the Canadian Foundation for Innovation through the Automotive Partnership Canada program and our industry partner Johnson-Matthey.

## CHAPTER 5 ARTICLE 2 - LiFePO<sub>4</sub> SPRAY DRYING SCALE-UP AND BINDERS FOR IMPROVED CYCLABILITY

Marco G. Rigamonti,<sup>a</sup> Marc Chavalle,<sup>b</sup> He Li,<sup>a</sup> Philippe Antitomaso,<sup>c</sup> Lida Hadidi,<sup>c</sup> Marta Stucchi,<sup>d</sup> Federico Galli,<sup>d</sup> Hayat Khan,<sup>a</sup> Mickael Dollé,<sup>c</sup> Daria Camilla Boffito,<sup>a</sup> and Gregory S. Patience<sup>a</sup>

Submitted in 2019 to: Johnson Matthey for review, later to *Energy & Environmental Science* for publication.

### 5.1 Abstract

Growing markets require fast solutions to manufacture inexpensive long-lasting batteries for vehicles. LiFePO<sub>4</sub> (LFP) melt synthesized from ore concentrate fits this role, but requires additional steps to grind the material into a nanoparticle suspension and to desiccate. Spray drying creates a mesoporous powder that promotes wettability. The addition to the suspension of lactose and high Mw polyvinyl alcohol (PVA) nanostructures the material and pyrolysis creates a carbon cage that interconnects the cathode nanoparticles, imparting better capacity (LiFePO<sub>4</sub>/C: 161 mA h g<sup>-1</sup> at 0.1C), discharge rate (flat plateau with 145 mA h g<sup>-1</sup> at 5C), and cyclability (91% capacity retention after 750 cycles at 1C). Spray dried particle size affects battery stability; PVA increases the suspension's viscosity and alters the powder morphology, from spherical to hollow particles. A model describes the rheology of the non-Newtonian ternary system: water-LFP-PVA, for shear and temperature variation. We investigate the calcination mechanism by measuring the carbon content and chemical composition of the pyrolyzed species by XPS and Raman. Carbon precursors prevent sintering of the nanoparticles but lactose gasifies 50% of the carbon. The PVA carbon grid imparts microporosity and we correlate the SEM and TEM powder's morphology with N<sub>2</sub> physisorption porosimetry. Ultrasonication of the LFP-organic precursors suspension leads to the fragmentation of the PVA chain, which is detrimental for the final cathode material.

---

<sup>a</sup> Department of Chemical Engineering, Polytechnique Montréal, C.P. 6079, Succ. CV Montréal, H3C 3A7 Québec, Canada.

<sup>b</sup> Laboratory of Soft Matter Science and Engineering, École supérieure de physique et de chimie industrielles de la Ville de Paris, 10 rue Vauquelin, 75005 Paris, France.

<sup>c</sup> Laboratory Chemistry and Electrochemistry of Solids, Université de Montréal, 2900 boul. Édouard-Montpetit, H3T 1J4 Montréal, Québec, Canada.

<sup>d</sup> Dipartimento di Chimica, Università degli Studi di Milano, via Golgi 19, 20133 Milano, Italy.

## 5.2 Introduction

Lithium-ion batteries power our life: cellphones and computers count in the billions of units, and a new technology sector aims to scale-up batteries for the automotive industry and for stationary energy storage systems.[21] For this strategic vision, batteries with high-efficiency, long-life and low-cost are the best choices to effectively transition to electric vehicles and decrease our dependency on fossil fuels; while electric storage units create a flexible and reliable grid system smoothing-out the fluctuating supply from renewable sources.[22] The cathode represents the bottle-neck of this technology as its capacity is one order of magnitude lower than the graphite anode.  $\text{LiCoO}_2$ , at  $273 \text{ mA h g}^{-1}$ , is the cathode of choice for electric vehicles, but is costly and has safety and environmental issues.[23]  $\text{LiFePO}_4$  has a lower capacity ( $170 \text{ mA h g}^{-1}$ ) but costs less, is thermally stable, and its precursors are environmentally benign.[24, 25] The lithium-sulfur cell with a glass solid-state electrolyte promises to lead the next generation of batteries, but despite their outstanding cycle life (above 15000), and improved capacity (reaching  $500 \text{ mA h g}^{-1}$ ), cost and scalability are potential deterrents for adoption.[26] Commercial  $\text{LiFePO}_4$  batteries discharging at 2.5C-rate maintain their temperature below  $55^\circ\text{C}$ ,[27] and in case of a short-circuit do not ignite.[28] On the other hand,  $\text{LiFePO}_4$  material has a poor electrical conductivity and slow  $\text{Li}^+$  diffusivity in the crystalline matrix. The addition of carbon black,[29] coating with carbon layer or metal oxides increases the electric conductivity;[30, 31] while doping it with cations improve the  $\text{Li}^+$  diffusivity.[32] Carbon nanotubes demonstrated high power output and excellent cycling performance in a  $\text{ZnFe}_2\text{O}_4\text{-C/LiFePO}_4\text{-CNT}$  battery, but only at a laboratory scale (10'000 cycles at 10C, retained 85 % of the initial capacity).[33] Other laboratory scale research improve the wettability by nanostructuring the material: a greater specific surface area exposes more material in contact with the electrolyte, which increases  $\text{Li}^+$  flow rate across the cathode; while nanoparticles shortens the diffusion path and inside the crystal structure.[34] While flame-spray pyrolysis demonstrated the importance of controlling the size of the powder also at a micron-scale level.[35] Coupling  $\text{LiFePO}_4$  with iodine modifies the redox cycle and improves the energy density,[36] and different carbon precursors lead to a better conductive carbon layer.[37]

In this paper we demonstrate the scale-up feasibility of spray drying melt-synthesized  $\text{LiFePO}_4$  and organic precursors that self assemble into a carbon cage, which increases the cathode cyclability, similarly to carbon nanotubes.[50] Melt-cast processes reduce the reactant cost by 40 %, starting from lower-grade purity precursors, but still yield a pure, crystalline material.[51, 52] In our process, a furnace produces LFP ingots. Subsequently, a jaw crusher, a roller grinder and a wet media mill reduce the size of the material to the nanoscale in

water. Organic precursors are mixed and spray drying dessicates the suspension. In the process, a two-fluid nozzle atomizes the suspension with compressed air. The hot air dries the microscopic droplets (up to 100  $\mu\text{m}$ ), and the suspended nanoparticles (primary particles, 0.07  $\mu\text{m}$  to 0.2  $\mu\text{m}$ ) agglomerate into a porous, spherical or doughnut-shaped, secondary particle (5  $\mu\text{m}$  to 50  $\mu\text{m}$ ) which forms the powder that is collected from the unit. The resulting porous powder is then calcined to pyrolyze the organic precursors to semi-graphitic carbon which enhances the electrical conductivity of the material. Finally, coin-cell batteries established the electrochemical quality of the LFP/C cathode.

### 5.3 Experimental section

#### 5.3.1 Nanoparticle suspension preparation

An induction furnace at 1100  $^{\circ}\text{C}$  melted the precursors and synthesized LFP in a graphite crucible. Starting from:  $\text{LiH}_2\text{PO}_4$ ,  $\text{P}_2\text{O}_5$ ,  $\text{Li}_2\text{CO}_3$  and iron ore concentrate (>99%  $\text{Fe}_2\text{O}_3$  with  $\text{SiO}_2$  impurity) with a Li/Fe/P: 1.03/1/1.03 stoichiometry,[14, 89, 90] casting 50 kg of LFP into 200 mm ingots.[91] LFP is the dry solid fraction of our feed material, constituted of 97.8%  $\text{LiFePO}_4$  and 2.2%  $\gamma\text{-Li}_3\text{PO}_4$  ( $\pm 0.4\%$   $CI_{n=6}^{95\%}$ , by AAS and XRD; 95% confidence interval estimate, with a two-tail  $t$ -test for a sample number  $n$ ).

A Pulverisette 1 model II, Fritsch jaw crusher ground the ingots to 1 mm to 3 mm gravel, processing 13  $\text{kg h}^{-1}$  of material. A roller grinder (MPE 6F granulizer, Chicago) further reduced the particle size to  $d_{v,50}$  of 27  $\mu\text{m}$  and  $d_{v,99}$  of 200  $\mu\text{m}$ ; treating 2  $\text{kg h}^{-1}$  of material at a 10% feed rate. A wet media mill (NETZSCH - LMZ 4) ground the powder, equipped with a 0.1 mm mesh filter and loaded with 3.2 L of 0.68 mm yttria-stabilized zirconia beads, which filled 75% of the total volume of the grinding chamber. Pilot and commercial grinding chambers are made of ceramic rather than stainless steel to minimize iron contamination. We filled the apparatus with 25 L of deionized water and loaded 25 kg of LFP, with a 0.008 mass ratio of Tween-20 surfactant in the mixing tank. We scaled-up the process using our previous laboratory practice and added LFP progressively at a rate slow enough to avoid plugging the mesh filters (20  $\text{kg h}^{-1}$ ).[15] A cooling system pumped water at 15  $^{\circ}\text{C}$  around the grinding chamber and mixing tank (ESI Fig. 1S).<sup>†</sup> We sampled the slurry at the outlet of the grinding chamber every 15 min and immediately analyzed by laser scattering to avoid agglomeration. We operated the wet media mill until the particle size distribution (PSD) median reached 200 nm.

### 5.3.2 Spray drying

Despite the Tween-20 surfactant, the suspended primary particles tended to settle when stored for weeks. A mechanical mixer homogenized the slurry periodically and an aliquot of material was weighed and ultrasonicated for 15 min before each experiment to de-agglomerate the nanoparticles.[87] For standard feed materials, we added binders (lactose, polyvinyl alcohol solution or colloidal silica, 1% to 7%) and mechanically stirred the suspension for an additional 15 min. For ultrasonicated slurries (US), we added the binders while stirring and ultrasonicated for 15 min. We spray dried the feed material with a GEA Niro Mobile Minor<sup>TM</sup>-PSR pilot-scale spray dryer (0.8 m I.D. x 0.8 m height / 60° cone chamber Fig. 5.1). An 11 kW electrical coil heated 90 kg h<sup>-1</sup> of drying air at 350(2) °C, which flowed co-currently with the spray, leaving the bottom of the chamber at 125(2) °C. We chose a two-fluid nozzle, with 0.7 mm I.D. for the liquid and 3.1 mm I.D. 5.0 mm O.D. for the atomizing air, based on laboratory-scale tests of flowability of LFP suspensions through a bore restriction.[7, 84] Compressed air at 0.25 MPa to 0.40 MPa fed the nozzle while a peristaltic pump fed the suspension at flow rates between 130 mL min<sup>-1</sup> to 180 mL min<sup>-1</sup>, creating a fine mist. A cyclone separated the resulting powder, with a 50% cut-off efficiency for 0.7 μm, 1600 kg m<sup>-3</sup> secondary particles. Before feeding the suspension, we reached thermal steady state with an equivalent volumetric flow of water (up to 90 mL min<sup>-1</sup>) during 2 h.

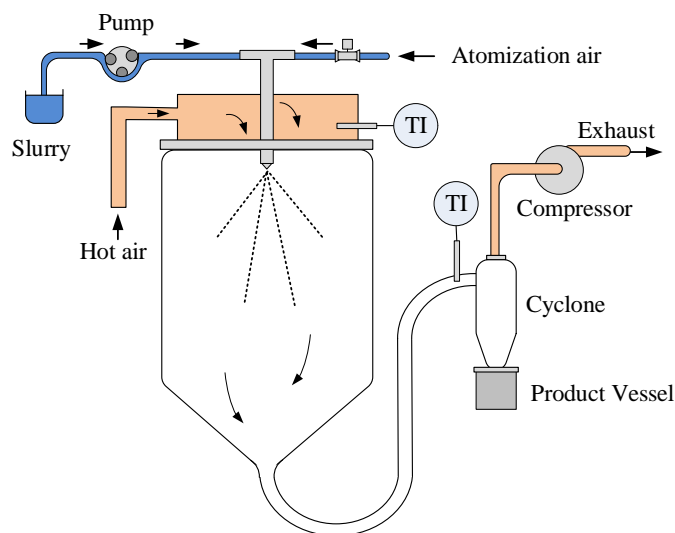


Figure 5.1 GEA Mobile minor spray dryer setup. The recovery yield averages 80%: 10% of the material coats the chamber and another 10% escapes the cyclone.

### 5.3.3 Calcination and electrochemical tests

We loaded 2 g of spray dried powder into an alumina crucible and inserted it in a tube furnace flushed with a  $N_2$  atmosphere. We let the powder outgas at  $100\text{ }^\circ\text{C}$  for 2 h and then increased the temperature to  $700\text{ }^\circ\text{C}$  for 2 h to calcine the material. The electrode of carbon coated LFP was prepared by mixing the pyrolyzed active material ( $\text{LiFePO}_4/\text{C}$ , 500 mg), with carbon black C65 as conductive additive, and polyvinylidene fluoride (PVDF) at a weight ratio of 84:9:7 in N-methyl-2-pyrrolidone (NMP) solvent. The mixture was then shaken in a Turbula 3D mixer for 20 min, and homogenized in a tube roller overnight with 5 mm by 6 mm cylindrical beads. The uniform slurry was spread onto a piece of aluminum foil current collector using the doctor blade technique. The electrode dried in a vacuum oven at  $80\text{ }^\circ\text{C}$  overnight. Disc-shaped electrodes with a loading of  $1.8(1)\text{ mg cm}^{-2}$ , and a thickness of  $24\text{ }\mu\text{m}$ , were cut and assembled in coin cells (2032) in an argon filled glove box. A lithium metal foil was used as the negative electrode,  $\text{LiFePO}_4/\text{C}$  as the positive one, Celgard 2400 as the separator, and 1 M  $\text{LiPF}_6$  in ethylene carbonate-dimethyl carbonate (weight ratio of 1:2) solvent as the electrolyte. The electrochemical tests were performed on the cells at  $30\text{ }^\circ\text{C}$  on a Arbin BT2000 electrochemical station with cut-off voltages of 2.2 V and 4.0 V vs  $\text{Li}^+/\text{Li}$  at a 0.1C-rate for galvanostatic cycling and at 0.1C to 10C-rates to determine the power performance.

### 5.3.4 Reagents and Characterization

D(+)-lactose monohydrate (>98 % Sigma-Aldrich). LUDOX<sup>®</sup> SM colloidal silica (30 % suspension in water, Sigma-Aldrich). Polyvinyl alcohol (PVA) with a weight average Mw 146,000-186,000  $\text{g mol}^{-1}$  was purchased from Sigma-Aldrich, and dissolved in boiling deionised water forming a 5 % solution. An X-ray diffractometer (XRD, BRUKER D8) recorded the diffractogram of the spray dried powder in a stepwise scan of the goni axis ( $10^\circ$  to  $80^\circ$   $2\theta$ ,  $0.02^\circ$  step), with a copper anode at 40 kV and 40 mA. The HighScore Plus software stripped the K-Alpha sidebands and refined the spectra using the Crystallography Open Database (COD) database:  $\text{LiFePO}_4$  orthorhombic Pnma, ref. 96-400-1849;  $\text{Li}_3\text{PO}_4$  orthorhombic Pnma, ref. 96-901-2822, and JCPDS card:  $\text{LiFePO}_4$  01-070-6684;  $\text{Li}_3\text{PO}_4$  00-015-0760. We solubilized 20 mg of spray dried powder in 5 mL of  $6\text{ mol L}^{-1}$  HCl (HPLC grade). Once completely dissolved we diluted the solution in 1 L of deionized water (reaching a pH of 1.5). An atomic absorption spectrometer (AAS, PerkinElmer AAnalyst 200) measured the absolute concentrations of  $\text{Li}^+$  and  $\text{Fe}^{3+}$  in the solution ( $\text{mg L}^{-1}$ ), using the manufacturer procedure (N0225001 Rev.C). A laser diffractometer (LA-950 Horiba) measured the PSD, from 30 nm to 3 mm, using the Mie algorithm, reporting the volume moment mean diameter (DeBroukere



mean)  $D_{4,3}$ , and one standard deviation as the square root of the variance in the distribution:

$$D_{4,3} = \frac{\sum d_i^4 \cdot N_i}{\sum d_i^3 \cdot N_i} \quad (5.1)$$

where  $N_i$  is the number of particles with the corresponding diameter  $d_i$ . Ultrasonication and stirring dispersed the slurry in water, while only stirring dispersed the spray dried powders during analysis. A refractive index of  $1.68 + 0.1i$  for LFP and  $1.333$  for water minimized below  $0.1$  the R and Chi fitting scores.[86] We measured the tapped density  $\rho_t$ , following the ASTM B527 procedure, by pouring the powder in a graduated volumetric cylinder and hand-tapping until the volume remained constant. A field emission scanning electron microscope (SEM, FE-SEM-JEOL JSM-7600F) equipped with an energy dispersive X-ray detector (EDS) acquired the images of the powder at  $2\text{ kV}$  with the SEI detector. A transmission electron microscope (TEM, JEOL JEM-2100F) recorded the images of the pyrolyzed material at  $200\text{ kV}$  in bright field imaging mode. A CS elemental analyzer (LECO CS744) measured the elemental carbon weight fractions after spray drying and after pyrolysis. The value has been corrected in terms of dried material ( $g_C/g_{LFP}\%$ ) without the residual moisture. A Quantachrome Autosorb-1 measured the  $N_2$  physisorption isotherms at  $77\text{ K}$ . The powder was degassed at  $200^\circ\text{C}$ , under vacuum, for  $12\text{ h}$  and weighed with an Entris224-1S balance ( $\pm 0.2\text{ mg}$ ). We regressed the total specific surface area ( $S_a$ ), over the best linear range, with the Brunauer-Emmett-Teller (BET) equation ( $P/P_0$ :  $0.07-0.20$ ,  $C$  constant  $60-200$ ). The Barrett-Joyner-Hallender (BJH) method estimates the mesopore size distribution (desorption branch,  $P/P_0$ :  $0.2-0.995$ , excluding the cavitation-induced artifact at  $P/P_0$ :  $0.45$ ,  $4\text{ nm}$ ). As comparison, the NLDFT method for siliceous materials with cylindrical pores, calculates the pore size distribution including the micropore region for the spray dried powders ( $P/P_0$ :  $0-0.98$  equilibrium adsorption-desorption). While pyrolyzed powders that have a carbon coat, use the NLDFT kernel for carbonaceous materials with cylindrical pores (same, up to  $0.95$ ).[92] The NLDFT method has a fitting error below  $1.2\%$  over the measured volume, and a lower confidence limit of  $1\text{ nm}$ . The  $V - t$  method regresses the specific surface area, characteristic pore size and volume for the microporous fraction over the best linear range (DeBoer thickness). The total pore volume is evaluated at  $P/P_0$ :  $0.995$ , which accounts for pores smaller than  $300\text{ nm}$  in diameter.[8] The intra-primary-particle void fraction (porosity  $\varphi$ , %) was calculated from the skeletal density of the material (LFP:  $\rho_{sk} = 3.57\text{ g cm}^{-3}$ ) and the measured pore volume ( $V_{\text{pore}}$ ,  $\text{cm}^3\text{ g}^{-1}$ ) (Eq. 5.2). While the apparent particle density  $\rho_p$ ,  $\text{g cm}^{-3}$  with Eq. 5.3.

$$\varphi = \frac{V_{\text{pore}}}{V_{\text{pore}} + \frac{1}{\rho_{\text{sk}}}} \quad (5.2)$$

$$\rho_{\text{p}} = \frac{\rho_{\text{sk}}}{1 + V_{\text{pore}}\rho_{\text{sk}}} \quad (5.3)$$

A HAAKE<sup>TM</sup> Viscotester<sup>TM</sup> iQ Air rheometer (Thermo Scientific<sup>TM</sup>) equipped with a CC27 coaxial cylinder double gap geometry (3.00(5) mL volume) and an external water/glycol temperature controller (Polystat<sup>®</sup> Cole-Parmer<sup>®</sup>  $-10.0(1)$  °C to  $80.0(1)$  °C) recorded the apparent viscosity of the LFP suspensions while increasing and decreasing stepwise the shear rate ( $10 \text{ s}^{-1}$  to  $4000 \text{ s}^{-1}$  range, after pre-shearing at  $10 \text{ s}^{-1}$  for 3 min). A VCX 500, Sonics & Materials, Inc. powered a 20 mm diameter ultrasonic horn at 500 W, resonating at 20 kHz and 40 % amplitude. The horn was immersed half-way in a magnetically stirred beaker, and the actual power delivered to a 0.6 L suspension was  $40 \text{ W L}^{-1}$ , calibrated with a calorimetric procedure.[93] An X-ray photoelectron spectrometer (XPS, VG ESCALAB 3 MkII) analyzed the carbon coating of our LFP powders.[8] A Mg  $K\alpha$  source at 15 kV gathered the spectra over a  $<10 \text{ nm}$  material thickness, reporting carbon and oxygen bonding information. We acquired the Raman spectra on 3 different spots per sample, with a Renishaw inVia Microscope, a 50x objective lens, 30 s exposure time,  $600 \text{ lines mm}^{-1}$  optical grating, giving a spectral resolution of  $3 \text{ cm}^{-1}$ . The 514.5 nm laser was reduced in power (to 10 %, 2.5 mW) to avoid damaging the carbon coat and irradiated the powder in a  $7 \mu\text{m}^2$  area.

## 5.4 Results and discussion

### 5.4.1 LFP characterization and elemental analysis

Spray drying atomizes the suspension into droplets that have a short residence time in the chamber (14s). As long as the droplets contain water, evaporation occurs below the boiling point of the solvent, and by the time the powder is bone-dry, the air's outlet temperature has decreased to  $125 \text{ °C}$ , due to the latent heat of vaporization of water. This phenomena prevents any oxidation or chemical alteration of the feed material, even when spray drying up to an inlet temperature of  $350 \text{ °C}$ , as long the outlet temperature remains below such transitions.[84] In comparison, drying the slurry on a hot plate at  $180 \text{ °C}$ , in air, partially overoxidizes the material to  $\text{Fe}^{3+}$ :  $\text{Li}_3\text{Fe}_2(\text{PO}_4)_3$  and  $\text{Fe}_2\text{P}$  each observable with a characteristic XRD peak at  $27.5^\circ$  and  $41.0^\circ 2\theta$ . [118, 120] Instead, the only additional crystalline phase ( $\gamma\text{-Li}_3\text{PO}_4$ ) is a constituent of the formulation, because a stoichiometric deficiency of iron is beneficial for the final battery formulation.[14] While an excess of phosphorus is added as part is lost as

airborne and part reacts with the graphite crucible forming  $\text{Fe}_2\text{P}$ , which remains embedded in the crucible pores. The synthesis yields  $\text{LiFePO}_4$  and the excess of lithium and phosphate recombine forming  $\gamma\text{-Li}_3\text{PO}_4$  (Fig. 5.2).

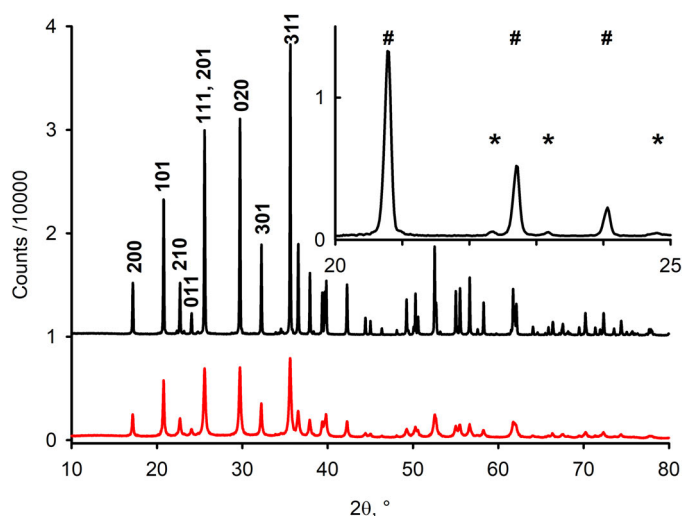


Figure 5.2 The spray dried LFP (red, bottom) presents broad peaks; calcination improves crystallinity and the sample diffracts three times more (black, top). Diffraction patterns between samples are the same (Table 5.1). Top-right insert: #  $\text{LiFePO}_4$ , \*  $\text{Li}_3\text{PO}_4$

Solid-state reactions form  $\gamma\text{-Li}_3\text{PO}_4$  (COD ref: 901-282), at a phase transition temperature of  $1170^\circ\text{C}$ , with improved ionic conductivity vs. the  $\beta\text{-Li}_3\text{PO}_4$  (COD ref: 901-2500), synthesized by wet chemical reaction ( $3 \times 10^{-7} \text{ S cm}^{-1}$  vs.  $4 \times 10^{-8} \text{ S cm}^{-1}$ ).<sup>[121]</sup> Milling in water and drying dissolves and recrystallizes this phase. However,  $\text{Li}_3\text{PO}_4$  is poorly soluble in water ( $0.4 \text{ g L}^{-1}$  at  $20^\circ\text{C}$ ). In a slurry containing 50 % LFP, there are  $11 \text{ g L}^{-1}$  of  $\text{Li}_3\text{PO}_4$ . Only 4 % of  $\text{Li}_3\text{PO}_4$  is in solution, the remaining is embedded in the solid matrix of LFP as  $\gamma\text{-Li}_3\text{PO}_4$ . The Retveld refinement estimates  $\gamma\text{-Li}_3\text{PO}_4$  at 1.4(3) % for our samples (Table 5.1). However, the calcined samples without carbon precursors diffract more (1.9 %  $\gamma\text{-Li}_3\text{PO}_4$ ), while spray dried samples or calcined samples with a carbon precursor diffract less (1.2(1) %  $\gamma\text{-Li}_3\text{PO}_4$ ), despite starting from the same feed material (2.2 %  $\text{Li}_3\text{PO}_4$  by AAS). The carbon's thickness covers a few nanometers and does not suppress the XRD signal from the bulk LFP (in our conditions the penetration length ranges from  $30 \mu\text{m}$  to  $200 \mu\text{m}$  along the  $2\theta$  angle). This indicates that, after spray drying, part of the  $\text{Li}_3\text{PO}_4$  is in amorphous state or coats the surface into mono-atomic layers. Calcination sinters  $\text{Li}_3\text{PO}_4$  and develops a better crystalline structure. While carbon precursors coat the LFP's surface, and the resulting carbon layer imposes a mass transfer resistance that limits crystal growth and sintering for both  $\text{LiFePO}_4$  and  $\gamma\text{-Li}_3\text{PO}_4$ . On the other hand, the Scherrer equation calculates 30 % smaller crystallite size after calcination; due to instrument resolution for this trace compound as  $\text{Li}_3\text{PO}_4$  volatilization

Table 5.1 Spray dried powders from LFP suspensions with additives in water, all slurries include the Tween-20 surfactant. PSD: secondary particle size mode and (distribution at one standard deviation). Carbon: total carbon relative to bone dry LFP powder ( $CI_{n=3}^{95\%}$ ).  $S_a$ : specific surface area ( $CI_{n=3}^{95\%}$ ),  $V_{\text{pore}}$ : pore volume ( $CI_{n=3}^{95\%} < 0.01 \text{ cm}^3 \text{ g}^{-1}$ ) and porosity  $\varphi$ . Average crystallite size considering the 3 most intense peaks (Scherrer equation), and  $\gamma$ - $\text{Li}_3\text{PO}_4$  composition (Retveld refinement). “Py”: pyrolyzed powders. “US”: ultrasonicated suspension.

Sample	$\omega_i$ LFP + additive g <sub>i</sub> /g <sub>total</sub> %	PSD $\mu\text{m}$	carbon gC/gLFP%	$S_a$ $\text{m}^2 \text{ g}^{-1}$	$V_{\text{pore}}$ $\text{cm}^3 \text{ g}^{-1}$	$\varphi$ %	$\text{LiFePO}_4$ nm	$\gamma\text{-Li}_3\text{PO}_4$ nm	$\gamma\text{-Li}_3\text{PO}_4$ $\text{g g}^{-1} \%$
LFP-neat	52% + none	11(10)	0.36(1)%	28.1(8)	0.27	49%	28	170	1.3%
LFP-neat-Py	52% + none	11(8)	0.1%	2.9(2)	0.06	17%	220	130	1.9%
LFP-1	50% + 4% lactose	12(11)	3.4%	27.5	0.24	46%	27	220	1.3%
LFP-1-Py	50% + 4% lactose	12(10)	1.7%	30.8	0.23	45%	94	170	1.1%
LFP-2	50% + 1% $\text{SiO}_2$	14(8)	0.4%	31.0	0.27	49%	27	220	1.1%
LFP-2-Py	50% + 1% $\text{SiO}_2$	12(18)	0.1%	5.1	0.10	27%	200	160	1.9%
LFP-3	50% + 4% lactose	7(3)	3.4(2)%	23.5	0.23	45%	27	250	1.2%
LFP-3-Py	50% + 4% lactose	7(5)	1.8%	29.7	0.23	46%	81	170	1.3%
LFP-4	41% + 1% PVA	37(21)	1.9%	20.1	0.24	46%	27	220	1.6%
LFP-4-Py	41% + 1% PVA	32(23)	1.1%	21.5(6)	0.23	45%	150		
LFP-5	40% + 3% lactose, 1% PVA	37(23)	5.00(7)%	16.8	0.22	43%	27	170	2.0%
LFP-5-Py	40% + 3% lactose, 1% PVA	32(21)	2.4(1)%	30.6	0.27	49%			
LFP-L	48% + 7% lactose	8(6)	5.9%	21.6	0.19	40%			
LFP-L-Py	48% + 7% lactose	8(6)	3.1%	28.9	0.20	42%			
LFP-LP	45% + 5% lactose, 0.45% PVA	12(20)	5.20(9)%	19.4	0.22	43%			
LFP-LP-Py	45% + 5% lactose, 0.45% PVA	12(22)	2.9%	32.3	0.23	45%	77		
LFP-LPU	45% + 5% lactose, 0.45% PVA, US	11(8)	5.1%	19.9	0.19	41%			
LFP-LPU-Py	45% + 5% lactose, 0.45% PVA, US	11(9)	2.9%	26.0	0.21	43%			

is unlikely (melting point:  $1206^\circ\text{C}$ , Table 5.1). The  $\text{LiFePO}_4$  average crystallite size, after spray drying, is invariant with respect to different mixtures of lactose, PVA or colloidal silica (27 nm by Scherrer equation from profile fitting and shape factor: 0.9), but it is a function of the LFP’s melt synthesis conditions. PSD laser scattering, SEM and TEM morphology confirm an average primary particle size of 80 nm by number distribution, thus indicating that several crystal grains constitute the milled primary particles.[86] Calcination of the spray dried powders induce sintering and improve crystallinity also for the  $\text{LiFePO}_4$  phase. The absence of carbon precursors (neat LFP or with colloidal silica) sinters the primary particles together forming 220 nm crystallites. While lactose hinders sintering, limiting crystallites growth to 80 nm (XRD, SEM). From AAS we converted the measured concentrations to molar ratio between the two ions (on average  $\text{Li}^+/\text{Fe}^{3+} = 1.09$ ). We assumed the excess lithium to form  $\text{Li}_3\text{PO}_4$  (as the only other component we detected on XRD). This corresponds to 0.03 mol of  $\text{Li}_3\text{PO}_4$  per mole of  $\text{LiFePO}_4$ , and in terms of mass fraction: 97.8%  $\text{LiFePO}_4$  and 2.2%  $\text{Li}_3\text{PO}_4$  ( $\pm 0.4\%$   $CI_{n=6}^{95\%}$ ). AAS and XRD measurements indicate either that the spray dried material suffers from a depletion in the iron content at some point during the process or an unintentional overload of lithium phosphate during the re-melt synthesis.

### 5.4.2 Particle size and powder morphology

The primary particles have an arithmetic mean  $D_{4,3}$  diameter of 130(60) nm, with a  $d_{v,10}$ ,  $d_{v,50}$ ,  $d_{v,90}$  of 70 nm, 120 nm and 190 nm. However, laser scattering fails to measure particles smaller than 30 nm, which are present (SEM, TEM), and underestimates the sub-100 nm fraction. The specific surface area measured by laser scattering, assuming LFP spherical particles with a skeletal density of  $3570 \text{ kg m}^{-3}$ , is  $15 \text{ m}^2 \text{ g}^{-1}$ , which underestimates the value measured by  $\text{N}_2$  physisorption (average  $23 \text{ m}^2 \text{ g}^{-1}$ , BET). Moreover, particle shape changes as a function of the particle size. Wet media milling attrits primary particles smaller than 50 nm to spherical shapes (TEM), while the others remain as an elongated prismatic shape, in which one dimension is twice the others (SEM: sphericity 0.8, aspect ratio 0.5). On the other hand, spray dried secondary particles are spherical or doughnut-shaped, and the mean diameter lies between  $5 \mu\text{m}$  to  $50 \mu\text{m}$  depending on the spray drying conditions (Fig. 5.3, Table 5.1).

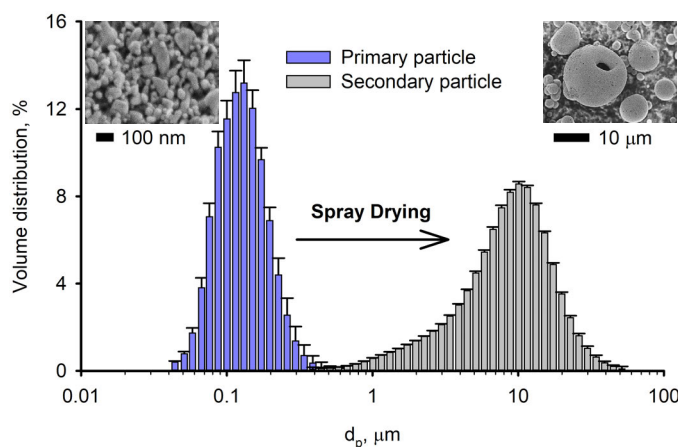


Figure 5.3 The primary particles suspended in water agglomerate to secondary particles during spray drying. The resulting powder is homogeneous and different samplings makes minimal deviations. However sampling the suspension leads to greater uncertainty, due to instrumental resolution and irregular particle shape. Error bars for a  $CI_{n=5}^{95\%}$ .

Spherical particles are preferred as they are denser, but a synergistic effect between excessive drying rate and slurry viscosity, creates doughnut holes in the higher-tail of the PSD (Fig. 5.4j).[84] PVA increases the mixture viscosity by a factor of 4, the secondary particles increase in size, produce more blowholes, and density decreases. A binderless suspension yields a powder (LFP-neat) with  $\rho_t = 1120(10) \text{ kg m}^{-3}$ ; the LFP-lactose powder (LFP-L) reaches  $\rho_t = 1140(10) \text{ kg m}^{-3}$ ; while adding PVA (LFP-LP and LFP-LPU):  $\rho_t = 1070(50) \text{ kg m}^{-3}$  ( $CI_{n=3}^{95\%}$ ). The organic binders fill the nano and mesopore fraction of the powder (porosimetry), as result, LFP-L should be denser than LFP-neat (calc:  $1200 \text{ kg m}^{-3}$ ). The two powders

have similar PSD and we attribute the inconsistency to blowholes. This macroporosity averages  $2\ \mu\text{m}$  to  $50\ \mu\text{m}$  (SEM) and reduces drastically the macroscopic density of the powder ( $\rho_t$ ), but not the microscopic packing efficiency of the primary particles. In fact, from porosimetry, the apparent particle density  $\rho_p$  is much higher, as we measure only for pores up to  $0.3\ \mu\text{m}$  in diameter. LFP-neat has  $\rho_p = 1820(30)\ \text{kg m}^{-3}$ ; LFP-L  $\rho_p = 2130\ \text{kg m}^{-3}$ ; LFP-LP  $\rho_p = 2020\ \text{kg m}^{-3}$ ; LFP-LPU  $\rho_p = 2110\ \text{kg m}^{-3}$ ; and the density increases coherently with the addition of binders (calc:  $2000\ \text{kg m}^{-3}$  to  $2100\ \text{kg m}^{-3}$ ). This measure gives a better estimate regarding how the primary particles pack together and suggests strategies to improve the energy density of the cathode: by re-milling the calcined powder to compact the blowholes (this work) or scaling spray-drying to achieve a slower drying-rate and avoid their formation. The structure of spherical, dense particles is not affected by calcination; while particles with blowholes are mechanically less resistant, break during calcination and reveal their internal voidage (Fig. 5.4p).

### 5.4.3 Pyrolysis and carbon layer

Lactose covers the primary particles and calcination pyrolyzes the carbon precursor into a  $1\ \text{nm}$  to  $3\ \text{nm}$  layer of semi-graphitic carbon (by TEM, Fig. 5.5a). Spray drying coats homogeneously the primary particles with the carbon precursors, even inside the secondary particles. We saw no difference in carbon thickness between the surface and the bulk of the secondary particles (from a fragment Fig. 5.5b). However, a long polymeric chain PVA adds a new morphology: a cage, reticular grid-like carbon that connects several primary particles, covering pores voids up to  $100\ \text{nm}$  diameter (Fig. 5.5c). Ultrasonication breaks the PVA's polymeric chain and the grid-like carbon appears smaller, between  $5\ \text{nm}$  to  $20\ \text{nm}$  in size (Fig. 5.5d). The surfactant Tween-20, lactose monohydrate and PVA are the three sources of carbon that coat the primary particles. Respectively, with a stoichiometric mass ratio  $\nu_i$ : 57 %, 40 %, 55 % of carbon, and their contribution is linear with the amount used ( $\omega_i$ :  $g_i/g_{\text{LFP}}$ ; Eq. 5.4a).

$$\begin{aligned} C_{\text{spray dried}} &= \sum \nu_i \omega_i \\ C_{\text{pyrolyzed}} &= \sum \nu_i \omega_i \beta_i \end{aligned} \tag{5.4}$$

The sample variability is comparable to the regression ( $C_{\text{spray dried}}$ :  $g_{\text{carbon}}/g_{\text{powder}}$ ): five random samples have been repeated three times, giving an average  $\pm 0.1\%$   $CI_{n=3}^{95\%}$  and a relative error between 1 % to 5 %. While the linear regression has a standard error of the mean of  $\pm 0.2\%$  with an  $R^2 = 99\%$  (ESI Fig. 2S).<sup>†</sup> During pyrolysis part of the carbon oxidizes to CO and CO<sub>2</sub>: excluding the direct reaction with gaseous oxygen, carbon at  $700\ ^\circ\text{C}$  reacts

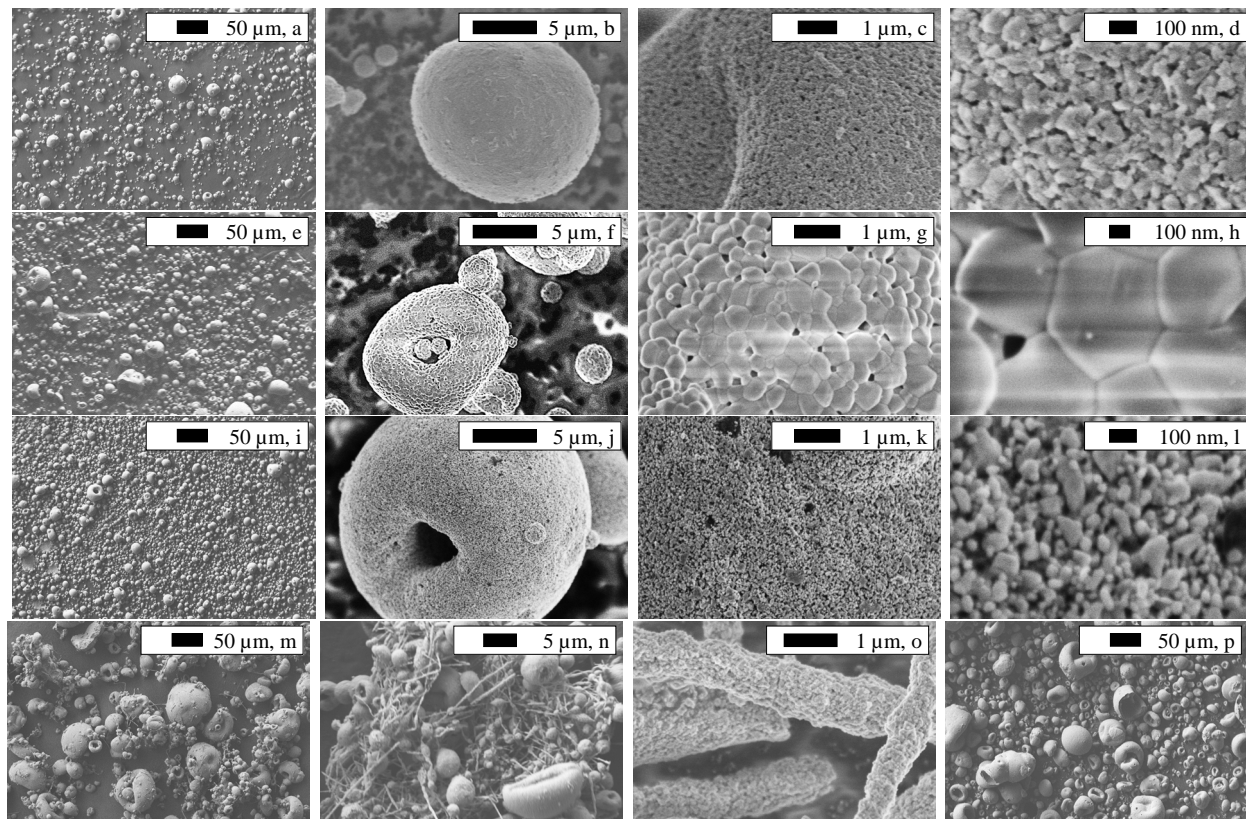


Figure 5.4 Particle morphology by SEM: “a” to “d” belong to the spray dried neat LFP suspension (adding lactose does not change the texture). However calcination of LFP powders without carbon precursor sinters the primary particles together “g” and “h”, but not the secondary: “e” and “f”. Lactose prevents sintering and the powder remains nanostructured: “i” to l”. Adding PVA changes the morphology of the spray dried material, creating submicron rods: “m” to “o”. Calcination of this material breaks some particles, revealing that they are hollow “p”.

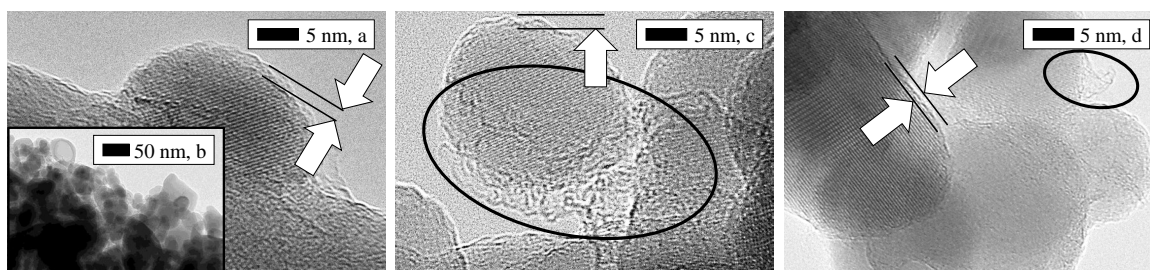


Figure 5.5 Carbon coat morphology by TEM after pyrolysis: lactose decomposes into a thin layer of semi-graphitic carbon (arrows, 1 nm to 3 nm, “a”), coating the primary LFP particles “b”. The addition of PVA superimposes over the thin layer of lactose a grid-like carbon structure interconnecting the primary particles (circled, “c”). Ultrasonication depolymerizes PVA into a short-chain polymer so the carbon grid is now smaller “d”.

with steam (water-gas reaction). The carbon precursors' hydroxyl groups dehydrate, cyclize the molecule, and form unsaturated species, generating semi-graphitic carbon and water.[10] From a regression analysis, the  $\beta_i$  coefficient indicates for each component the fraction of carbon left after pyrolysis (standard error of the mean is  $\pm 0.1\%$ ,  $R^2 > 99\%$ , Eq. 5.4b). Tween-20 loses the most carbon during pyrolysis ( $\beta_i = 0.15$ ), followed by lactose (0.52) and finally PVA (0.75).

#### 5.4.4 N<sub>2</sub> physisorption porosimetry

A high  $S_a$  promotes greater wettability and Li<sup>+</sup> flow from the solid material, however melt-synthesized LFP is intrinsically non-porous (type II isotherms). Milling LFP creates nanoparticles (primary particles), and spray drying coalesces the material into a meso-macro porous spherical secondary particle. The pore network correlates to the packing efficiency of the agglomerate. The lack of a plateau over a range of high  $P/P_0$  indicates incomplete pore filling and the development of a macroporous structure which correlates to the void fraction between secondary particles.[84] Scaling-up spray drying from a laboratory unit (Yamato GB-22) to a pilot unit (this work) did not modify the porosity of the material. Spray dried powders, with or without binders, all exhibit a type II isotherm with a small H1 hysteresis loop in the  $P/P_0$  0.85-0.995 range (Fig. 5.6).[113]

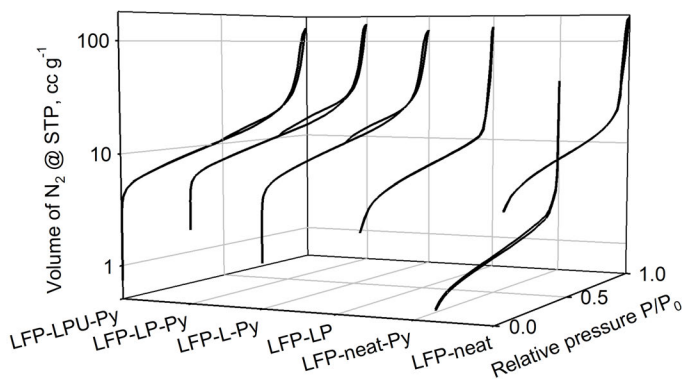


Figure 5.6 N<sub>2</sub> adsorption-desorption isotherms at 77K, STP at 0°C and 1 atm.

H1 hysteresis is often associated with agglomerates of approximately uniform spheres (the primary LFP particles).[114] While the small hysteresis' area correlates with the lack of narrow necks (ink-bottle pore shape), indicating no morphological difference in arrangements of the nanoparticles between the core and the shell of the secondary particle (homogeneous distribution).[122] Spray dried powders without binders have high specific surface area and pore volume ( $S_a$ :  $28 \text{ m}^2 \text{ g}^{-1}$ ,  $V_{\text{pore}}$ :  $0.27 \text{ cm}^3 \text{ g}^{-1}$ ), indicating no pore blockage in the secondary



particles. While the addition of binders lowers the  $S_a$  of the powder, as the pores are gradually filled with organic precursors ( $20 \text{ m}^2 \text{ g}^{-1}$ ,  $0.2 \text{ cm}^3 \text{ g}^{-1}$ , Table 5.1). Total  $V_{\text{pore}}$  decrease by 25 %, but pore size distribution is invariant, peaking at 45 nm, which corresponds to the average inter-primary-particle void length (blue vs. red, black and green Fig. 5.7).

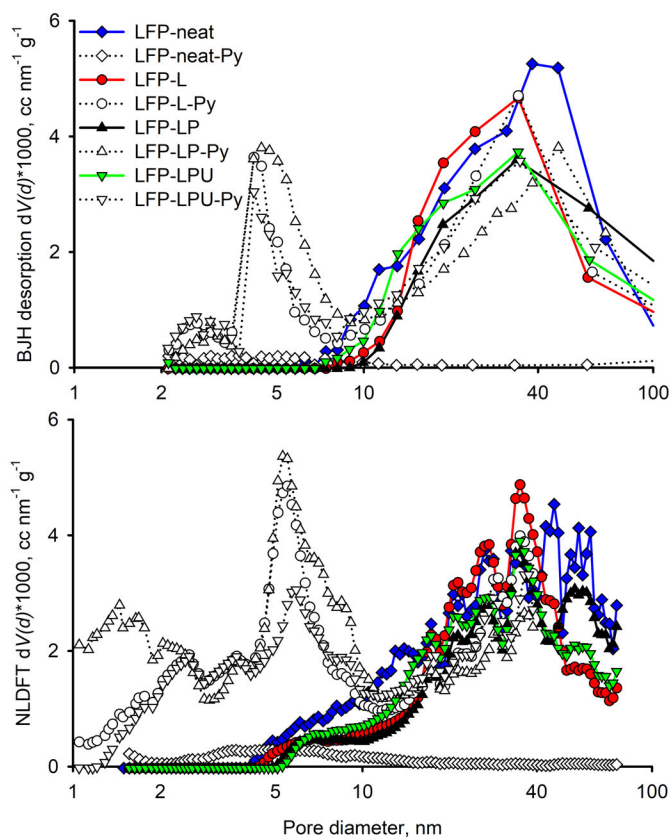


Figure 5.7 Comparison between BJH (top) and NLDFT (bottom) pore size distribution methods. Spray dried powders with (red, black green) or without carbon precursors (blue) shows similar pore morphology in the meso-macro pore region 5 nm to 300 nm. Calcination pyrolyzes the carbon precursors and partially sinters the LFP primary particles (open symbols).

This shows how spray drying disperses evenly the solvated organic binders over the surface of the solid LFP. In contrast, incipient wetness impregnation of a tungsten solution over a solid titania support selectively filled pores smaller than 10 nm as the tungsten loading increased.[123] Exceptionally, colloidal silica increases the  $S_a$ , but not the  $V_{\text{pore}}$ , as the smaller colloidal silica nanoparticles (6 nm diameter) cover the surface of the LFP primary particles and contribute additively to the  $S_a$  (Table 5.1). However calcination imparts a radical alteration of the material. The  $S_a$  for the samples deprived or with an insufficient quantity of carbon precursor, decrease from  $28 \text{ m}^2 \text{ g}^{-1}$  (before pyrolysis) to as low as  $3 \text{ m}^2 \text{ g}^{-1}$

(after pyrolysis). Loss of  $S_a$  is seen in SEM imaging and XRD: at 700 °C the uncoated LFP nanoparticles sinter. The primary particles grow in size up to 1  $\mu\text{m}$  (SEM) and XRD peaks are sharper and twice as intense. On the other hand, the samples containing the carbon precursor increase the  $S_a$  from  $20\text{ m}^2\text{ g}^{-1}$  to  $30\text{ m}^2\text{ g}^{-1}$  and produce a small microporous structure (5% to 15% of the total  $S_a$ ) and a novel pore structure between 5 nm to 10 nm (BJH and NLDFT). Accordingly, an additional H4 hysteresis loop appears between  $P/P_0$  0.45-0.85 for the pyrolyzed powders, which is associated with the filling of micropores, in micro-mesoporous carbons; as the adsorption branch is now a composite of Types I and II isotherms (Fig. 5.6).[122] The new narrow-mesopore structure arise from a combination of factors: calcination in the presence of carbon precursors induces partial sintering of the LFP's primary particles (XRD). The pore volume is invariant, but the pore size shifts from 45 nm (before pyrolysis, colour symbols) to 5 nm and 45 nm (after pyrolysis, open symbols, Fig. 5.7). In the absence of carbon (diamonds) the material extensively sinters, the secondary particle shrinks (SEM), and the  $V_{\text{pore}}$  drops to  $0.06\text{ cm}^3\text{ g}^{-1}$ . Lactose and PVA maximize the micropore  $V_{\text{pore}}$  and  $S_a$  (upward triangles:  $5.2\text{ m}^2\text{ g}^{-1}$  with the V-t method, and  $9.0\text{ m}^2\text{ g}^{-1}$  by NLDFT); lactose alone does not create a substantial microporosity (circles:  $0.7\text{ m}^2\text{ g}^{-1}$ , and  $2.5\text{ m}^2\text{ g}^{-1}$ ); while ultrasonication degrades the carbon precursors (downward triangles:  $0.8\text{ m}^2\text{ g}^{-1}$ , and  $0.9\text{ m}^2\text{ g}^{-1}$ ). To explain the difference in microporosity we propose that lactose coats evenly the LFP primary particles, pyrolysis decrease the thickness of the coating layer (from 6 nm to 3 nm from mass balance calculation),[124] which keeps adhering to the LFP surface (TEM). The thinner carbon layer exposes a gap that ranges in the micropore region. PVA creates a carbon grid that extends between nanoparticles, ranging between 30 nm to 100 nm (TEM), which correlates with the decrease in mesoporosity (open symbols, upward triangle Fig. 5.7). Instead, the carbon grid filament measures 1.1(1) nm in thickness (TEM), and could indicate the presence of narrow carbon nanotubes, catalyzed on the surface of LFP.[125] Single-wall carbon nanotubes have a thin diameter (1.35 nm),[126] and would explain the increased  $\text{N}_2$  adsorption in the micropore region (1.4 nm average pore volume by NLDFT); however, their characteristic peaks are absent in the Raman spectra. Hydrothermal synthesis of  $\text{LiFePO}_4$  with adenosine triphosphate and ascorbic acid, creates a similar mesoporous carbon nanowire that interconnects the  $\text{LiFePO}_4$  nanosheet.[127] Ultrasonication decomposes PVA and the pore size distribution follows the same trend as the sample with lactose.

#### 5.4.5 Rheology of the nanoparticles suspension

The Tween-20 surfactant exhibit a Newtonian rheology to the LFP suspension when the solid mass fraction does not exceed 20%. Increasing solid loadings contribute to shift the slurry

to a shear-thinning non-Newtonian fluid behavior (Fig. 5.8).

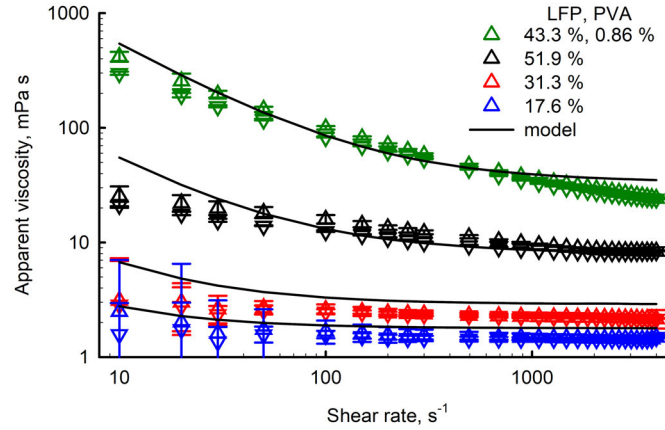


Figure 5.8 The shear increasing isotherms at 25.0 °C (upward triangles) overtop the shear decreasing curves (downward triangles). Viscosity increases with the solid mass fraction of LFP in water (blue, red, black). The addition of less than 7% lactose does not modify the rheology of the material; while PVA increases the viscosity of the slurry (green). Error bars for a  $CI_{n=3}^{95\%}$ .

Dynamic apparent viscosity ( $\mu$ , Pa s) decreases with shear rate ( $\dot{\gamma}_{sr}$ ,  $s^{-1}$ ) and the Herschel-Bulkley model fits best the data ( $R^2 > 99.5\%$ ):[128]

$$\mu = \tau_0/\dot{\gamma} + K\dot{\gamma}^{n-1} \quad (5.5)$$

Eq. 5.5 characterizes fluids with suspended solid, even in Newtonian conditions, and give three rheometric parameters: consistency ( $K$ ,  $\text{Pa s}^n$  relates to the apparent viscosity), flow index ( $n$ , a measure of shear-thinning) and yield stress ( $\tau_0$ , Pa). When  $\tau < \tau_0$  the material behaves as a solid ( $\tau_0 = 2\text{ Pa to } 3\text{ Pa}$ ), and occurs when the solid mass fraction of LFP is above 60% or at 50% along with binders (>3% lactose or >0.8% PVA). In those conditions, the Tween-20 surfactant fails to maintain the LFP nanoparticles suspended and after standing still for a few hours, the material reticulates into a bulk solid with the consistency of yogurt (i.e.  $\tau_0 = 10\text{ Pa}$  at room temperature). The process is reversible, indicating that the nanoparticles create a network through sol-gel physical bonds.[129] The network deforms elastically when stress is applied, via direct contact between particles. When the applied stress reaches  $\tau_0$ , the network breaks up, beyond which point the suspension flows viscously.[130] Shear increasing-decreasing curves also show this thixotropic behavior. The shear increasing curve has greater viscosity, and as the analysis progresses, more energy is transferred to the material, breaking more bonds and lowering the apparent viscosity during the shear decreasing isotherm. The two curves have a hysteresis area which is maximum when the material

has more suspended solid and in the presence of PVA binder ( $\omega_{\text{LFP}} = 43.3\%$  with  $\omega_{\text{PVA}} = 0.86\%$ :  $\Delta_{\text{hyst}} = 10\,000\text{ Pa s}^{-1}$ ,  $n = 0.68$ ). Below the mentioned conditions,  $\Delta_{\text{hyst}}$  decreases proportionally with the solid mass fraction (At  $\omega_{\text{LFP}} = 51.9\%$ :  $\Delta_{\text{hyst}} = 3000\text{ Pa s}^{-1}$ ,  $n = 0.81$ ;  $\omega_{\text{LFP}} = 35.6\%$ :  $\Delta_{\text{hyst}} = 700\text{ Pa s}^{-1}$ ,  $n = 0.91$  and  $\omega_{\text{LFP}} = 17.6\%$ :  $\Delta_{\text{hyst}} = 100\text{ Pa s}^{-1}$ ,  $n = 0.98$ ). Also the viscosity index follows the same trend, reaching Newtonian flow ( $n = 1$ ) in dilute, binder-less conditions. PVA contributes in creating a sol-gel network among LFP nanoparticles, probably by physical bonds via the PVA hydroxyl functional groups and not by dehydration reaction as the rheology is again reversible during consecutive shear increasing-decreasing isotherms and we are in the presence of an aqueous system weakly alkaline (pH 8).[123] PVA which is detrimental when spray-drying as viscosity increases and requires more energy for atomization, but is favorable when testing the electrochemistry of the material, as the PVA network pyrolyzes into a better electron conductive cage. Temperature reduces the apparent viscosity of the suspension with an exponential trend in a  $1/T$  plot; solid loading, binders or different shear rates modify the magnitude of the effect but not the trend (Table 5.2).

At  $-8.9^\circ\text{C}$  a  $\omega_{\text{LFP}} = 51.9\%$  binder-less suspension freezes. The process is not reversible, after thawing the material is 70% more viscous over the entire range of temperature. PSD scattering reveals that 20% of the solid nanomaterial agglomerates into  $2\text{ }\mu\text{m}$  to  $10\text{ }\mu\text{m}$  particles. Ultrasonication breaks the agglomerates and restore the original PSD and rheology. Since the change in apparent viscosity between the shear increasing and decreasing branches is negligible, we modelled the data considering four factors: LFP and PVA mass fraction, temperature and the increasing branch of the shear rate (Eq. 5.6).

$$\begin{aligned}
 A &= e^{\frac{E_a}{R} \left( \frac{1}{T} - \frac{1}{293} \right)} \\
 C &= 1 + c_{\text{PVA}} * \omega_{\text{PVA}} \\
 \tau_0 &= \tau^* \left( 1 + (c_{\text{PVA}} * \omega_{\text{PVA}})^2 \right) \left( \left( 1 - \frac{\omega_{\text{LFP}}}{\omega_0} \right)^{-4} - 1 \right) \\
 \mu &= A * \left[ \frac{\tau_0}{\dot{\gamma}_{sr}} + K * C * \dot{\gamma}_{sr}^{-0.2r_p} \left( \frac{\omega_{\text{LFP}}}{\omega_0} \right)^4 \left( 1 - \frac{\omega_{\text{LFP}}}{\omega_0} \right)^{-B\omega_0} \right]
 \end{aligned} \tag{5.6}$$

A modified Arrhenius type relationship ( $A$  term) explains the temperature variation ( $T$ , K) for the apparent viscosity ( $\mu$ , Pa s): at  $20^\circ\text{C}$   $A = 1$ ; when  $T = 5^\circ\text{C}$   $A = 1.4$  and when  $T = 70^\circ\text{C}$   $A = 0.4$ ; the  $E_a$  regress to  $16\,300(500)\text{ J mol}^{-1}$  (standard error). Interestingly, the regressed trend overlap with the viscosity variation of pure water (in mPas) and the regressed  $E_a$  agrees with previous studies for pure water ( $n = 7$ ,  $15\,800(200)\text{ J mol}^{-1}$ , standard error).[131, 132] When comparing our regressed data with another regression where we

Table 5.2 Rheology of LFP suspensions; the apparent viscosity ( $\mu$ ,  $\pm 0.05$  mPa s) increases with: increasing solid mass fraction ( $\omega_{\text{LFP}}$ ) and increasing PVA binder content ( $\omega_{\text{PVA}}$ ), while  $\mu$  decreases with increasing temperature ( $T$ ) and increasing shear rates ( $\dot{\gamma}_{sr}$ ). “US”: ultra-sonicated suspension.

$\omega_{\text{LFP}}$ g <sub>LFP</sub> /g <sub>total</sub>	$\omega_{\text{PVA}}$ g <sub>PVA</sub> /g <sub>total</sub>	$T$ °C	$\dot{\gamma}_{sr}$ s <sup>-1</sup>	$\mu$ mPa s
17.6	0	25.0	4000	1.5
31.3	0	25.0	4000	2.3
35.6	0	25.0	4000	5.2
51.9	0	45.0	4000	6.3
51.9	0	25.0	4000	8.4
60.2	0	25.0	4000	12.7
43.3	0.86	25.0	100	80.1
43.3	0.86	45.0	100	56.7
43.3	0.86	57.0	100	48.8
48.3	0	5.0	4000	10.5
48.3	0	25.0	4000	6.0
48.3	0	45.0	4000	4.2
48.3	0	65.0	4000	3.9
38.2	1.15	25.0	500	65.0
38.2	1.15	25.0	1500	43.4
38.2	1.15	25.0	4000	31.9
45.0	0.45	25.0	1000	22.4
45.0, US	0.45, US	25.0	1000	10.3
0	4.0	25.0	1000	31.8
0	4.0, US	25.0	1000	16.4

imposed the  $E_a$  of pure water, the Mann-Whitney U Statistic determined no statistically significant difference between the two groups ( $p = 0.934$ ). We can therefore infer that temperature only affects the rheology of the solvent, and not the solid or interfacial property of the suspended  $\text{LiFePO}_4$  nanoparticles. The PVA mass fraction linearly correlates with the consistency index  $K$  (C term) and quadratically with the yield stress  $\tau_0$ , for slurries up to 0.04  $\omega_{\text{PVA}}$  (g<sub>PVA</sub>/g<sub>total</sub>).<sup>[133]</sup> The quadratic function best fit the liquid-to-solid transition of our feed material when it contains PVA, the constant is set to 1 to impose neutrality for a binderless suspension, while the proportionality coefficient  $c_{\text{PVA}}$  regress to 700. The yield stress ( $\tau_0$ , Pa) increases with increasing particle volume fraction ( $\varphi$ , L L<sup>-1</sup>) with a Maron-Pierce relationship and  $\tau^*$  is a fitting parameter which correlates to the solid particle size.<sup>[130]</sup> When we regressed the same equation using mass fractions we obtained  $\tau^* = 0.006$  Pa and  $\omega_0 = 0.77$  which represents the maximum (mass) packing fraction. The remaining re-elaboration of the Herschel-Bulkley model include an empirical formula for evaluating the Newtonian index, as it depends systematically on particle aspect ratio (in our case  $r_p$

= 0.5) and solid loading.[134] The same rheological study on suspended particles regressed the Einstein coefficient  $B$  as a function of  $r_p$  (in our case  $B = 2.5$ ) and we decided to apply the Krieger equation,[135] as a modification formula, to include a concentrated regime flow, for the consistency index  $K$ . With the Krieger modification,  $K = 1.2 \times 10^{-3} \text{ Pa s}^n$  regress to the viscosity of the solvent (water at 20 °C is 1 mPa s), and our regression improves:  $R^2$  and adjusted  $R^2$  scores are equal;  $R^2$  passes from 99.3% to 99.9%; and the standard error of the estimate: from 10.0 mPa s to 4.5 mPa s (Fig. 5.9).

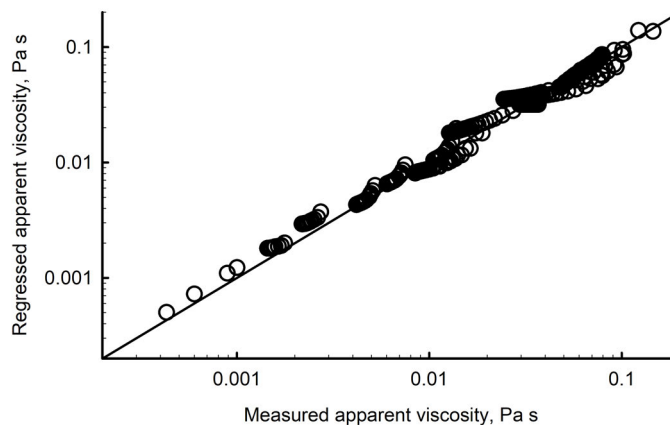


Figure 5.9 Eq. 5.6 model regression for 415 data points at different solid concentrations, increasing shear rates, temperatures and binder loadings. Most deviations come from low instrument sensitivity at low torque (when  $\mu < 3 \text{ mPa s}$ ) and low shear rate ( $\dot{\gamma}_{sr} < 50 \text{ s}^{-1}$ ).

Converting solid mass fractions to volume fractions, and writing Eq. 5.6 in terms of volume fraction, does not fit the data with respect to shear increase and solid loading. ( $R^2 = 99.6\%$  and standard error of the estimate: 7.7 mPa s). When regressing using volume fractions,  $E_a = 14\,300(900) \text{ J mol}^{-1}$ ,  $\tau^* = 0.25 \text{ Pa}$ ,  $K = 0.0030 \text{ Pa s}^n$ ,  $\varphi_0 = 0.66$  and  $c_{PVA} = 370$ . The maximum (volumetric) packing fraction is in agreement with experimental data on micron-sized particles but the yield stress fitting parameter diverges from the proposed trend: for 50  $\mu\text{m}$  particles,  $\tau^*$  measured 0.05 Pa; and for 2.5  $\mu\text{m}$ ,  $\tau^*$  measured 3 Pa.[134] We extend the study into the submicron region with a broad distribution of primary particle sizes and obtain  $\tau^* = 0.25 \text{ Pa}$ , indicating that nanoparticles act as viscosity reducers, as already demonstrated in crude oil rheology studies.[136] We also conducted a thixotropy study of a 50% solid slurry. When shear is applied,  $\dot{\gamma}_{sr}$  from 0  $\text{s}^{-1}$  to 50  $\text{s}^{-1}$ , it takes an average of 2.5 s to reach 95% of the steady state measured stress. Continuing from 50  $\text{s}^{-1}$  to 500  $\text{s}^{-1}$  it takes 1.3 s; 500  $\text{s}^{-1}$  to 5000  $\text{s}^{-1}$  0.9 s; while 5000  $\text{s}^{-1}$  to 500  $\text{s}^{-1}$  1.5 s; 500  $\text{s}^{-1}$  to 50  $\text{s}^{-1}$  3 s; 50  $\text{s}^{-1}$  to 0  $\text{s}^{-1}$  10 s. Imposing different temperatures ( $-5 \text{ }^\circ\text{C}$  to  $65 \text{ }^\circ\text{C}$ ) does not influence thixotropy, as there is no statistical difference between the temperature groups ( $p = 0.998$ ). This effect has to be

taken into consideration as the slurry that undergoes atomization is subject to a rheology different from the expected one. Feeding  $100 \text{ mL min}^{-1}$  of slurry from the tank through the pipe imposes a shear of  $500 \text{ s}^{-1}$ , and given the dimension of the apparatus, a contact time of 10 s. The pipe is then connected to the nozzle attachment, a steel duct in which the slurry passes at  $\dot{\gamma}_{sr} = 100 \text{ s}^{-1}$  for 7 s. Finally the nozzle reduces the cross-section to a 0.7 mm bore, where the slurry shear at  $50\,000 \text{ s}^{-1}$  for 2 ms. This final sudden change in diameter (and shear rate) is unlikely to impose any actual decrease in the apparent viscosity. The thixotropy of the feed material imposes a kinetic limitation for the apparent viscosity variation due to shear and the short contact time for both the atomizer and the droplet drying (few ms) leaves the material behaving in the  $100 \text{ s}^{-1}$  shear range.

#### 5.4.6 Ultrasonication

In water, long chain PVA organizes to a pseudo-micelle conformation around the nanoparticles. This increases the hydrodynamic radius and thus the intrinsic viscosity.[137] In fact, adding 0.45 % PVA to a suspension of 45 % LFP increases the apparent viscosity 4-fold with respect to a binderless slurry. However, when ultrasound (US) is applied to a suspension containing PVA, the apparent viscosity drops 2-fold, permanently (Table 5.2). The LFP primary particle size distribution remains unchanged (before US: 130(60) nm vs. after US: 120(50) nm, spanning from  $d_{v,10}$ : 70 nm,  $d_{v,50}$ : 110 nm, to  $d_{v,90}$ : 190 nm). So, we attributed this effect to the depolymerization of PVA; in fact, applying US to a 4.0 % PVA solution in water, registered a 2-fold drop in viscosity. Ultrasonication degrades organics and polymers via a macro-radical mechanism,[138, 139] and depolymerizes aqueous solutions of PVA, as cavitation and macro-turbulence induce shear forces that break the polymer's chemical bonds.[140, 141] The Mark—Houwink equation characterizes the intrinsic viscosity of a polymer with its molecular weight, while the Solomon—Ciuta equation estimates the intrinsic viscosity from single-concentration apparent viscosity measurement.[142] The 4.0 % PVA solution has an apparent viscosity of 32.0(8) mPa s at 25 °C, a Newtonian behavior, and an average molecular weight of  $M_w = 170\,000 \text{ g mol}^{-1}$  (manufacturer specifications). US depolymerizes the 4.0 % PVA solution to a  $90\,000 \text{ g mol}^{-1}$  polymer, halving the chain length ( $\mu = 16.8(2) \text{ mPa s}$ ). With 45 % LFP and 0.45 % PVA, the effect of US is even more pronounced. Lower polymer concentrations lead to higher polymer degradation because the polymer chains are less overlapped.[143] As a result, viscosity decreases from 22 mPa s to 10 mPa s at  $\dot{\gamma}_{sr} = 1000 \text{ s}^{-1}$ . Assuming both the LFP suspension and PVA contribute to the final viscosity in an additive way, a 45 % LFP suspension has a  $\mu = 6 \text{ mPa s}$ . Subtracting the LFP contribution from the LFP+PVA suspension, the PVA drops in viscosity 4-fold after US (16 mPa s to 4 mPa s), which corresponds to a  $30\,000 \text{ g mol}^{-1}$  low molecular weight polymer.

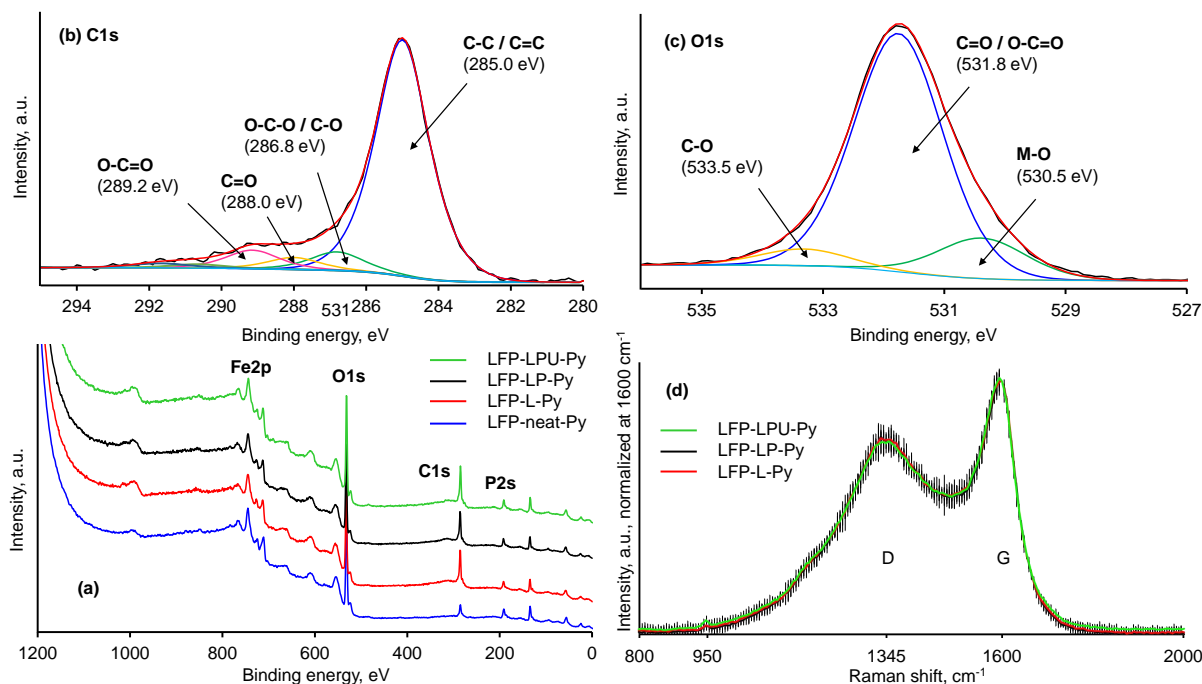


Figure 5.10 (a) XPS spectra for the different carbon coating and control sample, and high resolution spectra of C1s (b) and O1s (c) for LFP-LP-Py. (d) Raman spectra, the vertical bars are the  $CI_{n=3}^{95\%}$  for each material. The small peak at  $950\text{ cm}^{-1}$  correlates with the stretching modes of  $\text{PO}_4^{3-}$ .

#### 5.4.7 Carbon coat chemical analysis

X-ray photoelectron spectroscopy (XPS) is a surface sensitive technique that determines the chemical composition in atomic percentages of the elements and the amount of carbon-carbon/carbon-oxygen bonding (Table 5.3).

Table 5.3 XPS elemental composition (atomic  $\pm 0.2\%$ ).

Sample	P2p	C1s	O1s	Fe2p
LFP-L-Py - 7% lactose	7.5	41.5	46.6	4.4
LFP-LP-Py - 7% lactose, 0.45% PVA	8.4	39.8	46.3	5.4
LFP-LPU-Py - 7% lactose, 0.45% PVA, US	6.9	45.5	42.8	4.9
LFP-neat-Py - neat LFP	12.4	20.0	59.6	8.0

We investigated the effect of different carbon precursor coating on the LFP base material compared to the calcined control sample (LFP-neat-Py) by high resolution deconvolution of the C1s and O1s spectra. The XPS survey of the control and pyrolyzed samples containing lactose (LFP-L-Py), lactose-PVA (LFP-LP-Py), and ultrasonicated lactose-PVA (LFP-LPU-Py) clearly shows the elemental peaks of P, C, O and Fe, respectively (Fig. 5.10a). Due to



the presence of iron, the only lithium (Li1s) peak cannot be quantified, as they overlap. The Fe2p signal has a sensitivity factor over ten times greater than Li1s, also compared to peak intensity of carbon, lithium provides a very low sensitivity, approximately 1/18 that of carbon.[144] The calibration of all the samples peaks referred to the C1s species, corresponding to the adventitious carbon from the XPS instrument. In LFP-LP-Py, deconvoluting the C1s signal (Fig. 5.10b) yields four peaks, the binding energy at 285.0 eV (C–C/C=O) assigned to aliphatic and aromatic structures, 286.8 eV (C–O–C/C–O) ascribed to epoxy carbon and hydroxyl carbon, 288.0 eV (C=O) corresponds to carbonyl carbon and 289.2 eV (O–C=O) represent carboxylate carbon.[145] Fig. 5.10c shows the O1s core level spectrum: the binding energy at 530.5 eV (M–O) is characteristic of the "O<sup>2-</sup> (O<sub>I</sub>)" ions of the crystalline network bonded to a metal,[146] indicating Fe–O shear the orbital O1s in LiFePO<sub>4</sub> linkage. The characteristic peak at 531.8 eV (C=O/O–C=O) is attributed to the superoxide anions "O<sup>-</sup> (O<sub>II</sub>)" and the peak at 533.5 eV (C–O) represent the superoxide anion "O<sup>2-</sup> (O<sub>III</sub>)".[147] Comparing the high resolution spectra (ESI Fig. 3S)<sup>†</sup> and the atomic percentages (at. %) of the samples illustrated in Table 5.4 showed a higher proportion of C–O groups in the lactose sample, compared to lactose-PVA and the ultrasonicated one.

Table 5.4 Identification of functional groups and their at. % obtained from high resolution XPS spectra, fitting of the C1s (top) and O1s peaks (bottom). Raman intensity ratio between carbon's D and G bands (bottom, last column).

Sample (C1s)	C–C/C=C	C–O/C–O–C	C=O	O–C=O
LFP-L-Py	36.9	4.6	1.2	3.2
LFP-LP-Py	37.6	3.0	1.9	3.0
LFP-LPU-Py	36.8	3.3	1.9	2.7
LFP-neat-Py	18.1	1.1	–	1.7
Sample (O1s)	M–O	C=O/O–C=O	C–O	$I_D/I_G$
LFP-L-Py	7.2	40.7	4.5	0.77(3)
LFP-LP-Py	7.3	42.9	3.0	0.76(1)
LFP-LPU-Py	7.8	42.7	3.4	0.76(3)
LFP-neat-Py	13.0	64.4	1.7	

Similarly, a higher proportion of metal oxides is detected in the ultrasonicated sample compared to lactose and lactose-PVA samples. Instead, the at. % of the functional groups C–C/C=C is higher in the lactose-PVA powder compared to the other two. No other significant differences between the carbon and oxygen high resolution spectra could be observed in the coated samples. In comparison, the control sample LFP-neat-Py consist of very low at. % of aliphatic, aromatic and epoxy carbon, in addition no presence of carbonyl carbon, which justifies the uncoated behavior of the control sample (low percentages of C–O linkages are due to the presence of adventitious carbon). Instead, the control sample shows high

percentages of metal bonding (M–O) due to the interaction of metal with oxygen in the  $\text{LiFePO}_4$  base compound; this justifies that the interaction between oxygen and carbon been created by addition of the carbon precursors and the carbon coat adheres chemically with the  $\text{LiFePO}_4$ . We further investigated the  $\text{LiFePO}_4/\text{C}$  powders by calculating the intensity ratio between the D and G bands of carbon with Raman spectroscopy ( $I_D/I_G$ ) (Fig. 5.10d). The D band ( $1345\text{ cm}^{-1}$ ) is associated with out of plane vibrations: disordered  $\text{sp}^3$  tetrahedral amorphous carbon. The G band ( $1600\text{ cm}^{-1}$ ) correlates to in-plane vibrations: graphitic  $\text{sp}^2$  carbon.[148] The three samples' spectra overlap with no statistical differences, and the  $I_D/I_G$  is as-well invariant (one-way ANOVA test,  $p = 0.49$ , Tab. 5.4). This further confirms that the carbon coating is chemically equivalent and differs only in terms of morphology between the three main samples (carbon-grid, TEM).

#### 5.4.8 Electrochemical tests

Small particles, with a narrow size distribution, are more stable during cycling (by linearly extrapolating the trend between the 30<sup>th</sup> to 45<sup>th</sup> cycle). The spray dried LFP powder with lactose, with a  $D_{4,3}$  diameter of  $7(3)\ \mu\text{m}$  (distribution at one standard deviation) is stable after 15 cycles (red circles, Fig. 5.11).

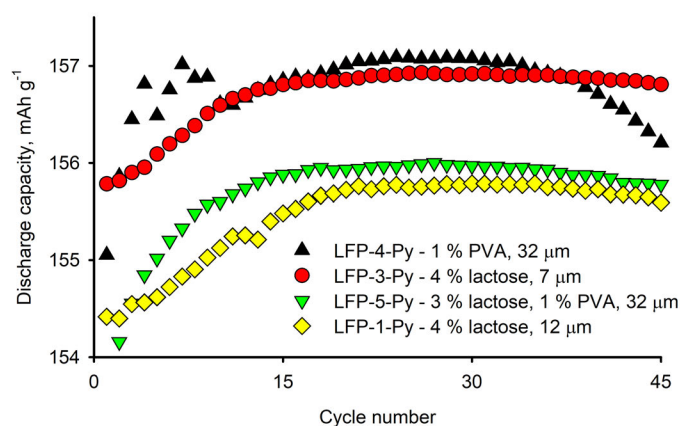


Figure 5.11 Preliminary test of cyclability at 0.1C discharge rate. PVA creates larger secondary particles, and a material with poor cyclability. Adding PVA and lactose stabilizes the trend, despite the same particle size. Smaller particles improve the discharge capacity.

Increasing the secondary particle diameter to  $12(10)\ \mu\text{m}$ , broadens the distribution and the cyclability rate drops twice as fast with respect to the previous material (yellow diamonds). PVA increases the viscosity of the slurry, and the size of the particles ( $32(23)\ \mu\text{m}$ ). The discharge capacity drops sooner and one battery fails, due to incomplete carbon coverage and probably mechanical detachment of the material (black upwards triangles). On the other

hand, adding lactose and PVA, maintains both batteries active and relatively stable, despite the larger particle size:  $32(21) \mu\text{m}$  (green downwards triangles). Therefore, we optimized the spray drying conditions to deliver a fine powder ( $D_{4,3} = 10 \mu\text{m}$ ). Spray drying the suspension without binders and calcination, produce a material with poor electrochemical capacity (due to the lack of a carbon coat and sintering) but stable cyclability (blue squares, Fig. 5.12).

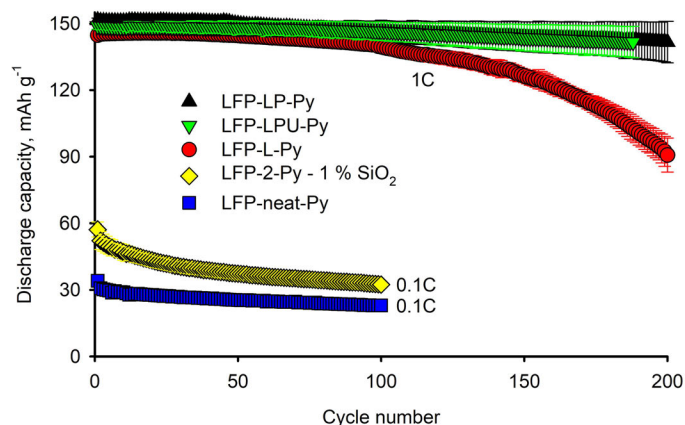


Figure 5.12 Cyclability at 1C discharge rate, and 0.1C for the neat LFP and the colloidal silica. Error bars represent 1 standard deviation,  $n=2$ . Adding PVA significantly improves the cyclability of the battery vs. the lactose based material ( $p < 0.02$ ).

The addition of colloidal silica to a neat LFP suspension and calcination increases the discharge capacity by 40% (yellow diamonds). Both materials sinter after calcination, but the colloidal silica slows the process by steric hindrance over the LFP surface, and the resulting  $S_a$  is 80% higher ( $5.1 \text{ m}^2 \text{ g}^{-1}$  vs.  $2.8 \text{ m}^2 \text{ g}^{-1}$  neat-LFP). Subsequently, we optimized the binder formulation, aiming for a 3% carbon coating after pyrolysis. During spray drying with binders, to compensate for the LFP suspension's higher viscosity, we increased the atomization pressure to 0.40 MPa and obtained particles with a mode below  $12 \mu\text{m}$ . We prepared three powders with similar characteristics after pyrolysis, in terms of: carbon content, secondary particle size and  $S_a$  (Table 5.1). For the first, we spray dried a suspension of LFP with 14.5% lactose (mass basis on dry LFP, LFP-L-Py, red circles). Then 11% lactose and 1% PVA (LFP-LP-Py, black upward triangles). While the third sample contained 11% lactose, 1% PVA and was ultrasonicated before and during spray drying (LFP-LPU-Py, green downward triangles), to compare the role of US as dispersing force. All materials are initially cycled at 0.1C for 10 cycles (not shown) and have a rapid activation, reaching the maximum capacity after 6 cycles. During the first 100 cycles the materials behave similarly, with no statistical differences (ANOVA on ranks test,  $p = 0.33$ ). After, however, the lactose-based material's discharge capacity quickly fades, while the lactose-PVA materials remain con-

stant. This supports the hypothesis that the carbon-cage helps to dissipate the charge and maintains the nanoparticles cohesive, thus improving the cathode's cyclability. We repeated and extended the cyclability tests over 750 cycles at 1C (Fig. 5.13), and to avoid charge accumulation and dendrite formation, one every 10 cycles is conducted at 0.1C.[75]

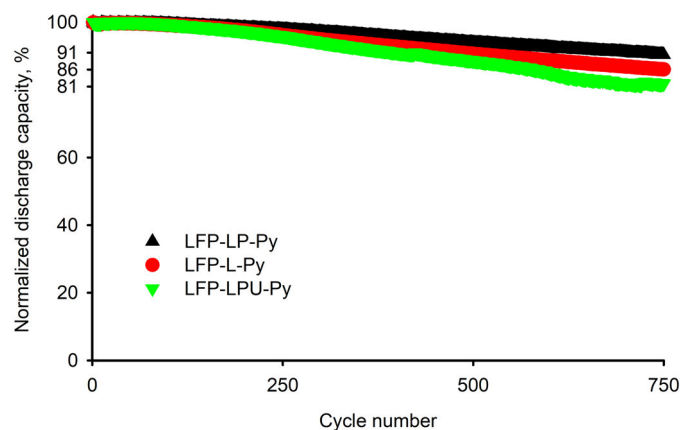


Figure 5.13 Normalized cyclability at 1C discharge rate (one every 10 cycles is conducted at 0.1C and not shown on the graph for simplicity). Lactose-PVA confer greater stability, the coin-cell battery would retain 80 % of the initial capacity after 1700 cycles (vs. lactose: 1100 cycles). Ultrasonication shortens the PVA's chain length and induce instability in the trend.

This methodology gives us a better understanding of the cathode's aging process, as the crystalline matrix deforms during  $\text{Li}^+$  intercalation. This results in mechanical stress that fractures the cathode and isolate part of the nanomaterial, consequently the discharge capacity drops. At 750 cycles, LFP-LP-Py retains 91 % of the initial capacity ( $150.7 \text{ mA h g}^{-1}$  at 1C). LFP-L-Py 86 % ( $153.7 \text{ mA h g}^{-1}$  at 1C). Both materials decline linearly, but the carbon cage further extends cyclability by 50 % vs. the lactose-based material. LFP-LPU-Py retains 81 % (initial:  $150.0 \text{ mA h g}^{-1}$  at 1C). Despite having an even better cyclability up to 100 cycles, the material quickly deteriorates and the trend becomes unstable. The PVA's chain length after ultrasonication is shorter, and the resulting carbon-cage does not connect the nanoparticles together (TEM). We speculate that ultrasonication induces a better dispersion of the lower-end tail of the primary particle size distribution. Small nanoparticles tend to clump together into bigger, more resistant clusters. Ultrasound breaks these clusters and the spray dried powder is less resistant to mechanical stress, and ages faster. This explains the lower cyclability, but the better rate performance with respect to the lactose based material, as the carbon cage still plays a role in dissipating the electric charge more efficiently.

Galvanostatic cycling at 0.1C, for LFP-LP-Py, LFP-LPU-Py and LFP-L-Py, shows a single flat plateau at 3.4 V versus  $\text{Li}^+/\text{Li}$ , indicating the two-phase reaction between the LFP

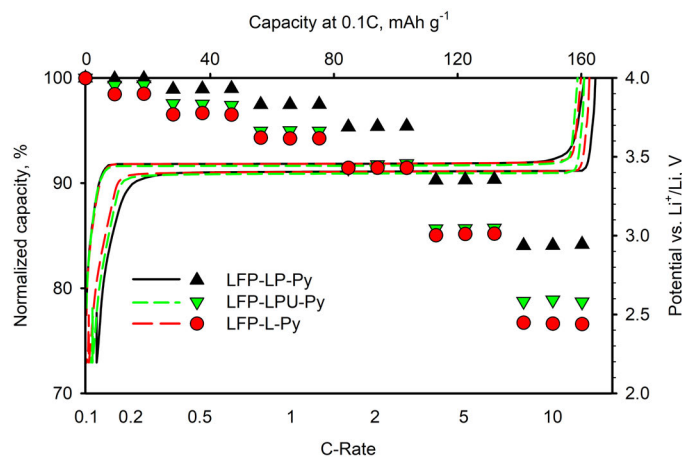


Figure 5.14 Rate performance (bottom-left axes, symbols) and Galvanostatic curves (top-right). The addition of high-Mw PVA (black lines and upward triangles) creates an extended carbon grid that better distributes the electric charge across the LFP nanoparticles, improving the discharge capacity.

triphylite and the heterosite  $\text{FePO}_4$  upon lithiation/de-lithiation reactions (Fig. 5.14). No extra plateau related to impurity phases was observed. A polarization of 50 mV was observed for all three samples indicating that all three samples are sufficiently well carbon coated for this cycling.[149] In the rate performance test, the capacities at different C-rate (0.1 to 10) were normalized with respect to the capacity at 0.1C (Fig. 5.14). The rate capabilities of the samples up to 10C are comparable to what is typically found for high performance materials.[150, 14] By increasing the C-rate, the difference in rate capability between these three samples becomes more obvious. LFP-LP-Py exhibited the highest discharge capacity of  $135 \text{ mA h g}^{-1}$  at 10C (84% normalized capacity vs. initial:  $161 \text{ mA h g}^{-1}$  at 0.1C); LFP-LPU-Py  $123 \text{ mA h g}^{-1}$  at 10C (79% vs. initial:  $156 \text{ mA h g}^{-1}$  at 0.1C); and LFP-L-Py  $124 \text{ mA h g}^{-1}$  at 10C (77% vs. initial:  $162 \text{ mA h g}^{-1}$  at 0.1C). Considering the pyrolyzed powders contain 94.9(4)%  $\text{LiFePO}_4$  active material (the rest is carbon and  $\gamma\text{-Li}_3\text{PO}_4$ ), LFP-LP-Py reaches the maximum attainable capacity at 0.1C:  $169.7(7) \text{ mAh/g(LiFePO}_4)$  ( $170 \text{ mA h g}^{-1}$  theoretical). The discharge curves have flat plateau up to 1C for all materials (Fig. 5.15). By increasing the discharge rate up to 5C, a single plateau is still found for the lactose-PVA material (solid line). The addition of high-Mw PVA creates an extended carbon grid, interconnecting LFP primary particles, that minimizes the polarization of the cathode during discharging. While for the other two samples, the discharge curves progressively fall shorter and the plateau disappears, indicating polarization (i.e. kinetic limitation) in the materials.

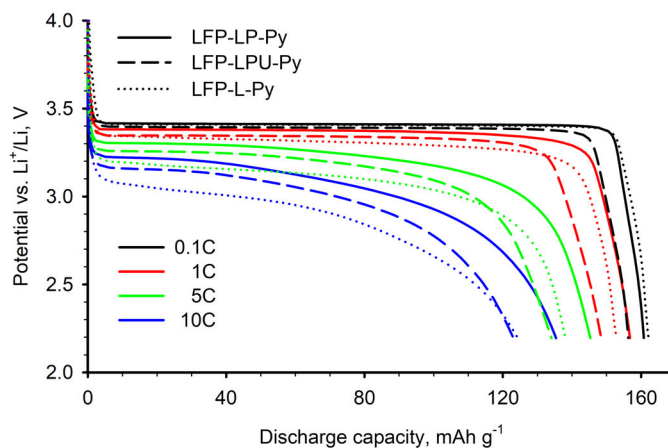


Figure 5.15 Discharge curves at increasing C-rates. An extended carbon-grid (solid line) dissipates the charge more efficiently at high C-rates with respect to a shorter carbon-grid (dashed) or no grid (dotted).

## 5.5 Conclusions

Melt-synthesized LFP nanoparticles, spray dried and coated with lactose and PVA, delivers a high-performance  $\text{LiFePO}_4/\text{C}$  cathode material ( $135 \text{ mA h g}^{-1}$  at 10C). We propose an industrially scalable route, from solid state reactions, to LFP nanoparticles suspended in water. The slurry feeds a 0.8 m I.D. spray dryer, that generates  $7 \text{ kg h}^{-1}$  of mesoporous powder, promoting  $\text{Li}^+$  wettability and providing a homogeneous dispersion of the carbon precursors, even inside the secondary particles. A fine powder ( $D_{4,3} < 12 \mu\text{m}$ ) improves cyclability, but a suspension containing PVA is more viscous and spray drying requires 0.40 MPa to atomize the slurry. We model the suspension rheology, based on shear, temperature, LFP and PVA loading in water. We prove that high-Mw PVA pyrolyzes into a carbon-cage that interconnects the nanoparticles and we model the pyrolysis step, as part of the carbon gasifies. The cage forms carbon-nanopores averaging 1.4 nm in diameter, and contributes to 30% of the  $S_a$ . The electrically conductive carbon-cage dissipates the charge more efficiently at high C-rates, and a bigger cage improves the cyclability by holding the nanoparticles together. This reduces the mechanical stress due to lattice deformation of the LFP's crystallites during  $\text{Li}^+$  de/intercalation, and delays the cathode's fracturing. Colloidal silica is an excellent filling agent and could lead to an even more cyclable cathode when coupled with lactose and PVA. Ultrasonication depolymerizes PVA; the resulting carbon-grid is smaller, does not interconnect the LFP nanoparticles, and induces battery failing. However, changing the acoustic frequency and amplitude, may better disperse the suspension without fragmenting the PVA chain.

## **Conflicts of interest**

There are no conflicts to declare.

## **Acknowledgements**

The authors recognize the support of Natural Science, Engineering Research Council of Canada and the Canadian Foundation for Innovation through the Automotive Partnership Canada program and our industrial partner Johnson-Matthey Battery Materials. The authors appreciate the collaboration of Dr. Pierre Sauriol (Polytechnique Montreal) and Dr. Delin Li, Dr. Wojciech Kasprzak, (and colleagues) of CanmetMATERIALS for generating the pilot scale melt-synthesized LFP ingots used for this study.

## CHAPTER 6 GENERAL DISCUSSION

We demonstrated that spray drying is capable of producing LFP powders at  $7 \text{ kg h}^{-1}$  at the pilot scale. The Bloomberg's 2018 New Energy Outlook report forecasts 550 G\$ investments in new battery capacity installations by 2050. Assuming a battery cost of 200 \$/kWh (average 2019 price), a  $\text{LiFePO}_4$  cathode capacity of  $110 \text{ W h kg}^{-1}$ , and a linear investment progression; the world needs a total output of 0.8 million tonnes of cathode per year. In 2013, the GEA company manufactured the world's largest dairy spray dryer, with a capacity of 30 tonnes of milk powder per hour, by drying around four and a half million liters of liquid milk daily ( $180\,000 \text{ kg h}^{-1}$ ). A single similar unit would almost supply the world's entire cathode production, drying a staggering 2 million tonnes of cathode suspension per year.

Upon revision of the proposed description for the formation of doughnut-shape secondary particles and discussion with an expert in drying technologies, a better explanation for the formation of the doughnut morphology is proposed, involving the formation of a single blowhole in the center of the droplet.[151, 152] As the droplet dries, a rigid shell of nanoparticles forms on the outside of the particle, moisture evaporation encounters a resistance in the flow and steam pressure creates a cavity (blowhole) in the center of the droplet. As moisture leaves the dried particle, the blowhole collapse and siphon the nanoparticles, forming a doughnut-shape.[110]



## 6.1 Powder formation: atomization and drying

The powder formation can be described in two steps: atomization and drying. The atomizing air  $50 \text{ m s}^{-1}$  to  $330 \text{ m s}^{-1}$  blasts co-currently the suspension feed (flowing at  $0.05 \text{ m s}^{-1}$  to  $2 \text{ m s}^{-1}$  through the nozzle bore). The kinetic energy of the air shatters the liquid jet into ligaments and then droplets. The turbulent nature of the atomization process and velocity gradient inside the jet creates a distribution of droplet diameters. Once dried, this reflects the particle size distribution of the final product (Figure 6.1).

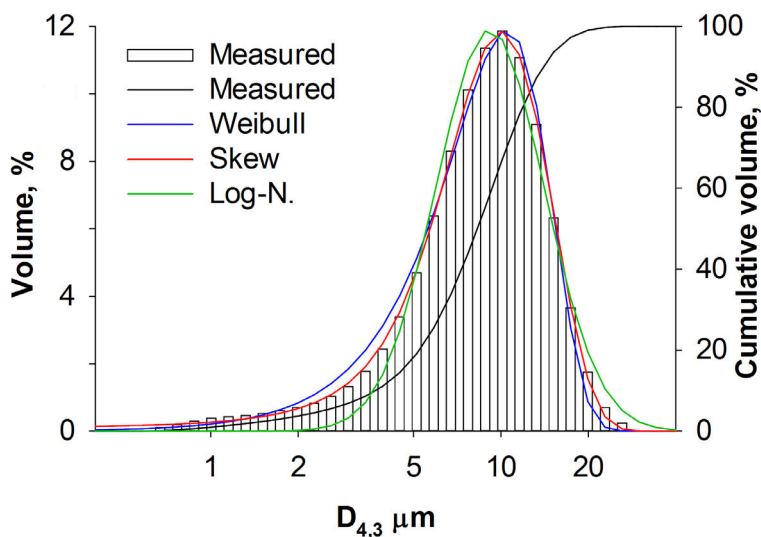


Figure 6.1 Three models describe the measured particle size distribution: the skew-normal distribution has the best fit ( $R^2 > 99\%$ ).

For general atomization applications using dual-fluid nozzles, three liquid properties are relevant: air-liquid relative velocity, surface tension, and viscosity. The kinetic energy balances the surface tension over the formation of new surface area. Viscosity inhibits the development of instabilities in the liquid jet emerging from the nozzle, and generally delays the onset of atomization.[153] The Weber number describes the energy balance, while the Ohnesorge number represents the ratio between the perturbations' viscous dissipation forces and the elastic force acting on the surface of a fluid. The smaller the droplet desired, the greater the Ohnesorge number and the longer the time required for the liquid stream to equilibrate to the final dimension.[110] However, the feed material used for this work is shear thinning, at worst the Ohnesorge number is not greater than 0.5 (if below 30% solid loading and without organic binders). Generally for Ohnesorge numbers less than 0.1, there is no significant change in droplet size in capillary jets.[154] Between 0.1 and 1 there is transition, thus making viscosity a low impacting parameter for modeling. Drying insists on the surface of the droplet. The

solvent evaporates while the primary particle migrates and agglomerate by van der Waals forces, leaving a round dried LFP secondary particle. This proposed mechanism agrees with literature:[155] the Peclet number of the droplet at worst conditions is 0.3 (at the nozzle tip, where the relative velocity is maximum). When the Peclet number is smaller than 1, the primary particle diffusion is faster compared to the radial velocity of the receding droplet surface.[156] This assumes a homogeneous composition inside the drying particle, avoiding the formation of a crust and blow-holes.[157]

For gas velocities  $< 140 \text{ m s}^{-1}$ , atomization creates droplets too big to be dried in time, wetting the internal walls of the spray dryer and lowering the yield. The resulting powder in these conditions reflect an atomization, in which only the lower distribution tail — the small droplets — is actually dried. In Figure 6.2, we were expecting  $35 \mu\text{m}$  dried particles at  $53 \text{ m s}^{-1}$ . While  $20 \mu\text{m}$  in the second. For the laboratory scale Yamato spray dryer, the biggest particle mode obtainable without binders[7] was only  $16 \mu\text{m}$  with a low yield of 14%. The higher the atomization gas speed, the smaller the particle obtained, since more kinetic energy is allowed to create more droplets surface. While higher inlet temperatures lead to bigger particle formation, due to variation in density of the drying gas.

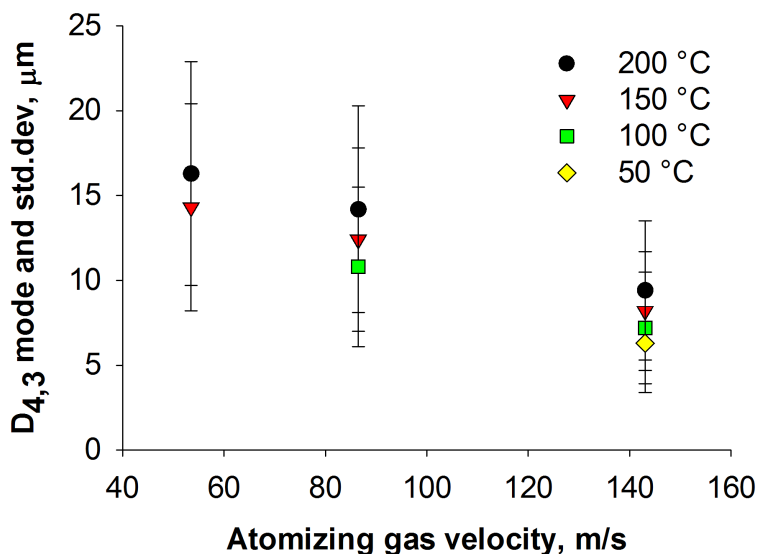


Figure 6.2 Nozzle n.4, same batch feed material, at concentration of 0.32 wt./wt. The bars represent the particle size distribution's standard deviation.

We use two semi-empirical approaches to calculate the final droplet size, not accounting for the distribution effect. The most simple consists in using the Weber number to calculate the spherical droplet diameter:[110]

$$D_{\text{drop}}^{\text{Weber}} = \frac{We \cdot \sigma}{\rho_{\text{dg}} \cdot v_{\text{ag}}^2} \quad (6.1)$$

where  $\sigma$ ,  $\text{N m}^{-1}$  is the surface tension of the slurry.  $\rho_{\text{dg}}$ ,  $\text{kg m}^{-3}$  is the drying air density, calculated using the ideal gas law at the inlet temperature. The  $v_{\text{ag}}$ ,  $\text{m s}^{-1}$  is the atomizing gas relative velocity with respect to the liquid flow.  $We$  is a constant dependent on the nozzle type and dimension. It is obtained after performing one experiment and matching the resulting particle size distribution mode with the result of this model. We obtained a value of 6 for the nozzle n.4, 15 for the **A** series of nozzles (because they have the same annulus surface area) and 14 for the remaining three (the annulus is slightly smaller).

Arthur Lefebvre[158] created an analogue equation for estimating the droplet diameter — a polynomial accounting for the Weber and the Ohnesorge numbers, based on external air blast type nozzles. So in this model, also the viscosity and flow properties like the air/liquid mass ratio are taken into account.[82]

$$D_{\text{drop}}^{\text{Lefebvre}} = 0.00333 \cdot (\sigma \rho_1 d_1)^{0.5} \rho_{\text{dg}}^{-1} v_{\text{ag}}^{-1} \left(1 + \frac{m_1}{m_g}\right) + 0.013 \cdot \frac{\mu_1^2}{\sigma \rho_1} d_1^{0.575} \left(1 + \frac{m_1}{m_g}\right)^2 \quad (6.2)$$

where the additional parameters are:  $\rho_1$ ,  $\text{kg m}^{-3}$  is the slurry density,  $d_1$ ,  $\text{m}$  is the nozzle air internal diameter (parameter C on table 4.1),  $m_1$  and  $m_g$ ,  $\text{kg s}^{-1}$  are the mass flowrate of liquid and atomizing air respectively and  $\mu_1$ ,  $\text{Pa s}$  the suspension dynamic viscosity. We found that the Weber approach better describes systems with  $\text{Oh} \leq 0.5$ , because of the fitting of the  $We$  constant with the data ( $R^2$  91%), for example when the concentration is below 50%. Instead, the Lefebvre model is less accurate but more consistent over a wider range of conditions,  $R^2$  78% (Figure 6.3).

We use the material properties to finally get to the spherical particle diameter:

$$D_{\text{particle}} = \sqrt[3]{D_{\text{drop}}^3 \cdot \omega \cdot \frac{\rho_1}{\rho_p}} \quad (6.3)$$

where  $\omega$ ,  $\text{g g}^{-1}$  the mass fraction of solid in the slurry and  $\rho_p$ ,  $\text{kg m}^{-3}$  is the particle density, obtained after mercury porosimeter analysis over two representative experiment and assumed constant for all the other analysis ( $1600 \text{ kg m}^{-3}$ ). This assumption only marginally impacts on the solid particle diameter: a 10% increase in the particle density only decrease the  $D_{\text{particle}}$  by 3.7%.

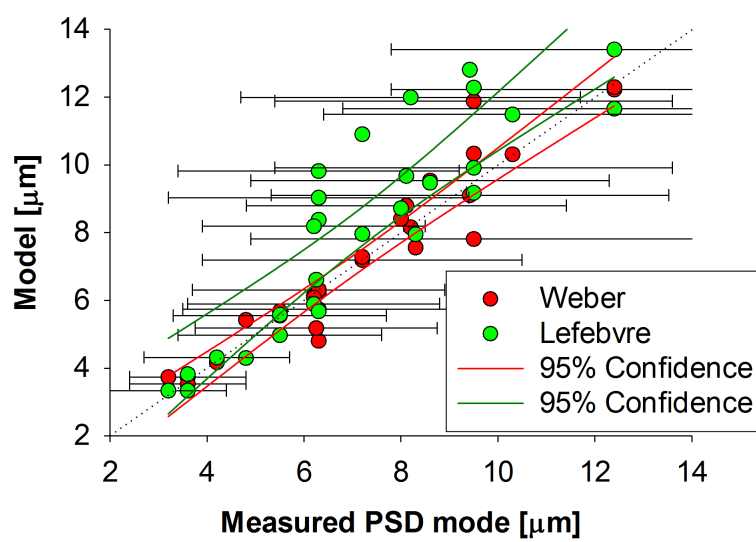


Figure 6.3 Bars represents the measured spray dried particles' standard deviation, not all are reported.

## 6.2 Suspension density, Nozzle' spray cone angle and infra-red investigation of the nozzle temperature

### 6.2.1 Materials and methods

**Density** A 100.0(5) mL graduated cylinder measured the volume, while a laboratory balance ( $\pm 20$  mg) the net weight. The slurry density  $\rho_L$  was measured after mixing and removal of the floating foam. The powder bulk density  $\rho_B$  by pouring the material through a funnel. The powder tapped density  $\rho_T$  by tapping the powder in the cylinder until compacted so that the volume remained constant during 1 min.

**Spray angle** A camera recorded a series of images of the spray cone angle, varying the atomizing pressure (0.5 barg to 3 barg), the inlet temperature (240 °C to 300 °C) and the water flowrate (25 mL min<sup>-1</sup> to 75 mL min<sup>-1</sup>). An image processing software (ImageJ 1.5)[159] calculated the spray cone angle.

**Infra-red camera** A FLIR T620-25 Thermal Imaging Camera took the infra red pictures (from 2  $\mu$ m to 20  $\mu$ m wavelength), the emissivity coefficient was adjusted to water: 0.96 to have a precise measure for the temperature of water. The steel's skin temperature therefore deviates from the actual temperature, as it's emissivity coefficient changes significantly (polished steel: 0.07, oxidized steel: 0.8). A NaCl window allowed to take the IR picture inside the spray drying chamber.

## Results and discussion

### 6.2.2 Slurry density

The liquid density  $\rho_L$ , g cm<sup>-3</sup>, linearly correlates with the composition of the slurry  $R^2 = 97\%$ , where  $\omega_i$  g<sub>i</sub>/g<sub>TOT</sub> is the mass fraction of  $i =$  LFP, lactose, water; and  $\rho_i$  (g cm<sup>-3</sup>) is the skeletal density of the material  $i$  at room temperature (lactose:  $\rho_{sk} = 1.5$  g cm<sup>-3</sup>, Eq. 6.4).

$$\rho_L = \frac{1}{\sum \frac{\omega_i}{\rho_i}} \quad (6.4)$$

Deviations are positive, proportional and due to a systematic error: above  $\omega_{LFP} = 30\%$ , mixing incorporates small bubbles that do not separate or foam on top. At  $\omega_{LFP} = 50\%$ ,  $\rho_L$  measures are depressed by 0.05 g cm<sup>-3</sup>, which corresponds to an air mass fraction of 0.003% in the slurry.

### 6.2.3 IR and nozzle temperature

Spraying deionized water at 27 °C, inside the spray dryer's chamber at 27 °C (room temperature) produced a fine mist which equilibrates at the wet bulb temperature of water (21 °C) flowing in a 92 kg h<sup>-1</sup> flow of “hot” air (Fig. 6.4).

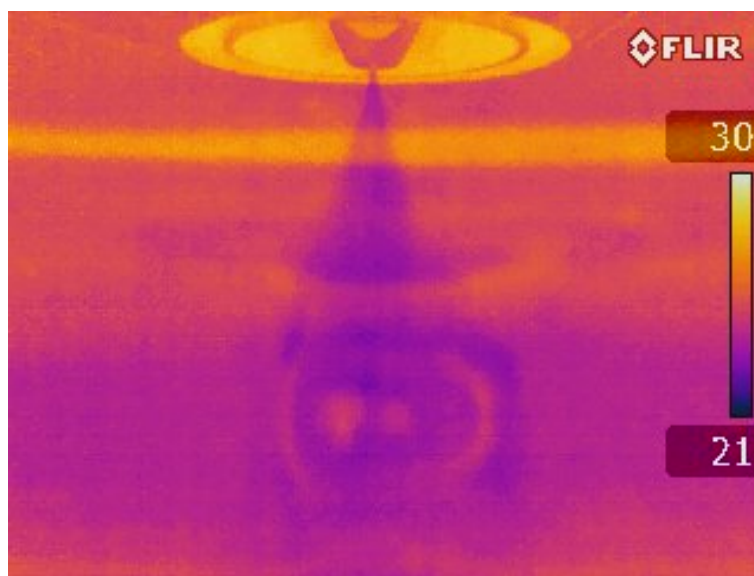


Figure 6.4 The slow evaporation rate allows to identify the spray pattern. Temperature (in °C) is displayed on the right, with a color-coding gradient.

Increasing the inlet temperature of the drying gas to 250 °C, with a flow of 100 mL min<sup>-1</sup> of deionized water, increased the temperature of the nozzle to 57 °C. However, the emissivity of the inlet intake of the hot drying air is small compared to the emissivity of the chamber, and the camera records a maximum inlet temperature of 102 °C (Fig. 6.5).

Zooming closer to the nozzle/intake portion of the chamber allows the camera to record a better reading for the temperature of the hot air. We also reduced the flow of water to 25 mL min<sup>-1</sup> and in these conditions the nozzle loses the cooling contribution from the flow of water and temperature increases to 85 °C (Fig. 6.6).

Increasing the water flow to 180 mL min<sup>-1</sup> demonstrate this phenomena and nozzle temperature decreases to 62 °C (Fig. 6.7).

Spray drying a suspension of 50% LFP in water at 100 mL min<sup>-1</sup> immediately produced a mist of dust and particles floating in the chamber. The emissivity of a mesoporous LFP particle is unknown and data is still calibrated to water, but we can appreciate that the temperature is low at the nozzle: 49 °C and also the dried powder remains cool: 62 °C (Fig. 6.8). Quickly the chamber got filled with dust and it was impossible to distinguish the

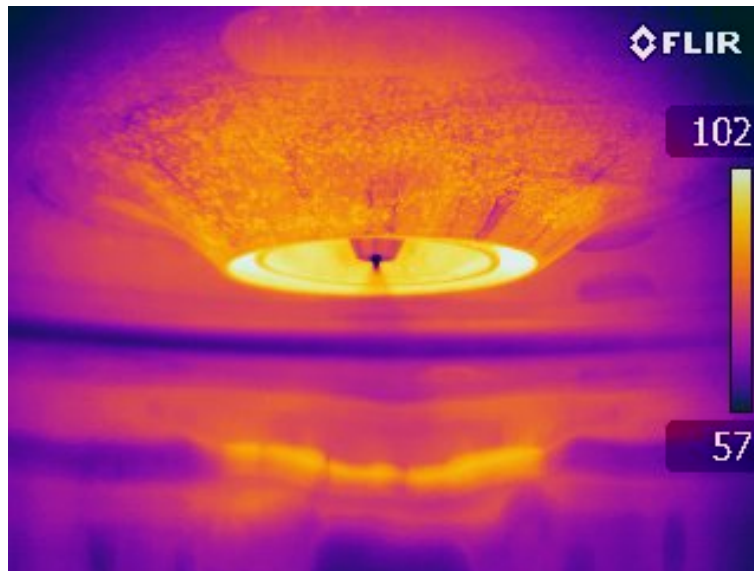


Figure 6.5 Temperature (in °C) is displayed on the right, with a color-coding gradient.

internal components of the chamber, as the IR image became blurred.

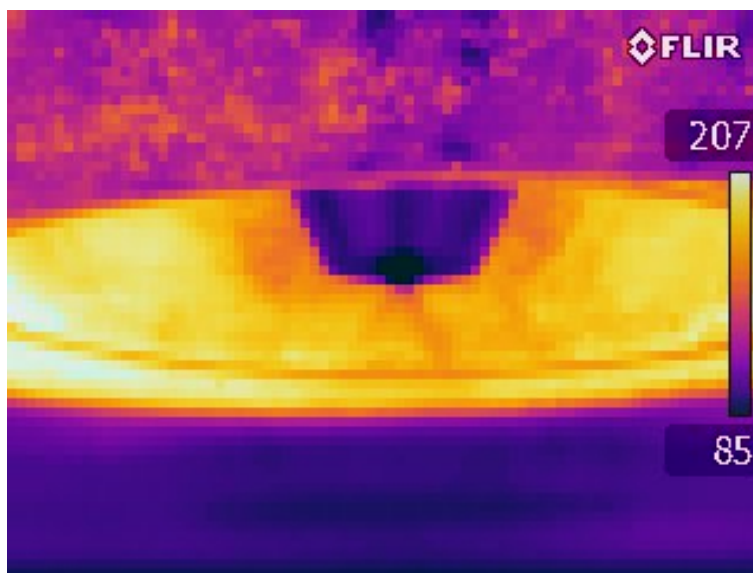


Figure 6.6 Low liquid flows reach higher temperatures as they heat up flowing through the nozzle. Temperature (in °C) is displayed on the right, with a color-coding gradient.

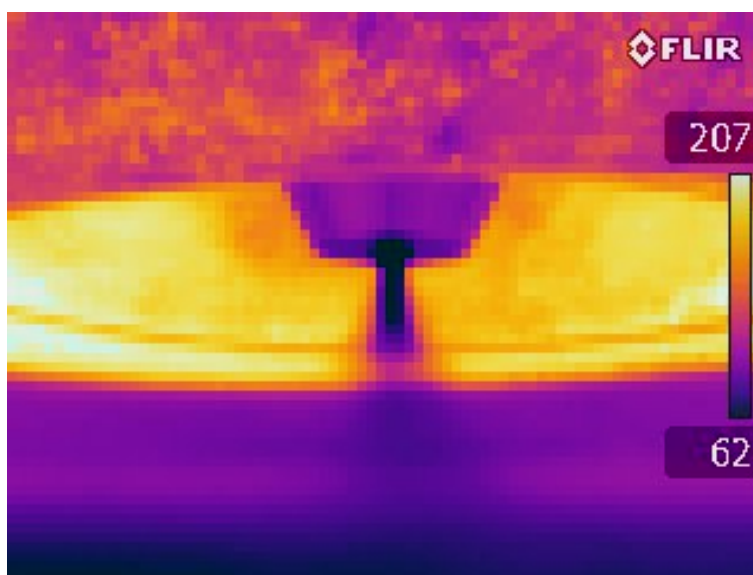


Figure 6.7 At  $180 \text{ mL min}^{-1}$  the liquid contact time inside the nozzle decreases to 4 s, decreasing also the specific heat flow from the hot metal. Temperature (in °C) is displayed on the right, with a color-coding gradient.



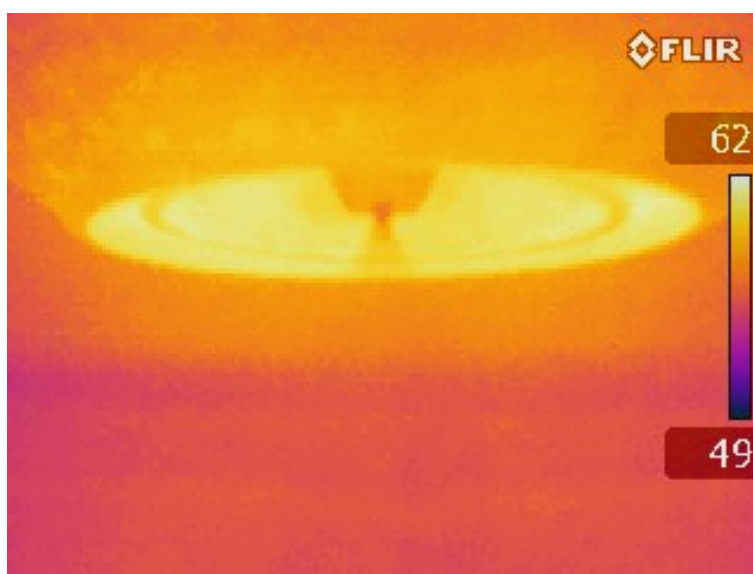


Figure 6.8 The “fog” inside the chamber demonstrates that the particles dry at the wet bulb temperature and do not overheat. Temperature (in °C) is displayed on the right, with a color-coding gradient.

### 6.2.4 Spray cone angle

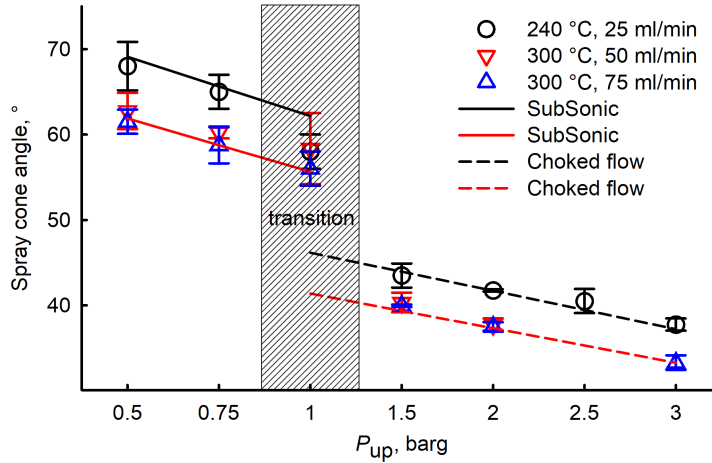


Figure 6.9 Error bars for a  $CI_{n=3}^{95\%}$ , the difference between the two groups is statistically significant regarding temperature ( $p < 0.05$ , two-tail  $t$ -test), but not regarding the liquid flowrate. Data in the transition zone are not regressed.

The dual fluid nozzle creates a conical spray pattern, whose angle gets narrower as the atomizing pressure increases. When the upstream atomization pressure exceeds 0.9 barg, the air flow in the nozzle becomes choked and the spray cone angle decreases suddenly. The inlet temperature of the drying air also helps in decreasing the cone angle: the drying air impact the spray cone on the outer annulus (Fig. 6.10), at a constant mass flow rate of  $80 \text{ kg h}^{-1}$  the drying air expands and the gas velocity increases by 10 % from 240 °C to 300 °C, imposing a narrower spray pattern. Different water flow rates do not alter the cone angle for our set of conditions (ALR: 0.5 - 2.0) (Fig. 6.9).

A two parameter model is proposed to describe the subsonic and choked flow conditions (Eq. 6.5). The spray cone angle ( $SCA$ , °) regresses in a linear fashion regarding the atomization pressure ( $P_{up}$ , barg) and inversely proportional with respect to the inlet drying air temperature ( $T_{in}$ , K). In subsonic conditions  $\beta_0 = 39000$ ,  $\beta_1 = -7100$  and the standard error of the estimate is  $2^\circ$ ,  $R^2 = 67\%$ . Indeed, when  $ALR < 1$ , the spray is unstable and the angle fluctuates overtime; this leads to a greater variance in the data. While in choked flow conditions  $\beta_0 = 26000$ ,  $\beta_1 = -2300$  and the standard error of the estimate is  $0.8^\circ$ ,  $R^2 = 96\%$  (Sigmaplot 12.5<sup>®</sup>).

$$SCA = \frac{\beta_0 + \beta_1 P_{up}}{T_{in}} \quad (6.5)$$



Figure 6.10 Nozzle and top portion of the chamber.

### **6.3 Experimental design and results on the pilot spray dryer**

We decided to follow a partial factorial experimental design in which we consider the variation of one factor at a time. (Table 6.1-6.5).

		SAMPLING DATE															
		26-5-17			29-5-17			29-5-17			29-5-17			30-5-17			6-6-17
SAMPLE		1	2	3	4	5	6	7	8	9	10	11	12				
FEED	Initial slurry mass (g)	100.00	100.00	100.00	100.00	100.00	100.00	100.00	100.00	100.00	100.00	100.00	100.00				
	Density (g/ml)	1.32	1.32	1.32	1.32	1.32	1.32	1.32	1.32	1.32	1.32	1.32	1.32				
	concentration (%)	35.6	35.6	35.6	35.6	35.6	35.6	35.6	35.6	35.6	35.6	35.6	35.6				
	mode size (um)	0.08	0.08	0.08	0.08	0.08	0.08	0.08	0.08	0.08	0.08	0.08	0.08				
	Binders (PVA - Ludox - H3PO4 m/m %)	fountain mode															
OPERATING CONDITIONS	Set inlet temperature (°C)	350.0	301.0	250	202	348	303	252	201	350	350	350	350				
	Measured outlet temperature (°C)	115.0	110.0	113	110	110	113	111	111	108	110	111	111				
	Process gas flow (kg/h)	80.0	80.0	80.0	80.0	80.0	80.0	80.0	80.0	80.0	80.0	80.0	80.0				
	Atom. Gas pressure TOP (barg)	0.9	0.9	0.9	0.9	0.9	0.9	0.9	0.9	0.9	2.5	2.0	1.5	0.6			
	Atom. Gas pressure BOTTOM (barg)	3.0	3.0	3.0	3.0	3.0	3.0	3.0	3.0	3.0	3.0	3.0	3.0				
	Atom. Gas flow (%)	38.0	37.5	37.5	37.5	43	43	43	43	90.5	75	60.5	33				
	Water flowrate (mL/min)																
	Feed flowrate (ml/min)	118.0	98.0	63.4	36.9	137	108	75	41	120	125	137	137				
YIELD	Product weight (g)	20.71	19.91	19.62	18.3	18.7	19.7	19.94	22.68	18.94	17.37	16.32	14.78				
	Yield (%)	58	56	55	51	53	55	56	64	53	49	46	42				
PSD	Mean size (um)	14.4	16.2	15.15	11.39	19.11	14.59	11.94	8.34	6.43	9.5	13.79	27.8				
	Median Size (um)	13.2	14.6	12.81	10.48	15.22	12.98	10.81	7.89	5.88	8.1	10.38	20.63				
	Mode size (um)	14.2	16.2	14.15	12.32	14.2	14.17	12.34	8.27	6.29	9.43	10.82	16.22				
	Standard Deviation (um)	8.6	10.0	11.19	6.67	14.3	9.16	7.39	4.09	3.35	6.75	13.24	21.74				
DENSITY	Bulk density (g/ml)	0.73	0.76	0.73	0.73	0.76	0.76	0.73	0.70	0.60	0.66	0.72	0.79				
	"Tapped" density (g/ml)	0.95	1.00	0.97	0.84	1.10	0.99	0.97	0.84	0.96	1.01	1.05	1.13				
	BET surface area (m2/g)	20.6				20.4	20.8	22.0	23.6	22.1							
BET	Micropore s.a. (m2/g)	0.7				0.6	0.4	0.5	1.4	1.1							
	Total pore volume (cc/g)	0.31				0.30	0.28	0.31	0.32	0.30							
	Residual moisture (%)	4.6	5.1			3.0	3.8	4.2	3.6	3.4	3.8						

Table 6.1 Experimental design and results of the pilot spray dryer (1/5).

		8-6-17										14-6-17					15-6-17					
SAMPLING DATE		13	14	15	16	17	18	19	20	21	22	23										
SAMPLE		co-current mode										co-current mode					co-current mode					
FEED	Initial slurry mass (g)	100.00	100.00	100.00	100.00	100.00	100.00	100.00	100.00	100.00	100.00	100.00	100.00	100.00	100.00	100.00	100.00					
	Density (g/ml)	1.32	1.32	1.32	1.32	1.32	1.32	1.32	1.32	1.32	1.32	1.32	1.32	1.32	1.32	1.32	1.32					
	concentration (%)	35.6	35.6	35.6	35.6	35.6	35.6	35.6	35.6	35.6	35.6	35.6	35.6	35.6	35.6	35.6	35.6					
	mode size (um)	0.08	0.08	0.08	0.08	0.08	0.08	0.08	0.08	0.08	0.08	0.08	0.08	0.08	0.08	0.08	0.08					
OPERATING CONDITIONS	Binders (PVA - Luddox - H3PO4 m/m %)	co-current mode										co-current mode					co-current mode					
	Set inlet temperature (°C)	250	300	350	350	350	350	350	350	350	350	350	350	350	350	350	350					
	Measured outlet temperature (°C)	113	111	109	111	110	110	110	110	110	110	110	110	110	75	100	125					
	Process gas flow (kg/h)	72	66	61	96	80	80	80	80	80	80	80	80	80	95	95	95					
	Atom. Gas pressure TOP (barg)	0.9	0.9	0.9	0.9	2.5	3.0	3.0	3.5	4.0	2.0	2.0	2.0	2.0	3.0	3.0	3.0					
	Atom. Gas pressure BOTTOM (barg)	3.0	3.0	3.0	3.0	3.0	5.0	5.0	5.0	5.0	3.0	3.0	3.0	3.0	78.5	78.5	78.5					
YIELD	Atom. Gas flow (%)	43	43	43	43	90.5	88	100	100	100	148	120	95									
	Water flowrate (ml/min)	65	84	107	161	120	125	128	129	177	177	177	146									
	Feed flowrate (ml/min)	17.87	15.5	13	13.67	17.69	15.46	16.85	16.89	11.91	11.8	14.45										
PSD	Product weight (g)	50	44	37	38	50	43	47	47	33	33	41										
	Yield (%)	9.68	11.29	11.71	15.87	6.32	5.8	5.23	4.95	9.41	9.53	8.38										
DENSITY	Mean size (um)	9.1	10.28	11.04	14.12	5.85	5.36	4.85	4.59	8.22	8.29	7.41										
	Median Size (um)	10.76	10.86	12.38	16.22	6.29	6.25	5.47	4.81	9.45	9.45	8.25										
	Mode size (um)	5.12	6.75	6.29	10.09	3.33	2.98	2.49	2.43	6.29	6.57	5.4										
BET	Standard Deviation (um)	0.72	0.70	0.75	0.72	0.58	0.58	0.58	0.57	0.67	0.66	0.68										
	Bulk density (g/ml)	1.04	1.03	1.09	1.1	0.96	0.96	0.95	0.93	0.99	1	1										
BET	"Tapped" density (g/ml)	co-current mode										co-current mode					co-current mode					
	BET surface area (m2/g)	23.1										23.2					23.5					
	Micropore s.a. (m2/g)	1.7										1.2					1.1					
	Total pore volume (cc/g)	0.30										0.29					0.30					
BET	Residual moisture (%)	4.4										6.8					5.3					

Table 6.2 Experimental design and results of the pilot spray dryer (2/5).

SAMPLING DATE		20-06-17					28-06-17					04-07-17			07-07-17		11-07-17	
		24	25	26	27	28	29	30	31	32	33	34	35	36				
FEED	Initial slurry mass (g)	100.00	100.00	100.00	100.00	200	200	200	200	200	200	200	200	200	200	200		
	Density (g/ml)	1.28	1.22	1.17	1.12	1.32	1.31	1.30	1.17	1.15	1.3	1.32	1.32	1.32	1.52			
	concentration (%)	30	25	20	15	34.4	34.4	34.4	30.2	29.6	34.6	35.6	35.6	49.9				
	mode size (um)	0.08	0.08	0.08	0.08	0.08	0.08	0.08	0.08	0.08	0.08	0.08	0.08	0.08				
Binders (PVA - Ludox - H3PO4 m/m %)		co-current mode					10% lacto; 10% glyce; 2.5% PVA; PVA; 7.5% 2.5% ludox											
OPERATIONS	Set inlet temperature (°C)	350	350	350	350	350	350	350	350	350	350	350	350	350	350			
	Measured outlet temperature (°C)	110	110	110	110	125	125	125	125	125	125	125	125	125				
	Process gas flow (kg/h)	95	95	95	95	95	95	95	95	95	95	95	95	95				
	Atom. Gas pressure TOP (barg)	0.9	0.9	0.9	0.9	2.5	2.5	2.5	2.0	2.0	2.5	2.0	2.3	2.5				
	Atom. Gas pressure BOTTOM (barg)	3.0	3.0	3.0	3.0	3.0	3.0	3.0	3.0	3.0	3.0	3.0	3.0	3.0				
CONDITONS	Atom. Gas flow (%)	43	43	43	43	92	92	92	77	77	92	77	87	92				
	Water flowrate (ml/min)	105	110	110	110	86	89	89	97	100	100	40	58	95				
	Feed flowrate (ml/min)	150	145	135	127	133	133	133	145	149	149	62	90	150				
YIELD	Product weight (g)	8.35	8.68	7.31	6.38	40.2	40.96	39.58	13.86	12.25	33.5	24.97	34.37	60.38				
	Yield (%)	28	35	37	43	58	60	58	23	21	48	35	48	62				
PSD	Mean size (um)	13.27	10.85	9.97	8.1	8.4	7.98	8.48	28.37	26.99	7.4	4.6	6.33	12.64				
	Median Size (um)	11.75	10.09	8.82	7.51	7.36	6.98	7.49	24.99	24.18	6.58	4.35	5.82	10.33				
	Mode size (um)	12.43	12.31	10.75	8.25	8.26	8.22	8.26	27.95	27.92	7.2	4.77	6.29	10.84				
	Standard Deviation (um)	8.85	6.37	5.12	4.13	5.6	5.29	5.52	17.08	15.7	4.6	1.93	3.39	10.1				
DENSITY	Bulk density (g/ml)	0.68	0.65	0.59	0.59	0.71	0.80	0.68	0.64	0.63	0.66	0.59	0.64	0.77				
	"Tapped" density (g/ml)	0.96	0.96	0.92	0.88	1.05	1.13	1.03	0.89	0.91	1.05	0.98	1.02	1.11				
BET	BET surface area (m2/g)	23.8																
	Micropore s.a. (m2/g)	1.1																
	Total pore volume (cc/g)	0.25																
	Residual moisture (%)	5.2																

Table 6.3 Experimental design and results of the pilot spray dryer (3/5).

SAMPLING DATE		25-07-17			26-07-17			01-08-17		16-11-17		
SAMPLE		37	38	39	40	41	42	43	44	45	46	47
FEED	Initial slurry mass (g)	200	200	200	200	200	200	200	200	200	164.5	200
	Density (g/ml)	1.52	1.56	1.52	1.52	1.39	1.40			1.61	1.26	1.26
	concentration (%)	49.9	49.9	50.2	49.9	43.3	42.3	41.2	40.0	48.3	36.7	38.2
	mode size (um)	0.08	0.08	0.08	0.08	0.08	0.08	0.08	0.08	0.08	0.08	0.08
	Binders (PVA - Ludox - H3PO4 m/m %)	8% lactose 2% ludox 8% lactose 2% PVA 4: 6% lact. 2.5%PVA 7.5% lact. 0.617%T; 3%T; 10%L; 9%L; 3%P										
OPERATI NG CONDITI ONS	Set inlet temperature (°C)	350	350	350	350	350	350	350	350	350	350	350
	Measured outlet temperature (°C)	125	125	125	125	125	125	125	125	125	125	125
	Process gas flow (kg/h)	95	95	95	92	92	92	90	90	92	92	92
	Atom. Gas pressure TOP (barg)	2.5	2.5	2.3	4.0	4.0	4.0	4.0	4.0	4.0	4.0	4.0
	Atom. Gas pressure BOTTOM (barg)	3.0	3.0	3.0	5.0	5.0	5.0	5.0	5.0	4.3	4.3	4.3
	Atom. Gas flow (%)	92	92	85	max	max	max	max	max	max	max	max
	Water flowrate (ml/min)	96	96	96	85	88	88	85	85	90	90	90
	Feed flowrate (ml/min)	150	149	149	133	140	140	124	124	184	184	184
YIELD	Product weight (g)	61.41	71.25	69.1	48.84	46.91	39.88	27.44	18.96	103.2	61.2	81.8
	Yield (%)	62	71	69	49	54	47	33	24	107	101	107
PSD	Mean size (um)	12.56	14.18	12.88	6.68	43.58	51.36	29.35	30.3	8.48	50.13	49.75
	Median Size (um)	10.25	11.66	11.88	6.28	38.63	46.82	24.14	24.48	7.33	35.5	39.22
	Mode size (um)	10.84	12.39	14.13	7.18	62.97	71.68	36.71	36.7	8.26	71.9	71.9
	Standard Deviation (um)	10.03	10.98	7.6	3.47	39.81	41.21	21.27	23.21	5.88	52.8	46.71
DENSITY	Bulk density (g/ml)	0.78	0.81	0.85	0.67	0.65	0.66	0.63	0.65	0.75	0.52	0.55
	"Tapped" density (g/ml)	1.12	1.17	1.17	1.09	0.98	0.98	0.92	0.95	1.14	0.79	0.84
BET	BET surface area (m2/g)	28.1	27.5	31.0	23.5		25.0		16.8	21.6		19.3
	Micropore s.a. (m2/g)	0.0	0.0	0.0	0.0		0.0		0.0	0.0		0.0
	Total pore volume (cc/g)	0.27	0.24	0.27	0.23		0.26		0.22	0.19		0.22
	Residual moisture (%)	3.2	6.3	3.8	6.0		7.0		5.0	6.1		7.0

Table 6.4 Experimental design and results of the pilot spray dryer (4/5).





## 6.4 Article highlights and scientific contribution as author

Here we list the author's scientific contribution and articles' highlights as first author

### 6.4.1 INFLUENCE OF ATOMIZATION CONDITIONS ON SPRAY DRYING LITHIUM IRON PHOSPHATE NANOPARTICLE SUSPENSIONS

Published in 2018, in the *Canadian Journal of Chemical Engineering*, under the special issue *Melt Synthesis of  $\text{LiFePO}_4$  for batteries*. [84] (Chapter 4)

#### Article highlights

- Agglomeration of LFP nanoparticles into a porous micron-sized particle.
- Weibull distribution best fits the particle size distribution.
- Correlation of drying and atomization to particle size, density, residual moisture.
- Drying at 200 °C maximize the powder surface area.
- Bulk density increases with feed concentration.

**Scientific contribution** We prepare — via spray drying — a  $\text{LiFePO}_4$  powder, starting from a suspension of nanoparticles in water.

We correlate how the drying conditions in the chamber and the atomizer affect the particle morphology, size distribution, density and flowability for both the liquid suspension and the solid powder.

We are the first to offer a modeling interpretation of the results and we disclose how the particle porosity and surface area are optimized with respect to temperature and particle size.

The feed material derives of a melt-synthesis process and we are the first to characterize its morphological properties and the process feasibility at the laboratory scale .

We assess the scale-up criteria for a future pilot unit regarding nozzle dimensions, atomization pressure and drying temperature.

### 6.4.2 $\text{LiFePO}_4$ SPRAY DRYING SCALE-UP AND BINDERS FOR IMPROVED CYCLABILITY

Submitted in 2019 to: Johnson-Matthey for review, later to *Energy & Environmental Science* for publication. (Chapter 5)

## Article highlights

- We demonstrate the scale-up for  $\text{LiFePO}_4/\text{C}$  production in a pilot spray dryer unit.
- High-Mw polyvinyl alcohol pyrolyzes into a carbon grid that interconnects the LFP nanoparticles.
- High-Mw polyvinyl alcohol and lactose improve the discharge rate and cyclability of the cathode.
- We propose a rheological model for the nanoparticle suspension, based on shear, temperature, LFP and PVA loading in water.
- We correlate particle size, carbon precursor and ultrasonication to discharge rate and cyclability.

**Scientific contribution** The research scale-up cathode technology, and assess feasibility from a melt synthesis, milling, and we are the first to scale-up and test spray drying; producing  $7\text{ kg h}^{-1}$  of mesoporous powder in a 0.8 m I.D. spray dryer, and test the electrochemical properties of this material.

We ensure that laboratory-scale criteria and performance are respected or improved.

We characterize the starting material from the melt-cast synthesis, milling and spray drying, assessing no material alteration during the process.

We are the first to model the nanoparticle suspension rheology, based on shear, temperature, LFP and PVA loading in water.

We are the first to quantify the carbon gasification loss, during pyrolysis, based on different carbon precursors; and characterize the type carbon coat based on morphology, chemistry and microporosity.

We prove that high-MW PVA pyrolyzes into a carbon-grid that interconnects the nanoparticles and we model the pyrolysis step, as part of the carbon gasifies. We propose a mechanical effect, for the carbon grid, in connecting and holding together the nanoparticles.

We are the first to test ultrasonication as dispersing force, and colloidal silica as additive, and test the electrochemical properties of the cathode material.

We are the first to correlate secondary particle size, carbon precursor and additives, the effect of ultrasonication, versus micro and mesoporosity, particle morphology, chemical characterization of the carbon surface and electrochemical properties of the cathode material.

We discovered that the addition of high MW polyvinyl alcohol pyrolyzes into a long-range carbon grid that improves even further the discharge rate and cyclability of the base lactose-covered material. Material characterizations at the nanoscale support our claims and spray drying applies to many research areas dealing with nano-meso porous powders. Our contribution would be beneficial to other authors dealing with nanomaterials, porosity, powder, suspensions and dispersion technologies.

### 6.4.3 EXPERIMENTAL METHODS IN CHEMICAL ENGINEERING: NUCLEAR MAGNETIC RESONANCE

Published in 2019, in the *Canadian Journal of Chemical Engineering*, under the special issue *Experimental Methods in Chemical Engineering*. [160] Selected as front-page for the “March 2019 *Canadian Journal of Chemical Engineering* issue highlights” (Chapter ??)

#### Article highlights

- Chemical engineers apply  $^1\text{H}$  liquid NMR for polymer analysis most.
- Major research clusters: aqueous sol'n, biotech, chemosensor, solid-state & simulation.
- Benchtop NMR analyzes small molecules on-line but sacrifice resolution.
- NMR quantifies composition, reaction kinetics, mechanism, and structure.

**Scientific contribution** Nuclear magnetic resonance (NMR) spectroscopy measures free induction decay signals that spin-active atomic nuclei emit when excited by a radio-frequency pulse, in a static magnetic field. The spectrum shows peaks; whose position, area and multiplicity, correlate to molecular structure, bonds, functional groups, and purity.

We highlight the strength, detection limits and sources of error for NMR spectroscopy and its applications.

Researchers publishing in The Canadian Journal of Chemical Engineering focus most on: liquid-state characterization for: polymers, reaction kinetics and equilibrium.

A bibliometric network map links NMR in 5 research clusters: solid-state analysis; biology and metabolomics; crystal structure; liquid-state analysis for polymers, aqueous solutions, nano-particles, drug delivery; and chemosensors. We are the first one to report the interaction between the different research areas, and highlight how different sectors connect to each other.

We follow up the recent development of benchtop NMR and give a concise description of the instrument and the theory behind the measure.

We believe that this document will be helpful for non-practitioners and young researchers to grasp how it works, have a clear and direct overview of the possible applications; highlighting: limitations, source of errors, detection limits and costs.

## **6.5 Article highlights and scientific contribution as co-author**

Here we list the author's direct scientific contribution as co-author in a series of papers related to spray drying, powder technologies, laboratory work, experimental design, kinetic and statistics data analysis. The author was able to lead a team and collaborate cross-team while managing multiple projects: design and synthesis of cathode materials, heterogeneous catalysts, kinetic modeling and ultrasonication reactions.

### **6.5.1 Spray dried $\text{SiO}_2$ $\text{WO}_3/\text{TiO}_2$ and $\text{SiO}_2$ vanadium pyrophosphate core-shell catalysts**

N. Saadatkah, M. G. Rigamonti, D. C. Boffito, H. Li, and G. S. Patience

Published in 2017, in *Powder Technology*.<sup>[7]</sup>

Fluidized bed reactors require spherical catalytic particles of 70  $\mu\text{m}$  to 500  $\mu\text{m}$  is size, with a strong mechanical resistance to sustain the attrition inside the reactor. In this manuscript we spray dry  $\text{WO}_3/\text{TiO}_2$  vanadium pyrophosphate catalysts, but the resulting material has poor attrition resistance. The addition of a combination of colloidal silica, polyvinyl alcohol and  $\text{H}_3\text{PO}_4$  formed a thin shell of silica around the secondary particles. We investigate drying temperature, particle agglomeration, suspension concentration and nozzle blocking.

### 6.5.2 Spray dried TiO<sub>2</sub>/WO<sub>3</sub> heterostructure for photocatalytic applications with residual activity in the dark

H. Khan, M. G. Rigamonti, G. S. Patience, and D. C. Boffito

Published in 2018, in *Applied Catalysis B: Environmental*.<sup>[8]</sup>

We spray dry a sol-gel of TiO<sub>2</sub> and a crash precipitated suspension of WO<sub>3</sub> to create a micron sized TiO<sub>2</sub>/WO<sub>3</sub> heterostructure. The material is perfectly dispersed thanks to the short drying time and small particle size (12 μm), the synthesis creates nano-crystallites which creates 220 m<sup>2</sup> g<sup>-1</sup> of surface area. Surprisingly, the heterostructure maintains a residual catalytic activity for the degradation of methylene blue even after we stop the UV light irradiation.

#### EXPERIMENTAL

A Quantachrome Autosorb-1 recorded the N<sub>2</sub> adsorption and desorption isotherms at 77 K, after degassing the sample under vacuum at 200 °C for 20 h. The weight change after and before degassing estimates the residual solvent remaining on the material after spray drying. The Brunauer-Emmett-Teller (BET) theory estimates the specific surface area (P/P0 0.05-0.30, C constant 50-200). The Barrett-Joyner-Hallender (BJH) theory estimates the mesopore size distribution (desorption branch, P/P0 0.15-0.995). The  $V-t$  method calculates the characteristic pore size, volume and specific surface area for microporous samples (DeBoer thickness). The total pore volume is evaluated at the maximum filling pressure (P/P0 0.995), integrating pores smaller than 330 nm in diameter.

#### Hybrid powder synthesis

Titanium Precursor : Tungsten Precursor : Ethanol : Formic Acid : Water : Hydrochloric Acid (ml) 9.9 : 0.075 : 29.19 : 0.5 : 27 : 15

#### Spray Drier Conditions

Drying Air: 0.2 m<sup>3</sup> min<sup>-1</sup>

Outlet Temperature: in range of 115 °C - 125 °C

Inlet Temperature: 270 °C

Atomizing Air: 0.4 barg

Pump speed: 2.5

Spray nozzle diameter: n.4

#### RESULTS AND DISCUSSION

The spray dried materials have overlapping type I(b) - type II isotherms, indicating the coexistence of micro, meso and macropores (Figure 6.11). Type I(b) is associated with materials with broad micropore size distribution and narrow mesopores ( $< 2.5$  nm). Type II reveal a macroporous structure due to the lack of plateau at the maximum filling pressure.  $\text{WO}_3$  sample has a type 2 hysteresis, attributed to pore-blocking or percolation as the pore diameter reduces in size at the neck. All other samples have a type 3 hysteresis associated to plate-like aggregates connected through a network of macropores, incompletely filled with the adsorbate (Table 6.6).

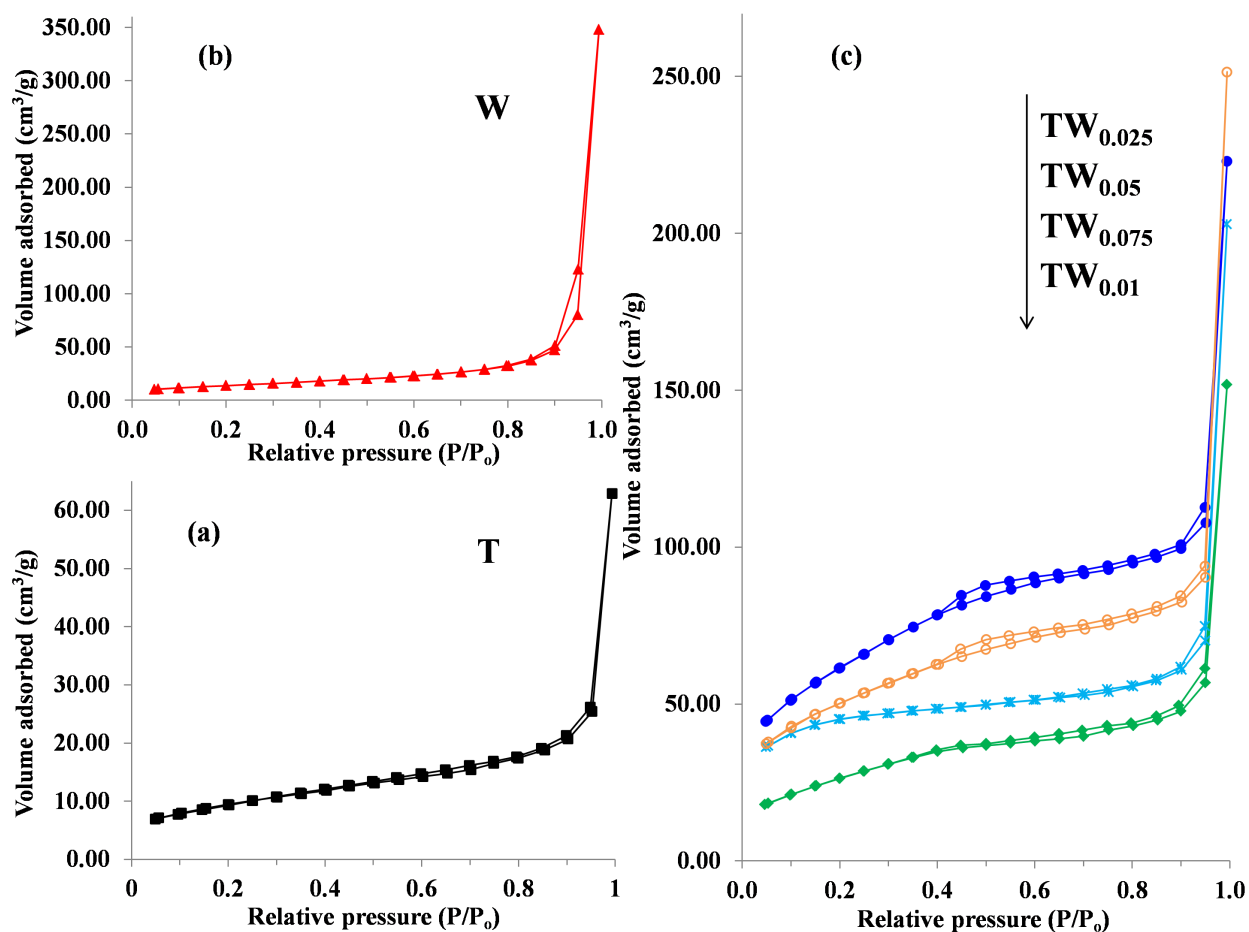


Figure 6.11 Nitrogen adsorption-desorption isotherms of the calcined control and hybrid powders.[8]

	MO3	TI02	S1	S2	S3	S4	S5	S6	S7	S8	S9	S10	S11
Solvent degassed, %	34.2	na	10.9	10.6	15.3	2.3	10.2	16.6	18.1	20.7	26.3	25.4	25.6
BET total area, m <sup>2</sup> /g	36.1	34.3	165.5	221.0	99.1	49.4	180.2	20.0	57.3	6.5	9.4	57.2	248.0
V-t micropore area (DeBoer), m <sup>2</sup> /g	13.6	17.7	146.0	189.4	78.1	1.4	150.7	0.0	0.0	0.0	0.0	37.5	217.7
V-t mesopore area, m <sup>2</sup> /g	22.6	16.6	19.5	31.6	21.0	48.0	29.5	20.0	57.3	6.5	9.4	19.7	30.3
V-t micropore mode, nm	1.7	1.4	1.4	1.5	1.3	na	1.5	na	na	na	na	1.1	1.4
BJH mesopore mode, nm	3.8	2	na	na	na	2	3.4	2.5	3.8	2	3.3	na	na
Total pore volume, cc/g	0.06	0.10	0.31	0.34	0.23	0.54	0.39	0.12	0.23	0.05	0.07	0.25	0.36
V-t micropore volume, cc/g	0.01	0.01	0.07	0.11	0.04	0.00	0.09	0.00	0.00	0.00	0.00	0.02	0.11
Mesopore volume, cc/g	0.04	0.09	0.25	0.23	0.19	0.54	0.30	0.12	0.23	0.05	0.07	0.23	0.25
Isotherm type	1b - 2	1b - 2	1b - 2	1b - 2	1b - 2	2	1b - 2	2	2	2	2	2	2
Hysteresis type	2	3	absent	3	3	3	3	absent	H2a	absent	absent	absent	absent

Table 6.6 N<sub>2</sub> physisorption data.



### 6.5.3 Water treatment: Mn-TiO<sub>2</sub> synthesized by ultrasound with increased aromatics adsorption

M. Stucchi, A. Elfiad, M. Rigamonti, H. Khan, and D. Boffito

Published in 2018, in *Ultrasonics Sonochemistry*. [138]

Contributor for surface analysis and porosimetry measures. We regressed the adsorption reaction data to an equilibrium kinetic using acetaminophen, APAP and amoxicillin, AMO as template pollutants.

#### Amoxicillin degradation's kinetic

We linearly regressed the degradation of amoxicillin into its sub-products with the integral method assuming a variable-volume ( $V(t)$ ) isothermal batch reactor and measuring the variation of moles of AMO ( $N$ ) over time ( $t$ ). The temperature increased, reached steady state after 60 min; however, temperature variation did not deviate the initial data from the linear regression. For this reason, we neglected the effect of temperature and assumed the US emissions as the main degradation pathway for our substrates. We hypothesized a zero-order degradation kinetic,  $dN/dt = -k_0 * V(t)$  because the first and second order linear regression gave lower  $R^2$  correlation coefficients or presented data inconsistency (on average, 90 %, 84 % and 89 % respectively, table 6.7).

US power, W	Conc. ppm	$k_0$ , mol L <sup>-1</sup> min <sup>-1</sup>	R <sup>2</sup>	$k_2$ , L min mol <sup>-1</sup>	R <sup>2</sup>
15	100	2E-07	76	2	71
25	100	4E-07	93	4	90
30	100	5E-07	99	5	99
40	100	4E-07	98	4	99
15C	100	2E-07	71	2	66
15P	100	2E-07	94	2	92
40C	100	4E-07	99	4	99
40P	100	4E-07	99	4	99
40	25	3E-07	79	65	78
40	100	4E-07	89	4	92

Table 6.7 AMO's degradation regressed zero and second order kinetic constants.

We interpolated the zero-order degradation kinetic ( $k_0(P)$ , mol L<sup>-1</sup> min<sup>-1</sup>) with respect of the US power ( $P$ , watt) at 100 ppm AMO concentration, with a polynomial quadratic function ( $R^2$ : 98 %).

$$k_{0(P)} = -1.0 * 10^{-9}P^2 + 6.3 * 10^{-8}P - 5.3 * 10^{-7}$$

The choice of a linear, vs. quadratic, or higher order polynomial depends on the significance (p-value) of each effect (Figure 6.12).

Data Source: Data 1 in Notebook1  
 Equation: Polynomial, Quadratic  
 $f = y_0 + a*x + b*x^2$

R	Rsqr	Adj Rsqr	Standard Error of Estimate	
0.9913	0.9826	0.9768	1.7220E-008	
Coefficient Std. Error t P				
y0	-5.2504E-007	6.1599E-008	-8.5235	0.0001
a	6.3229E-008	5.1360E-009	12.3109	<0.0001
b	-1.0016E-009	9.2257E-011	-10.8571	<0.0001

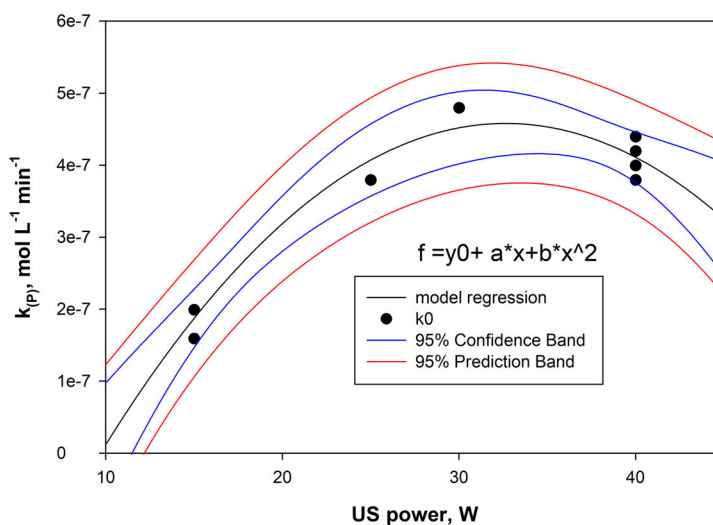


Figure 6.12 Correlation between US power and adsorption kinetic constant for Amoxicillin.

The proposed model accounts for 90 % of the variance in the data,  $R^2$  when we correlate the measured AMO conversion versus the regressed conversion as a function of the US power (Figure 6.13):

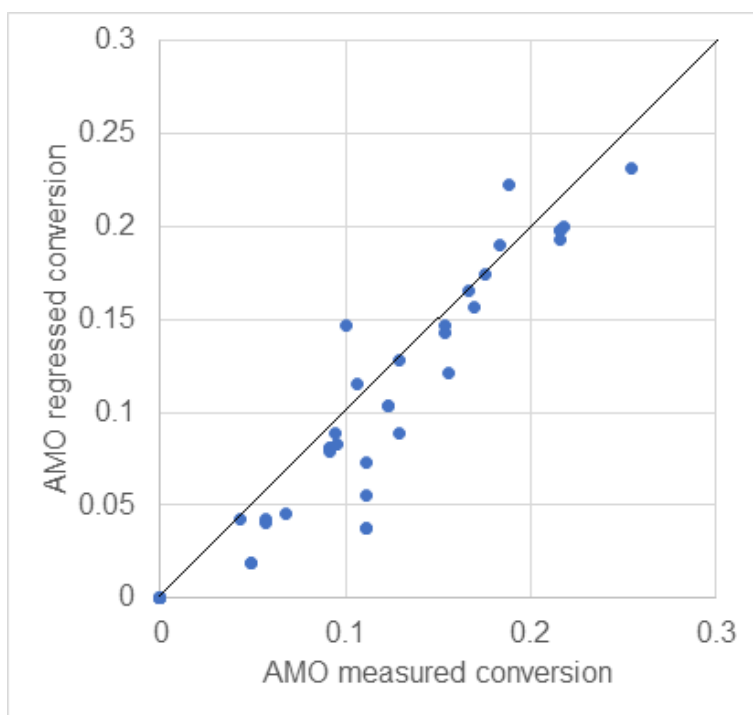


Figure 6.13 Experimental and regressed data validation.

### 6.5.4 Ultrasound assisted wet stirred media mill of high concentration $\text{LiFePO}_4$ and catalysts

H. Li, M. Rostamizadeh, K. Mameri, D. C. Boffito, N. Saadatkah, M. G. Rigamonti, and G. S. Patience

Published in 2018, in *The Canadian Journal of Chemical Engineering*. [86]

(doi:10.1002/cjce.23212)

Under normal conditions,  $\text{LiFePO}_4$  and vanadyl pyrophosphate can be milled with a surfactant up to a 50% solid mass fraction. Ultrasonication deagglomerates the cluster of nano-material that eventually plug the filters of the instrument under heavier solid mass fractions, allowing to reach 60% solid mass fraction, 50% faster than traditional milling (Figure 6.14).

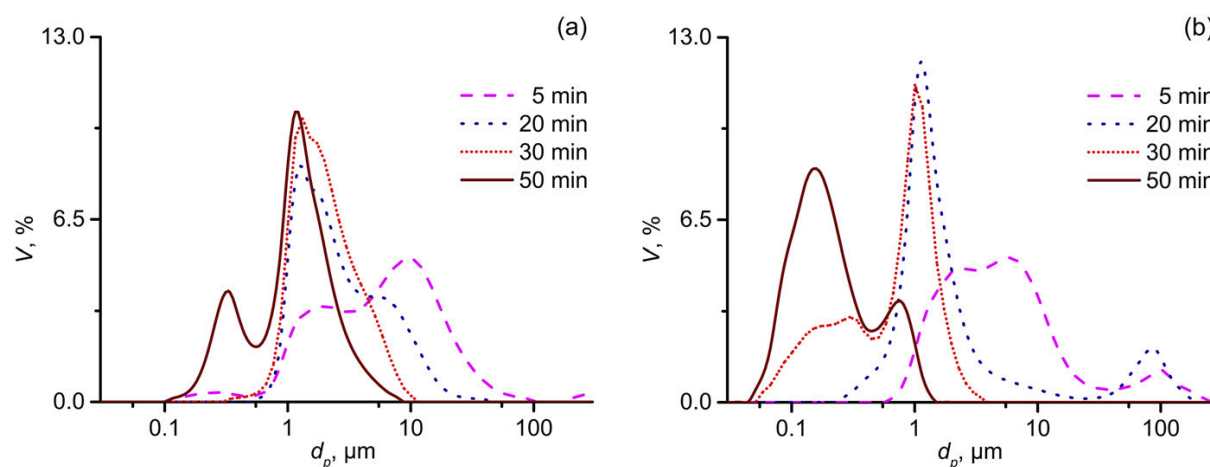


Figure 6.14 Milling vanadyl pyrophosphate over time. The particle size distribution assume a bimodal trend and most material remains above 1  $\mu\text{m}$  in size without ultrasound (a). Ultrasound milling speeds-up the process, achieving mostly submicron primary particles (b).

### 6.5.5 Gas-phase fructose conversion to furfural in a microfluidized bed reactor

D. Carnevali, O. Guévremont, M. G. Rigamonti, M. Stucchi, F. Cavani, and G. S. Patience

Published in 2018, in *ACS Sustainable Chemistry & Engineering*. [123]

We prepared spray dried catalyst for a microfluidized bed reactor for the conversion of fructose to furfural. We tested several formulations to carry out this reaction. Surface area and porosity analysis correlate with the catalytic activity and coke formation decrease the pore size volume for pores smaller than 10 nm. A model regress the data as we increase the loading of  $\text{WO}_3$  over the  $\text{TiO}_2$  support.

## EXPERIMENTAL

### Material Characterization

A  $\text{N}_2$  physisorption instrument (Quantachrome Autosorb-1) recorded at 77 K the adsorption and desorption isotherms, after degassing the sample under vacuum at 300 °C for 6 h. [106] The Brunauer-Emmett-Teller (BET) theory regress the specific surface area at  $P/P_0$  0.05-0.30 ( $C$  constant 100–200). The Barrett-Joyner-Hallender (BJH) theory estimates the mesopore size distribution over the desorption branch ( $P/P_0$  0.15-0.995). The total pore volume is evaluated at the maximum filling pressure ( $P/P_0$  0.995), considering all pores with a diameter smaller than 300 nm.

## RESULTS AND DISCUSSION

### Nitrogen Physisorption

The support ( $\text{TiO}_2$ ) dictates the specific surface area, pore size distribution and pore volume of all analyzed samples (Fig. 6.15). They possess a type IV isotherm with a H2 hysteresis loop, indicating a mesoporous structure with a narrow distribution of pore necks, inducing pore-blocking. [122]

Indeed BJH reports a well-defined surface and volume variation between 4 nm to 20 nm diameter (D98). The BJH  $dV$  median increases with the  $\text{WO}_3$  loading, as more catalyst fills selectively pores smaller than 10 nm (Fig. 6.16)

The pore volume ( $PV$ ,  $\text{cm}^3 \text{g}^{-1}$ ) linearly decreases with the loading, as more catalyst (mass fraction,  $\omega_{\text{cat}}$ ,  $\text{g}_{\text{WO}_3}/\text{g}_{\text{total}}$ ) occupies the internal pores of the bare support and when coke ( $\omega_{\text{C}}$ ,  $\text{g}_{\text{coke}}/\text{g}_{\text{total}}$ ) layers on the surface as the reaction progresses. Assuming a linear correlation (Eq. 6.6,  $R^2 = 0.97$ ), the data regress when  $\rho_{\text{cat}} = 3.3 \text{ g cm}^{-3}$  and  $\rho_{\text{C}} = 0.70 \text{ g cm}^{-3}$ . This indicates

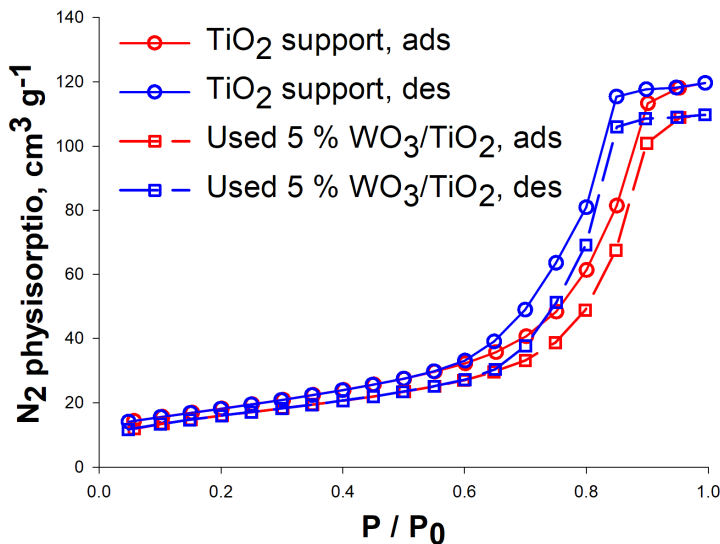


Figure 6.15 All fresh catalysts with loading  $<5\%$  express the same trend as the bare support. Higher loading and used catalysts have occluded pores that decrease the amount of  $N_2$  adsorbed.

a non-homogeneous surface coverage as the catalyst (true density  $\rho_{\text{WO}_3} = 7.1 \text{ g cm}^{-3}$ ) and coke ( $\rho_{\text{coke}} = 1.8 \text{ g cm}^{-3}$  to  $2.1 \text{ g cm}^{-3}$ ) blocks the pores below 10 nm.

$$PV_{(\omega_{\text{cat}}, \omega_{\text{C}})} = PV_{\text{TiO}_2} - \frac{\omega_{\text{cat}}}{\rho_{\text{cat}}} - \frac{\omega_{\text{C}}}{\rho_{\text{C}}} \quad (6.6)$$

Similarly, the specific surface area ( $SSA, \text{m}^2 \text{g}^{-1}$ ) proportionally decreases with respect to the correlated pore volume ( $PV_{(\omega_{\text{cat}}, \omega_{\text{C}})}, \text{cm}^3 \text{g}^{-1}$ ). Assuming a linear correlation (Eq. 6.7), the data regress with a  $R^2 = 0.93$  (Figure 6.17) when basing the equation on the specific surface area and pore volume of the bare support,  $\frac{SSA_{\text{TiO}_2}}{PV_{\text{TiO}_2}} = 350 \text{ m}^2 \text{cm}^{-3}$  (Table 6.8).[84]

$$SSA_{(\omega_{\text{cat}}, \omega_{\text{C}})} = \frac{SSA_{\text{TiO}_2}}{PV_{\text{TiO}_2}} \cdot \left( PV_{\text{TiO}_2} - \frac{\omega_{\text{cat}}}{\rho_{\text{cat}}} - \frac{\omega_{\text{C}}}{\rho_{\text{C}}} \right) \quad (6.7)$$

## CONCLUSIONS

We were able to correlate the variation of surface area of the catalyst with the loading of our active material and the amount of carbon deposited during the reaction, based only on the properties of the support.

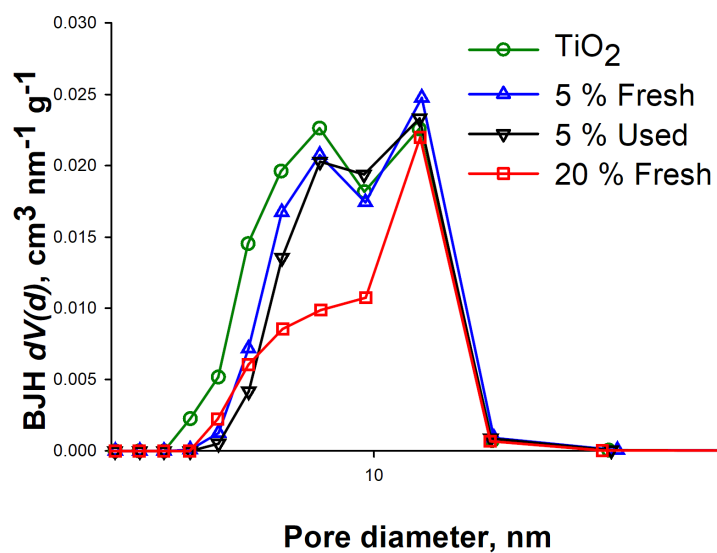


Figure 6.16 The pore fraction below 10 nm is filled as the  $\text{WO}_3$  loading and coke formation increases.

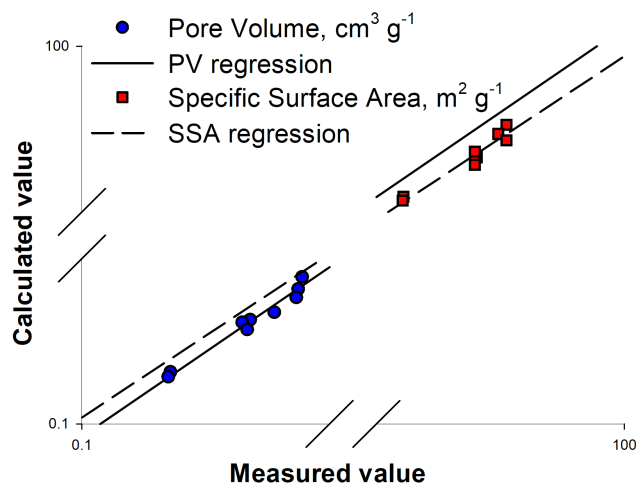


Figure 6.17 Pore volume and specific surface area model fitting.

Table 6.8 BET surface area by nitrogen physisorption, results are within  $\pm 3\%$  (95% confidence interval),  $\phi$  pore volume,  $\Delta_{dV(d)}$  BJH  $dV(d)$  mesopore median, *coke* carbon content (0.05% precision, 95% confidence interval).

	BET $\text{m}^2 \text{g}^{-1}$	$\phi$ $\text{cm}^3 \text{g}^{-1}$	$\Delta_{dV(d)}$ nm	<i>coke</i> %
TiO <sub>2</sub>	64.7	0.185	8.8	na
3%WO <sub>3</sub> /TiO <sub>2</sub>	62.8	0.183	9.6	na
5%WO <sub>3</sub> /TiO <sub>2</sub>	64.7	0.182	9.5	na
10%WO <sub>3</sub> /TiO <sub>2</sub>	58.0	0.160	9.6	na
20%WO <sub>3</sub> /TiO <sub>2</sub>	44.2	0.128	10.3	na
Used 3%WO <sub>3</sub> /TiO <sub>2</sub>	56.7	0.154	9.0	1.60
Used 5%WO <sub>3</sub> /TiO <sub>2</sub>	57.2	0.170	9.6	0.72
Used 10%WO <sub>3</sub> /TiO <sub>2</sub>	57.3	0.158	9.7	0.43
Used 20%WO <sub>3</sub> /TiO <sub>2</sub>	44.0	0.127	10.0	0.18



### 6.5.6 Platinum doped $\text{WO}_3/\text{TiO}_2$ catalyst.

## EXPERIMENTAL

### Material Characterization

An X-ray diffractometer (Philips X'PERT) generated the XRD spectra with a monochromatic  $\text{Cu-K}\alpha$  beam,  $\lambda = 0.15406$  nm, at 50 kV and 40 mA. We scanned the gonio axis from  $20^\circ$  to  $85^\circ$ , at a rate of  $0.01^\circ \text{ s}^{-1}$ . The crystalline phases were identified using the ICDD database and the Rietveld refinement (X'PERT highscore) gave a semi-quantitative characterization for the phases' weight composition. The Scherrer approximation defined the average cubic crystallite size:  $D = 0.94\lambda/\beta\text{Cos}\theta$ , where  $\lambda$  is the mentioned instrument wavelength,  $\beta$  is the full-width at half-maximum peak height (FWHM, rad), and  $\theta$  is the Bragg angle for the most intense peak (half of the  $2\theta$  position).

The FE-SEM-JEOL JSM-7600F scanning electron microscope (SEM) acquired the SEM images of the catalyst between 5 kV to 30 kV, using secondary and backscattered electrons detectors (SEI, LEI and LABE). The energy dispersive X-ray detector (EDS) mapped the surface of the catalyst and qualitatively quantified the composition and the different phase regions.

An LA-950 Horiba laser diffractometer measured the particle size distribution (PSD) of the catalyst dispersed in water. After mixing, the Mie algorithm gave the volume moment mean diameter  $D_{4,3}$  using the titania refractive index ( $2.75 + 0i$ ,  $R$  and  $Chi$  parameter below 0.02).

A  $\text{N}_2$  physisorption instrument (Quantachrome Autosorb-1) recorded at 77 K the adsorption and desorption isotherms, after degassing the sample under vacuum at  $300^\circ\text{C}$  for 6 h and taking its weight (Entris224-1S, repeatability 0.2 mg).[106] The Brunauer-Emmett-Teller (BET) theory regressed the specific surface area at  $P/P_0$  0.0005-0.25, depending whether the sample was meso or microporous ( $C$  constant 200–1100). The Barrett-Joyner-Hallender (BJH) theory estimates the mesopore size distribution for adsorption and desorption ( $P/P_0$  0.15-0.995). For the microporous sample, the QSDFIT equilibrium model (for slit pores on carbon) predicted the pore size distribution. The  $V - t$  method regressed the characteristic pore size, volume and specific surface area for the microporous sample over the best linear range (De-Boer thickness,  $P/P_0$  0.20-0.70). The total pore volume was evaluated at the maximum filling pressure ( $P/P_0$  0.995), considering all pores with a diameter smaller than 300 nm.

## RESULTS AND DISCUSSION

### X-ray diffraction

We analyzed the calcined catalyst “Fresh”, before reaction, in two formulations: 5 %  $\text{WO}_3$  supported on  $\text{TiO}_2$  with a 0.5 % Pt loading, or 1.5 % Pt. The latter was also characterized after reaction (“Used”, t12). Despite EDS confirmed the presence of W, the XRD only detected two crystalline phases: anatase titania (ref: 96-900-9087) and platinum (ref: 96-101-1114) (Figure 6.18). The titania support kept its tetragonal structure during calcination and reaction, the crystal planes have already been identified in another work.[8] The platinum was identified with a cubic structure and a submicron crystallite size, growing with the higher Pt loading and decreasing on the used catalyst due to coke deposits. SEM pictures showed crystal sizes of several hundred nanometers and a round-prismatic shape. Each crystal contained several crystallites, growing in different directions. The Rietveld refinement quantified the Pt weight fractions, which exceeded the preparation dosages. Indeed at 50 kV, the X-ray penetrated the catalyst down to 35  $\mu\text{m}$  (Pott’s equation):[7] this surface analysis overestimated the Pt fraction with respect the supporting  $\text{TiO}_2$ . As coke builds up, the Pt signal decreased in intensity and became broader (as a result, the Scherrer crystallite size decreased). This demonstrated that Pt was selectively distributed on the surface of the particle and coke was in amorphous state (Table 6.9). The lack of tungsten oxide’s signals was attributed to the intimate distribution of the  $\text{WO}_3$  precursor during the catalyst preparation. Subsequently, calcination conditions avoided phase segregation and kept the material amorphous. In fact, we also reported in a previous manuscript that loading of  $\text{WO}_3$  below 10% couldn’t be detected. A weak, unidentified peak emerged at  $31.6^\circ$  after reaction. Despite its shift of approximately  $1^\circ$  from its reference, we speculate it belonged to a tungsten oxide hemihydrate phase (ref: 96-100-1359). Reaction conditions may have crystallized part of the amorphous  $\text{WO}_3$  in the mesoporous titania structure (however, SEM-EDS could not identify  $\text{WO}_3$  crystal on the surface of the catalyst but  $\text{N}_2$  physisorption detected a decrease in pore size after reaction). The small crystallite size (30 nm) and the strong chemical interaction with the surrounding environment (coke and titania) could be responsible for the signal shift.

### SEM-EDS

All percentage are weight percentage.

The fresh catalyst consisted of spherical particles of titania (support) with tungsten oxides homogeneously dispersed in the porous structure (EDS mapping on a fractured surface).

Table 6.9  $D$  crystallite size (standard deviation among Pt signals); Riet.Pt Rietveld refinement of the Pt phase, the complementary fraction was anatase  $\text{TiO}_2$ ; BET surface area by nitrogen physisorption, results are within  $\pm 3\%$  ( $n = 3$ , 95% confidence interval C.I.);  $\phi$  pore volume (C.I.  $\pm 8 \times 10^{-5} \text{ cm}^3 \text{ g}^{-1}$ );  $\Delta_{dS(d)}$   $dS(d)$  characteristic pore median (ads. BJH for mesopore and QSDFT for micro);  $V-t$  micropore area.

	$D$ nm	Riet.Pt <i>wt.</i> %	BET $\text{m}^2 \text{ g}^{-1}$	$\phi$ $\text{cm}^3 \text{ g}^{-1}$	$\Delta_{dV(d)}$ nm	$V-t$ $\text{m}^2 \text{ g}^{-1}$
Fresh $\text{WO}_3/\text{TiO}_2$	na	na	63.8(0.1)	0.180	9.6(0.1)	4.3(0.5)
Fresh 0.5%Pt/ $\text{WO}_3/\text{TiO}_2$	52(7)	0.8	na	na	na	na
Fresh 1.5%Pt/ $\text{WO}_3/\text{TiO}_2$	88(2)	3.0	51.4(0.1)	0.165	11.0(0.1)	1.0(0.5)
Used, t12, 1.5%Pt/ $\text{WO}_3/\text{TiO}_2$	60(10)	2.0	71(2)	0.064	0.7(0.3)	50(2)

Pt crystals covered the surface as bright spots, individually well dispersed but not homogeneously distributed between each particle (Figure 6.19). The Pt submicron crystals had an average size of  $250 \mu\text{m}$  (Figure 6.20). After reaction, those Pt submicron particles coalesced into clusters composed of several hundred of those crystals, but remained dispersed of the surface. It seemed that the Pt crystals did not initiated the growth of the coke layer, which covers the  $\text{WO}_3/\text{TiO}_2$  surface. A mortar mechanically broke the coke agglomerate into chunks, exposing their shiny surface. Part of the catalyst resulted broke in the same way. About half the material was heavily covered by a thick layer of coke ( $20 \mu\text{m}$ ), the remaining particles still contained carbon (EDS) but on the surface they appeared loose with few spots of submicron-coke layer (Figure B.2).

The EDS spectrum qualitatively confirmed the presence of W (3% to 6%) on both the fresh and used catalysts, and the EDS mapping showed an homogeneous distribution of W on the support. Pt on the contrary was distributed on the surface of the support in submicron crystals (10%, as the EDS at 20 kV analyzed the surface of the material down to a depth of approximately  $10 \mu\text{m}$  and not the whole bulk). EDS qualitatively confirmed the expected amount of tungsten (expected: 5%) used during impregnation and assessed that the platinum crystallized exclusively on the surface of the catalyst (expected: 1.5%). EDS spectra on areas deprived of the Pt crystals did not record any trace of Pt in the elemental analysis. Titanium over oxygen molar ratios were coherent with the  $\text{TiO}_2$  composition. Oxygen signal was complementary with respect the platinum: Pt bulk crystals were in metallic form. An EDS spectrum on the coke deposit identified a molar composition of 90% carbon and 10% oxygen (Figure 6.22).

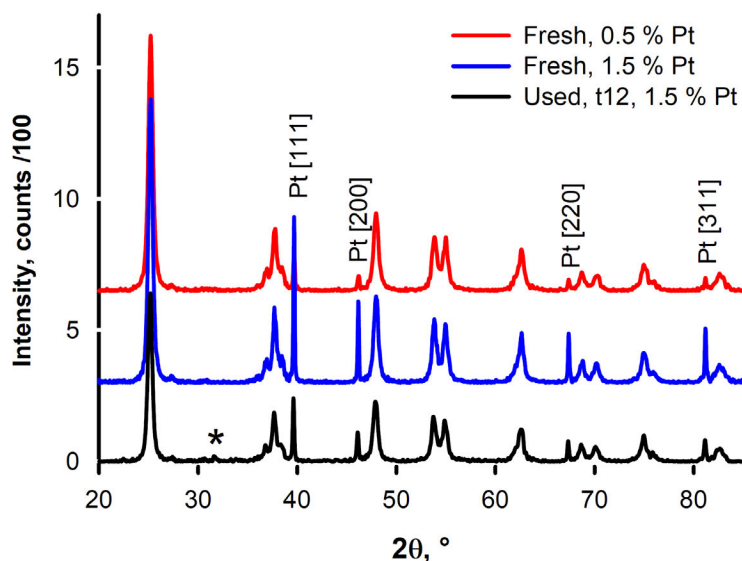


Figure 6.18 Stacked spectra recorded with the same conditions and smoothed with an 11 points cubic function, Cu- $\alpha$  sidebands were removed: coke deposits on the used sample reduced the signal to noise ratio. Four sharp Pt signals ( $39.6^\circ$ ,  $46.0^\circ$ ,  $67.4^\circ$ ,  $81.2^\circ$ ) and their respective planes [hkl] have been identified. The remaining peaks belong to the Titania support (anatase).[8]

## PSD

Laser scattering quantified the average spherical particle diameter: it increased from  $85\ \mu\text{m}$  for the fresh catalyst (independently with respect the platinum loading), to  $95\ \mu\text{m}$  for the used “t12” catalyst. Coke covered the surface (SEM-EDS) and increased the average particle diameter by  $10\ \mu\text{m}$ . This may had impacted on the reactor fluid-dynamic and favored settling of this heavy fraction of particles on the bottom of the fluid bed reactor. As a result, catalyst turnover rate increased, yielding to more coke production and increased coke thickness (Figure 6.23).

## Nitrogen Physisorption

The support ( $\text{TiO}_2$ ) and the tungsten salt precursor dictated the specific surface area (SSA), pore size distribution and pore volume (PV) of all fresh samples upon calcination, as already discussed in a previous work (Fig. 6.24). The fresh catalyst possessed a type IV isotherm and an H2 hysteresis loop, indicating a mesoporous structure with a narrow distribution of pore necks, inducing pore-blocking.[122] The addition of 1.5% Pt (1 eq. salt precursor) decreased the SSA with respect to the calcined  $\text{WO}_3/\text{TiO}_2$  catalyst. The absence of Pt signal in the core and internal shell of the catalyst (EDS) indicated that the SSA and PV

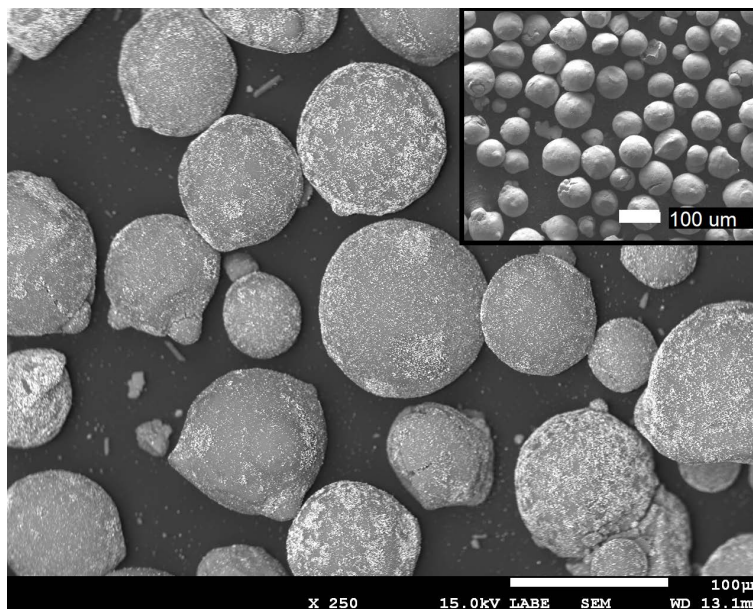


Figure 6.19 Fresh 1.5% Pt over  $\text{WO}_3/\text{TiO}_2$  particles. The LABE detector enhanced the signal from heavy elements and the Pt crystals appeared as bright white spots.[9]

decreased as a result of Pt pore-blocking. Pt blocking pores smaller than 10 nm increased the characteristic pore median ( $dS(d)$ ) by of 1 nm. The used catalyst “t12” possessed a type I-IV isotherm and an open H4 hysteresis: a microporous network developed as coke partially filled the internal mesoporous structure. Despite coke deposit, catalyst selectivities improved overtime. The SSA also increased with respect to the fresh catalyst, suggesting a selective coke deposit, which promoted the fructose conversion to HMF and did not slow down the reaction kinetic despite the significant decrease in size of the pores (11.0 nm to 0.7 nm) and PV and subsequent increase in mass transfer resistances (Table 6.9). For the same reason we concluded that the experimental reactor design was chemical-kinetic limiting, rather than mass-transfer limiting, making it suitable for future kinetic studies.

Adsorption and desorption branches for the fresh samples gave similar results in terms of pore size distribution: the BJH surface distribution had a mesopore median ( $dS(d)$ ) that decreased by only 1 nm between adsorption and desorption, indicating uniform pore distribution between the core and the shell of the catalyst. QSDFT SSA was in good agreement with the BET SSA (less than 5% deviation). The  $V-t$  method estimated a negligible micropore SSA for the fresh samples, but for the used sample, micropores contributed for almost 80% of the SSA and 40% of the PV (QSDFT method,  $V-t$  method had 5% deviation from those values).

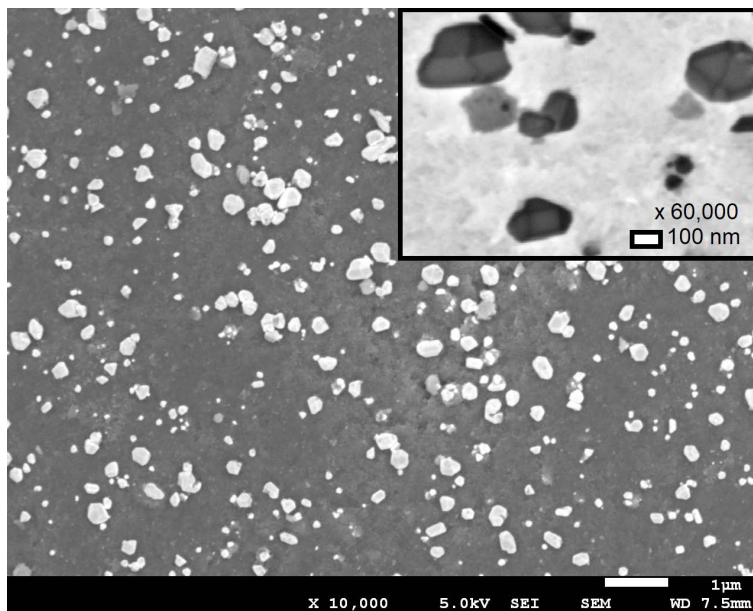


Figure 6.20 Fresh 1.5 % Pt over  $\text{WO}_3/\text{TiO}_2$  particles. The metallic platinum crystals appeared as multi-facets prisms. Considering their sizes (submicron), the crystallite size of 88 nm (XRD) and the crystal structure of metallic Pt (cubic), we could conclude that each crystal was composed of several crystallites.

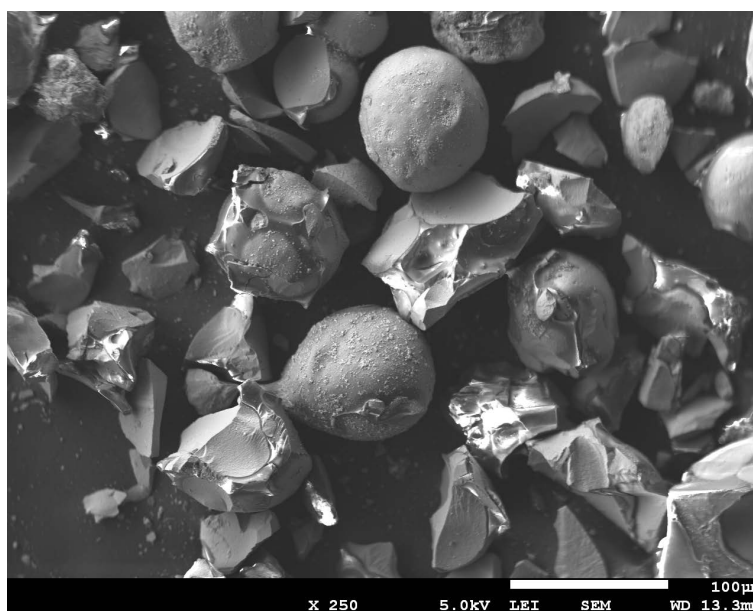


Figure 6.21 Used “t12” catalyst’s surface. Shiny “metallic-lookalike” coke chunks were dispersed around the spherical catalyst particles after mechanical breakage. Some particles broke as well.

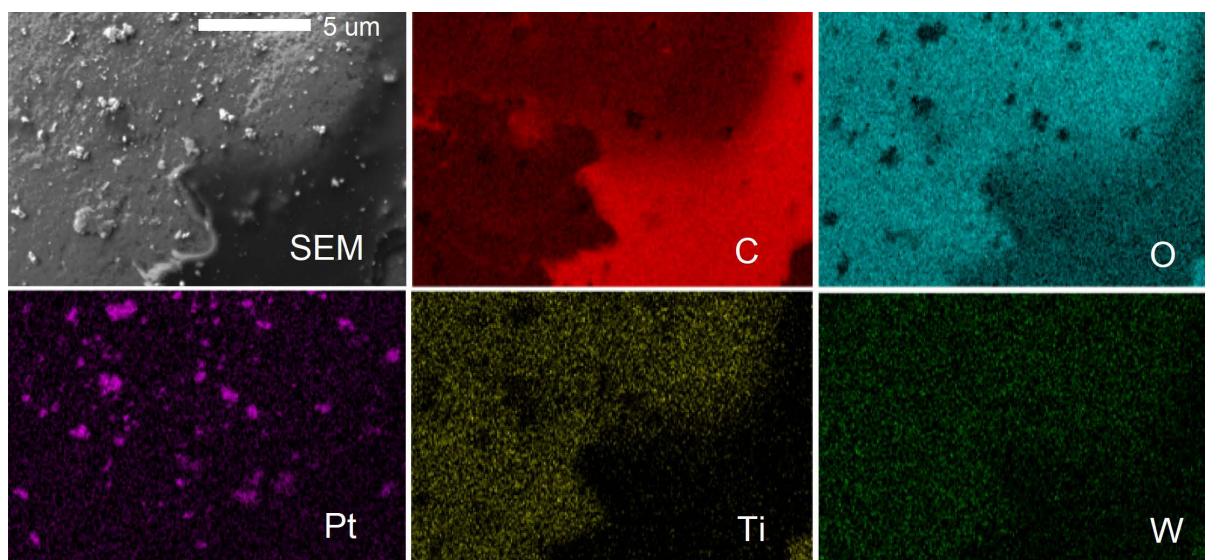


Figure 6.22 SEM and EDS mapping of the used “t12” catalyst’s surface. Carbon (C, red) partially covered the surface and suppressed the underlying elements’ signals. Oxygen (O, blue) was predominant were titanium was also present (Ti, yellow), less were carbon was present and absent were platinum was present (Pt, violet). Tungsten (W, green) was homogeneously distributed along with titanium.

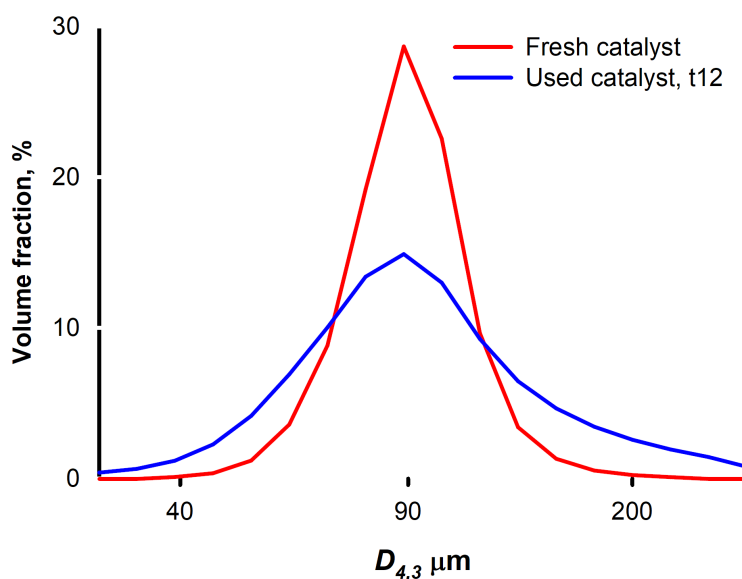


Figure 6.23 Catalyst particle size distribution in logarithmic scale. Coke deposits broadened the peak and increased the average.

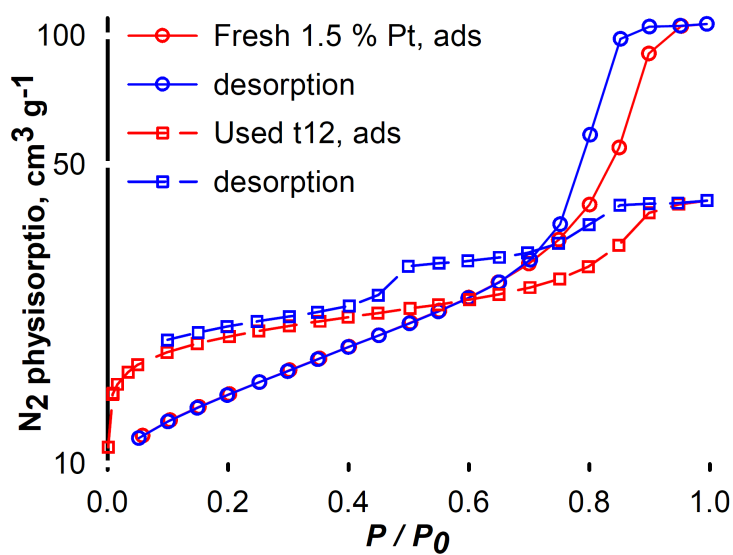


Figure 6.24 The fresh catalyst was mesoporous and after reaction resulted microporous. In the latter, the adsorption rapidly grows to plateau ( $P/P_0$  0.0005-0.1) and the type 4 hysteresis remained open. This is often associated to narrow slit micropores.



### 6.5.7 Levulinic acid upgrade to succinic acid with hydrogen peroxide

D. Carnevali, M. G. Rigamonti, T. Tabanelli, G. S. Patience, and F. Cavani

Published in 2018, in *Applied Catalysis A: General*. [10]

In this paper we propose two competitive mechanism for the conversion of levulinic acid. The Baeyer-Villiger oxidation with hydrogen peroxide favors the conversion of levulinic acid to succinic acid under acid conditions. Tungstic acid catalyzes the reaction and we modeled the ratio catalyst:hydrogen-peroxide to achieve the highest selectivity.

#### The regioselectivity in Baeyer-Villiger oxidation of levulinic acid

The  $\text{H}_2\text{WO}_4$  catalyst controls the regioselectivity of levulinic acid conversion to either succinic acid or 3-hydroxypropionic acid. 10 % molar ratio of catalyst achieve a selectivity ratio succinic acid:3-HPA of >98 % after 6 h. Each increment of  $\text{H}_2\text{O}_2$  also increased the selectivity ratio of the two-competitive kinetics (Figure 6.25).

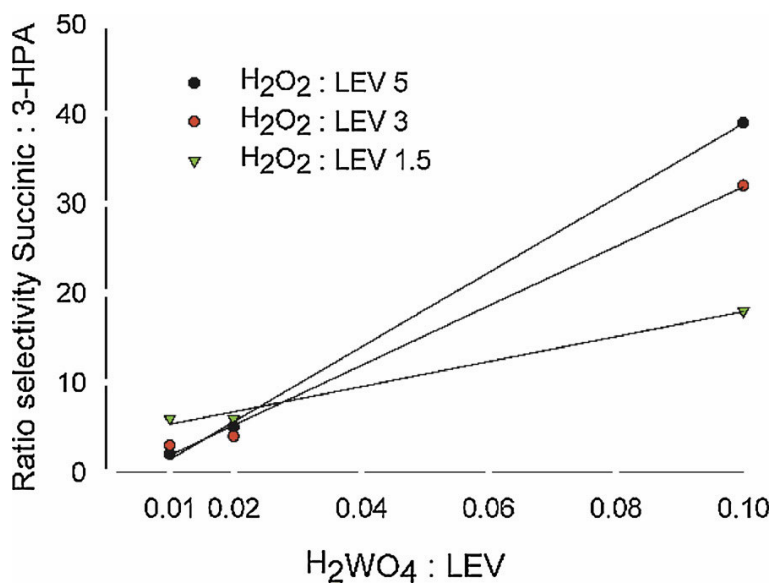


Figure 6.25 Correlation between catalyst loading and selectivity. [10]

We propose that  $\text{H}_2\text{WO}_4$  arranges with the carboxylic group of levulinic acid to form an octagonal cyclic adduct by hydrogen bonding (Figure 6.26). This conformation locks the molecule and impedes the Baeyer-Villiger migration of the secondary carbon by steric hindrance. This interaction locks levulinic acid and also impedes the dehydration and the consequent cyclization to  $\alpha$ -angelica lactone; as the selectivity to the lactone decreased when using more catalyst (38 % to 4 % lactone selectivity).

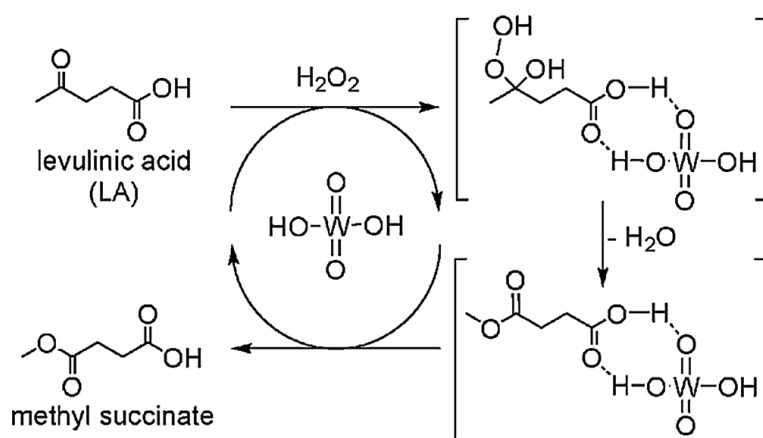


Figure 6.26 Interaction of the  $\text{H}_2\text{WO}_4$  catalyst with the levulinic acid substrate. This octagonal adduct enhances the formation of methyl succinate.[10]

### 6.5.8 Enhanced photocatalytic activity of Pt-TiO<sub>2</sub>/WO<sub>3</sub> hybrid material with energy storage ability

H. Khan, M. G. Rigamonti, and D. C. Boffito

Published in 2019, in *Applied Catalysis B: Environmental*. [145]

Ideal water-treatment uses sunlight to degrade pollutants by means of a TiO<sub>2</sub> catalyst, however TiO<sub>2</sub> cannot absorb in the visible wavelength. Spray drying a sol-gel TiO<sub>2</sub> and crash precipitated WO<sub>3</sub> with a Pt precursor creates a micron sized TiO<sub>2</sub>/WO<sub>3</sub> heterostructure that overcomes this problematic. The addition enhances even more the surface area (265 m<sup>2</sup> g<sup>-1</sup>) and spray drying disperses the platinum in small crystallites on the surface of the TiO<sub>2</sub>/WO<sub>3</sub> catalyst. Platinum creates a photocatalyst which has activity under visible and UV light. The heterostructure maintains a residual catalytic activity for the degradation of methylene blue even after we stop the UV-vis light irradiation.

#### EXPERIMENTAL

A Quantachrome Autosorb-1 measured the N<sub>2</sub> physisorption isotherms at 77 K, after degassing under vacuum at 200 °C (stepwise) for 20 h and weighting the sample (Entris224-1S, repeatability ±0.2 mg). We regressed the total Specific Surface Area (SSA) with the Brunauer-Emmett-Teller (BET) equation over the best linear range (microporous: P/P<sub>0</sub>: 0.005-0.10, C constant 200-2000; mesoporous: P/P<sub>0</sub> 0.05-0.30, C constant 100). [122] The Barrett-Joyner-Hallender (BJH) method estimates the pore size distribution for the mesoporous material (desorption branch, P/P<sub>0</sub> 0.15-0.995). The  $V - t$  method regresses the characteristic pore size, volume and specific surface area for the microporous samples over the best linear range (DeBoer thickness, P/P<sub>0</sub> 0.45-0.85). The total pore volume is evaluated at P/P<sub>0</sub> 0.98, for pores smaller than 100 nm in diameter. The intraparticle void fraction (porosity  $\varphi$ , %) was calculated from the skeletal density of the material ( $\rho$ , TiO<sub>2</sub> anatase, 3.78 g cm<sup>-3</sup>, WO<sub>3</sub> 7.16 g cm<sup>-3</sup>) and the measured pore volume ( $V_{\text{pore}}$ , cm<sup>3</sup> g<sup>-1</sup>) (Eq. 6.8).

$$\varphi = \frac{V_{\text{pore}}}{V_{\text{pore}} + \frac{1}{\rho}} \quad (6.8)$$

#### RESULT AND DISCUSSION

The spray dried materials have overlapping type I(b) - type II isotherms, indicating the coexistence of micro, meso and macropores (Figure 6.27).

Type I(b) (P/P<sub>0</sub> 0.005-0.1) is associated with materials with broad micropore size distribution and narrow mesopores (< 2.5 nm). In fact, the measured characteristic diameter of

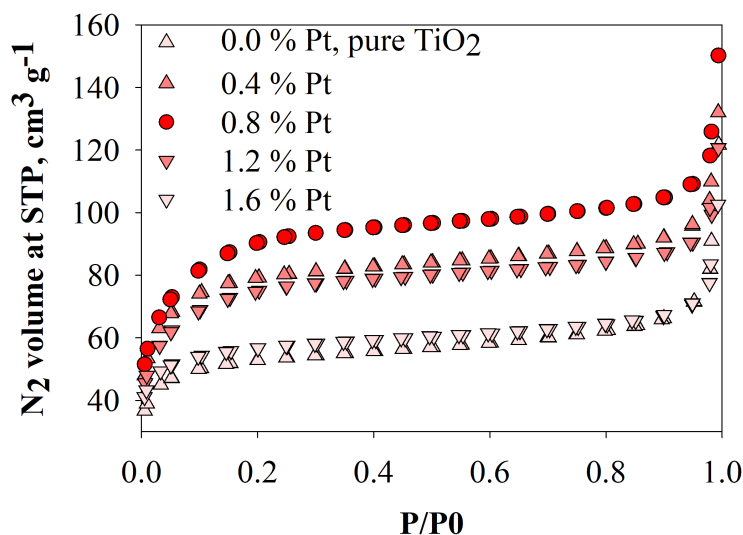


Figure 6.27  $N_2$  physisorption isotherms at different catalyst loadings (0.7 mm I.D. nozzle). The lack of hysteresis superimposes the adsorption and desorption isotherms. 0.8 % Pt maximize adsorption.

such pores is comprised between 1.1 nm and 1.6 nm ( $V-t$  method). The subsequent type II isotherms ( $P/P_0$  0.1-0.995) reveals a meso macroporous structure due to the lack of plateau at the maximum filling pressure, which is typical for spray dried nanoparticles' suspensions. When spray drying such materials, as the droplet dries, the suspended nanoparticles (primary particles) agglomerate together into a spherical micron-sized secondary particle. The resulting internal network of meso (2 – 50 nm) and macro pores ( $> 50$  nm) is a direct characteristic of the primary particle size, shape and drying speed (Tinlet 270 °C). The lack of hysteresis between the adsorption and desorption isotherms indicates isotropy between external and internal pores, thus the pore network is open and deprived of restrictions (necks) that could limit the mass transfer between the external crust and the catalyst's core.

We compared the SSA and porosity of two set of spray dried particles: using a 1.5 mm (liquid) internal diameter dual fluid nozzle, the porosity of the particle increased by 5 % on average. Spray drying the  $TiO_2$  precursor alone generated a compact microporous high SSA material ( $264\text{ m}^2\text{ g}^{-1}$ , 52 %  $\varphi$ ). Spray drying the  $WO_3$  precursor alone created a mesoporous material with low SSA and high porosity ( $55\text{ m}^2\text{ g}^{-1}$ , 73 %  $\varphi$ ). When spray drying the Pt-W-Ti composite (Ti-W ratio 9.9:0.075), the resulting materials retains the morphological properties of the main component (Figure 6.28). However, the dried material yield was unsatisfactory (55 %), as this bore improperly atomized the suspension, coating one side of the drying chamber (Air to Liquid Ratio: 3.5).

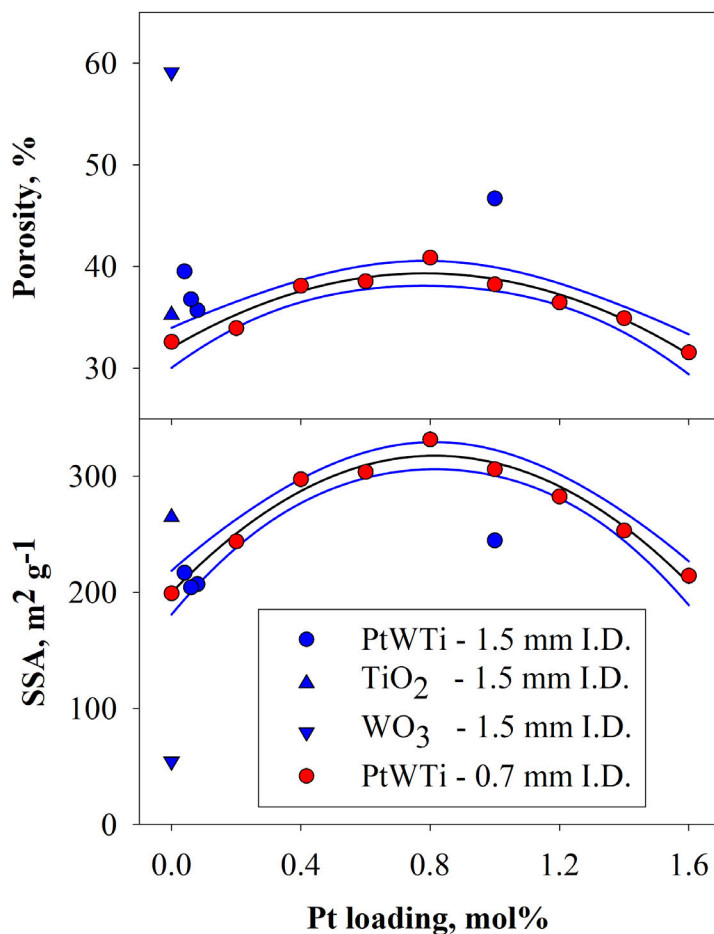


Figure 6.28 Porosity and SSA for the two set of spray drying conditions, with regression and 95 % confidence bands.

A second set of experiments carried with a 0.7 mm I.D. homogeneously atomized the feed material (ALR: 2.5, yield 75 %). Total porosity and SSA follow a parabolic trend with respect to the Pt precursor loading, with a maximum at 0.8 %. The microporous structure accounts for 90 % to 95 % of the total SSA and 60 % to 75 % of the total pore volume ( $V-t$  method) and follow the same parabolic trend with respect the Pt loading. Meso and macroporosity contribution is limited and invariant with respect to the Pt loading (Figure 6.29).

This indicates that the choice of metal-organic precursors is the main factor in achieving a high SSA microporous material, while spray drying conditions mostly affects the upper porous structure, modifying the powder bulk properties. We regressed the total SSA ( $\text{m}^2 \text{g}^{-1}$ ;  $R^2 = 97\%$ ) and the porosity ( $\varphi$ , %;  $R^2 = 92\%$ ) with a quadratic polynomial as a function of the Pt precursor loading ( $\lambda$ , mol%) (Eq. 6.9 and 6.10).

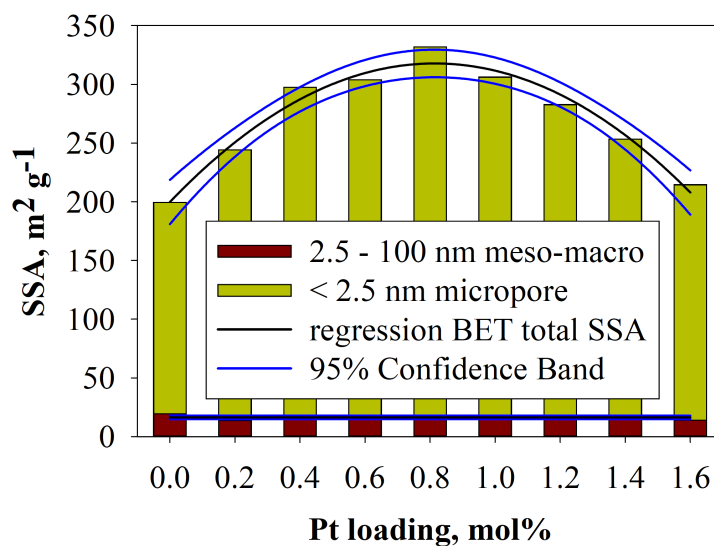


Figure 6.29 The Pt-W-Ti composite formulation creates a network of micropores that dictates the high SSA (0.7 mm I.D. nozzle). Meso- and macropores contribute for 5-10 % of the total SSA, invariant with the Pt loading.

$$SSA = 178\lambda^2 + 290\lambda + 200 \quad (6.9)$$

$$\varphi = -11.0\lambda^2 + 18.7\lambda + 32.0 \quad (6.10)$$

## SUPPORTING INFORMATION

Table of N<sub>2</sub> physisorption data

	Pt loading, mol%		(Pt-TiO <sub>2</sub> -WO <sub>3</sub> )							(Pt-TiO <sub>2</sub> -WO <sub>3</sub> )						
	WO <sub>3</sub>	TiO <sub>2</sub>	0	0.04	0.06	0.08	1.0	0.0	0.2	0.4	0.6	0.8	1.0	1.2	1.4	1.6
BET total SSA, m <sup>2</sup> /g	54.5	264.8	217.1	204.5	207.3	244.9	199.4	244.1	297.6	303.9	331.8	306.1	282.7	253.4	214.5	
SSA (micropores), m <sup>2</sup> /g	4.3	249.3	190.8	179.5	188.4	209.8	179.8	230.2	281.4	285.9	313.6	290.8	267.3	236.1	200.5	
SSA (meso-macro pores), m <sup>2</sup> /g	50.2	15.5	26.3	25.0	18.9	35.1	19.6	13.9	16.2	18.0	18.2	15.3	15.4	17.3	14.0	
Pore average diameter, nm	30	1.3	1.3	1.6	1.1	1.3	1.6	1.5	1.6	1.3	1.4	1.4	1.5	1.2	1.6	
Total pore volume (<100nm), cc/g	0.383	0.144	0.173	0.154	0.147	0.232	0.128	0.136	0.163	0.166	0.183	0.164	0.152	0.142	0.122	
Micropore volume, cc/g	0.002	0.106	0.08	0.079	0.078	0.088	0.076	0.096	0.12	0.122	0.138	0.126	0.115	0.099	0.085	
Meso-macro pore volume, cc/g	0.381	0.038	0.093	0.075	0.069	0.144	0.052	0.04	0.043	0.044	0.045	0.038	0.037	0.043	0.037	
ratio <u>microSSA/totalSSA</u>	0.08	0.94	0.88	0.88	0.91	0.86	0.90	0.94	0.95	0.94	0.95	0.95	0.95	0.95	0.93	
ratio <u>microPV/totalPV</u>	0.01	0.74	0.46	0.51	0.53	0.38	0.59	0.71	0.74	0.73	0.75	0.77	0.76	0.70	0.70	
Porosity, %	73.3	35.2	39.5	36.8	35.7	46.7	32.6	34.0	38.1	38.6	40.9	38.3	36.5	34.9	31.6	
Porosity - micro, %	1.4	28.6	23.2	23.0	22.8	25.0	22.3	26.6	31.2	31.6	34.3	32.3	30.3	27.2	24.3	
Porosity - meso-macro, %	73.2	12.6	26.0	22.1	20.7	35.2	16.4	13.1	14.0	14.3	14.5	12.6	12.3	14.0	12.3	

Table 6.10 Table of N<sub>2</sub> physisorption data.

### 6.5.9 Ultrasonic intensification to produce diester biolubricants

N. A. Patience, F. Galli, M. G. Rigamonti, D. Schieppati, and D. C. Boffito

Published in 2019, in *Industrial & Engineering Chemistry Research*. [161]

(doi:10.1021/acs.iecr.9b00717)

#### Pareto Chart of standardized effect

Esterification reactions are lengthy (6 h) and require temperatures above 120 °C. Ultrasonication in the presence of an acid heterogeneous catalyst (Amberlyst15-H) intensifies the process, the reaction achieves completion at 100 °C in 3 h. A partial factorial DOE highlights temperature, US power, and initial molar ratio of reactants as main contributors for the reaction (Figure 6.30).

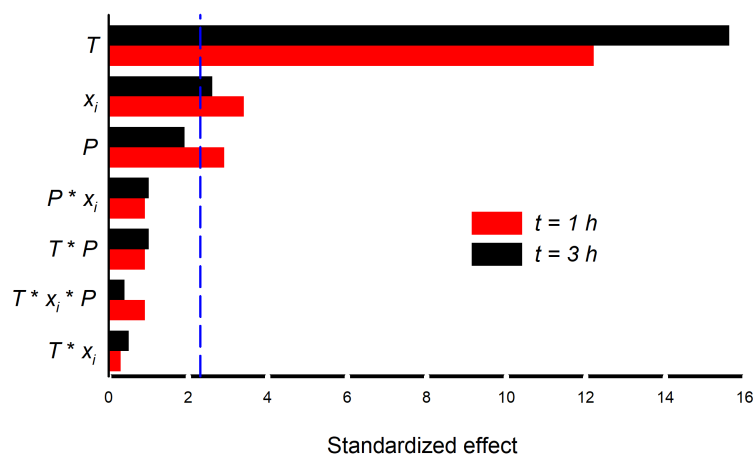


Figure 6.30 Pareto chart of standardized effect. Response variable: FFA concentration at 1 h (red) and 3 h (black). 2.3 is the value above which the variable ( $T$  = temperature,  $P$  = ultrasound power and  $X_j$  = alcohol/FFA molar ratio) has a significant effect ( $\alpha = 0.1$ )

After 1 h, all individual factors affect conversion ( $p < 0.05$ ), while at 3 h, US power becomes statistically insignificant. In fact, after 3 h, the reaction approaches equilibrium, which is thermodynamically fixed at a certain temperature. Temperature is always significant, and becomes even more important at 3 h as the reaction equilibrium is pushed towards the formation of the diester by evaporating water. The Pareto chart identified these three significant factors and we regressed the coefficients assuming a linear model for FFA conversion at 1 h and 3 h (eq. 6.11 and 6.12), considering: US power ( $P$ , W), molar ratio ( $R$ ), and temperature ( $T$ , °C):

$$X_{FFA,model,t=1h} = -100 + 1.6T + 9.7R + 0.15P \quad (6.11)$$

$$X_{FFA,model,t=3h} = -110 + 1.9T + 9.2R + 0.12P \quad (6.12)$$



Both  $R^2$  are higher than 90 % and coefficients p values were lower than 0.05, except for US power at 3 h, that increased to  $p = 0.09$  for the aforementioned situation. The standard of error of the estimate was 9 %, which is on the same order of magnitude as the uncertainty on the experimental results.

### Biolubricant rheometry

Samples are very sensitive to temperature variation; an increase of 0.1 °C decrease the apparent viscosity by 0.1 mPas. This leads to apparent non-Newtonian trends when increasing the shear rate as the higher spinning rate generates more heat by friction. Despite the external liquid temperature controller and because of the thermal inertia of the bio-lubricant, temperature increases locally, and therefore viscosity decreases when increasing the shear rate (by 0.1-0.3 mPas over the entire range). For this reason and given the fact that the viscosity variation (between 2-4 %) is negligible compared to the average value, we decided to assume a Newtonian behavior for our bio-lubricant. Similarly, when we investigated a possible time-dependency rheology at 20 °C and at a constant shear rate of 1000 s<sup>-1</sup>, the sample took 200 s to reach steady state, starting from 54.60(5) mPas and reaching 54.75(5) mPas (0.3 % variation). We attributed this negligible variation to thermal inertia and assumed that our biolubricant's rheology is not time dependent either. We chose three random samples and recorded a temperature ramp analysis at 20 °C to 79 °C at constant shear 1000 Hz (Figure 6.31).

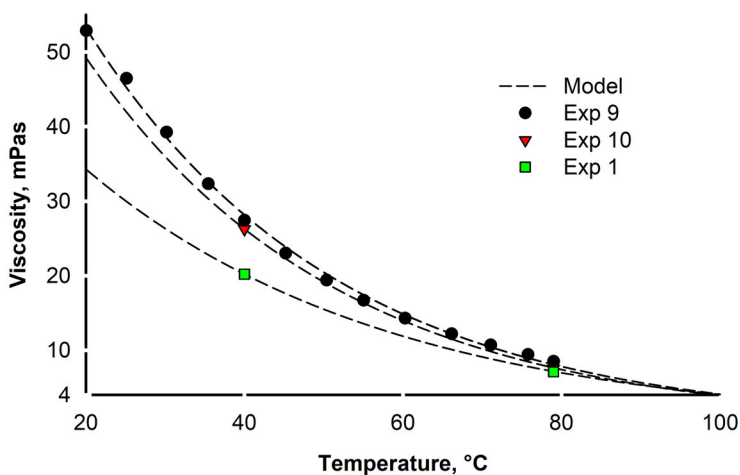


Figure 6.31 Viscosity of biolubricants vs T and logarithmic regression and extrapolation up to 100 °C.

The HAAKE rehowin data manager software regressed the data and in all cases the best fit was obtained with a logarithmic equation,  $\log \mu = a + b * T$  ( $\mu$  in mPas, T in °C,  $Chi^2 <$

0.01 and  $R^2 > 0.99$ ). This function then fitted the a and b parameters from the viscosity data for each sample, recorded at  $1000 \text{ s}^{-1}$  at a constant temperature of  $40^\circ\text{C}$  and  $79^\circ\text{C}$ , after sample temperature equilibration.

### 6.5.10 Influence of frequency and amplitude on the mucus viscoelasticity of the novel mechano-acoustic frequencer<sup>TM</sup>

D. Schieppati, R. Germon, F. Galli, M. G. Rigamonti, M. Stucchi, and D. C. Boffito

Accepted in 2019, in *Respiratory Medicine*.

Patients suffering from cystic fibrosis have an abnormal high-viscosity mucus in their lungs. We regressed mucus rheology and its adhesion strength as a mechano-acoustic instrument provide acoustic vibrations that lower those factors.

The Mucus has a shear thinning characteristic, 12 experiments, data analysis and regression identify in the Carreau model A the best fit (Figure 6.32).

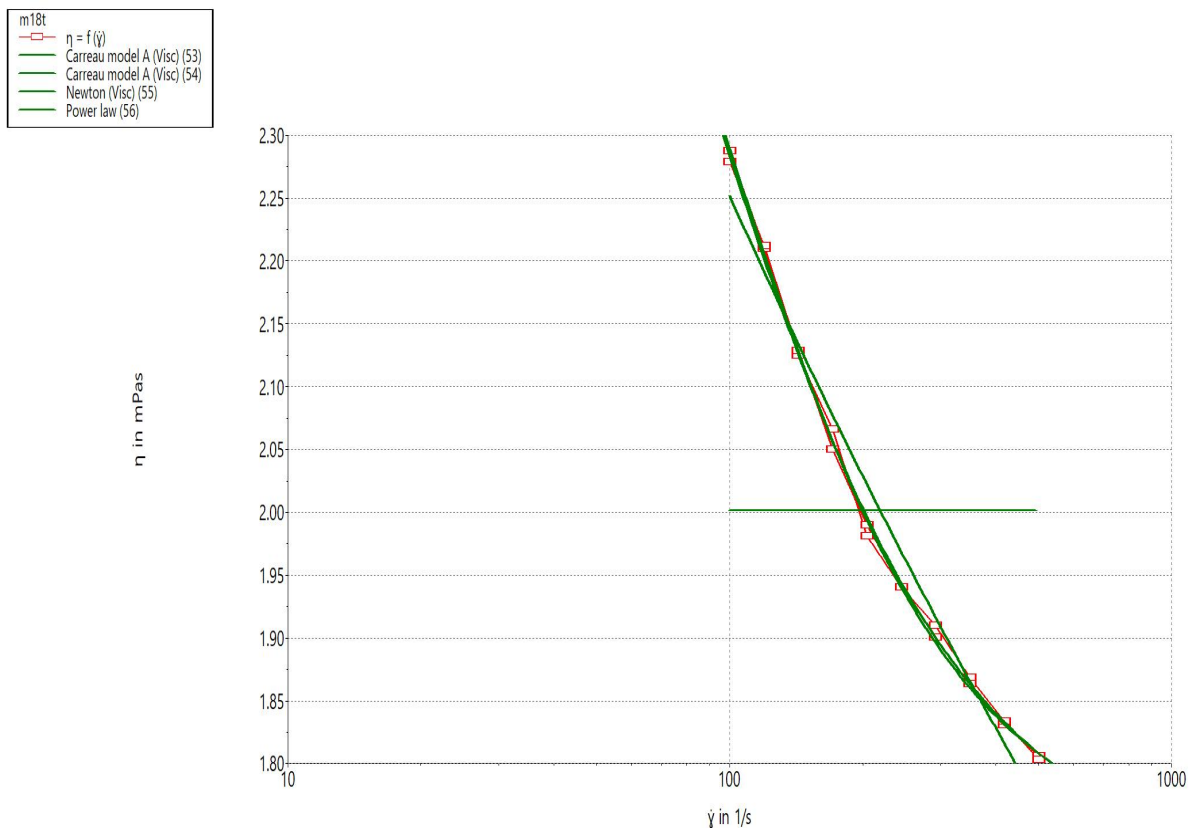


Figure 6.32 Mucus becomes less viscous at high shear rates.

Initial DOE regression leads to highlight the insensitive factors that statistically do not contribute to the variation of the output variable WA, work of adhesion (Table 6.11).

Stepwise elimination of the insignificant factors leads to a refined model.  $R^2$  obviously decrease (poorer fitting), but the model is more robust; the adjusted  $R^2$  increase and p-values remain below a defined threshold (Table 6.12).

**Data Source: Data 2 in mucus project.JNB**  
**Equation: User-Defined, Mucus in STANDARD 2.JFL**  
 $f = b_1 + b_2 * S^2 + b_3 * F + b_4 * S + b_6 * M * F + b_7 * M * S + b_8 * F * S + b_9 * M * F * S$

<b>R</b>	<b>Rsqr</b>	<b>Adj Rsqr</b>	<b>Standard Error of Estimate</b>	
0.7855	0.6170	0.5500	11.1273	
	<b>Coefficient</b>	<b>Std. Error</b>	<b>t</b>	<b>P</b>
<b>b1</b>	140.1187	5.0808	27.5782	<0.0001
<b>b2</b>	0.0003	0.0214	0.0117	0.9907
<b>b3</b>	0.5873	0.1343	4.3737	<0.0001
<b>b4</b>	6.1032E-015	7.7003	7.9260E-016	1.0000
<b>b6</b>	-0.2042	0.0286	-7.1329	<0.0001
<b>b7</b>	-0.0415	0.0157	-2.6348	0.0119
<b>b8</b>	-0.0028	0.0011	-2.4910	0.0170
<b>b9</b>	0.0012	0.0004	3.0916	0.0036

Table 6.11 Initial DOE regression.

Finally, a contour plot defines the model for the response variable. Still, a careful analysis has to be carried out to verify model inconsistencies. For example, the response variable WA cannot encounter negative values or discontinuities, a critical check of the variability of the WA model leads to exclude quadratic and higher order effects (Figure 6.33).

**Data Source: Data 2 in mucus project.JNB**  
**Equation: User-Defined, Mucus in STANDARD 2.JFL**  
 $f = b1+b3*F+b4*S+b6*M*F+b7*M*S+b8*F*S+b9*M*F*S$

R	Rsqr	Adj Rsqr	Standard Error of Estimate	
0.7851	0.6164	0.5602	10.9993	
	Coefficient	Std. Error	t	P
b1	140.1269	4.8525	28.8773	<0.0001
b3	0.5868	0.1327	4.4209	<0.0001
b4	0.0895	0.0473	1.8907	0.0657
b6	-0.2042	0.0283	-7.2159	<0.0001
b7	-0.0413	0.0156	-2.6517	0.0113
b8	-0.0028	0.0011	-2.5051	0.0163
b9	0.0011	0.0004	3.1151	0.0034

Table 6.12 Refined DOE regression.

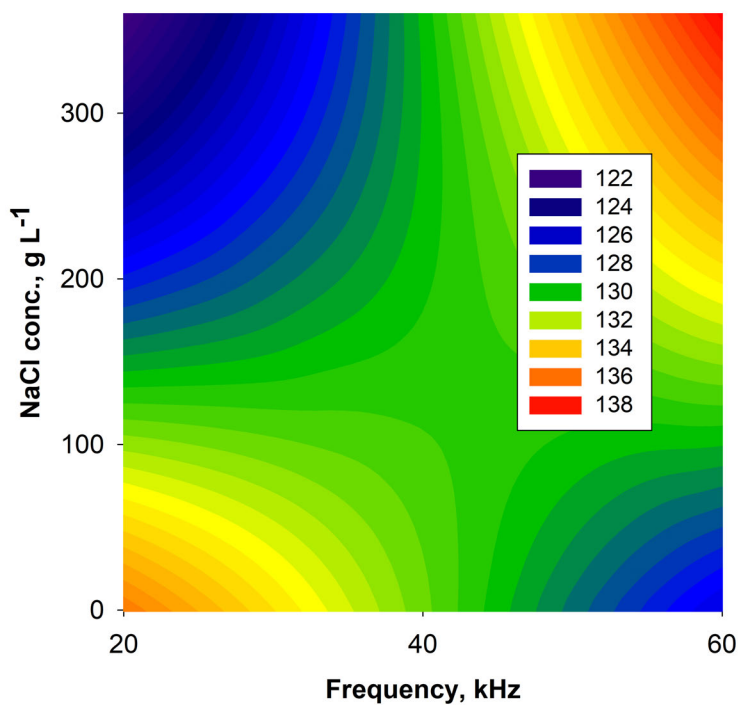


Figure 6.33 Work of adhesion (mN/m) response surface when the mucin fraction reaches 4 %. A saddle contour identifies the areas where WA is minimum (cold colours): lowest frequency with highest salt concentration and high frequency with no salt.

### 6.5.11 LiFePO<sub>4</sub> synthesis via ultrasound assisted mechanochemistry

H. Li, F. P. Cabanas-Gac, L. Hadidi, M. Bilodeau-Calame, A. Abid, K. Mameri, M. G. Rigamonti, S. Rousselot, D. Mickael, and G. S. Patience

Submitted in 2019, to *Journal of Power Sources*.

In this paper we synthesized LiFePO<sub>4</sub> from inorganic salt precursors and spray dried the material to achieve an homogeneous powder. Pyrolysis and electrochemical tests follow.

The author instructed and participated in the spray drying of the feed materials.

#### Abstract

Using wet ball milling we reduced the particle size of the precursors of LFP to the nano-size. We tested different milling time, carbon sources and treatment with ultrasound during milling, to characterize the effect of those factors on the final LFP. In particular Pore size distribution and surface area.

#### Methodology

##### BET

A Quantachrome Autosorb-1 instrument for N<sub>2</sub> physisorption measured the adsorption and desorption isotherms at 77 K, after degassing the sample under vacuum at 350 °C for 5 h and taking the weight (Entris224-1S, ±0.2 mg).[106] The BET theory (Brunauer-Emmett-Teller) regressed the specific surface area (SSA, adsorption branch,  $P/P_0$  0.05-0.25,  $C$  constant 100–250). The BJH theory (Barrett-Joyner-Hallender) gave the mesopore size distribution during adsorption ( $P/P_0$  0.15-0.995). We evaluated the total pore volume at the maximum filling pressure ( $P/P_0$  0.995), this approach sums the volume for all pores with a diameter smaller than 300 nm.

#### Result and discussion

##### BET

All powder samples follow a Type IV(a) isotherm, which corresponds to a mesoporous material (Figure 6.34).[122] The initial monolayer-multilayer adsorption on the mesopore walls corresponds to a Type II isotherm ( $P/P_0$  0.05-0.5), followed by pore condensation and incomplete pore filling (as the adsorption seems to increase without a limit).[8] This phenomena is common for spray dried materials because of the interparticle void fraction, measurable

by mercury porosimetry, which range in pore size between  $0.3\ \mu\text{m}$  to  $2\ \mu\text{m}$ . [84] The carbon precursor forces the material to aggregate in two different ways: glucose in the presence of US creates a Type H3 hysteresis loop: non-rigid aggregates of plate-like particles in a network of heterogeneous pore size distribution including macropores; while in the absence of US create a Type H2(b) hysteresis. Lignin and cellulose create a Type H2(b) hysteresis: pores are organized in a bottle-neck network of broad size distribution of neck diameters that induce pore blocking during desorption. All hysteresis loops close at the cavitation-induced pressure of  $P/P_0 = 0.45$  and are larger compared to spray drying LFP nanoparticles, [84] this indicates larger interconnectivity between the pores and a more ordered material. [92]

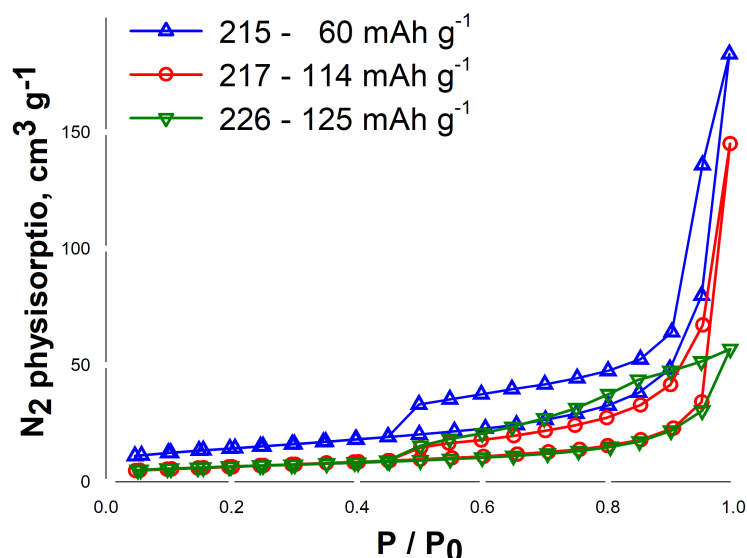


Figure 6.34 Type IV(a) isotherms, glucose arranges the material in plate-like particles (blue and red) while cellulose and lignin create a bottle-neck network (green).

The BJH pore volume size distribution  $dV(d)$  can be divided in two regions: from a reference material, LFP has two sharp peaks around 2 nm to 3 nm and 4 nm to 5 nm, and one broad between 5 nm to 200 nm. The first two peaks belong to a morphological LFP's property and the milling conditions. The broad one represents the spray drying conditions and is a function of the drying temperature. [84] By introducing US milling and changing the carbon precursor we also induced a morphological modification in the meso- and macropore region (Figure 6.35). Milling the precursors for 9 h with glucose and low amplitude US, yields mainly LFP with Fe nanocrystals (sample 215 - blue), the SSA and pore volume are significantly higher than the average ( $51\ \text{m}^2\ \text{g}^{-1}$  vs.  $28\ \text{m}^2\ \text{g}^{-1}$ , Table BET) because of the presence of the Fe nanocrystals, this leads to a poor EC capacity in the coin-cell battery ( $60\ \text{mA h g}^{-1}$ ). Also the  $dV(d)$  deviates from the LFP reference pattern in both regions. Reducing the

milling time to 3 h while increasing the amplitude (sample 217 - red) prevents the previous phenomena, yielding LFP (from XRD). However the  $dV(d)$  shows multiple peaks in the narrow mesopore region, deviating from the reference pattern. This indicates a different agglomeration mechanism or the presence of impurities, at levels undetectable on XRD, that alter the LFP crystal morphology. Removing US requires to double the milling time (sample 228 - black), it yields again LFP (XRD) but the first peak on the BJH plot is broad. Milling the precursors with cellulose requires 6 h and high amplitude (sample 226 - green), but forms pure LFP and also the  $dV(d)$  peaks are sharp and correspond to the reference material. This powder expressed the highest EC capacity and the smallest pore volume ( $0.09 \text{ cm}^3 \text{ g}^{-1}$ ), suitable for storing high energy volume densities.

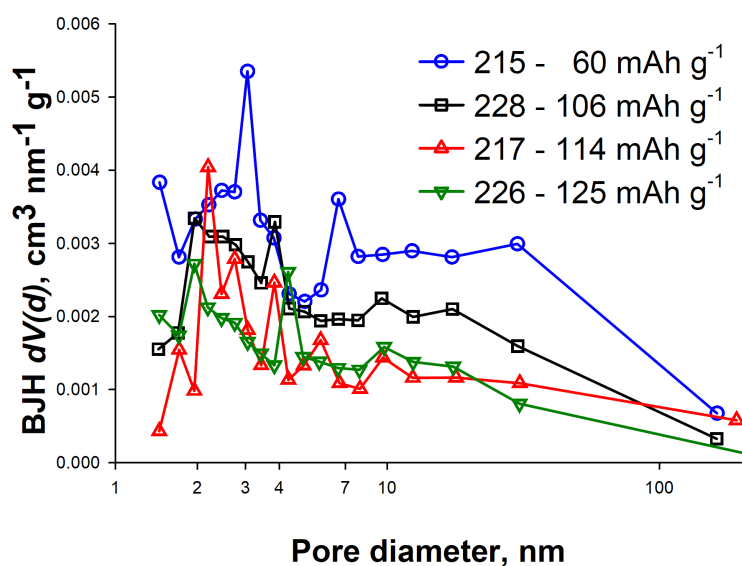


Figure 6.35 Pore size distribution: when the material has two sharp peaks around 2 nm and 4 nm, it exhibits higher EC performances.

A contour plot defines the impact of US and milling time (Figure 6.36): 3 h milling without US creates a small pore volume, but the material is not completely synthesized and contains small impurities ( $\text{Li}_3\text{PO}_4$ , by XRD). Milling for 9 h contributes in reducing the size of the pores but creates Fe impurity and lowers drastically the EC of the battery. An optimum of 6 h and 70 % amplitude yielded small porosity, LFP material and high EC capacity (sample 226).



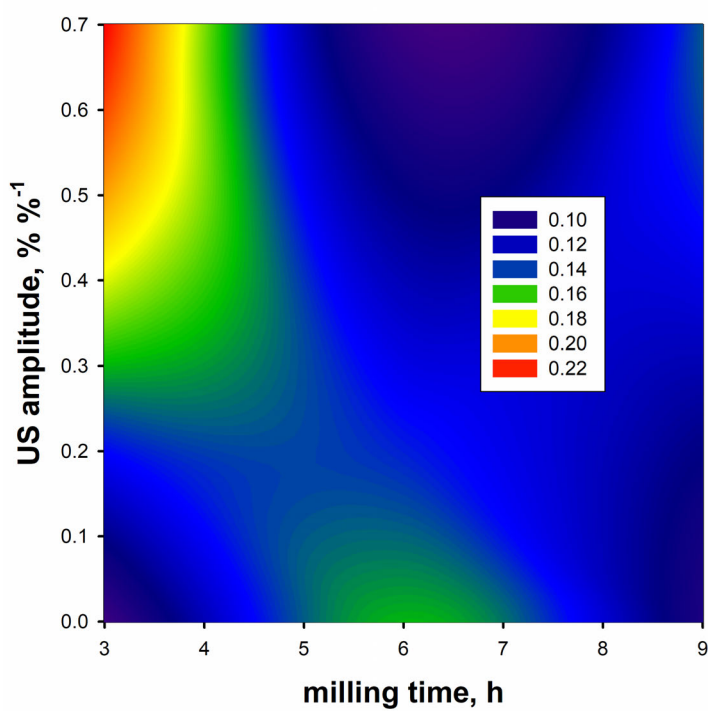


Figure 6.36 Pore volume contour plot: the aberrant data (sample 215) has been excluded.

## CHAPTER 7 CONCLUSION

### 7.1 Summary of work

All spray drying conditions creates semi-spherical doughnut-shaped secondary particles. A two-parameter skew normal distribution fits the experimental PSD better than the log-normal and the Weibull distribution, with a skew value of 1.8 ( $R^2 > 98\%$ ). The nozzle  $n_2$  yields the best (liquid bore  $508\ \mu\text{m}$ ), atomizing the feed material into ultimately a fine narrow powder (mode  $6 \pm 3\ \mu\text{m}$ ), but LFP suspension clogs more frequently this small bore nozzle. Nozzle  $n_4$  does not clog (liquid bore  $1530\ \mu\text{m}$ ) and creates larger particles with a wider distribution (mode  $9 \pm 4\ \mu\text{m}$ ). The distribution's standard deviation is linearly proportional (40%) with respect to the PSD mode. High temperature and atomization velocity ( $200\ ^\circ\text{C}$ ,  $>250\ \text{m s}^{-1}$ ) increase the yield ( $>70\%$ ). Higher solid content in the slurry increases the final bulk density of the powder, up to  $750\ \text{kg m}^{-3}$  at 60% loading. But fine material (mode  $<16\ \mu\text{m}$ ), have poor flowability (Hausner ratio 1.5). Spray dried sample porosity is distributed mainly in the macroporous region, in particular the pore mode diameter has the same order of magnitude as the primary particle. The surface area derived from the PSD (assuming spherical particles) is proportional and within 80% with respect to the BET surface area, indicating that melt-synthesized LFP is non-porous. The secondary particles however, possess a mesoporous structure that increases in volume by 10% when the drying temperature is increased from  $100\ ^\circ\text{C}$  to  $200\ ^\circ\text{C}$ . This suggests that slower drying rates (at lower temperatures) form a more compact material. Operating at  $200\ ^\circ\text{C}$  maximizes the surface area ( $26.4\ \text{m}^2\ \text{g}^{-1}$ ). Also 20% smaller primary particle mode leads a gain of 55% more surface area.

Melt-synthesized LFP nanoparticles, spray dried and coated with a carbon-grid forming agent, outperforms most commercial  $\text{LiFePO}_4/\text{C}$  cathodes. We propose this synthetic route which is industrially scalable and produces pure LFP nanoparticles suspended in water. Spray drying yields  $7\ \text{kg h}^{-1}$  of mesoporous powder that promotes  $\text{Li}^+$  wettability and provides an homogeneous dispersion of the carbon precursors, even inside the secondary particles. We prove that the addition of high-MW PVA to lactose creates a carbon grid that interconnects the nanoparticles, the grid forms carbon-nanopores averaging  $1.5\ \text{nm}$  in diameter and contribute for 30% of the SSA. This in turn improves the cyclability and discharging performance of the battery at high C-rate. Colloidal silica is an excellent filling agent and could lead to an even more cyclable cathode when coupled with lactose and PVA, by reducing the mechanical stress between the nanoparticles. Ultrasonication proved detrimental when combined with organic precursors. However, changing the frequency of the instrument may

allow to better disperse the suspension without fragmenting the PVA chain.

## 7.2 Limitations

LiMnO<sub>2</sub> batteries manufacturers are researching on a flame pyrolysis approach, in which spray drying and oven pyrolysis are coupled in one unit operation. However, our GEA spray dryer has a temperature upper limit of 400 °C, making the pyrolysis step unfeasible at once (which requires 700 °C for 2 h).

Small dried particles are more appealing since they minimize pore occlusion. However economical solid-gas separation requires using a cyclone, limiting the secondary particle cut-off diameter to 2 μm.

Despite optimization, spray-dried LFP secondary particles possess a low bulk density due to blowholes and doughnut-shapes inside the particle. Scaling spray drying to a bigger tower and slowing down the evaporation rate may allow the liquid slurry droplet to coalesce in a spherical denser particle.

The lack of a scaled-up process for pyrolysis and electrochemical battery tests posed a limitation in the number of allowed tests we could perform and their significance. Pyrolysis was conducted in a 2 g batch tubular reactor, battery tests use few milligrams of active material each. Although the spray dried powder is fairly homogeneous and multiple sampling could not determine any significant differences in terms of particle size distribution, density and surface area; a proper scale up require processing more material during pyrolysis and electrochemical battery tests. The electrochemical tests were carried out using coin-cell batteries, which are very susceptible to slight imperfections in the active material and the operator technique of assembling. Puncturing the electrodes with more or less force, coating of the electrodes with the doctor blade and how the electrolyte covers and soaks in the assembled battery are all factors which are strongly connected to the operator handiness and produce different results during battery test. Cycling stability is also known to be dependent on the synthesis conditions, and pouch-cells batteries would demonstrate the material performance in more realistically conditions. In fact, there are several mechanisms related to capacity loss of coin-cells batteries over cycling, including loss of Li due to side reaction, dendrite formation, materials dissolution, acidic side reactions and losing active materials due to particle cracking. In order to conclude which ones are involved, further post-mortem characterization would be necessary. A pouch-cell tests more active material (grams) and is assembled in a machine, with a standardized procedure; pouch-cell are also one of the main standards in industry for cell-pack assembly.

The choice of carbon-precursors is limited to materials which will decompose before boiling: glycerol, diesel oil, Tween-20, vegetable oil (canola) have been tested but failed during pyrolysis. The resulting LFP is partially coated and oxidized and turned red, indicating the thermal decomposition of LFP to  $\text{Fe}_3^+$ . A pressurized pyrolysis vessel can resolve this issue and extend the research investigation to more materials.

### 7.3 Future Research

Commercial scalability should consider material buildup inside the drying chamber, because of two reasons: improper atomization conditions create big droplets that hit the wall before drying and partial nozzle clogging creates a jet of liquid in one direction that splash the wall. This detrimental situation lowers the yield, force more frequent maintenance shut-down, overoxidizes and sinters LFP in chunks.

Nozzle clogging is a serious concern that can be avoided by maintaining the nozzle apparatus at room temperature. Thermal insulation avoids solid precipitation inside the nozzle line and grants more time-on-stream, without the need to stop spray drying and clean.

A single-phase pressure nozzle eliminates the need of compressed air (opex and capex) but requires a high performance pump and may introduce erosion and clogging problems in the nozzle, as the suspension is accelerated in the nozzle and not outside (like in the dual fluid nozzle).

An economic evaluation whether if a more efficient cyclone allows to reduce the PSD of the spray dried material compared to the compression costs to overcome the incremented pressure drop. And an overall comparison with a filter-bag system with periodic manual discharge and maintenance.

Recycling and sustainability are fundamental aspects to forecast when planning mass production goods. Our work has the potential to re-melt spent batteries into a functional material. However, it is missing a full investigation of recycling the LFP/C cathode from spent batteries, re-melting, and process sustainability.

Cycling stability is known to be dependent on the synthesis conditions, and pouch-cells batteries would demonstrate the material performance in more realistic conditions. In fact, there are several mechanisms related to capacity loss of LFP coin-cells over cycling, dendrite formation, materials dissolution, acidic side reactions and losing active materials due to particle cracking. In order to conclude which ones are involved, further post-mortem characterization would be necessary, including an investigation on the condition of the pyrolyzed PVA grid.

## REFERENCES

- [1] J. Molenda and M. Molenda, "Composite cathode material for Li-ion batteries based on  $\text{LiFePO}_4$  system," *Metal, Ceramic and Polymeric Composites for Various Uses*, 2011. [Online]. Available: <http://dx.doi.org/10.5772/21635>
- [2] R. Vehring, "Pharmaceutical particle engineering via spray drying," *Pharmaceutical Research*, vol. 25, no. 5, pp. 999–1022, 2008. [Online]. Available: <http://www.ncbi.nlm.nih.gov/pmc/articles/PMC2292490/>
- [3] E. Lintingre, F. Lequeux, L. Talini, and N. Tsapis, "Control of particle morphology in the spray drying of colloidal suspensions," *Soft Matter*, vol. 12, pp. 7435–7444, 2016. [Online]. Available: <http://dx.doi.org/10.1039/C6SM01314G>
- [4] S. Poozesh and E. Bilgili, "Scale-up of pharmaceutical spray drying using scale-up rules: A review," *International Journal of Pharmaceutics*, vol. 562, pp. 271–292, 2019. [Online]. Available: <http://www.sciencedirect.com/science/article/pii/S0378517319302339>
- [5] J. W. Ivey and R. Vehring, "The use of modeling in spray drying of emulsions and suspensions accelerates formulation and process development," *Computers & Chemical Engineering*, vol. 34, no. 7, pp. 1036–1040, 2010, process Modeling and Control in Drug Development and Manufacturing. [Online]. Available: <http://www.sciencedirect.com/science/article/pii/S0098135410000748>
- [6] R. Mei, Y. Yang, X. Song, Z. An, and J. Zhang, "Triple carbon coated  $\text{LiFePO}_4$  composite with hierarchical conductive architecture as high-performance cathode for li-ion batteries," *Electrochimica Acta*, vol. 153, pp. 523–530, 2015. [Online]. Available: <http://www.sciencedirect.com/science/article/pii/S0013468614011335>
- [7] N. Saadatkah, M. G. Rigamonti, D. C. Boffito, H. Li, and G. S. Patience, "Spray dried  $\text{SiO}_2$   $\text{WO}_3/\text{TiO}_2$  and  $\text{SiO}_2$  vanadium pyrophosphate core-shell catalysts," *Powder Technology*, vol. 316, no. Supplement C, pp. 434–440, 2017. [Online]. Available: <http://www.sciencedirect.com/science/article/pii/S0032591016307501>
- [8] H. Khan, M. G. Rigamonti, G. S. Patience, and D. C. Boffito, "Spray dried  $\text{tio}_2/\text{wo}_3$  heterostructure for photocatalytic applications with residual activity in the dark," *Applied Catalysis B: Environmental*, vol. 226, pp. 311–323, 2018. [Online]. Available: <http://www.sciencedirect.com/science/article/pii/S0926337317311980>

- [9] G. S. Patience, *Experimental Methods and Instrumentation for Chemical Engineers*, 2nd ed. Amsterdam, Netherlands: Elsevier B.V., 2017.
- [10] D. Carnevali, M. G. Rigamonti, T. Tabanelli, G. S. Patience, and F. Cavani, "Levulinic acid upgrade to succinic acid with hydrogen peroxide," *Applied Catalysis A: General*, vol. 563, pp. 98–104, 2018. [Online]. Available: <http://www.sciencedirect.com/science/article/pii/S0926860X18303120>
- [11] M. G. Rigamonti and F. G. Gatti, "Stereoselective synthesis of hernandulcin, peroxy-lippidulcine a, lippidulcines a, b and c and taste evaluation," *Beilstein Journal of Organic Chemistry*, vol. 11, pp. 2117–2124, 2015.
- [12] A. Perianes-Rodriguez, L. Waltman, and N. J. van Eck, "Constructing bibliometric networks: A comparison between full and fractional counting," *Journal of Informetrics*, vol. 10, no. 4, pp. 1178–1195, 2016.
- [13] N. J. van Eck and L. Waltman, "Software survey: Vosviewer, a computer program for bibliometric mapping," *Scientometrics*, vol. 84, pp. 523–538, 2010.
- [14] M. Talebi-Esfandarani, S. Rousselot, M. Gauthier, P. Sauriol, G. Liang, and M. Dollé, "LiFePO<sub>4</sub> synthesized via melt synthesis using low-cost iron precursors," *Journal of Solid State Electrochemistry*, vol. 20, no. 7, pp. 1821–1829, 2016. [Online]. Available: <http://dx.doi.org/10.1007/s10008-015-3049-7>
- [15] H. Li, A. Ndjamo, P. Sauriol, and G. S. Patience, "Optimization of LiFePO<sub>4</sub> wet media milling and regressive population balance modeling," *Advanced Powder Technology*, vol. 28, no. 3, pp. 1000–1007, 2017. [Online]. Available: <http://www.sciencedirect.com/science/article/pii/S0921883117300055>
- [16] J. Liu, Z. Wang, G. Zhang, Y. Liu, and A. Yu, "Size-controlled synthesis of LiFePO<sub>4</sub>/C composites as cathode materials for lithium ion batteries," *Int. J. Electrochem. Sci.*, vol. 8, pp. 2378–2387, 2013.
- [17] J. Wang and X. Sun, "Olivine lifepo4: the remaining challenges for future energy storage," *Energy Environ. Sci.*, vol. 8, pp. 1110–1138, 2015. [Online]. Available: <http://dx.doi.org/10.1039/C4EE04016C>
- [18] R. Younesi, G. M. Veith, P. Johansson, K. Edstrom, and T. Vegge, "Lithium salts for advanced lithium batteries: Li-metal, li-O<sub>2</sub>, and li-s," *Energy Environ. Sci.*, vol. 8, pp. 1905–1922, 2015. [Online]. Available: <http://dx.doi.org/10.1039/C5EE01215E>

- [19] C. T. Love, A. Korovina, C. J. Patridge, K. E. Swider-Lyons, M. E. Twigg, and D. E. Ramaker, “Review of  $\text{LiFePO}_4$  phase transition mechanisms and new observations from x-ray absorption spectroscopy,” *Journal of The Electrochemical Society*, vol. 160, no. 5, pp. A3153–A3161, 2013. [Online]. Available: <http://jes.ecsdl.org/content/160/5/A3153.abstract>
- [20] R. Malik, A. Abdellahi, and G. Ceder, “A critical review of the li insertion mechanisms in  $\text{LiFePO}_4$  electrodes,” *Journal of The Electrochemical Society*, vol. 160, no. 5, pp. A3179–A3197, 2013. [Online]. Available: <http://jes.ecsdl.org/content/160/5/A3179.abstract>
- [21] J. Wang and X. Sun, “Olivine lifepo4: the remaining challenges for future energy storage,” *Energy Environ. Sci.*, vol. 8, pp. 1110–1138, 2015. [Online]. Available: <http://dx.doi.org/10.1039/C4EE04016C>
- [22] Z. P. Cano, D. Banham, S. Ye, A. Hintennach, J. Lu, M. Fowler, and Z. Chen, “Batteries and fuel cells for emerging electric vehicle markets,” *Nature Energy*, vol. 3, pp. 279–289, 2018. [Online]. Available: <https://doi.org/10.1038/s41560-018-0108-1>
- [23] J.-M. Tarascon and M. Armand, “Issues and challenges facing rechargeable lithium batteries,” *Nature*, vol. 414, p. 359, 2001. [Online]. Available: <https://doi.org/10.1038/35104644>
- [24] A. K. Padhi, K. S. Nanjundaswamy, C. Masquelier, S. Okada, and J. B. Goodenough, “Effect of structure on the  $\text{Fe}_3^+/\text{Fe}_2^+$  redox couple in iron phosphates,” *Journal of The Electrochemical Society*, vol. 144, no. 5, pp. 1609–1613, 1997. [Online]. Available: <http://jes.ecsdl.org/content/144/5/1609.abstract>
- [25] J. Li, J. K. Barillas, C. Guenther, and M. A. Danzer, “A comparative study of state of charge estimation algorithms for lifepo4 batteries used in electric vehicles,” *Journal of Power Sources*, vol. 230, pp. 244–250, 2013. [Online]. Available: <http://www.sciencedirect.com/science/article/pii/S0378775312019039>
- [26] J. B. Goodenough and M. H. Braga, “Batteries for electric road vehicles,” *Dalton Trans.*, vol. 47, pp. 645–648, 2018. [Online]. Available: <http://dx.doi.org/10.1039/C7DT03026F>
- [27] W. Yuan, Z. Yan, Z. Tan, W. Chen, and Y. Tang, “Heat-pipe-based thermal management and temperature characteristics of li-ion batteries,” *Canadian Journal*

- of Chemical Engineering*, vol. 94, no. 10, pp. 1901–1908, 2016. [Online]. Available: <http://dx.doi.org/10.1002/cjce.22566>
- [28] S. P. Ong, A. Jain, G. Hautier, B. Kang, and G. Ceder, “Thermal stabilities of delithiated olivine  $\text{MPO}_4$  ( $m = \text{Fe}, \text{Mn}$ ) cathodes investigated using first principles calculations,” *Electrochemistry Communications*, vol. 12, pp. 427–430, 2010.
- [29] F. Croce, A. D’Epifanio, J. Hassoun, A. Deptula, T. Olczac, and B. Scrosati, “A novel concept for the synthesis of an improved lifepo4 lithium battery cathode,” *Electrochemical and Solid-State Letters*, vol. 5, no. 3, pp. A47–A50, 2002. [Online]. Available: <http://esl.ecsdl.org/content/5/3/A47.abstract>
- [30] A. S. Arico, P. Bruce, B. Scrosati, J. M. Tarascon, and W. V. Schalkwijk, *Nat. Mater.*, vol. 4, p. 366, 2005.
- [31] Y. Wang, Y. Wang, E. Hosono, K. Wang, and H. Zhou, “The design of a lifepo4/carbon nanocomposite with a core-shell structure and its synthesis by an in situ polymerization restriction method,” *Angewandte Chemie International Edition*, vol. 47, no. 39, pp. 7461–7465. [Online]. Available: <https://onlinelibrary.wiley.com/doi/abs/10.1002/anie.200802539>
- [32] S.-Y. Chung, J. T. Bloking, and Y.-M. Chiang, “Electronically conductive phospho-olivines as lithium storage electrodes,” *Nature Materials*, vol. 1, p. 123, 2002. [Online]. Available: <https://doi.org/10.1038/nmat732>
- [33] A. Varzi, D. Bresser, J. von Zamory, F. Müller, and S. Passerini, “Znfe2o4-c/lifepo4-cnt: A novel high-power lithium-ion battery with excellent cycling performance,” *Advanced Energy Materials*, vol. 4, no. 10, p. 1400054. [Online]. Available: <https://onlinelibrary.wiley.com/doi/abs/10.1002/aenm.201400054>
- [34] J. Lu, Z. Chen, Z. Ma, F. Pan, L. A. Curtiss, and K. Amine, “The role of nanotechnology in the development of battery materials for electric vehicles,” *Nature Nanotechnology*, vol. 11, p. 1031, 2016. [Online]. Available: <http://dx.doi.org/10.1038/nnano.2016.207>
- [35] N. Saadatkah, S. Aghamiri, M. R. Talaie, and G. S. Patience, “Flame-assisted spray pyrolysis to size-controlled  $\text{Li}_y\text{Al}_x\text{Mn}_{2-x}\text{O}_4$ : a supervised machine learning approach,” *CrystEngComm*, vol. 20, pp. 7590–7601, 2018. [Online]. Available: <http://dx.doi.org/10.1039/C8CE01026A>



- [36] Q. Huang, J. Yang, C. B. Ng, C. Jia, and Q. Wang, “A redox flow lithium battery based on the redox targeting reactions between lifepo4 and iodide,” *Energy Environ. Sci.*, vol. 9, pp. 917–921, 2016. [Online]. Available: <http://dx.doi.org/10.1039/C5EE03764F>
- [37] W. Jiang, M. Wu, F. Liu, J. Yang, and T. Feng, “Variation of carbon coatings on the electrochemical performance of lifepo4 cathodes for lithium ionic batteries,” *RSC Adv.*, vol. 7, pp. 44 296–44 302, 2017. [Online]. Available: <http://dx.doi.org/10.1039/C7RA08062J>
- [38] L. Gauthier, M. Gauthier, D. Lavoie, C. Michot, and N. Ravet, “Process for preparing electroactive insertion compounds and electrode materials obtained therefrom,” May 19 2009, uS Patent 7,534,408. [Online]. Available: <https://www.google.com/patents/US7534408>
- [39] M. Talebi-Esfandarani, S. Rousselot, L. Jin, T. Bibienne, M. Gauthier, P. Chartrand, P. Sauriol, A. Seifitokaldani, G. Liang, and M. Dollé, “Melt synthesis of LiFePO<sub>4</sub>: Fundamentals, versatility and application,” *Meeting Abstracts*, vol. MA2016-02, no. 3, p. 503, 2016. [Online]. Available: <http://ma.ecsdl.org/content/MA2016-02/3/503.abstract>
- [40] P. G. Bruce, B. Scrosati, and J.-M. Tarascon, “Nanomaterials for rechargeable lithium batteries,” *Angew. Chem. Int.*, vol. 47, pp. 2930–2946, 2008.
- [41] T. E. Ashton, J. V. Laveda, D. A. MacLaren, P. J. Baker, A. Porch, M. O. Jones, and S. A. Corr, “Muon studies of Li<sup>+</sup> diffusion in lifepo4 nanoparticles of different polymorphs,” *J. Mater. Chem. A*, vol. 2, pp. 6238–6245, 2014. [Online]. Available: <http://dx.doi.org/10.1039/C4TA00543K>
- [42] Y. Zhou, J. Lu, C. Deng, H. Zhu, G. Z. Chen, S. Zhang, and X. Tian, “Nitrogen-doped graphene guided formation of monodisperse microspheres of lifepo4 nanoplates as the positive electrode material of lithium-ion batteries,” *J. Mater. Chem. A*, vol. 4, pp. 12 065–12 072, 2016. [Online]. Available: <http://dx.doi.org/10.1039/C6TA03440C>
- [43] Y. Zhang, L. Chen, J. Ou, J. Wang, B. Zheng, H. Yuan, Y. Guo, and D. Xiao, “Improving the performance of a lifepo4 cathode based on electrochemically cleaved graphite oxides with high hydrophilicity and good conductivity,” *J. Mater. Chem. A*, vol. 1, pp. 7933–7941, 2013. [Online]. Available: <http://dx.doi.org/10.1039/C3TA10736A>

- [44] J. Liu, T. E. Conry, X. Song, M. M. Doeff, and T. J. Richardson, "Nanoporous spherical  $\text{LiFePO}_4$  for high performance cathodes," *Energy Environ. Sci.*, vol. 4, pp. 885–888, 2011. [Online]. Available: <http://dx.doi.org/10.1039/C0EE00662A>
- [45] L. Spreutels, B. Haut, J. Chaouki, F. Bertrand, and R. Legros, "Conical spouted bed drying of baker's yeast: Experimentation and multi-modeling," *Food Research International*, vol. 62, pp. 137–150, 2014. [Online]. Available: <http://www.sciencedirect.com/science/article/pii/S0963996914001379>
- [46] L. Yu, D. Cai, H. Wang, and M.-M. Titirici, "Synthesis of microspherical lifepo4-carbon composites for lithium-ion batteries," *Nanomaterials*, vol. 3, no. 3, pp. 443–452, 2013. [Online]. Available: <http://www.mdpi.com/2079-4991/3/3/443>
- [47] A.-M. Demers, R. Gosselin, J.-S. Simard, and N. Abatzoglou, "In-line near infrared spectroscopy monitoring of pharmaceutical powder moisture in a fluidised bed dryer: An efficient methodology for chemometric model development," *The Canadian Journal of Chemical Engineering*, vol. 90, no. 2, pp. 299–303, 2012. [Online]. Available: <http://dx.doi.org/10.1002/cjce.20691>
- [48] J. Chaouki, "Catalytic drying of digested sludge," *International Journal of Chemical Reactor Engineering*, vol. 2, pp. 1–13, 2004. [Online]. Available: <https://doi.org/10.2202/1542-6580.1088>
- [49] J. Aluha, P. Boahene, A. Dalai, Y. Hu, K. Bere, N. Braidy, and N. Abatzoglou, "Synthesis and characterization of co/c and fe/c nanocatalysts for fischer-tropsch synthesis: A comparative study using a fixed-bed reactor," *Industrial & Engineering Chemistry Research*, vol. 54, no. 43, pp. 10 661–10 674, 2015. [Online]. Available: <http://dx.doi.org/10.1021/acs.iecr.5b03003>
- [50] D. Bresser, D. Buchholz, A. Moretti, A. Varzi, and S. Passerini, "Alternative binders for sustainable electrochemical energy storage – the transition to aqueous electrode processing and bio-derived polymers," *Energy Environ. Sci.*, vol. 11, pp. 3096–3127, 2018. [Online]. Available: <http://dx.doi.org/10.1039/C8EE00640G>
- [51] M. Gauthier, M. K. Domroese, J. A. Hoffman, D. D. Lindeman, J. R. G. Noel, V. E. Radewald, J. Rouillard, R. Rouillard, T. Shiota, and J. L. Trice, "In-situ short circuit protection system and method for high-energy electrochemical cells," US6099986, 1997.
- [52] M. Gauthier, M. Armand, K. Zaghib, S. Poirier, and R. Bellemare, "Alloyed and dense anode sheet with local stress relaxation," US6265099, 2001.

- [53] Y.-J. Lv, Y.-F. Long, J. Su, X.-Y. Lv, and Y.-X. Wen, "Synthesis of bowl-like mesoporous  $\text{LiFePO}_4/\text{C}$  composites as cathode materials for lithium ion batteries," *Electrochimica Acta*, vol. 119, pp. 155–163, 2014. [Online]. Available: <http://www.sciencedirect.com/science/article/pii/S0013468613024857>
- [54] Y.-J. Lv, J. Su, Y.-F. Long, X.-Y. Lv, and Y.-X. Wen, "Effect of milling time on the performance of bowl-like  $\text{LiFePO}_4/\text{c}$  prepared by wet milling-assisted spray drying," *Ionics*, vol. 20, no. 4, pp. 471–478, 2014. [Online]. Available: <http://dx.doi.org/10.1007/s11581-013-1002-2>
- [55] F. Yu, J. Zhang, Y. Yang, and G. Song, "Porous micro-spherical aggregates of  $\text{LiFePO}_4/\text{c}$  nanocomposites: A novel and simple template-free concept and synthesis via sol-gel-spray drying method," *Journal of Power Sources*, vol. 195, no. 19, pp. 6873–6878, 2010. [Online]. Available: <http://www.sciencedirect.com/science/article/pii/S0378775310000984>
- [56] F. Yu, J.-J. Zhang, Y.-F. Yang, and G.-Z. Song, "Up-scalable synthesis, structure and charge storage properties of porous microspheres of  $\text{LiFePO}_4/\text{c}$  nanocomposites," *J. Mater. Chem.*, vol. 19, pp. 9121–9125, 2009. [Online]. Available: <http://dx.doi.org/10.1039/B916938E>
- [57] V. Naglieri, D. Gutknecht, V. Garnier, P. Palmero, J. Chevalier, and L. Montanaro, "Optimized slurries for spray drying: Different approaches to obtain homogeneous and deformable alumina-zirconia granules," *Materials*, vol. 6, no. 11, pp. 5382–5397, 2013. [Online]. Available: <http://www.mdpi.com/1996-1944/6/11/5382>
- [58] J.-K. Kim, "Supercritical synthesis in combination with a spray process for 3d porous microsphere lithium iron phosphate," *CrystEngComm*, vol. 16, pp. 2818–2822, 2014. [Online]. Available: <http://dx.doi.org/10.1039/C3CE42264J>
- [59] M. Y. Son, J.-K. Lee, and Y. C. Kang, "Fabrication and electrochemical performance of  $0.6\text{Li}_2\text{MnO}_3\text{-}0.4\text{Li}(\text{Ni}_{1/3}\text{Co}_{1/3}\text{Mn}_{1/3})\text{O}_2$  microspheres by two-step spray-drying process," *Scientific Reports*, vol. 4, p. 5752, 2014. [Online]. Available: <http://dx.doi.org/10.1038/srep05752>
- [60] J.-F. Zhang, C. Shen, B. Zhang, J.-C. Zheng, C.-L. Peng, X.-W. Wang, X.-B. Yuan, H. Li, and G.-M. Chen, "Synthesis and performances of  $2\text{LiFePO}_4\text{Li}_3\text{V}_2(\text{PO}_4)_3/\text{C}$  cathode materials via spray drying method with double carbon sources," *Journal of Power Sources*, vol. 267, pp. 227–234, 2014. [Online]. Available: <http://www.sciencedirect.com/science/article/pii/S0378775314006636>

- [61] A. Feng, M. Boraey, M. Gwin, P. Finlay, P. Kuehl, and R. Vehring, "Mechanistic models facilitate efficient development of leucine containing microparticles for pulmonary drug delivery," *International Journal of Pharmaceutics*, vol. 409, no. 1–2, pp. 156–163, 2011. [Online]. Available: <http://www.sciencedirect.com/science/article/pii/S0378517311001840>
- [62] G. S. Patience and R. E. Bockrath, "Butane oxidation process development in a circulating fluidized bed," *Applied Catalysis A: General*, vol. 376, no. 1–2, pp. 4–12, 2010. [Online]. Available: <http://www.sciencedirect.com/science/article/pii/S0926860X09007327>
- [63] j. v. marco gil and filipe gaspar, *Chemistry Today*, vol. 28, pp. 18–22, 2010.
- [64] J. Berman and P. Page, *Drug Development and Industrial Pharmacy*, vol. 20, pp. 731–755, 1994.
- [65] P. Thybo and S. Andersen, *Pharmaceutical Research*, vol. 25, pp. 1610–1620, 2008.
- [66] D. Dobry and R. Beyerink, *J Pharm Innov.*, vol. 4, pp. 113–142, 2009.
- [67] K. Masters, "Scale-up of spray dryers," *Drying Technology*, vol. 12, no. 1-2, pp. 235–257, 1994. [Online]. Available: <https://doi.org/10.1080/07373939408959955>
- [68] A. Al-Khattawi, A. Bayly, A. Phillips, and D. Wilson, "The design and scale-up of spray dried particle delivery systems," *Expert Opinion on Drug Delivery*, vol. 15, no. 1, pp. 47–63, 2018, PMID: 28423954. [Online]. Available: <https://doi.org/10.1080/17425247.2017.1321634>
- [69] G. D. Park, J. H. Kim, Y. J. Choi, and Y. C. Kang, "Large-scale production of MoO<sub>3</sub>-reduced graphene oxide powders with superior lithium storage properties by spray-drying process," *Electrochimica Acta*, vol. 173, pp. 581–587, 2015. [Online]. Available: <http://www.sciencedirect.com/science/article/pii/S001346861501213X>
- [70] L.-H. Hu, F.-Y. Wu, C.-T. Lin, A. N. Khlobystov, and L.-J. Li, "Graphene-modified LiFePO<sub>4</sub> cathode for lithium ion battery beyond theoretical capacity," *Nature Communications*, vol. 4, p. 1687, 2013. [Online]. Available: <http://dx.doi.org/10.1038/ncomms2705>
- [71] X. Zhou, F. Wang, Y. Zhu, and Z. Liu, "Graphene modified LiFePO<sub>4</sub> cathode materials for high power lithium ion batteries," *J. Mater. Chem.*, vol. 21, pp. 3353–3358, 2011. [Online]. Available: <http://dx.doi.org/10.1039/C0JM03287E>

- [72] F. Gao, Z. Tang, and J. Xue, "Preparation and characterization of nanoparticle  $\text{LiFePO}_4$  and  $\text{LiFePO}_4/\text{c}$  by spray-drying and post-annealing method," *Electrochimica Acta*, vol. 53, no. 4, pp. 1939–1944, 2007. [Online]. Available: <http://www.sciencedirect.com/science/article/pii/S0013468607010730>
- [73] R. Vehring, W. R. Foss, and D. Lechuga-Ballesteros, "Particle formation in spray drying," *Journal of Aerosol Science*, vol. 38, no. 7, pp. 728–746, 2007. [Online]. Available: <http://www.sciencedirect.com/science/article/pii/S0021850207000699>
- [74] X. Huang, Y. You, Y. Ren, H. Wang, Y. Chen, X. Ding, B. Liu, S. Zhou, and F. Chu, "Spray drying-assisted synthesis of hollow spherical  $\text{Li}_2\text{FeSiO}_4/\text{c}$  particles with high performance for li-ion batteries," *Solid State Ionics*, vol. 278, pp. 203–208, 2015. [Online]. Available: <http://www.sciencedirect.com/science/article/pii/S0167273815002544>
- [75] N. D. Trinh, D. Lepage, D. Aymé-Perrot, A. Badia, M. Dollé, and D. Rochefort, "An artificial lithium protective layer that enables the use of acetonitrile-based electrolytes in lithium metal batteries," *Angewandte Chemie International Edition*, vol. 57, no. 18, pp. 5072–5075, 2018. [Online]. Available: <https://onlinelibrary.wiley.com/doi/abs/10.1002/anie.201801737>
- [76] W.-J. Zhang, "Structure and performance of lifepo4 cathode materials: A review," *Journal of Power Sources*, vol. 196, no. 6, pp. 2962–2970, 2011. [Online]. Available: <http://www.sciencedirect.com/science/article/pii/S037877531002104X>
- [77] J. Wang and X. Sun, "Understanding and recent development of carbon coating on lifepo4 cathode materials for lithium-ion batteries," *Energy Environ. Sci.*, vol. 5, pp. 5163–5185, 2012. [Online]. Available: <http://dx.doi.org/10.1039/C1EE01263K>
- [78] X. Zhi, G. Liang, L. Wang, X. Ou, J. Zhang, and J. Cui, "The cycling performance of  $\text{LiFePO}_4/\text{c}$  cathode materials," *Journal of Power Sources*, vol. 189, no. 1, pp. 779–782, 2009, selected Papers presented at the 14th INTERNATIONAL MEETING ON LITHIUM BATTERIES (IMLB-2008). [Online]. Available: <http://www.sciencedirect.com/science/article/pii/S0378775308015723>
- [79] M. V. Chaubal and C. Popescu, "Conversion of nanosuspensions into dry powders by spray drying: A case study," *Pharmaceutical Research*, vol. 25, no. 10, pp. 2302–2308, 2008. [Online]. Available: <http://dx.doi.org/10.1007/s11095-008-9625-0>

- [80] D. L. Anderson, “An evaluation of current and future costs for lithium-ion batteries for use in electrified vehicle powertrains,” 2009.
- [81] M. Singh, J. Kaiser, and H. Hahn, “Thick electrodes for high energy lithium ion batteries,” *Journal of The Electrochemical Society*, vol. 162, no. 7, pp. A1196–A1201, 2015. [Online]. Available: <http://jes.ecsdl.org/content/162/7/A1196.abstract>
- [82] G. Nasr, A. Yule, and L. Bendig, *Industrial Sprays and Atomization*. Springer, 2002. [Online]. Available: <http://dx.doi.org/10.1007/978-1-4471-3816-7>
- [83] F. J. Petersen, O. Wørts, T. Schæfer, and P. E. Sojka, “Design and atomization properties for an inside-out type effervescent atomizer,” *Drug Development and Industrial Pharmacy*, vol. 30, no. 3, pp. 319–326, 2004, pMID: 15109031. [Online]. Available: <http://dx.doi.org/10.1081/DDC-120030427>
- [84] M. G. Rigamonti, Y.-X. Song, H. Li, N. Saadatkah, P. Sauriol, and G. S. Patience, “Influence of atomization conditions on spray drying lithium iron phosphate nanoparticle suspensions,” *The Canadian Journal of Chemical Engineering*, vol. 0, pp. 0–0, 2017. [Online]. Available: <http://dx.doi.org/10.1002/cjce.23106>
- [85] S. Ferreira, C. R. Malacrida, and V. R. N. Telis, “Influence of emulsification methods and use of colloidal silicon dioxide on the microencapsulation by spray drying of turmeric oleoresin in gelatin-starch matrices,” *Canadian Journal of Chemical Engineering*, vol. 94, no. 11, pp. 2210–2218, 2016. [Online]. Available: <http://dx.doi.org/10.1002/cjce.22596>
- [86] H. Li, M. Rostamizadeh, K. Mameri, D. C. Boffito, N. Saadatkah, M. G. Rigamonti, and G. S. Patience, “Ultrasound assisted wet stirred media mill of high concentration  $\text{LiFePO}_4$  and catalysts,” *The Canadian Journal of Chemical Engineering*, 2018. [Online]. Available: <http://dx.doi.org/10.1002/cjce.23212>
- [87] N. Abatzoglou, R. Gosselin, and M. A. Inam, “Rheological characterisation and phenomenological modelling of non-aqueous nano-suspensions of iron carbide produced by plasma spray,” *The Canadian Journal of Chemical Engineering*, vol. 92, no. 1, pp. 68–74, 2014. [Online]. Available: <http://dx.doi.org/10.1002/cjce.21859>
- [88] M. J. D. Mahboub, S. Lotfi, G. S. Patience, and J.-L. Dubois, “Gas phase oxidation of 2-methyl 1,3 propanediol to methacrylic acid over heteropolyacid catalysts,” *Catalysis Science and Technology*, vol. 6, no. 17, pp. 6525–6535, 2016.

- [89] W. Kasprzak, D. Li, G. S. Patience, P. Sauriol, H. Villazon-Amaris, M. Dolle, M. Gauthier, S. Rousselot, M. Talebi-Esfandarani, T. Bibienne, X. Sun, Y. Liu, and G. Liang, "Using induction melting to make lithium-ion battery material," *Advanced Materials & Processes*, vol. 175, no. 8, pp. 16–22, 2017.
- [90] H. Villazon, P. Sauriol, S. Rousselot, M. Talebi-Esfandarani, T. Bibienne, M. Gauthier, G. Liang, M. Dollé, and P. Chartrand, "Melt-synthesis of  $\text{LiFePO}_4$  over a metallic bath," *The Canadian Journal of Chemical Engineering*, vol. 0. [Online]. Available: <https://onlinelibrary.wiley.com/doi/abs/10.1002/cjce.23406>
- [91] D. Li, W. Kasprzak, G. S. Patience, P. Sauriol, H. Villazón-Amarís, M. Dollé, M. Gauthier, S. Rousselot, M. Talebi-Esfandarani, T. Bibienne, X. Sun, Y. Liu, and G. Liang, "Production of lithium-ion cathode material for automotive batteries using melting casting process," in *9th International Symposium on High-Temperature Metallurgical Processing*, J.-Y. Hwang, T. Jiang, M. W. Kennedy, D. Gregurek, S. Wang, B. Zhao, O. Yücel, E. Keskinilic, J. P. Downey, Z. Peng, and R. Padilla, Eds. Cham: Springer International Publishing, 2018, pp. 135–146.
- [92] R. G. Kaldenhoven and J. M. Hill, "Determining the pore structure of activated carbon by nitrogen gas adsorption," in *Catalysis: Volume 30*. The Royal Society of Chemistry, 2018, vol. 30, pp. 41–63. [Online]. Available: <http://dx.doi.org/10.1039/9781788013048-00041>
- [93] D. C. Boffito, S. Mansi, J.-M. Leveque, C. Pirola, C. L. Bianchi, and G. S. Patience, "Ultrafast biodiesel production using ultrasound in batch and continuous reactors," *ACS Sustainable Chemistry & Engineering*, vol. 1, no. 11, pp. 1432–1439, 2013. [Online]. Available: <https://doi.org/10.1021/sc400161s>
- [94] F. Renard, *International conference on olivine for rechargeable batteries, OREBA 1.0, Montreal, 25–28 May, 2014*.
- [95] L.-H. Hu, F.-Y. Wu, C.-T. Lin, A. N. Khlobystov, and L. J. Li, "Graphene-modified  $\text{LiFePO}_4$  cathode for lithium ion battery beyond theoretical capacity," *Nature Communications*, vol. 4, p. 1687, 2013.
- [96] B. Yan, X. Li, Z. Bai, Y. Zhao, L. Dong, X. Song, D. Li, C. Langford, and X. Sun, "Crumpled reduced graphene oxide conformally encapsulated hollow  $\text{V}_2\text{O}_5$  nano/microsphere achieving brilliant lithium storage performance," *Nano Energy*, vol. 24, pp. 32–44, 2016. [Online]. Available: <http://www.sciencedirect.com/science/article/pii/S2211285516300507>

- [97] B. Wu, Y. Ren, and N. Li, *LiFePO<sub>4</sub> cathode material, electric vehicles and the benefits and barriers*. Dr. Seref Soylu (Ed.) InTech, 2011. [Online]. Available: [www.intechopen.com](http://www.intechopen.com)
- [98] B. Starke, S. Seidlmayer, S. Jankowsky, O. Dolotko, R. Gilles, and K.-H. Pettinger, “Influence of particle morphologies of LiFePO<sub>4</sub> on water- and solvent-based processing and electrochemical properties,” *Sustainability*, vol. 9, no. 6, p. 888, 2017. [Online]. Available: <http://www.mdpi.com/2071-1050/9/6/888>
- [99] I. C. Kemp, “Progress in dryer selection techniques,” *Drying Technology*, vol. 17, no. 7-8, pp. 1667–1680, 1999. [Online]. Available: <http://dx.doi.org/10.1080/07373939908917644>
- [100] G. Hasegawa, *Studies on Porous Monolithic Materials Prepared via Sol-Gel Processes*, 1st ed., ser. Springer Theses. Springer Tokyo, 2013.
- [101] J.-H. Lee, J.-S. Kim, Y. C. Kim, D. S. Zang, and U. Paik, “Dispersion properties of aqueous-based LiFePO<sub>4</sub> pastes and their electrochemical performance for lithium batteries,” *Ultramicroscopy*, vol. 108, pp. 1256–1259, 2008.
- [102] M. R. R. Niño and J. M. R. Patino, “Surface tension of bovine serum albumin and tween 20 at the air-aqueous interface,” *Journal of the American Oil Chemists’ Society*, vol. 75, no. 10, p. 1241, 1998. [Online]. Available: <http://dx.doi.org/10.1007/s11746-998-0169-6>
- [103] T. Okubo, “Surface tension of structured colloidal suspensions of polystyrene and silica spheres at the air-water interface,” *Journal of Colloid and Interface Science*, vol. 171, no. 1, pp. 55–62, 1995. [Online]. Available: <http://www.sciencedirect.com/science/article/pii/S0021979785711502>
- [104] Ş. Volkan, S. Özen, S. Pat, and Ş. Korkmaz, “Optical and surface properties of LiFePO<sub>4</sub> thin films prepared by rf magnetron sputtering,” *The European Physical Journal D*, vol. 69, no. 3, p. 76, 2015. [Online]. Available: <http://dx.doi.org/10.1140/epjd/e2015-50847-7>
- [105] V. Gelinas and D. Vidal, “Determination of particle shape distribution of clay using an automated {AFM} image analysis method,” *Powder Technology*, vol. 203, no. 2, pp. 254–264, 2010. [Online]. Available: <http://www.sciencedirect.com/science/article/pii/S0032591010002652>
- [106] C. Orr and J. Dallavalle, *Fine Particle Measurement*, no. 42, 51, 64, 79, 1959.



- [107] F. Iskandar, L. Gradon, and K. Okuyama, "Control of the morphology of nanostructured particles prepared by the spray drying of a nanoparticle sol," *Journal of Colloid and Interface Science*, vol. 265, no. 2, pp. 296–303, 2003. [Online]. Available: <http://www.sciencedirect.com/science/article/pii/S0021979703005198>
- [108] W. J. J. Walker, J. S. Reed, and S. K. Verma, "Influence of slurry parameters on the characteristics of spray-dried granules," *Journal of the American Ceramic Society*, vol. 82, no. 7, pp. 1711–1719, 1999. [Online]. Available: <http://dx.doi.org/10.1111/j.1151-2916.1999.tb01990.x>
- [109] K. Higashitani, H. Yoshida, and H. Masuda, *Powder Technology: Fundamentals of Particles, Powder Beds, and Particle Generation*. CRC Press, 2006.
- [110] N. Ashgriz, *Handbook of Atomization and Sprays*, 2011.
- [111] A. U. Vanarase, J. G. Osorio, and F. J. Muzzio, "Effects of powder flow properties and shear environment on the performance of continuous mixing of pharmaceutical powders," *Powder Technology*, vol. 246, pp. 63–72, 2013. [Online]. Available: <http://www.sciencedirect.com/science/article/pii/S0032591013003471>
- [112] R. Grey and J. Beddow, "On the hausner ratio and its relationship to some properties of metal powders," *Powder Technology*, vol. 2, pp. 323–326, 1969.
- [113] K. S. W. Sing, D. H. Everett, R. A. W. Haul, L. Moscou, R. A. Pierotti, J. Roquerol, and T. Siemieniewska, *Pure Appl. Chem.*, vol. 57, p. 603, 1985.
- [114] Q. Instruments, *Gas sorption system operating manual*. Quantachrome Instruments, 2015.
- [115] M. J. D. Mahboub, M. Rostamizadeh, J.-L. Dubois, and G. S. Patience, "Partial oxidation of 2-methyl-1,3-propanediol to methacrylic acid: Experimental and neural network modeling," *RSC Advance*, vol. 6, no. 115, pp. 114 123–114 134, 2016.
- [116] Z. Caban-Huertas, O. Ayyad, D. P. Dubal, and P. Gomez-Romero, "Aqueous synthesis of  $\text{LiFePO}_4$  with fractal granularity," *Scientific Reports*, vol. 6, p. 27024, 2016. [Online]. Available: <http://dx.doi.org/10.1038/srep27024>
- [117] C. L. Bianchi, C. Pirola, F. Galli, M. Stucchi, S. Morandi, G. Cerrato, and V. Capucci, "Nano and micro-tio2 for the photodegradation of ethanol: experimental data and kinetic modelling," *RSC Adv.*, vol. 5, pp. 53 419–53 425, 2015. [Online]. Available: <http://dx.doi.org/10.1039/C5RA05385D>

- [118] N. Ravet, M. Gauthier, K. Zaghbi, J. Goodenough, A. Mauger, F. Gendron, and C. Julien, "Mechanism of the  $\text{Fe}^{3+}$  reduction at low temperature for  $\text{LiFePO}_4$  synthesis from a polymeric additive," *Chemistry of Materials*, vol. 19, no. 10, pp. 2595–2602, 2007. [Online]. Available: <http://dx.doi.org/10.1021/cm070485r>
- [119] W. Ma, H. Li, W. Jiang, H. Bai, H. Qu, and L. Lu, "Characterization for  $\text{Li}_3\text{PO}_4$  catalysts toward elucidation of crystalline form and performance relationship," *Canadian Journal of Chemical Engineering*, vol. 93, no. 5, pp. 849–854, 2015. [Online]. Available: <http://dx.doi.org/10.1002/cjce.22176>
- [120] T. Satyavani, A. S. Kumar, and P. S. Rao, "Methods of synthesis and performance improvement of lithium iron phosphate for high rate li-ion batteries: A review," *Engineering Science and Technology, an International Journal*, vol. 19, no. 1, pp. 178–188, 2016. [Online]. Available: <http://www.sciencedirect.com/science/article/pii/S2215098615001020>
- [121] N. I. P. Ayu, E. Kartini, L. D. Prayogi, M. Faisal, and Supardi, "Crystal structure analysis of  $\text{Li}_3\text{PO}_4$  powder prepared by wet chemical reaction and solid-state reaction by using x-ray diffraction (xrd)," *Ionics*, vol. 22, no. 7, pp. 1051–1057, Jul 2016. [Online]. Available: <https://doi.org/10.1007/s11581-016-1643-z>
- [122] M. Thommes, K. Kaneko, A. V. Neimark, J. P. Olivier, F. Rodriguez-Reinoso, J. Rouquerol, and K. S. Sing, "Physisorption of gases, with special reference to the evaluation of surface area and pore size distribution (iupac technical report)," *Pure and Applied Chemistry*, vol. 87, pp. 1051–1069, 2015.
- [123] D. Carnevali, O. Guévremont, M. G. Rigamonti, M. Stucchi, F. Cavani, and G. S. Patience, "Gas-phase fructose conversion to furfural in a microfluidized bed reactor," *ACS Sustainable Chemistry & Engineering*, vol. 6, no. 4, pp. 5580–5587, 2018. [Online]. Available: <https://doi.org/10.1021/acssuschemeng.8b00510>
- [124] M. Trudeau, D. Laul, R. Veillette, A. Serventi, A. Mauger, C. Julien, and K. Zaghbi, "In situ high-resolution transmission electron microscopy synthesis observation of nanostructured carbon coated  $\text{LiFePO}_4$ ," *Journal of Power Sources*, vol. 196, no. 18, pp. 7383–7394, 2011. [Online]. Available: <http://www.sciencedirect.com/science/article/pii/S0378775311007889>
- [125] W. Cheung, F. Pontoriero, O. Taratula, A. M. Chen, and H. He, "Dna and carbon nanotubes as medicine," *Advanced Drug Delivery Reviews*, vol. 62, no. 6, pp. 633–649, 2010, from Biology to Materials: Engineering DNA

- and RNA for Drug Delivery and Nanomedicine. [Online]. Available: <http://www.sciencedirect.com/science/article/pii/S0169409X10000761>
- [126] A. C. Torres-Dias, T. F. Cerqueira, W. Cui, M. A. Marques, S. Botti, D. Machon, M. A. Hartmann, Y. Sun, D. J. Dunstan, and A. San-Miguel, "From mesoscale to nanoscale mechanics in single-wall carbon nanotubes," *Carbon*, vol. 123, pp. 145–150, 2017. [Online]. Available: <http://www.sciencedirect.com/science/article/pii/S0008622317307194>
- [127] X. Zhang, Z. Bi, W. He, G. Yang, H. Liu, and Y. Yue, "Fabricating high-energy quantum dots in ultra-thin  $\text{LiFePO}_4$  nanosheets using a multifunctional high-energy biomolecule-atp," *Energy Environ. Sci.*, vol. 7, pp. 2285–2294, 2014. [Online]. Available: <http://dx.doi.org/10.1039/C3EE44187C>
- [128] W. H. Herschel and R. Bulkeley, "Konsistenzmessungen von gummi-benzollösungen," *Kolloid-Zeitschrift*, vol. 39, no. 4, pp. 291–300, 1926. [Online]. Available: <https://doi.org/10.1007/BF01432034>
- [129] A. R. Studart, E. Amstad, and L. J. Gauckler, "Colloidal stabilization of nanoparticles in concentrated suspensions," *Langmuir*, vol. 23, no. 3, pp. 1081–1090, 2007, pMID: 17241017. [Online]. Available: <https://doi.org/10.1021/la062042s>
- [130] L. Heymann, S. Peukert, and N. Aksel, "On the solid-liquid transition of concentrated suspensions in transient shear flow," *Rheologica Acta*, vol. 41, no. 4, pp. 307–315, Jan 2002. [Online]. Available: <https://doi.org/10.1007/s00397-002-0227-1>
- [131] R. Haj-Kacem, N. Ouerfelli, J. Herráez, M. Guettari, H. Hamda, and M. Dallel, "Contribution to modeling the viscosity arrhenius-type equation for some solvents by statistical correlations analysis," *Fluid Phase Equilibria*, vol. 383, pp. 11–20, 2014. [Online]. Available: <http://www.sciencedirect.com/science/article/pii/S037838121400538X>
- [132] A. Messaâdi, N. Dhouibi, H. Hamda, F. B. M. Belgacem, Y. H. Adbelkader, N. Ouerfelli, and A. H. Hamzaoui, "A new equation relating the viscosity arrhenius temperature and the activation energy for some newtonian classical solvents," *Journal of Chemistry*, vol. 2015, p. 12, 2015. [Online]. Available: <http://dx.doi.org/10.1155/2015/163262>
- [133] M. Mohsen-Nia and H. Modarress, "Viscometric study of aqueous poly(vinyl alcohol) (pva) solutions as a binder in adhesive formulations," *Journal of Adhesion*

- Science and Technology*, vol. 20, no. 12, pp. 1273–1280, 2006. [Online]. Available: <https://doi.org/10.1163/156856106778456636>
- [134] S. Mueller, E. W. Llewellyn, and H. M. Mader, “The rheology of suspensions of solid particles,” *Proceedings of the Royal Society of London A: Mathematical, Physical and Engineering Sciences*, vol. 466, no. 2116, pp. 1201–1228, 2010. [Online]. Available: <http://rspa.royalsocietypublishing.org/content/466/2116/1201>
- [135] I. M. Krieger, “Rheology of monodisperse latices,” *Advances in Colloid and Interface Science*, vol. 3, no. 2, pp. 111–136, 1972. [Online]. Available: <http://www.sciencedirect.com/science/article/pii/0001868672800010>
- [136] E. A. Taborda, C. A. Franco, S. H. Lopera, V. Alvarado, and F. B. Cortés, “Effect of nanoparticles/nanofluids on the rheology of heavy crude oil and its mobility on porous media at reservoir conditions,” *Fuel*, vol. 184, pp. 222–232, 2016. [Online]. Available: <http://www.sciencedirect.com/science/article/pii/S0016236116306081>
- [137] B. M. Budhlall, K. Landfester, E. D. Sudol, V. L. Dimonie, A. Klein, and M. S. El-Aasser, “Characterization of partially hydrolyzed poly(vinyl alcohol). effect of poly(vinyl alcohol) molecular architecture on aqueous phase conformation,” *Macromolecules*, vol. 36, no. 25, pp. 9477–9484, 2003. [Online]. Available: <https://doi.org/10.1021/ma030027d>
- [138] M. Stucchi, A. Elfiad, M. Rigamonti, H. Khan, and D. Boffito, “Water treatment: Mn-tio2 synthesized by ultrasound with increased aromatics adsorption,” *Ultrasonics Sonochemistry*, vol. 44, pp. 272–279, 2018. [Online]. Available: <http://www.sciencedirect.com/science/article/pii/S1350417718301251>
- [139] A. Akyüz, H. Catalgil-Giz, and A. T. Giz, “Kinetics of ultrasonic polymer degradation: Comparison of theoretical models with on-line data,” *Macromolecular Chemistry and Physics*, vol. 209, no. 8, pp. 801–809, 2008. [Online]. Available: <https://onlinelibrary.wiley.com/doi/abs/10.1002/macp.200700533>
- [140] D. C. Boffito, E. Martinez-Guerra, V. G. Gude, and G. S. Patience, *Conversion of Refined and Waste Oils by Ultrasound-Assisted Heterogeneous Catalysis*. Singapore: Springer Singapore, 2016, pp. 931–963. [Online]. Available: [https://doi.org/10.1007/978-981-287-278-4\\_12](https://doi.org/10.1007/978-981-287-278-4_12)
- [141] A. Grönroos, P. Pirkonen, J. Heikkinen, J. Ihalainen, H. Mursunen, and H. Sekki, “Ultrasonic depolymerization of aqueous polyvinyl alcohol,” *Ultrasonics*

- Sonochemistry*, vol. 8, no. 3, pp. 259–264, 2001. [Online]. Available: <http://www.sciencedirect.com/science/article/pii/S1350417701000864>
- [142] A. V. Mohod and P. R. Gogate, “Ultrasonic degradation of polymers: Effect of operating parameters and intensification using additives for carboxymethyl cellulose (cmc) and polyvinyl alcohol (pva),” *Ultrasonics Sonochemistry*, vol. 18, no. 3, pp. 727–734, 2011. [Online]. Available: <http://www.sciencedirect.com/science/article/pii/S1350417710002178>
- [143] M. T. Taghizadeh and A. Mehrdad, “Calculation of the rate constant for the ultrasonic degradation of aqueous solutions of polyvinyl alcohol by viscometry,” *Ultrasonics Sonochemistry*, vol. 10, no. 6, pp. 309–313, 2003. [Online]. Available: <http://www.sciencedirect.com/science/article/pii/S135041770300110X>
- [144] K. Tsutsumi, M. Shima, and A. Tanaka, “Advanced analysis of active material in li-ion battery by xps and aes,” *JEOL News*, vol. 49, no. 1, pp. 59–72, 2014.
- [145] H. Khan, M. G. Rigamonti, and D. C. Boffito, “Enhanced photocatalytic activity of Pt-TiO<sub>2</sub>/WO<sub>3</sub> hybrid material with energy storage ability,” *Applied Catalysis B: Environmental*, vol. 252, pp. 77–85, 2019. [Online]. Available: <http://www.sciencedirect.com/science/article/pii/S0926337319303352>
- [146] J.-C. Dupin, D. Gonbeau, P. Vinatier, and A. Levasseur, “Systematic xps studies of metal oxides, hydroxides and peroxides,” *Phys. Chem. Chem. Phys.*, vol. 2, pp. 1319–1324, 2000. [Online]. Available: <http://dx.doi.org/10.1039/A908800H>
- [147] Y. Guo, C. Li, S. Lu, and C. Zhao, “Low temperature co catalytic oxidation and kinetic performances of koh-hopcalite in the presence of CO<sub>2</sub>,” *RSC Adv.*, vol. 6, pp. 7181–7188, 2016. [Online]. Available: <http://dx.doi.org/10.1039/C5RA23806D>
- [148] X. Lou and Y. Zhang, “Synthesis of LiFePO<sub>4</sub>/c cathode materials with both high-rate capability and high tap density for lithium-ion batteries,” *J. Mater. Chem.*, vol. 21, pp. 4156–4160, 2011. [Online]. Available: <http://dx.doi.org/10.1039/C0JM03331F>
- [149] M. Talebi-Esfandarani, S. Rousselot, M. Gauthier, P. Sauriol, M. Duttine, A. Wattiaux, Y. Liu, A. X. Sun, G. Liang, and M. Dollé, “Control of the LiFePO<sub>4</sub> electrochemical properties using low-cost iron precursor in a melt process,” *Journal of Solid State Electrochemistry*, vol. 20, no. 9, pp. 3481–3490, 2016. [Online]. Available: <https://www.ingentaconnect.com/content/ssam/14328488/2016/00000020/00000012/art00028>

- [150] B. Wang, W. Al Abdulla, D. Wang, and X. S. Zhao, "A three-dimensional porous lifepo4 cathode material modified with a nitrogen-doped graphene aerogel for high-power lithium ion batteries," *Energy Environ. Sci.*, vol. 8, pp. 869–875, 2015. [Online]. Available: <http://dx.doi.org/10.1039/C4EE03825H>
- [151] M. Eslamian, M. Ahmed, and N. Ashgriz, "Modeling of solution droplet evaporation and particle evolution in droplet-to-particle spray methods," *Drying Technology*, vol. 27, no. 1, pp. 3–13, 2009. [Online]. Available: <https://doi.org/10.1080/07373930802565665>
- [152] A. Amighi and N. Ashgriz, "Global droplet size in liquid jet in a high-temperature and high-pressure crossflow," *AIAA Journal*, vol. 57, no. 3, pp. 1260–1274, 2019. [Online]. Available: <https://doi.org/10.2514/1.J056496>
- [153] A. H. Lefebvre, "Atomization," 2011. [Online]. Available: <http://www.thermopedia.com/content/573/>
- [154] D. F. Rutland and G. J. Jameson, "Theoretical prediction of the sizes of drops formed in the breakup of capillary jets," *Chem. Eng. Sci.*, vol. 11-E, no. 25, pp. 1689–1698, 1970.
- [155] V. Reinhard, "Pharmaceutical particle engineering via spray drying," *Pharmaceutical Research*, vol. 25, no. 5, pp. 999–1022, 2016. [Online]. Available: <http://doi.org/10.1007/s11095-007-9475-1>
- [156] S. Zellmer, G. Garnweitner, T. Breinlinger, T. Kraft, and C. Schilde, "Hierarchical structure formation of nanoparticulate spray-dried composite aggregates," *ACS Nano*, vol. 9, no. 11, pp. 10 749–10 757, 2015, pMID: 26505280. [Online]. Available: <http://dx.doi.org/10.1021/acsnano.5b05220>
- [157] L. J. van der, "Simulation of heat and mass transfer in spray drying," *Agricultural Research Review*, p. 845, 1976.
- [158] A. H. Lefebvre, *Atomization and Sprays*, Hemisphere NY, 1987.
- [159] C. A. Schneider, W. S. Rasband, and K. W. Eliceiri, "Nih image to imagej: 25 years of image analysis," *Nature Methods*, vol. 9, pp. 671–675, 2012.
- [160] M. G. Rigamonti, F. G. Gatti, and G. S. Patience, "Experimental methods in chemical engineering: Nuclear magnetic resonance," *The Canadian Journal of Chemical Engineering*, vol. 97, no. 3, pp. 628–635, 2019. [Online]. Available: <https://onlinelibrary.wiley.com/doi/abs/10.1002/cjce.23409>

- [161] N. A. Patience, F. Galli, M. G. Rigamonti, D. Schieppati, and D. C. Boffito, "Ultrasonic intensification to produce diester biolubricants," *Industrial & Engineering Chemistry Research*, vol. 0, no. 0, p. null, 0. [Online]. Available: <https://doi.org/10.1021/acs.iecr.9b00717>
- [162] J. H. van der Waals, *van der Waals, J. H.: Gorter's Footprints on the Trail That Led to Magnetic Resonance*. American Cancer Society, 2007. [Online]. Available: <https://onlinelibrary.wiley.com/doi/abs/10.1002/9780470034590.emrhp0188>
- [163] P. Vollhardt and N. Schore, *Organic chemistry structure and functions*, 6th ed. London, United Kingdom: W.H. Freeman and Co., 2010.
- [164] H. Metz and K. Mader, "Benchtop-nmr and mri-a new analytical tool in drug delivery research," *International Journal of Pharmaceutics*, vol. 364, pp. 170–175, 2008.
- [165] T. Polenova, R. Gupta, and A. Goldbourn, "Magic angle spinning nmr spectroscopy: A versatile technique for structural and dynamic analysis of solid-phase systems," *Analytical Chemistry*, vol. 87, pp. 5458–5469, 2015.
- [166] S. Wang, R. A. Munro, L. Shi, I. Kawamura, T. Okitsu, A. Wada, S.-Y. Kim, K.-H. Jung, L. S. Brown, and V. Ladizhansky, "Solid-state nmr spectroscopy structure determination of a lipid-embedded heptahelical membrane protein," *Nature Methods*, vol. 10, pp. 1007–1012, 2013.
- [167] J. D. Pleil and K. K. Isaacs, "High-resolution mass spectrometry: basic principles for using exact mass and mass defect for discovery analysis of organic molecules in blood, breath, urine and environmental media," *Journal of Breath Research*, vol. 10, no. 1, p. 012001, 2016.
- [168] J. L. Markley, R. Brüschweiler, A. S. Edison, H. R. Eghbalnia, R. Powers, D. Raftery, and D. S. Wishart, "The future of nmr-based metabolomics," *Current Opinion in Biotechnology*, vol. 43, pp. 34–40, 2017.
- [169] M. Lim, H. Ye, N. Panoskaltis, E. M. Drakakis, X. Yue, A. E. Cass, A. Radomska, and A. Mantalaris, "Intelligent bioprocessing for haemotopoietic cell cultures using monitoring and design of experiments," *Biotechnology Advances*, vol. 25, no. 4, pp. 353–368, 2007.
- [170] B. Gouilleux, B. Charrier, S. Akoka, F.-X. Felpin, M. Rodriguez-Zubiri, and P. Girardeau, "Ultrafast 2d nmr on a benchtop spectrometer: Applications and perspectives," *TrAC Trends in Analytical Chemistry*, vol. 83, pp. 65–75, 2016.

- [171] M. Barfield, A. J. Dingley, J. Feigon, and S. Grzesiek, "A dft study of the interresidue dependencies of scalar j-coupling and magnetic shielding in the hydrogen-bonding regions of a dna triplex," *Journal of the American Chemical Society*, vol. 123, no. 17, pp. 4014–4022, 2001. [Online]. Available: <https://doi.org/10.1021/ja003781c>
- [172] E. G. Stein, L. M. Rice, and A. T. Brünger, "Torsion-angle molecular dynamics as a new efficient tool for nmr structure calculation," *Journal of Magnetic Resonance*, vol. 124, no. 1, pp. 154–164, 1997. [Online]. Available: <http://www.sciencedirect.com/science/article/pii/S1090780796910277>
- [173] L. Kay, P. Keifer, and T. Saarinen, "Pure absorption gradient enhanced heteronuclear single quantum correlation spectroscopy with improved sensitivity," *Journal of the American Chemical Society*, vol. 114, pp. 10 663–10 665, 1992.
- [174] H. J. Reich, "What's going on with these lithium reagents?" *The Journal of Organic Chemistry*, vol. 77, no. 13, pp. 5471–5491, 2012.
- [175] A. D. Chowdhury, K. Houben, G. T. Whiting, S.-H. Chung, M. Baldus, and B. M. Weckhuysen, "Electrophilic aromatic substitution over zeolites generates wheland-type reaction intermediates," *Nature Catalysis*, vol. 1, pp. 23–31, 2018.
- [176] K. A. Giffin, L. A. Pua, S. Piotrkowski, B. M. Gabidullin, I. Korobkov, R. P. Hughes, and R. T. Baker, "Generation of hydrofluoronickelacycles from trifluoroethylene and ni(0): Ligand effects on regio-/stereoselectivity and reactivity," *Journal of the American Chemical Society*, vol. 139, no. 11, pp. 4075–4086, 2017. [Online]. Available: <https://doi.org/10.1021/jacs.6b12607>
- [177] E. Brenna, F. Distante, F. G. Gatti, and G. Gatti, "Substituent and catalyst effects on gac lactonization of [gamma]-hydroxy esters," *Catal. Sci. Technol.*, vol. 7, pp. 1497–1507, 2017.
- [178] E. Brenna, G. Fronza, C. Fuganti, F. G. Gatti, A. Manfredi, F. Parmeggiani, and P. Ronchi, "On the stereochemistry of the baker's yeast-mediated reduction of regioisomeric unsaturated aldehydes: Examples of enantioselectivity switch promoted by substrate-engineering," *Journal of Molecular Catalysis B: Enzymatic*, vol. 84, pp. 94–101, 2012.
- [179] W. T. Dixon, "Spinning-sideband-free and spinning-sideband-only nmr spectra in spinning samples," *The Journal of Chemical Physics*, vol. 77, no. 4, pp. 1800–1809, 1982. [Online]. Available: <https://doi.org/10.1063/1.444076>



- [180] O. N. Antzutkin, Z. Song, X. Feng, and M. H. Levitt, "Suppression of sidebands in magic angle spinning nuclear magnetic resonance: General principles and analytical solutions," *The Journal of Chemical Physics*, vol. 100, no. 1, pp. 130–140, 1994. [Online]. Available: <https://doi.org/10.1063/1.466983>
- [181] A. Sutrisno and Y. Huang, "Solid-state nmr: A powerful tool for characterization of metal–organic frameworks," *Solid State Nuclear Magnetic Resonance*, vol. 49-50, pp. 1–11, 2013. [Online]. Available: <http://www.sciencedirect.com/science/article/pii/S0926204012000847>
- [182] B. Perrone, S. Springhetti, F. Ramadori, F. Rastrelli, and F. Mancin, "“nmr chemosensing” using monolayer-protected nanoparticles as receptors," *Journal of the American Chemical Society*, vol. 135, no. 32, pp. 11 768–11 771, 2013.
- [183] O. Boyron, A. J. Cancelas, M. Taam, C. Boisson, and T. McKenna, "A new straightforward method for measuring xylene soluble for high impact polypropylene," *Canadian Journal of Chemical Engineering*, vol. 95, pp. 939–943, 2017.
- [184] B. Bulgakov, D. Kalugin, A. Babkin, I. Makarenko, A. Malakho, A. Kepman, V. Avdeev, N. Garadja, and A. Rogozin, "Propargylated novolac resins for fibre-reinforced plastics: Processing aspects," *Canadian Journal of Chemical Engineering*, vol. 94, pp. 46–52, 2016.
- [185] M. Daud, F. Shehzad, and M. A. Al-Harthi, "Crystallization behaviour and lamellar thickness distribution of metallocene-catalyzed polymer: Effect of 1-alkene comonomer and branch length," *Canadian Journal of Chemical Engineering*, vol. 95, pp. 491–499, 2017.
- [186] R. E. D. de Leon Gomez, F. J. Enriquez-Medrano, H. M. Textle, R. M. Carrizales, K. R. Acosta, H. R. L. Gonzalez, J. L. O. Romero, and L. E. L. Uribe, "Synthesis and characterization of high cis-polymyrcene using neodymium-based catalysts," *Canadian Journal of Chemical Engineering*, vol. 94, pp. 823–832, 2016.
- [187] H. Sahu and K. Mohanty, "One pot peroxidation of oleic acid rich azadirachta indica oil over bio-waste derived heterogeneous catalyst," *Canadian Journal of Chemical Engineering*, vol. 95, pp. 1526–1536, 2017.
- [188] I. A. Malik, U. A. Al-Mubaiyedh, A. S. Sultan, M. S. Kama, and I. A. Hussein, "Rheological and thermal properties of novel surfactant-polymer systems for eor applications," *Canadian Journal of Chemical Engineering*, vol. 94, pp. 1693–1699, 2016.

- [189] S. Frattari, F. Gironi, R. Sabia, and C. Villani, "Equilibrium condition and stabilization kinetics of lactic acid oligomers in aqueous solutions," *Canadian Journal of Chemical Engineering*, vol. 95, pp. 863–870, 2017.
- [190] S. D. Kirupha, R. Narayanasamy, M. Sornalatha, S. Sivanesan, and L. Ravikumar, "Synthesis and metal ion uptake studies of chelating polyurethane resin containing donor atoms: Experimental optimization and temperature studies," *Canadian Journal of Chemical Engineering*, vol. 95, pp. 944–953, 2017.
- [191] S. A. Kedzior, L. Graham, C. Moorlag, B. M. Dooley, and E. D. Cranston, "Poly(methyl methacrylate)-grafted cellulose nanocrystals: One-step synthesis, nanocomposite preparation, and characterization," *Canadian Journal of Chemical Engineering*, vol. 94, pp. 811–822, 2016.
- [192] E. Sirbu, S. Eyley, and W. Thielemans, "Coumarin and carbazole fluorescently modified cellulose nanocrystals using a one-step esterification procedure," *Canadian Journal of Chemical Engineering*, vol. 94, pp. 2186–2194, 2016.
- [193] M. Maric, J. Seok, A. Metafiot, and K. Wylie, "Nitroxide-mediated polymerization of adamantyl-functional methacrylates for 193 nm photoresists," *Canadian Journal of Chemical Engineering*, vol. 95, pp. 708–716, 2017.
- [194] L. Pan, L. Pan, T. Wang, Z. Wang, Z. Wu, Y. Li, C. Zuo, and Y. Liu, "Extraction of bisphenol f three isomers from water with 1-octyl-3-methylimidazolium tetrafluoroborate ionic liquid," *Canadian Journal of Chemical Engineering*, vol. 95, pp. 516–523, 2017.
- [195] M. F. Marcone, S. Wang, W. Albabish, S. Nie, D. Somnarain, and A. Hill, "Diverse food-based applications of nuclear magnetic resonance (nmr) technology," *Food Research International*, vol. 51, no. 2, pp. 729–747, 2013.
- [196] H. J. Reich and R. J. Hondal, "Why nature chose selenium," *ACS Chemical Biology*, vol. 11, no. 4, pp. 821–841, 2016.
- [197] W. S. Price, "Water signal suppression in nmr spectroscopy," ser. Annual Reports on NMR Spectroscopy, G. Webb, Ed. Academic Press, 1999, vol. 38, pp. 289–354.
- [198] K. Meyer, S. Kern, N. Zientek, G. Guthausen, and M. Maiwald, "Process control with compact nmr," *TrAC Trends in Analytical Chemistry*, vol. 83, pp. 39–52, 2016.

- [199] V. Sans and L. Cronin, "Towards dial-a-molecule by integrating continuous flow, analytics and self-optimisation," *Chem. Soc. Rev.*, vol. 45, pp. 2032–2043, 2016.
- [200] M. V. Gomez and A. de la Hoz, "Nmr reaction monitoring in flow synthesis," *Beilstein Journal of Organic Chemistry*, vol. 13, pp. 285–300, 2017.
- [201] E. Danieli, J. Perlo, A. L. L. Duchateau, G. K. M. Verzijl, V. M. Litvinov, B. Blümich, and F. Casanova, "On-line monitoring of chemical reactions by using bench-top nuclear magnetic resonance spectroscopy," *ChemPhysChem*, vol. 15, no. 14, pp. 3060–3066, 2014.
- [202] G. R. Fulmer, A. J. M. Miller, N. H. Sherden, H. E. Gottlieb, A. Nudelman, B. M. Stoltz, J. E. Bercaw, and K. I. Goldberg, "Nmr chemical shifts of trace impurities: Common laboratory solvents, organics, and gases in deuterated solvents relevant to the organometallic chemist," *Organometallics*, vol. 29, pp. 2176–2179, 2010.
- [203] H. E. Gottlieb, V. Kotlyar, and A. Nudelman, "Nmr chemical shifts of common laboratory solvents as trace impurities," *The Journal of Organic Chemistry*, vol. 62, no. 21, pp. 7512–7515, 1997, PMID: 11671879. [Online]. Available: <https://doi.org/10.1021/jo971176v>
- [204] P. Moutzouri, Y. Chen, M. Foroozandeh, P. Kiraly, A. R. Phillips, S. R. Coombes, M. Nilsson, and G. A. Morris, "Ultraclean pure shift nmr," *Chem. Commun.*, vol. 53, pp. 10 188–10 191, 2017. [Online]. Available: <http://dx.doi.org/10.1039/C7CC04423B>
- [205] R. E. Hoffman and E. D. Becker, "Temperature dependence of the  $^1\text{H}$  chemical shift of tetramethylsilane in chloroform, methanol, and dimethylsulfoxide," *Journal of Magnetic Resonance*, vol. 176, no. 1, pp. 87–98, 2005. [Online]. Available: <http://www.sciencedirect.com/science/article/pii/S1090780705001680>
- [206] H. J. Reich and J. H. Rigby, *Acidic and Basic Reagents, Handbook of Reagents for Organic Synthesis*, 1st ed. Wiley, 1999.
- [207] K. Klimke, M. Parkinson, C. Piel, W. Kaminsky, H. W. Spiess, and M. Wilhelm, "Optimisation and application of polyolefin branch quantification by melt-state  $^{13}\text{C}$  nmr spectroscopy," *Macromolecular Chemistry and Physics*, vol. 207, pp. 382–395, 2006.
- [208] K. Hashi, S. Ohki, S. Matsumoto, G. Nishijima, A. Goto, K. Deguchi, K. Yamada, T. Noguchi, S. Sakai, M. Takahashi, Y. Yanagisawa, S. Iguchi, T. Yamazaki, H. Maeda,

R. Tanaka, T. Nemoto, H. Suematsu, T. Miki, K. Saito, and T. Shimizu, "Achievement of 1020mhz nmr," *Journal of Magnetic Resonance*, vol. 256, pp. 30–33, 2015.

## APPENDIX A ARTICLE 3 - EXPERIMENTAL METHODS IN CHEMICAL ENGINEERING: NUCLEAR MAGNETIC RESONANCE

Marco G. Rigamonti,<sup>a</sup> Francesco G. Gatti,<sup>b</sup> Gregory S. Patience<sup>a</sup>

Published in 2019, in the *Canadian Journal of Chemical Engineering*. [160]

**Abstract** Nuclear magnetic resonance (NMR) spectroscopy measures free induction decay (FID) signals that atomic nuclei emit when excited by a radio-frequency (RF) pulse in a static magnetic field. The Fourier-transformed spectrum shows chemically shifted peaks, area intensity and multiplicity; which give information on molecular structure, bonds, functional groups and purity. Web of Science Core Collection indexed 46000 articles that mentioned NMR in 2016 and 2017. The VosViewer software grouped the research into 5 clusters: solid-state analysis including metabolomics; biology with *in-vitro* and antibacterial applications; coupled analytical techniques to identify crystal structure for which X-ray diffraction and density functional theory figure prominently; liquid-state analysis for polymers, aqueous solutions, nano-particles and drug delivery; and, chemosensors. Researchers publishing in the *Canadian Journal of Chemical Engineering* focus most on: liquid-state NMR to characterize polymers, branching and monomers; quantify conformation, reaction kinetics and equilibrium; assess surfactant stability, ionic liquids, and composition. We introduce the theory behind NMR spectroscopy and common applications in chemistry and material science. We highlight the strength and limitations, source of error and the detection limit for this analytical technique, as manufacturers develop massive magnets for high-resolution spectra (1 GHz), and benchtop NMR for real-time, in-situ analysis (80 MHz).

**Introduction** In 1901 Marconi built an instrument to deliver voice message through radio waves and established the first transatlantic radio communication. Also in the microscopic world of atoms, the nuclei with a magnetic moment emit a radio frequency signal (RF) when subject to a magnetic field. In both scales, resonance at a precise frequency is a fundamental phenomenon to detect those RF. This was initially proposed by Cornelis J. Gorter in 1936 and first demonstrated for molecular beams by Isidor I. Rabi in 1937. Finally, in 1945 Bloch and Purcell refined the methodology to the experimental technique we have today, winning

---

<sup>a</sup> Department of Chemical Engineering, Polytechnique Montréal, C.P. 6079, Succ. CV Montréal, H3C 3A7, Québec, Canada.

<sup>b</sup> Dipartimento di Chimica, Materiali e Ingegneria Chimica "Giulio Natta", Politecnico di Milano, P.zza Leonardo da Vinci 32, 20133, Milano, Italy.

the Nobel prize.[162] NMR spectrometers are non-destructive, ex-situ instruments that measure the RF associated to nuclei that possess a magnetic moment (a non-zero spin quantum number). We determine the molecular structure following a series of rules related to the spectrum and derive reaction kinetics, dynamics and conformation evolution while collecting spectra over time and at temperatures from  $-150^{\circ}\text{C}$  to  $200^{\circ}\text{C}$ . [9] NMR revolutionized medical diagnostics with Magnetic Resonance Imaging (MRI). The word *nuclear* was omitted to bely patients fears of exposure to *ionizing nuclear radiation*. MRI is a non-invasive procedure that displays internal anatomy and tissues.[163, 164] Gas chromatography (GC) and mass spectrometry (MS) are the standard analytical techniques for gas phase applications but researchers are applying emerging solid-state NMR techniques for polymers, proteins and complexes up to hundred thousand Daltons.[165, 166] The advent of cryoprobes and digital lock technology substantially decreased the instrument electronic noise (RF interferences) and field fluctuations overtime. Consequently, the signal to noise ratio ( $s/n$ ) improved so much that these instruments detect nanomolar samples in seconds rather than hours, which has opened it up to research in biology, proteomics and metabolomics. Along with high-resolution MS,[167] NMR achieved an important milestone in lowering the analyte concentration limit.[168] It is one of the few spectroscopic techniques to study bio-molecules in their native environment. Industrial quality control applies either IR or NMR spectroscopy on-line to monitor over-expression in host microorganisms to produce proteins. NMR is more accurate than IR as it identifies isomers together with functional groups and can identify which functional groups react.[169] Benchtop instruments sacrifice resolution and sensitivity but are less expensive and analyze—on-line operando—the evolving flow composition.[170]

**Description** The NMR spectrometer is a massive instrument weighing up to 10 t, mainly composed of a superconducting coil cooled with liquid He, that generates an intense static magnetic field up to 23.5 T. Like other spectroscopic techniques, it analyzes the structure of molecules based on differences when absorbing electromagnetic radiation. In particular, NMR works in the radio-waves domain, affecting a transition in the alignment of nuclear spin (Figure A.1).

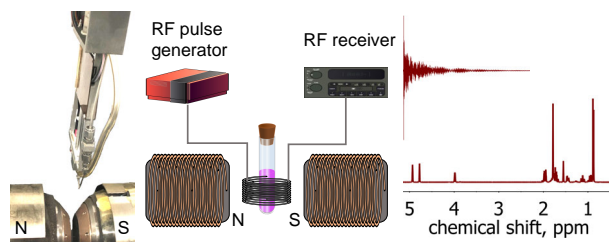


Figure A.1 On the left an old ('80) FT-NMR Spectrometer; a pneumatic arm lowers the sample between the 80 MHz resistive magnets. An RF pulse generator activates the test sample in the center of a static magnetic field (N–S) and an RF receiver measures the fluctuations. The recorded spectrum (FID, free induction decay) sums multiple scans into a sinusoid that decays exponentially with time. A Fourier-Transform of the FID identifies the dominant frequencies that belongs to atoms in the molecule.

High-fields NMR instruments are expensive to purchase and to maintain operational and require a constant supply of liquid He and N<sub>2</sub> to maintain the magnet and coil superconductive and avoid an explosive quench. A 43 MHz benchtop instrument, with proton-carbon detectors, costs 60 k\$; a 400 MHz magnet, with a multi-nuclear probe, liquid and solid-state capabilities, costs 0.5 M\$ (half with only liquid capabilities); a 500 MHz, 0.8 M\$; and the highest-rating 1 GHz, 10 M\$. An exponential equation estimates the order of magnitude for the instrument cost with full capabilities ( $c$ , 2018 U.S. M\$), with respect the magnet field strength in terms of <sup>1</sup>H resonance frequency ( $f$ , MHz):

$$c = 0.05e^{0.005f} \quad (\text{A.1})$$

**Theory** Many nuclear isotopes are magnetically active with non-zero nuclear spin (<sup>1</sup>H, <sup>2</sup>H (deuterium), <sup>13</sup>C, <sup>14</sup>N and <sup>15</sup>N, <sup>19</sup>F, and <sup>31</sup>P are all NMR active). Spin 1/2 nuclei have a spherical charge distribution, while in quadrupolar nuclei (quantum spin number greater than 1/2) the charge is distributed as a prolate or oblate spinning body. When a magnet imposes an external static magnetic field, nuclei with 1/2 spin align their magnetic dipole either in the same direction ( $\alpha$  spin state, slightly more favorable because it is at a lower energy state), or in the opposite direction ( $\beta$  spin state). For quadrupolar nuclei there are additional energy levels which increase the complexity of the splitting pattern and will not be discussed here. The difference between energy levels (and therefore nuclei population) linearly increases with a stronger magnetic field (bigger instrument) and is characteristic of the type of nucleus. Reducing the temperature of the sample shift the population distribution, promoting more nuclei in the  $\alpha$  spin state. The difference in population between the two energy levels follows a Boltzmann distribution and is minimal: for a <sup>1</sup>H at rt and under

a 5.87 T magnetic field, the  $\alpha$  state represents 50.001 % of the population. The alignment of the nuclei in the direction of the magnetic field is not perfect and they precess around their axis. The Larmor's frequency of precession (how many times the nucleus' spin axis completes a full circle) increases with the strength of the magnetic field and each isotope precesses at a characteristic frequency. In a 7.05 T magnetic field, the  $^1\text{H}$  nucleus precesses at 300 MHz, while in a 21.1 T at 900 MHz. Similarly, at 7.05 T, the  $^2\text{H}$  precesses at 45.7 MHz, the  $^{13}\text{C}$  at 75.3 MHz, the  $^{19}\text{F}$  at 282 MHz and so on. Resonance occurs when the frequency of the external electromagnetic radiation (from the RF pulse generator) matches the nucleus' precession. During resonance, the incoming RF radiation promotes the  $\alpha$  spin state nuclei to flip to the  $\beta$  spin state, increasing its population at higher energy. The process continues until the two energy levels are evenly populated by an equal number of nuclei (saturation). At this point there is an equal probability that  $\alpha$  flip to  $\beta$  and vice versa and the RF pulse generator is turned off. Without an energy input, resonance quickly dies out. The system reverts back at the previous equilibrium condition and the unstable excess of  $\beta$  spin state nuclei relax exponentially into the  $\alpha$  spin state, emitting a quantum of energy as RF radiation. During this time, the RF receiver records the intensity of the emission from each nucleus: the FID looks like a periodic sinusoid, exponentially decaying with time. This concludes one *pulse sequence* (one scan), reiterating the sequence allows to sum multiple scans to reduce data noise. A Fourier transform converts the FID from the time domain to the frequency domain, revealing a baseline and a series of peaks. Finally, a software calculates the peaks properties (position, area intensity, multiplicity,  $J$ -couplings) required to evaluate the molecule.[163]

**Applications** A one dimension (1D) NMR spectrum of a magnetically active isotope, produces a series of signals: each signal has a position (chemical shift), an area intensity (integral), multiplicity and  $J$ -couplings (how many peaks and how much they are spaced in between, depending on the measuring technique, Figure A.2). The chemical shift is a unique marker: it does not change, regardless of the instrument or magnetic field strength. The signal corresponds to one or more nuclei (if they are chemically equivalent) and integration quantifies their number. Multiplicity correlates with the position of the atom in the molecule and  $J$ -couplings represent connectivity. As a more in-depth refinement,  $J$ -couplings can be used to correlate bond distances (comparing density functional theory—DFT calculations)[171] and angles (in conjunction with XRD).[172] To identify different species and quantify their concentration, most analytical techniques require a standard: a pure compound that fingerprints with the sample and calibrate the response output of the instrument with an imposed concentration. However, when standards are not available, an alternative is to go through a separate chemical synthesis and purification, which can be time consuming. On the other hand, NMR does not necessarily require a standard to fingerprint with the sample. A refer-



ence compound is required to assign the chemical shifts and a calibration compound to determine the absolute concentration. Both can be as simple and available as common solvents diluted at a precise concentration in the deuterated solvent. In a  $^1\text{H}$  spectrum, comparing the integral area from one proton from the sample with one from the calibration compound—at a known concentration—gives the sample absolute concentration and yield. In the same manner, comparing the desired product with contaminants or sideproducts gives purity. In this case, integrals are evaluated relative to each other, and a calibration compound is not required to measure purity.

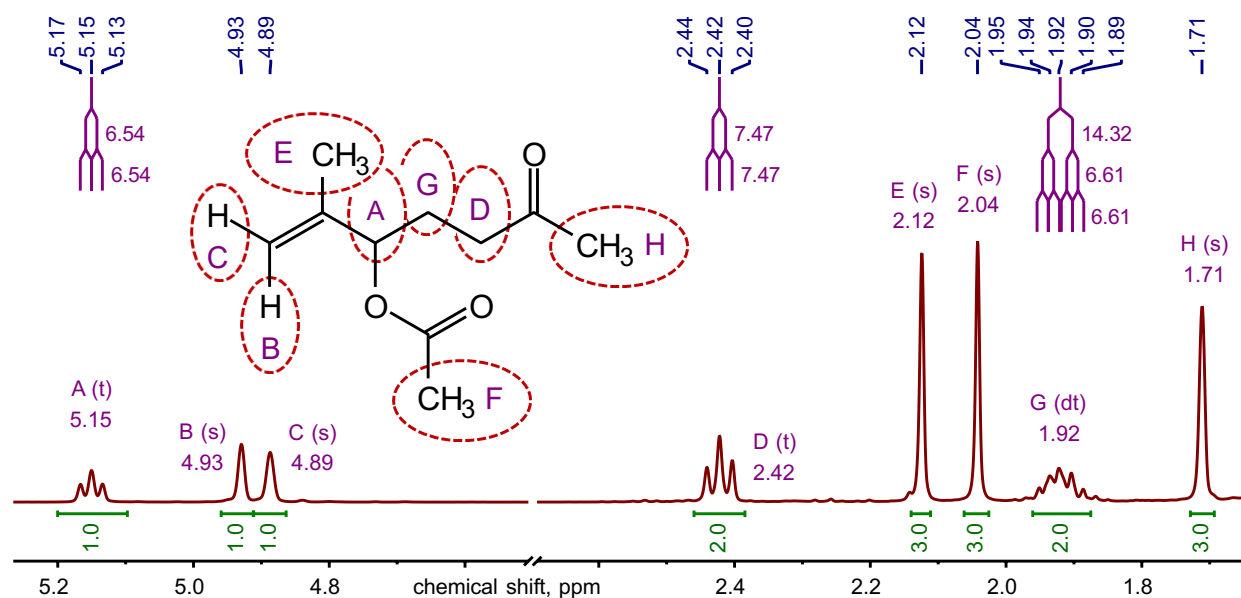


Figure A.2 The  $^1\text{H}$  spectrum for a derivative of 6-methylhept-6-en-2-one in  $\text{CDCl}_3$ , recorded at 400 MHz at rt.[11] The signal from "A" has three peaks (t: triplet) and its integration gives an area that is normalized to 1.0 (in green, one proton). Each peak has a distinctive chemical shift (blue) and their distance (in Hz) measure the  $J$ -coupling constant (violet). The "J-tree" (violet) is a representation of the Pascal's triangle: a rule that correlates the shape of the NMR signal with the number of vicinal protons. "A" couples with the two protons in "G" and creates a triplet. "B", "C", "E", "F" and "H" are all singlets (s), meaning that close to them there are no protons available. "E", "F" and "H" belong to the methyl groups, as their area integral is three times the one from "A". Between them "E" in the most deshielded group: the electron cloud is displaced towards the double bond, so the peak appears at high chemical shifts. Unlike in the methyl group, where all three protons are chemically equivalent, the protons bonded to a  $\text{sp}^2$  carbon are not. Therefore "B" and "C" appear as two distinctive singlets as none of them correlates with a vicinal proton, with an integral of one. "D" follows the same rule as "A", but the integral is double as it has two protons. "G" has also two protons, but it also has a more complex coupling: on the left it couples with one proton from "A" and on the right with two protons from "D". Because the two couplings have different  $J$ -constants (14.3 and 6.6 Hz), the doublet (d) from "A" splits the triplet from "D" in two branches. Following the Pascal's triangle rule, this shape (dt) appears with five peaks, as the two branches in the center overlap and increase in intensity.

A two dimensional (2D) heteronuclear correlation spectrum is a bi-dimensional plot in which a contour line shows the signal intensity as a function of the two isotopes' chemical shift. This methodology reveals the interaction between different nuclei and overcomes the limitation of only relying on coupling constants from 1D spectra (for complex structures, peaks overlap and  $J$ -constants cannot be determined).[173] Low temperature ( $-100\text{ }^{\circ}\text{C}$ ) multinuclear NMR spectra detail bonding configuration in organolithium solutions and quantify the interconversion transition energy.[174] Solid-state NMR elucidates the mechanism and catalytic cycle for the heterogeneous reaction of ethylation of benzene over zeolite. The 2D spectra identifies the various adducts adsorbed on the surface of the catalyst, by measuring the  $J$ -couplings associated with the molecule's mobility.[175] Peak integration quantifies the molar ratio of the selected nucleus in a specific position in the molecule.  $^{19}\text{F}$  NMR resolves complex mixtures of isomers —impossible to separate or quantify in GC or HPLC columns— by measuring the geminal coupling constants between  $^{19}\text{F}$  and  $^1\text{H}$  for the various isomers. This procedure identifies each molecule, and  $^{19}\text{F}$  peak integration quantifies the mixture.[176] Recording more spectra overtime displays—*in-situ*—structural changes due to chemical reactions and physical interactions. The creation or change in position of a peak, as well as its change in relative intensity, correlates with the portion of the molecule affected. Peak integration reveals quantitative kinetic data.[177] We follow the reaction mechanism by marking a nucleus with one of its isotopes and analyzing how it migrates with time.[178] A common procedure to keep the magnetic field stable is to use an internal standard: in liquid-state NMR is the  $^2\text{H}$  signal from the deuterated solvent. When field fluctuations alter the observation frequency of deuterium (lock frequency), the instrument compensates and corrects the magnetic field frequency accordingly, limiting drift and increasing the resolution. The deuterated solvent also provides a medium transparent to the electromagnetic pulses ( $^1\text{H}$  and  $^2\text{H}$  have different resonance frequencies): the solvent signals do not appear on the spectrum. However diluting the sample reduces the signal intensity so we run the test longer, especially for low abundance isotopic species (ex.  $^{13}\text{C}$  has 1.1% abundance). Solid-state NMR overcomes this limitation but peaks are broader as the low-to-null molecular mobility in a solid matrix gives anisotropic interactions. To sharpen the signal, a cell holder spins the sample up to 110 kHz at a precise angle with respect to the direction of the magnetic field ( $54.74^{\circ}$  magic angle spinning, MAS). This signal is sharper but it creates sidebands: predictable secondary peaks equally spaced around each main peak. Their appearance on the spectrum is directly proportional to the rotational speed and a sequence of pulses, synchronized with the rotor, suppress those signals but makes the main peak non-quantitative (TOSS *total suppression of sidebands* technique).[179, 180] Solid-state NMR is a complementary technique to liquid-state, in which we look for the interaction of the molecule in its own bulk environ-

ment. It distinguishes solid polymorphs, determines the extent of crystallinity, characterize nanomaterials and catalysts and analyze the molecular structure and its arrangement in a solid matrix: all these properties cannot be attained from liquid-state NMR.

Web of Science Core Collection indexed 46 114 articles that mention NMR in 2016 and 2017, which makes it among the top 5 experimental methods in science but at the 50-percentile for *Canadian Journal of Chemical Engineering* articles. A bibliometric map of the 10 000 most cited articles with NMR or nuclear magnetic resonance topic,[12, 13] identifies five research clusters: solid-state NMR in green, aqueous solution in red, structural characterization and simulation in yellow, biology in blue, and NMR-chemosensors in violet (Figure A.3).

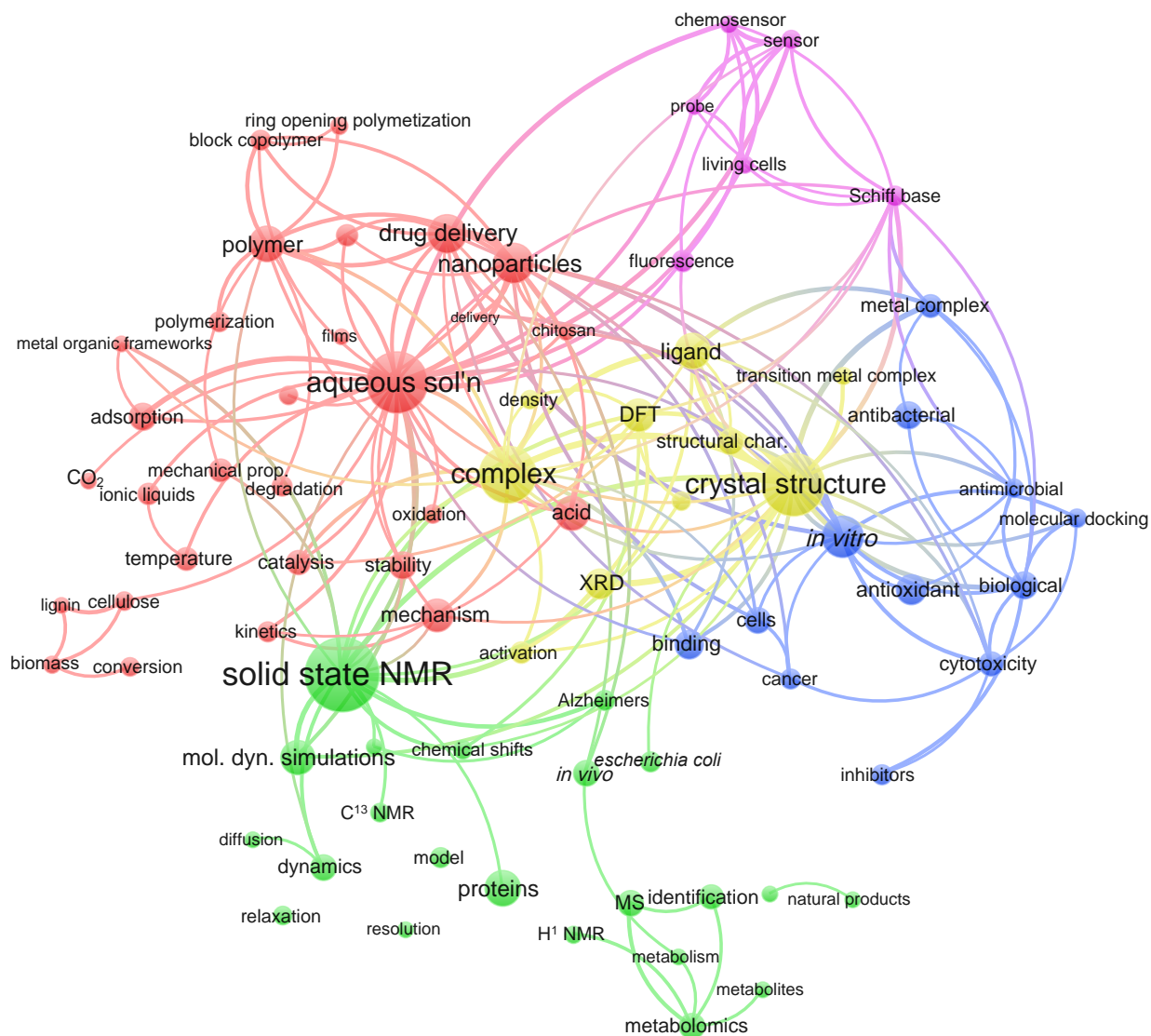


Figure A.3 NMR bibliometric network:[12, 13] the size of the keyword is proportional to the number of occurrences (from 80 to 640). The distance between keywords shows how two topics closely relate each other. The number of links was limited in order to elucidate the main connections between different areas.

**Solid-state NMR** (which includes MAS-NMR) has the highest number of occurrences in our selected pool of articles (640). It has a strong link with XRD, crystal structure, DFT and molecular dynamic simulation which are complementary techniques for investigating solid phase. Metal organic frameworks (MOFs) are porous materials with applications in areas including ion-exchange, catalysis, separation, molecular recognition, drug delivery and gas storage.  $^{129}\text{Xe}$  solid-state NMR establish porosity and identify the adsorption sites in MOFs,  $^1\text{H}$  and  $^{13}\text{C}$  characterize organic linkers with the solid framework and dynamics of guest molecules.[181] Proteins and metabolomics belong to the same cluster. However metabolomics and proteins are closer to MS rather than solid-state NMR. This confirms a recent trend in which LC-MS instruments have taken precedence over NMR to identify and quantify protein structure.[168] The lower cost of the instrument and the presence of a database for proteins contributed to the switch from NMR to MS.

Alzheimer's disease is near the center of the map, indicating that this research is closely related to all five categories, but mostly with **biological** since its colour is green. In vitro studies, cell-protein binding cancer, cytotoxicity and antimicrobial belong to the same cluster. The network connects these topics with drug delivery and nanoparticles: they belong to the aqueous solution cluster, as most in vitro biological NMR studies are analyzed in liquid-state instruments.

A third cluster, **NMR-chemosensor**, links the previous one and aqueous solution. This ensemble describes drug delivery medical applications for sensing the response of living cells through nanoparticles interaction in biological studies.[182]

A broad list of research topics belongs to the **aqueous solution** cluster: material science, polymer, temperature, kinetic, catalysis, biomass and mechanism. Liquid-state analysis remains the most common methodology (also for researchers publishing in the *Canadian Journal of Chemical Engineering*) to investigate temperature effects, kinetics, mechanisms, and catalysis. This cluster also comprises solid materials like biomass and polymers, in which solid-state NMR offers additional characterizations. In fact, the network established a strong link between polymer and solid-state NMR. Also catalysis, mechanisms and kinetics are close to it. This indicates a preferential choice when investing in an NMR instrument: solid-state NMR are more expensive and the spectrum is more complex to analyze; whereas some solid samples can be solubilized and processed with a liquid-state NMR.

**Structural characterization and simulation** is also in the center of the map and include computational techniques (DFT) and crystallography (XRD) to simulate and complementary techniques to validate organic and metallorganic complexes and biological ligands.

Few articles in *Canadian Journal of Chemical Engineering* (2016 and 2107) reported NMR scans: among all analytical methods, NMR is among the lower 50<sup>th</sup> percentile. In fact, the cost of the instrument surpasses several times that of more standard techniques like GC-MS, HPLC and FTIR. Comparing the results with our bibliometric map (Figure A.3), *Canadian Journal of Chemical Engineering* authors publish in material science (aqueous solution cluster, in red): polymers and nanoparticles. Liquid-state NMR dominates over solid-state (90 % of the case), which is consistent with the trend among the top cited 10 000 WoS manuscripts. 7 papers out of 10 only analyze the <sup>1</sup>H spectrum, for which liquid-state instruments achieve the best resolution. Xylene solubilize plastic materials like polypropylene and polyethylene; this allows to take advantage of liquid-state NMR and a <sup>13</sup>C spectrum is able to quantify the fraction of each component in a copolymer.[183] Curing time control prevents exothermic hotspots in propargylated novolac resins: in the monomer preparation, the propargyl chloride load controls the curing kinetics, and spectroscopic data quantifies the propargyl signal intensity as different precursor loadings affect the temperature, curing time and final mechanical properties of the resin.[184] Copolymers' formulations require a catalyst to selectively distribute each component along the chain. Metallocene complexes catalyze the branching insertion of *n*-alkenes and branching is the main factor that affects the plastic's degree of crystallinity. <sup>13</sup>C spectra quantifies the branching density, with the ASTM method 5017-96, integrating the peaks relative to the methylene resonance at 30.0 ppm.[185] *Cis*-polymyrcene has better mechanical properties than an atactic plastic. Two neodymium-based Ziegler-Natta catalysts increase the stereoselectivity of  $\beta$ -myrcene polymerization up to 92 %. Integrating the olefinic signals in proton and carbon spectra quantifies the *cis/trans* ratio.[186] Another example of olefinic protons peak integration characterizes the catalytic epoxidation mechanism of oleic acid on ZnO.[187] An FTIR instrument alone is incapable to determine the extent of thermal decomposition of an anionic surfactant (Alfoterra 123-8s), while a <sup>13</sup>C NMR quantifies the decomposition and reveals which bonds react and how the starting material rearranges.[188] Routine characterization quantify the degree of oligomerization in lactic acid, up to 0.1 %, [189] as well as the effectiveness of poly-condensation in polyurethane resins.[190] Cellulose nanocrystals are novel reinforcing agents for polymer nanocomposites; but hydrophilic, so unsuitable in non-polar composite matrices. Grafting with polymethylmethacrylate (PMMA) overcomes this limitation and a <sup>13</sup>C MAS-NMR measures the degree of crystallinity with 1 % to 2 % error on a 20 T magnet.[191] However, liquid-state proton NMR successfully characterizes the cellulose nanocrystals' precursors with carbazole and coumarin functionalities.[192] A liquid-state proton NMR, quantifies the degree of polymerization and the presence of different co-polymers in PMMA resins.[193] NMR detects chemical bonds and <sup>1</sup>H spectroscopy detect the hydrogen bond interactions between Bisphenol F and

an extracting agent in ionic liquids. DFT (Gaussian 09<sup>®</sup>) supports the experimental data, proving that the extraction mechanism passed through hydrogen bond interaction.[194] The food domain is a missing discipline on the *Canadian Journal of Chemical Engineering*: in 2017, WoS indexed 400 articles with NMR and food (*vs.* 2500 articles for polymers). Food chemistry and microbiology require quantitative analyses to validate the water, lipid and protein content in raw meats, vegetables and processed foods. Metabolites and vitamins, often at ppm levels, quantify the nutritional value. NMR also examines the packaging material, to test the polymer performance to preserve food at different storage conditions (temperature, humidity, and acidity). For example, polystyrene maintains its mechanical and chemical properties even when gamma radiations sterilize the food.[195]

**Uncertainty** A *pulse sequence* is a set of predefined commands, iterated at each analysis' scan that imposes the time, strength and how many times the RF irradiates the sample. Most routine pulse sequences for spin 1/2 nuclei (<sup>1</sup>H, <sup>12</sup>C, <sup>19</sup>F, <sup>31</sup>P, <sup>77</sup>Se, ...) are available in the instrument's software and are integrated as standard algorithms. Their magnetic spin result in sharp peaks and allows homo and heteronuclear coupling. Low isotopic abundance species (<sup>12</sup>C) decrease the sensitivity of the analysis and require longer acquisition time. Quadrupolar nuclei (<sup>7</sup>Li, <sup>17</sup>O, <sup>33</sup>S, ...) complicate the spectrum with broad peaks (5 Hz to 500 Hz) and unresolved *J*-couplings. A dedicated pulse sequence improves the quality of the analysis; a reaction involving a selenolate/diselenide exchange was compared with a thiol/disulfide system, with enough resolution to assess a 10<sup>7</sup> increase in kinetic ratio between the two reaction systems.[196] The spectrum contains multiple information not easily accessible: a software calculates all the quantities related to peak analysis and from literature data the user can fingerprint the compound's chemical shifts and *J*-couplings. However, interpreting a spectrum for a novel compound, requires a chemical/physical background and knowledge of NMR spectroscopy. This discourages scientists from other fields of study to pursue this type of analysis.

**Limitations** Liquid-state NMR requires the sample to be soluble in a deuterated solvent for frequency field lock. However not all materials are compatible with this methodology: in metabolomics, the biochemical reactions evolve in water systems. Drying or organic-based deuterated solvents would alter the starting material. Thus, non-routine methods are required to suppress the signal from water and tune the NMR in a deuterium-free environment.[197] The classic NMR instrument is fixed to the ground, both because of its weight and to minimize external vibrations and ensure a RF-free environment. In-situ, real-time recording of an evolving system is limited to liquid phase and milliliter volumes in batches. Flow-chemistry, process control and small research groups take advantage of benchtop spectrometers when analyzing small molecules (hundreds of Daltons).[198] A permanent magnet design (up to



80 MHz) does not require cryogenic fluids and shrinks the whole apparatus to the size of a 0.5 m box. The weaker magnetic field limits the resolution and sensitivity, but the instrument design allows continuous flow, analytics and real-time system optimization.[199] On-line reaction monitoring requires new pulse sequences (NOESY with WET sequence to suppress the protonated solvent signal). Bubbles and turbulent flow regimes distort NMR signals.[200] A single scan acquisition, in a 60 MHz bench top spectrometer produces quantitative kinetic data for small molecules at a concentration of  $1 \text{ mmol L}^{-1}$ , flowing in a PTFE tube at  $1 \text{ mL min}^{-1}$ . On the catalytic hydrogenation of acetophenone with isopropanol by iridium complexes, the  $s/n$  was strong enough to establish the reaction order and dependence of the kinetic constant with respect to the catalyst loading.[201]

**Sources of error** NMR detectors measure contributions from samples and the enclosing-cell environment. Water moisture diffusing into an un-sealed deuterated solvent bottle affects the spectrum. The residual reaction's solvents must be removed too, which requires high-vacuum. However, an external database has registered these common contaminants in proton and carbon spectra, and they can be flagged-out by comparing their unique chemical shifts.[202, 203] When handling mixtures, signals belonging to different molecules overlap, which degrades the signal quality and compromises its interpretation. Peak deconvolution attributes the intensity of a crowded region to each compound, but only when the composition of the mixture is known. Silica chromatographic purification helps to produce clear spectra of a single compound, unambiguously integrating peaks and assigning them to the proper nucleus. Poor shimming of inhomogeneous magnetic fields decreases the signal resolution; spinning the sample in the probe sharpens the peaks, but also generates sidebands (Figure A.4). In crowded spectra is difficult to attribute peaks or multiplicity to a nucleus, and sidebands increase the complexity of processing the analysis. The integral intensity of the sidebands is proportional to the main peak, but when sidebands overlap with another signal, they overestimate the integral from this other signal and underestimate the main peak's one. TOSS (for solid-state), spinning at different rate, or "ultraclean pure shift"[204] pulse sequence (for liquid-state) suppress the sidebands' signals. Insufficient relaxation times (0.1 s to 100 s, the time required for a nucleus to return from an excited to the ground state) saturates the nuclear spin and suppresses/depresses signals that require longer time, resulting in lower integral attribution. Relaxation depends on the chemical environment; quaternary carbons are more demanding. A long-running analysis requires optimizing the relaxation time: insufficient time invalidates peak integration while excessive time limits the number of scans and  $s/n$  in a defined period of time. Deformed NMR cells and tubes, even imperceptible deformations, induce anisotropic magnetic fields, proportionally distorting the signals and broadening the peaks. Sample inhomogeneities (precipitation in liquid samples, packing

voids in solid samples, paramagnetic impurities, and temperature gradients) also degrade signal quality. Temperature alters the molecule conformation and therefore the chemical shifts. For example, we calibrate the temperature inside an NMR tube by measuring the distance between the two peaks of methanol, and they split further as the temperature decrease. The reference chemical shift is also affected: tetramethylsilane (TMS) in chloroform is commonly attributed with the reference shift of 0 at rt. However at 100 °C, it shifts at 0.05 ppm, and at −70 °C at −0.05 ppm.[205] However, in standardized spectra recorded at room temperature, all peaks are shifted by aligning the internal reference chemical shift to a standard value, compensating for small temperature variations between instruments.

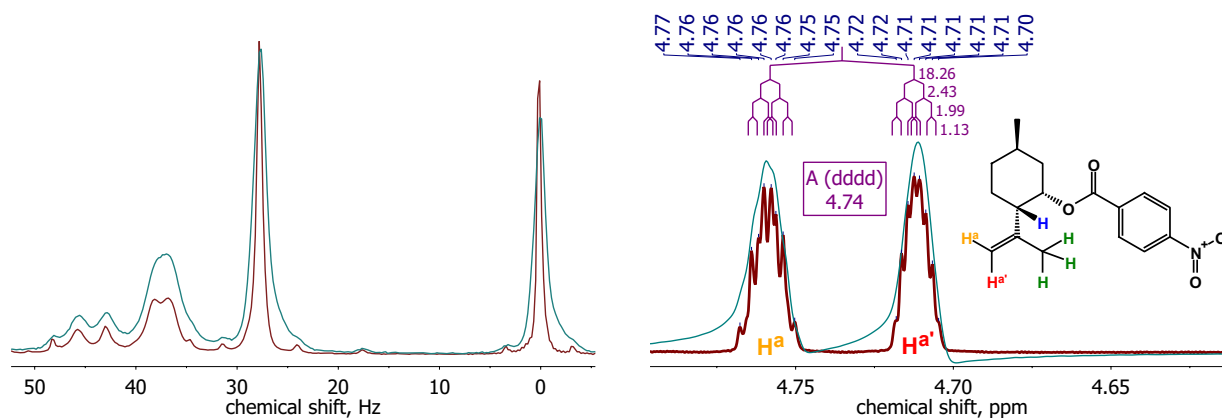


Figure A.4 On the left: non-spinning samples' peaks appear broader (blue). A spinning sample sharpens the peaks and allow multiplicity detection, but creates secondary peaks — sidebands— equally spaced (3 Hz, which corresponds to the rotational sample's rate) from the main peak (red). On the right: a poorly shimmed and phased 100 MHz proton spectrum (blue) and a 400 MHz one (red). On the latter each peak is symmetrical (good shim and phase) and the stronger magnet resolve the multiplicity (dddd) for the two exocyclic doublebond's protons (H<sup>a</sup> and H<sup>a'</sup>).

**Detection limits** NMR signals depend on the relaxation of  $\beta$  nuclei to the  $\alpha$  spin state, however the difference in nuclei population between these two states is low: resonating a proton at 60 MHz, creates a population difference between the  $\beta$  and  $\alpha$  spin state of only 5 ppm and  $0.02 \text{ J mol}^{-1}$  energy difference. A stronger magnetic field —600 MHz— increases linearly the NMR signal strength by increasing ten times the  $\beta$ - $\alpha$  population difference and the emitted energy upon relaxation. It increases the separation-resolution of two close chemical shifts (in Hz) and allows to identify the multiplicity of a signal (Figure A.4). A proton spectrum of 2-methyl-2-butanol recorded at 200 MHz doubles the shift window in which the signal is recorded (500 Hz), with respect to a 100 MHz analysis. In the latter case, signals

are crowded in a 250 Hz window and the poor resolution, makes impossible to retrieve the coupling constants' information.[206] Quantifying trace compounds is a time constraint: in a liquid-state NMR, polymers are often only partially soluble in the solvent (decreasing the signal intensity) and quantifying the trace signals of branching (as low as 0.003 %), requires up to 300 h.[207] In fact, the  $s/n$  increases with the square root of the number of scans ( $n$ ) and linearly with the sample mass ( $m$ ): equation A.2, (Figure A.5). On the other hand, maximum peak resolution has an optimum: in liquid-state, 10 mg and 100 mg are typical loadings for proton and carbon spectra respectively. Higher sample loadings broadens the peaks, while lower loadings require more scans to achieve an acceptable  $s/n$  and amplify the signals from external contaminants. Cryoprobes are more sensitive for  $^1\text{H}$  and require 4 times less mass with respect to a standard probe.

$$s/n \propto m\sqrt{n} \tag{A.2}$$

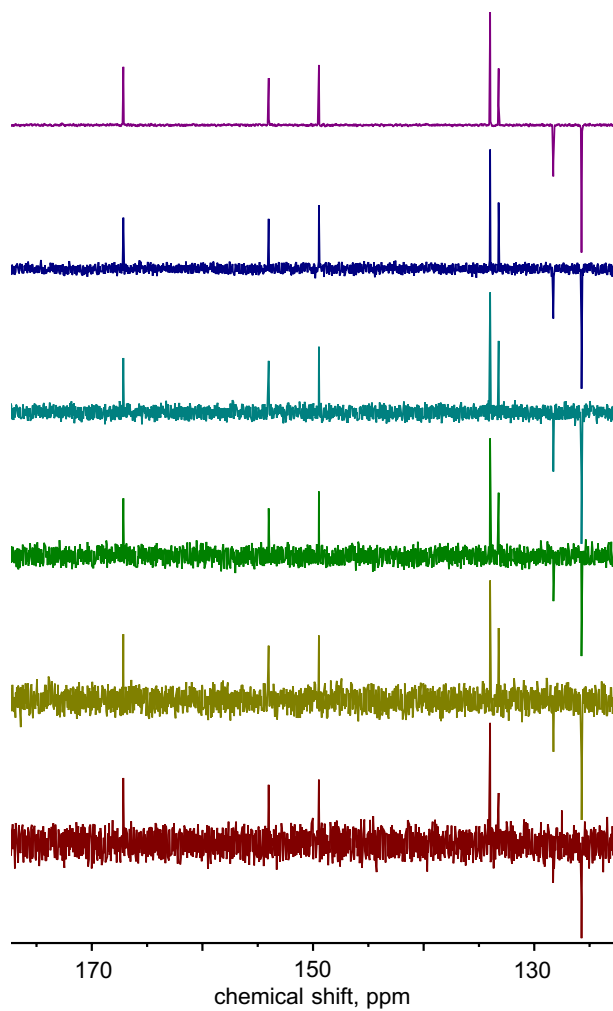


Figure A.5  $^{13}\text{C}$  spectra of a solution of an organic compound in  $(\text{CD}_3)_2\text{SO}$ , recorded at 100 MHz in J-MOD, to separate primary and tertiary carbons (top peaks) from secondary and quaternary ones (bottom). From bottom to top after: 2 (red), 4 (yellow), 8 (green), 16 (cyan), 32 (blue) and 256 scans (violet), the  $s/n$  increases from 13, 19, 27, 35, 52 to 150 (top peak).

However, long run analyses suffer from signal-drifting: as the external environmental conditions change, peaks' chemical shifts drift: this broadens the peaks. Therefore, a Faraday cage shields the spectrometer from external RF oscillations and an internal standard (usually the solvent) locks the signals in place and compensates for the drift. A custom built 1 GHz instrument has a proton drift of 0.001 ppm/10 h in the liquid phase and 0.2 ppm/10 h for solid phase samples with an external lock (chemical shifts with a precision of a decimal of a ppm are commonly accepted).[208] The Bruker company is currently the only manufacturer to offer ultra-high field 1 GHz NMR (Aeon<sup>®</sup>), with one unit installed in the University of Bayreuth and another at University of Toronto. This new technology requires cryogenic cooling to 2 K of a new superconductive rectangular NbTi-Nb<sub>3</sub>Sn coil, generating a 23.5 T magnetic field, without current fluctuations, which would compromise the stability required for high-resolution NMR analyses. This imposed a closed-loop sub-cooling to reduce the consumption of cryogenics to a yearly refill schedule. The improved shielding design also reduced the stray-field leaving the instrument, which interfered with the ongoing analysis and imposed a disengagement metal-free zone about half as big as an unshielded magnet (4 m vs. 12 m).

**Conclusions** NMR offers multiple analytical tools in one instrument: from quality control to research, it is ideal to identify intermediates during reaction, novel chemical species, conformational exchange and purity; for liquids, solids and gases. Interpreting a spectrum requires a knowledge in NMR spectroscopy, but fingerprinting the spectrum with a reference from literature is straightforward and results are comparable between different instruments. Solid-state NMR is currently a hot-topic, versus the standard techniques and is coupled with experimental crystallographic data and theoretical approaches. For new instruments, internal refrigeration systems, and new magnet designs to decrease operational expenses will replace cryogenic liquid refilling. 1 GHz magnets are commercially available and are expected to grow in strength by 100 MHz every 5 years. Liquid-state proton NMR remains the preferred way to quantify polymers for soluble samples. Carbon quantification in solid-state often requires the development of a dedicated pulse-sequence and is therefore not viable for routine polymer analysis. Benchtop NMR are new, portable and less expensive; and we speculate will find more applications in the future for process control and routine laboratory analysis.

## APPENDIX B Additional scientific contribution as co-author

Here we list the author's direct scientific contribution as co-author in a series of papers related to imaging and spectroscopic techniques: scanning electron microscopy, energy-dispersive X-ray spectroscopy and nuclear magnetic resonance spectroscopy.

### **Experimental Methods and Instrumentation for Chemical Engineers, 2nd ed.**

G. S. Patience

Book published in 2017, in *Elsevier*.<sup>[9]</sup>

Contributor for the chapters "Analysis of solids and powders" and "Spectroscopy".

### **The Scanning Electron Microscope**

Curiosity thrives the scientist to go deeper in details. In practice magnification of an object to better see its morphology has always pushed the researcher to develop more refined instruments to increase the resolution. The optical microscope is the first instrument that answered that need and became so famous that its logo represents today science and research. However, when the optical microscope magnification reached 1000x, diffraction, halted its progression. This phenomenon occurs when we try to visualize objects so small that their characteristic dimensions are comparable with the visible light electromagnetic wavelength (380 nm to 750 nm). This diffract one beam into multiple ones, creating interference and blurring the image.

### **SEM: Scanning Electron Microscopy**

The scanning electron microscope adopts the same principle of the optical microscope, substituting photons with a much shorter wave: X-rays (0.1 nm to 10 nm). The sample is placed in a vacuum chamber, where air does not interfere with the analysis. Then, like for the incandescence light-bulb, a filament (1 kV to 20 kV) generates an electron beam. A series of magnets adjust the position of the beam hitting the sample; for each position (pixel) a response is detected and recorded by the instrument, generating the image. There are four typical response signals generated by the sample hit by the electron beam, and for each signal there is a specific detector.

Secondary electrons are generated when the beam excite and eject the electrons in the innermost electron shell of the atom. They correspond to low energy ionization electrons (<50 eV) and are emitted by the firsts layers of atoms on the surface of the sample. The detector (SEI or LEI) counts the number of emitted secondary electrons for each pixel and compares them:

as the morphology varies across the sample, bright spots correspond to plain, accessible zones where more secondary electrons directly cross the chamber to the detector; while darker pixel are deeper holes, where most of the secondary electrons are lost by interaction through the sample.

Backscattered electrons are electron beam reflected upon interaction with the sample. The detector (LBE) use the same counting methodology as for secondary electrons with one crucial addition: heavy elements backscatter more than light elements (since the denser electron cloud). Therefore pixel of area with different chemical compositions appear brighter (heavy elements) or darker (light elements).

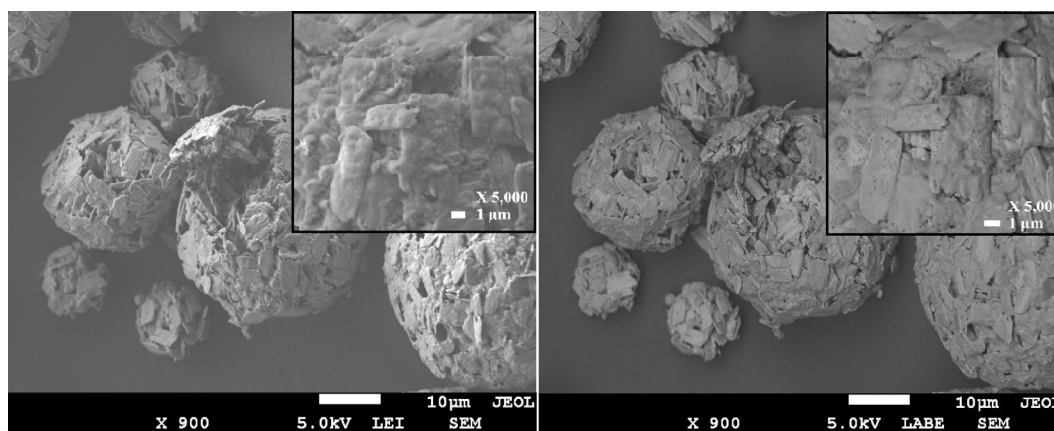


Figure B.1 LEI detector: spray dried spherical VPO secondary particles, in detail the primary particles composing the aggregates. LBE detector: in detail the detector can better visualize the vanadyl primary particle in respect to the silica coating.

### **EDS: Energy-dispersive X-ray spectroscopy**

X-rays are emitted when an higher shell electron replace the vacancy left by the ejected secondary electron. The interactions between incoming and emitting energy are more complex, however each element possesses its own characteristic X-ray energy (ranging from 0 keV to 10 keV). Therefore the detector can either acquire a spectrum over a selected sample area, for qualitative superficial elemental analysis; or flag each pixel area with the dominant element, creating an elemental map of the sample's surface.

### **TEM: Transmission electron microscopy**

Transmitted electrons are the beam's electrons that pass through a few atoms thick sample. The detector (TEM, Transmission electron microscopy) placed below the sample counts the number of electrons passed through. The instrument maximum resolution depends on the wavelength of the accelerated electrons, making possible to even see the atoms lined up in

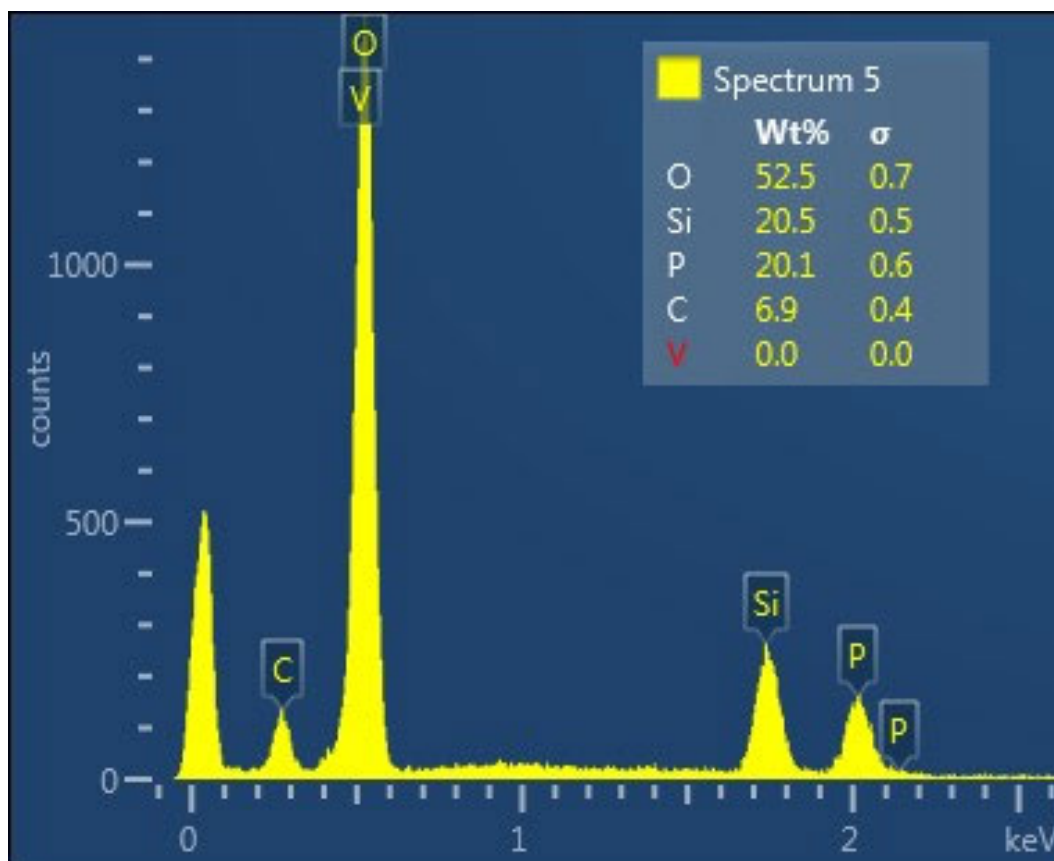


Figure B.2 EDS spectrum (left), note how vanadium is not detected since is coated with a layer of silica. EDS mapping (right) of a spray dried core-shell VPO catalyst, the external silica shell (red), covers the bulk vanadyl pyrophosphate salt (green).

their crystal structure as bright spots. Measuring the distance between the atoms allow to calculate the lattice spacing parameters of the crystal matrix.



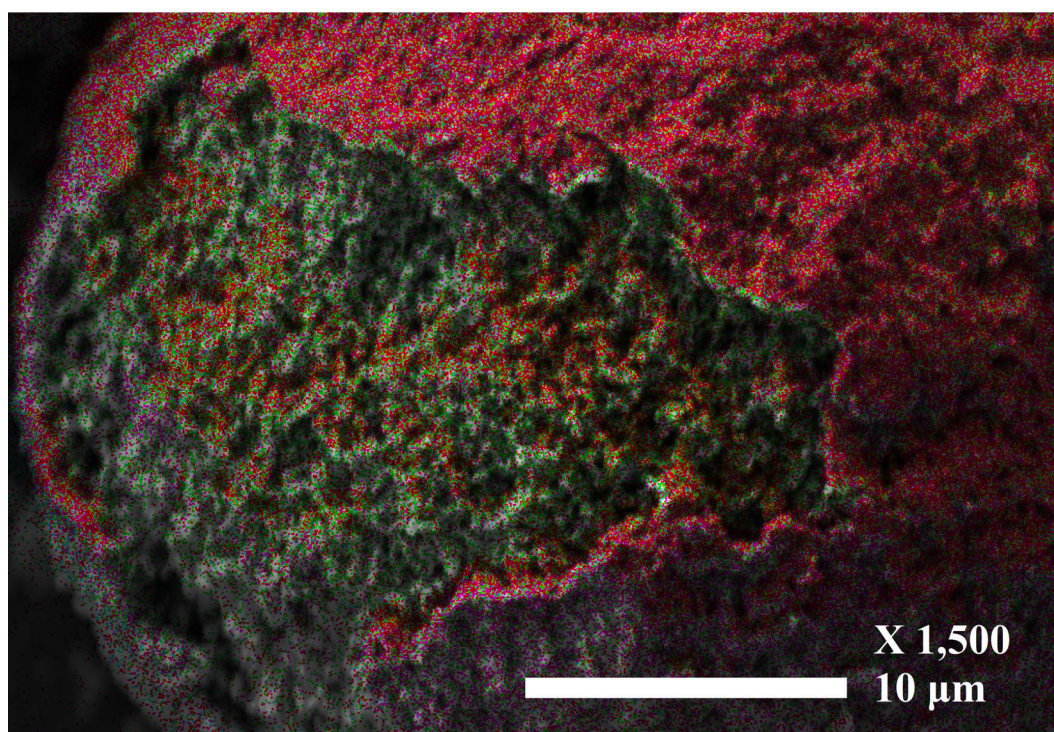
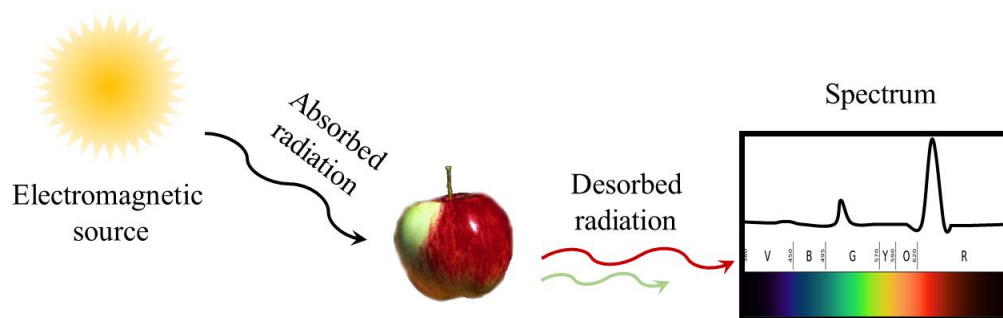


Figure B.3 SEM (a) and TEM (a') of VPO precursor.

## 11.5 Nuclear Magnetic Resonance Spectroscopy

NMR is one of the few instrument to offer a comprehensive chemical analysis of the unknown. For organic chemist it has become the state of the art technique for understanding chemical structure, thermodynamic data, elemental analysis, reaction kinetic and many others characteristic of a molecule.

The principle of spectroscopy consists in irradiating your sample with a precise electromagnetic radiation; based on how differently each diverse molecule absorbs and desorbs this radiation, it is possible to understand their structure. Since electromagnetic radiation covers a wide area of different wavelength, called spectrum, for each of these zones has been made a different type of spectroscopy analysis. To understand this practical aspect, consider the 400-800 nm wavelength portion of the spectrum (visible light) and your eyes as a spectrometer. When the sunlight brightens an object it absorbs some wavelengths and reflects the others: the colour of an object is just the analysis made by our eyes on the desorbed radiation. By this way we are able to differentiate different substances based on the visible part of the spectra.



**FIGURE 11.5.1** Interpretation of the visible spectrum of an apple.

Old spectrometers, as they were originally intended, works in continuous-wave: the sample is continuously irradiated over time while changing the wavelength of radiation. If the sample does not absorb the selected wavelength, the detector registers no change in the intensity of the signal (over time seen as a straight line, called baseline). But when the wavelength of radiation matches the excitation state of the sample, the detector registers a peak, a deviation from the baseline. The modern spectrometers uses the opposite process, instead of scoping all the various wavelengths one by one, they emit all the entire spectrum of interest in a single, strong pulse, and then register the desorption of the radiation overtime.

A huge improvement of this type of analysis has been made when it was understood that the energy content of an electromagnetic radiation is a discrete wave function and molecules respond in a predictable pattern when irradiated with a precise quantum of energy. The absorption of energy in a molecule will cause the passage from a ground state to an excited state. The X-rays spectrum radiation has a high energy content and is capable of excite electrons from the inner shell to the outer shell of an atom. By increasing the wavelength in the spectrum, the quantum energy content decreases; therefore the ultraviolet and visible radiation excite the valence electrons mostly from the HOMO to the LUMO. Infra red radiation has an even lower energy content but a higher wavelength and excitation cause a response in the vibrational energetic level, basically how bonded atoms vibrate. Microwave radiation affect the rotational energetic level. Finally radio wavelength can create a response in the alignment of the nuclei magnetism and this is the premise for a discovery of a new and fascinating machine: the Nuclear Magnetic Resonance instrument.

But not all nuclei spin, so not all nuclei create their own magnetic field; for instance spinning  $^1\text{H}$ ,  $^2\text{H}$  (deuterium),  $^{13}\text{C}$ , N,  $^{19}\text{F}$ ,  $^{31}\text{P}$ , etc. are all active towards NMR analysis. Since electromagnetic radiation is a wave, it can be quantified both by its wavelength or its frequency. In NMR spectroscopy, it is common to refer to frequencies.

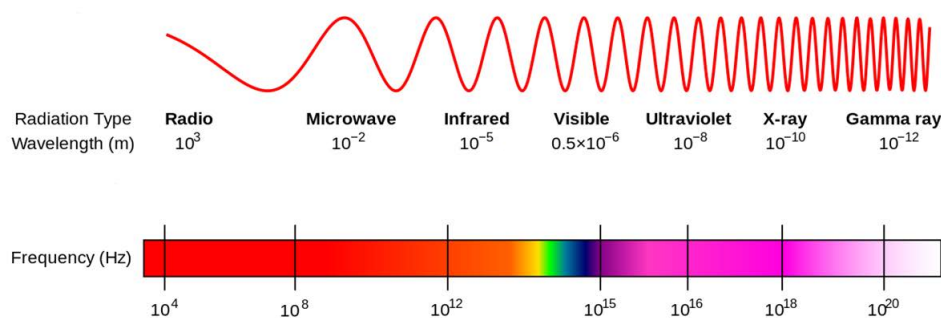


**FIGURE 11.5.2** "EM Spectrum Properties edit" by Inductiveload, NASA.

Without going into details, when a sample is placed into a magnetic field, its active nuclei align their magnetic field with the external one. They align almost equally into two forms: with field ( $\alpha$  spin state), energetically favourable and slightly more abundant; and against field ( $\beta$  spin state) at higher energy. According to the intensity of the external magnetic field, a very precise quantum of energy of a very precise frequency can excite the active nucleus isotope spin, from the  $\alpha$  spin, to the less stable and higher in energy  $\beta$  spin. For example a 7.05 Tesla magnetic field will make the  $^1\text{H}$  nucleus resonates at 300 MHz, a 2.35 Tesla at 100 MHz, while a 21.1 Tesla at 900 MHz.

This phenomenon is called magnetic resonance, because when the radiation ceases, the  $\beta$  spin nuclei relaxes to its more stable  $\alpha$  spin, by emitting a quantum of energy capable of exciting another  $\alpha$  spin nuclei to  $\beta$ . This process decreases exponentially over time but is acquired by the detector; and by integrating the wave function over time using a Fourier transform, the result is no more a wave signal but a distinctive peak. The point is that different active nuclei resonate at different frequencies, therefore it is possible to differentiate them. For example a 7.05 Tesla magnetic field will make the  $^1\text{H}$  nucleus resonate at 300 MHz, the  $^2\text{H}$  at 45.7 MHz, the  $^{13}\text{C}$  at 75.3 MHz, the  $^{19}\text{F}$  at 282 MHz and so on.

But more important, the NMR instrument has a resolution so high that can also expand near the magnetic resonance frequency of a nucleus, thus becoming possible to understand how this nucleus is bonded in the molecule.

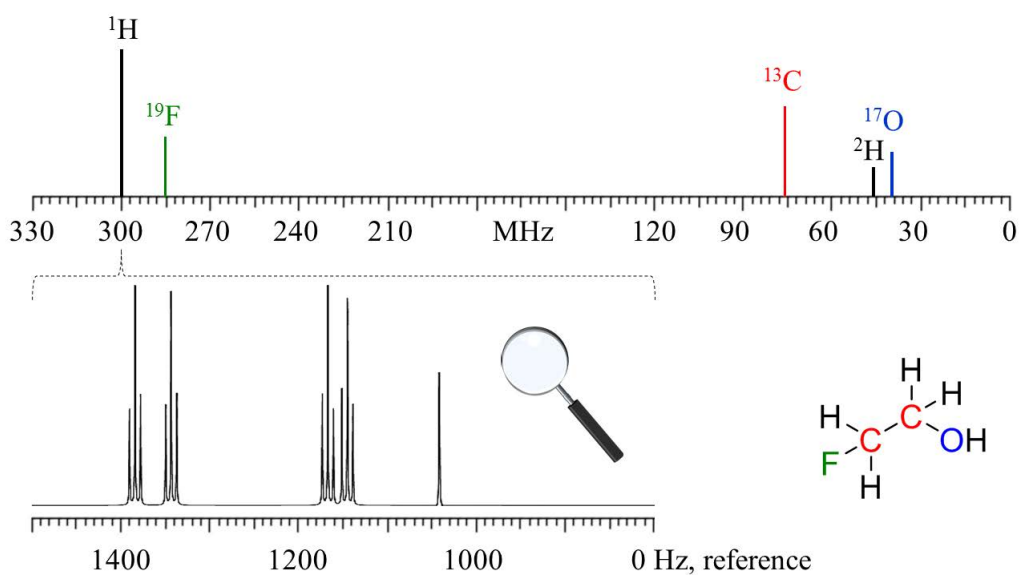


**FIGURE 11.5.3** NMR spectrum of 2-fluoroethanol and  $^1\text{H}$  high resolution analysis.

### Performing a $^1\text{H}$ and $^{13}\text{C}$ liquid NMR analysis

Performing an NMR analysis is very easy and quick, the difficult part is understanding the obtained spectrum. So the NMR is usually performed on a purified sample of a single compound. The sample needs to be carefully dried, any traces of organic solvent, water included, is accordingly seen in the spectrum. The amount of material required for a proton ( $^1\text{H}$ ) analysis should be less than few milligrams for having sharp peaks, vice versa for  $^{13}\text{C}$ , a hundred times loading is beneficial. This is mainly due to the different natural abundance of the two nuclei:  $^{13}\text{C}$  isotope has only 1% abundance! The sample is put in the NMR tube and filled with 3-4 cm of deuterated solvent and mixed by gentle agitation. Its role is the solvation

of your compound while not being detected by the instrument, since  $^2\text{H}$  resonates far away from the  $^1\text{H}$ . The most common is  $\text{CDCl}_3$  deuterated chloroform. Another important aspect of the solvent is that it usually contains on purpose a small amount of its non deuterated form and TMS, which are called internal references, and are later used to calibrate the analysis.

The NMR tube is attached to a plastic ring at a precise height depending on the model of the instrument. It is important when approaching the NMR to remove all worn metallic objects, keys, phone and wallet, sometimes even the belt, due to the strong magnetic field of the instrument. Depending on the model, the tube is introduced from the top using a pneumatic system.

Now the instrument has to be calibrated according to the resonance frequency of the active atom we want to analyse, for recent models the software at the workstation takes charge of everything. For older models it has to be done manually on the shimming pad, by slightly changing the magnetic field of the instrument. The aim is to create an homogeneous magnetic field, represented by the shim curve, the higher you achieve to obtain, the sharpest will be the signals. In order to keep the magnetic field homogeneous overtime, the instrument locks on the  $^2\text{H}$  resonance frequencies of the solvent, any slight discrepancy overtime on  $^2\text{H}$  will be corrected automatically also on the  $^1\text{H}$  that is being analysed. There are countless acquisition methodologies, the most common are the proton and carbon analysis. The user has to choose basically four things: the number of acquisition (usually 16 for  $^1\text{H}$ ; 64 or more for  $^{13}\text{C}$ ) which determine the peak to noise ratio. The relaxation time between each acquisition (3 seconds for simple molecules, 6 for shielded atoms and quaternary carbons). The width of the spectrum (in chemical shift, generally all protons signals are in the 0-12 ppm zone, for carbon 0-240 ppm). And finally H-Nucleus coupling, usually proton analysis are performed with H-H coupling (also called spin-spin splitting or spin-spin coupling), while carbon are not H-C coupled. This will lead to have multiplets in the proton spectrum, which reveal more information on the structure of the molecule but will increase the difficulty of reading the spectrum. Vice versa in the carbon spectrum, all  $^{13}\text{C}$  will be reported as sharps singlet peaks.

### Reading a NMR spectrum

After acquisition, the Fourier transform will reveal the true nature of the spectrum, combining all the wavefunctions into a single line. On the Y axis it is reported the intensity of the signal. On the X axis it is reported the frequency of resonance at high resolution of the selected nucleus. For practical reasons, it is commonly replaced by the chemical shift  $\delta$  [ppm]: which is ratio between the distance in Hz of any peaks from the internal reference of TMS, and the nucleus resonance frequency in MHz. Then the TMS chemical shift is cal-

ibrated to 0 ppm; if used other internal references, they will be calibrated accordingly. The use of chemical shift respect to the frequency is useful due to the fact that the same analysis, performed in any NMR, independently from its magnetic field intensity, will give the same results in terms of chemical shift.

A  $^{13}\text{C}$  decoupled spectrum is easy to understand, first of all, after calibration to its internal reference, the number of peaks are counted and they should match the number of carbon in the sampled molecule. Obviously the internal reference peaks are not counted. It is important to mention that not all carbons are supposed to generate a peak. Due to the fact that the molecule or a functional group can be symmetric towards one or more planes, all equivalent carbons will appear as a single peak. For example benzene will appear as a single peak because all carbon are equivalent with each other. Methylcyclohexane instead has two pairs of equivalent carbons due to its symmetry plan, so it will show five distinctive peaks. Another equivalence of nuclei is given from the rotational contribution; isopropyl group for example shows the tertiary carbon as a peak and the two equivalent methyl as another single one.

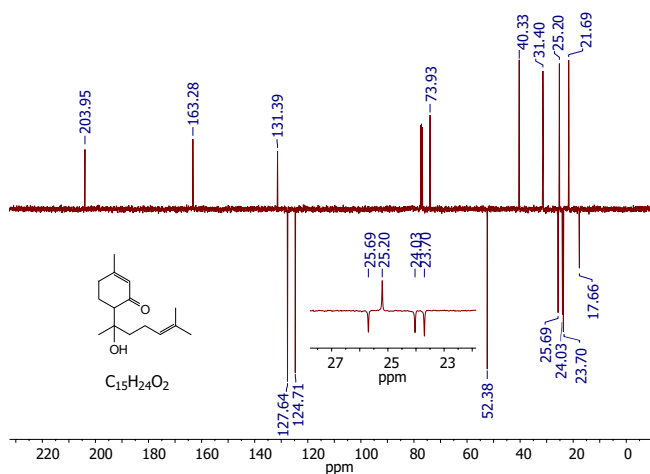


**FIGURE 11.5.4**  $^{13}\text{C}$  spectrum of hernandulcin, at 100 MHz in  $\text{CDCl}_3$  using J-MOD method for separating odd carbons (positive peaks) from even (negative). Rigamonti M. G.; Gatti F. G. *Beilstein J. Org. Chem.* **2015**, 11, 2117–2124. doi:10.3762/bjoc.11.228

If the peaks are less than they should be, either the analyzed molecule is different from the expected one or performing another analysis with more acquisitions and longer relaxation time will increase the signal to noise ration and will reveal the hidden quaternary carbon. It is also possible that two non-equivalent carbon peaks are overlapped, if so, only an analysis

performed on a stronger magnet will be able to distinguish among the two signals. If the peaks are more, it is usually due to solvent contamination or bad purification of the compound or a stereogenic center which reveals the two isomers of the molecule.

The attribution of a peak to a specific carbon in the molecule using only a  $^{13}\text{C}$  analysis is not certain. However there are two main criteria: functionalized carbons have their own chemical shift range attribution (Figure 11.5.5) and the deshielding effect. The electron density of a nucleus plays an important role in terms of chemical shift, the higher the density, the more the nucleus will appear at low chemical shifts. Vice versa, at low electron density, the nucleus becomes deshielded, and will appear at higher chemical shifts.

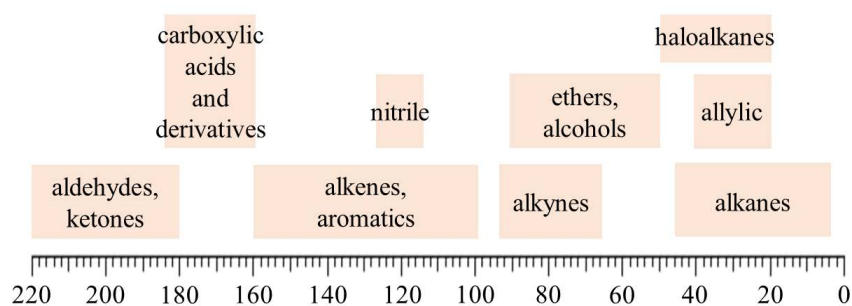


**FIGURE 11.5.5** Typical chemical shifts  $\delta$  in ppm for a  $^{13}\text{C}$  spectrum

A  $^1\text{H}$  coupled spectrum will require more time to be understood. After calibration, likewise the carbon analysis, we have to understand what are the equivalent protons in the molecule. For example in a methyl group, all three hydrogens will appear as a single signal. However due to H-H coupling, each signal has now multiplicity. This methodology is applied to understand the chemical environment of the nucleus signal, in practice the signal of the proton or the equivalent ones is correlated to the presence of the vicinal protons, on the  $\alpha$ -carbon and in some cases also on the  $\beta$ -carbon. Let's analyse the simple spectrum of propanal. There are three groups of equivalent protons, the carbonyl group proton signal, called "a"; the  $-\text{CH}_2-$  equivalent protons signal, called "b"; and the methyl group signal called "c". Using H-H coupling we see "a" as a triplet (three close peaks) at high chemical shift since it is strongly deshielded, the distance in Hz between its peaks is the same and is called coupling constant, in this case  $J_{ab}$  since we are coupling our signal "a" with the vicinal "b". The triplet shape is given by the N+1 rule: the multiplicity of the signal is given by the number of the vicinal protons, plus 1 which is the signal of the proton or equivalent protons analyzed. Likewise the equivalent protons "c" are seen as a triplet but at low chemical shift since it has a high electron density, the N+1 rule applies and the coupling constant will be  $J_{bc}$ . However signal

“b” couples with “a” and also “c”, in this case if the coupling constants  $J_{ab}$  and  $J_{bc}$  are different, the N+1 rule is applied in sequence. The multiplicity of the signal “b” will have two contributions: coupling “b” with “c” will rise to a quartet (3+1), and coupling “b” with “a” will split each peak of the quartet in two other peaks (doublet 1+1), so the spectrum of the protons “b” will show an octet with two different coupling constants.

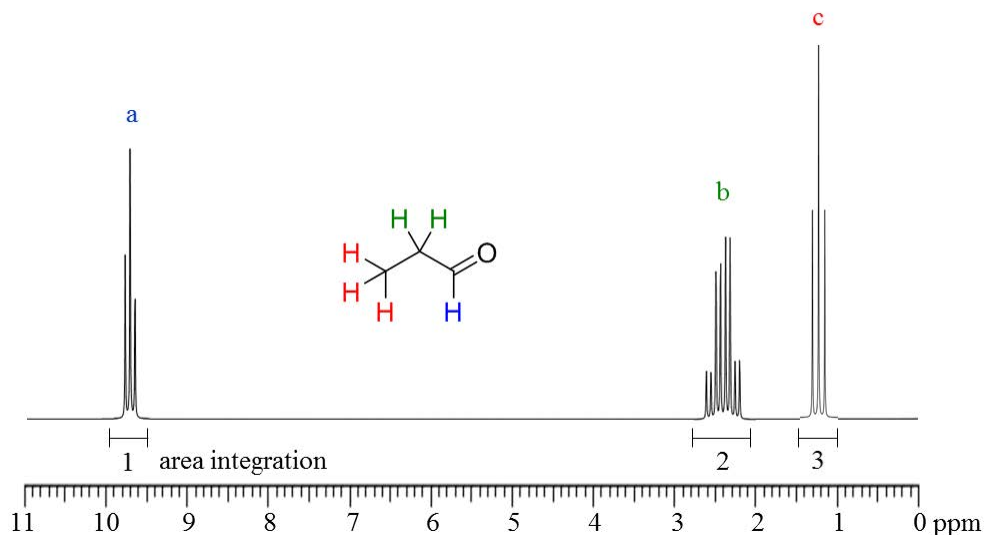


**FIGURE 11.5.6**  $^1\text{H}$  simulated spectrum of propanal with area integration, the peaks are magnified for better exposition.

If the two coupling constants are the same or have very close frequencies, like in isopropanol, the proton bonded to the secondary carbon will appear as a septet, the N+1 rule is applied at the same time coupling the two methyl groups (6 protons) with the signal analyzed (1). It is noteworthy to mention that protons bonded to heteroatoms does not couple, they will always appear as singlets. Another instrument that helps reading the  $^1\text{H}$  spectrum is integration, by calculating the area underneath each signal. The ratio between each integer will reveal how many protons participate in the signal.



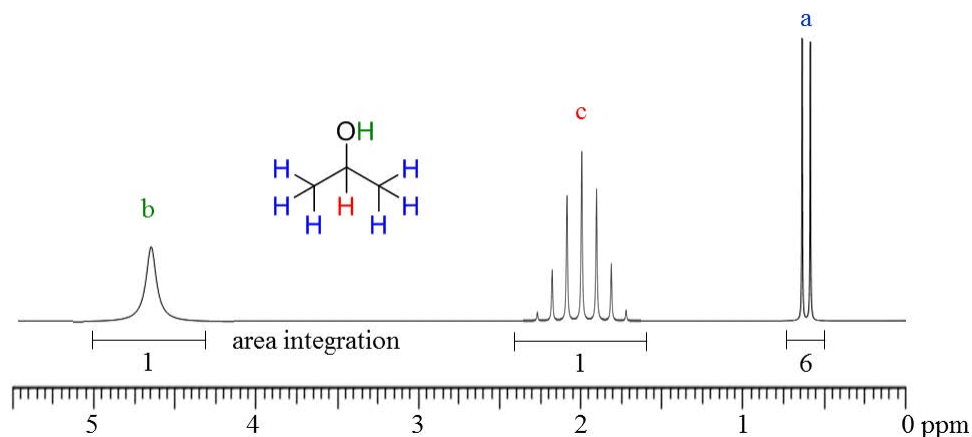


**FIGURE 11.5.7**  $^1\text{H}$  simulated spectrum of isopropanol with area integration, the peaks are magnified for better exposition.

A common problem in H-H coupling is that often some signal with their multiplicity overlap, especially in the shielded region of the spectrum. In this case attribution of a signal to the protons of a molecule can't be done properly, however it is still possible to integrate and see if the number of the protons in the spectrum matches the expected formula.

Likewise for the proton, the same rules apply for the  $^1\text{H}$  attribution of signals to the structure of the molecule. By knowing the expected chemical shifts of specific functional groups and the deshielding effect as reported in Figure 11.5.8.

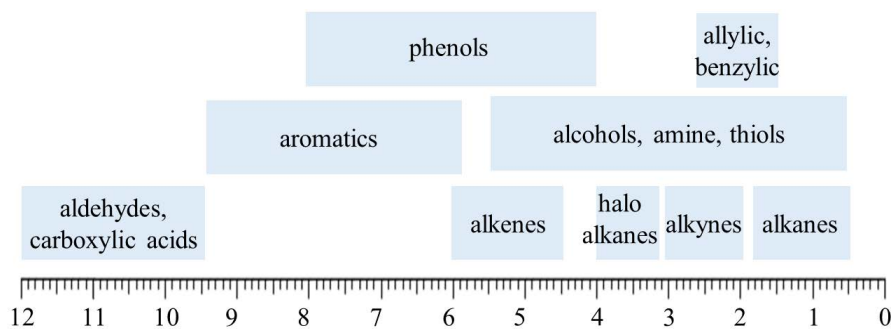
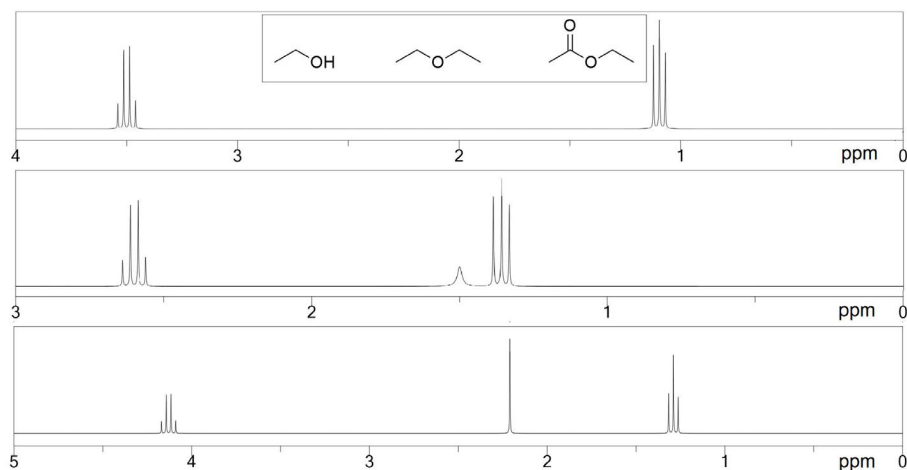


**FIGURE 11.5.8** Typical chemical shifts  $\delta$  in ppm for a  $^1\text{H}$  spectrum

**Reference book:** Peter Vollhardt, Neil Schore; Organic chemistry structure and functions 6<sup>th</sup> ed.; W. H. Freeman and Company

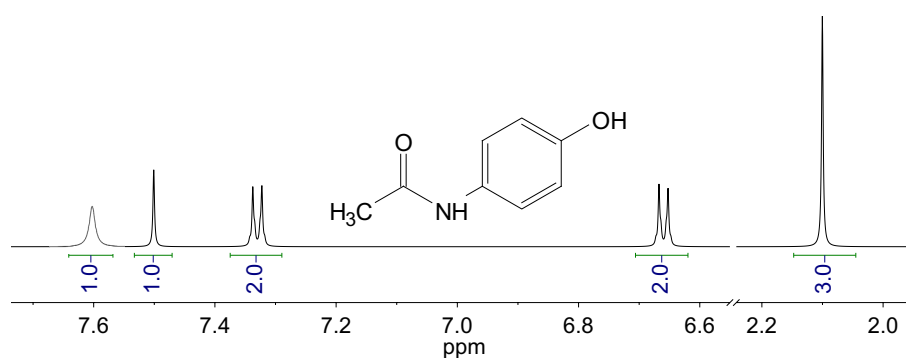
### Exercise 1

Associate each molecule (ethanol, diethyl ether and ethyl acetate) to the respective  $^1\text{H}$  spectrum. Recognize multiplicity and associate each group of equivalent proton to their respective peak.



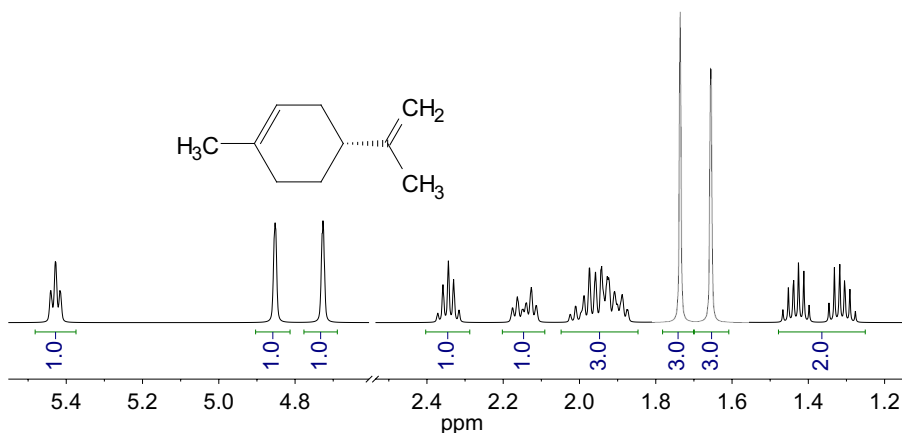
### Exercise 2

Associate each  $^1\text{H}$  signal to the paracetamol molecule. Recognize multiplicity and associate each group of equivalent proton to their respective peak. Use peak integration on the bottom of each signal for better understanding.



### Exercise 3

Associate each  $^1\text{H}$  signal to d-limonene. Recognize multiplicity and associate each group of equivalent proton to their respective peak. Use peak integration on the bottom of each signal for better understanding. Remember that diastereotopic protons are not equivalent.



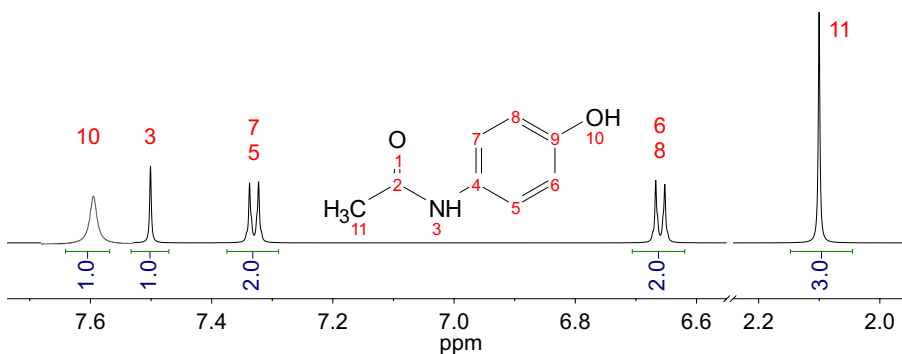
### Exercise 1 - solution

The first spectrum from the top is diethyl ether: protons on the primary carbon see two hydrogen on the secondary carbon, thus the signal is a triplet and appears at low chemical shift (shielded). Oxygen electronegativity deshields the proton on the secondary carbon, those see three hydrogen, thus the signal is a quartet.

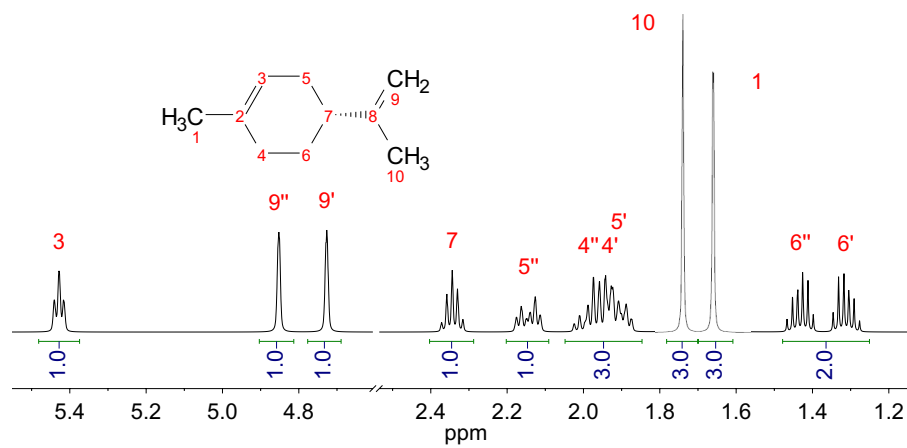
The second spectrum is ethanol: the same rule applies, plus the hydrogen on the alcohol creates a broad signal.

The third spectrum is ethyl acetate: it differs from ethanol since its quartet happens at higher chemical shift, indicating a stronger deshielding. In fact ester deshield more than alcohols. Moreover, the primary carbon on the acetate group sees no other protons, thus appears as a sharp singlet.

### Exercise 2 - solution



### Exercise 3 - solution



## APPENDIX C CHAPTER 5 - SUPPLEMENTARY INFORMATION

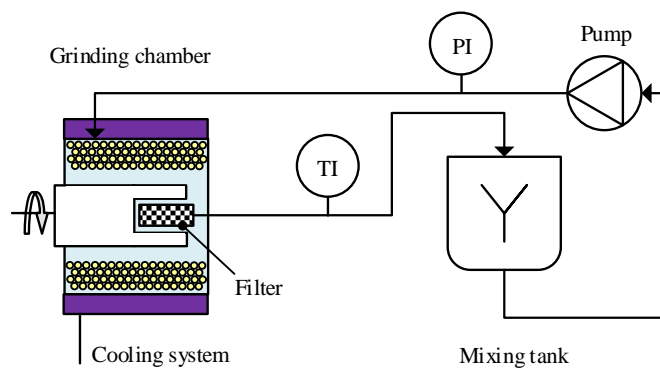


Figure C.1 Sketch of the wet media mill, reducing the size of the primary particle from 27  $\mu\text{m}$  to 200 nm took 4 h for a batch of 50 kg.

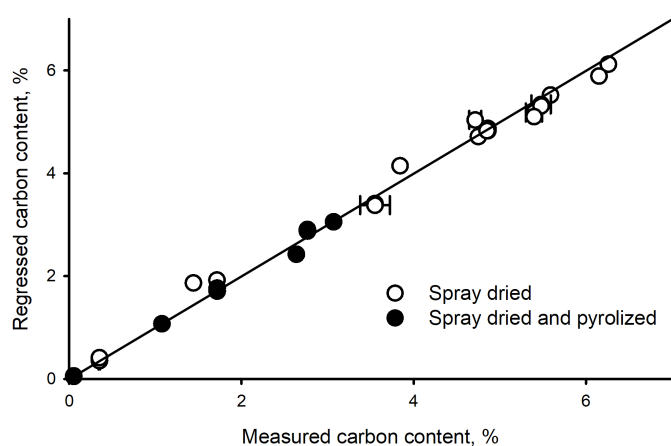


Figure C.2 Model regression for estimating the carbon contribution of each precursor.

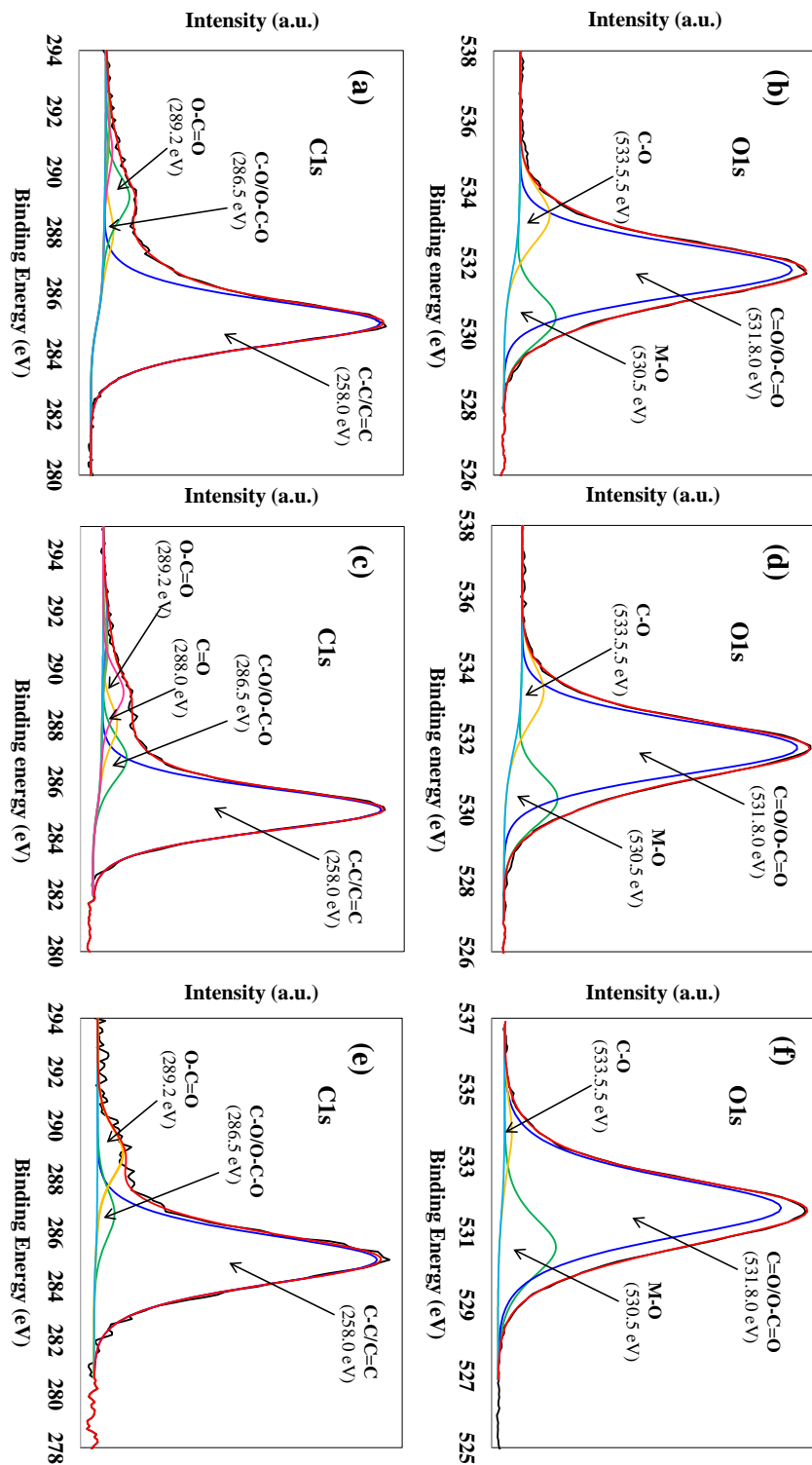


Figure C.3 High-resolution spectra of C1s and O1s of the pyrolyzed samples: LFP-L-Py with lactose (a-b), LFP-LPU-Py with lactose, PVA and ultrasonicated (c-d) and LFP-neat-Py calcined with no carbon precursor (e-f).

## APPENDIX D MILESTONES

## LIST OF PUBLICATIONS:

- 2019 - H. Li, F. P. Cabanas-Gac, L. Hadidi, M. Bilodeau-Calame, A. Abid, K. Mameri, M. G. Rigamonti, S. Rousselot, M. Dollé, and G. S. Patience; “LiFePO<sub>4</sub> synthesis via ultrasound assisted mechanochemistry”; submitted
- 2019 - D. Schieppati, R. Germon, F. Galli, M. G. Rigamonti, M. Stucchi, and D. C. Boffito; “Influence of frequency and amplitude on the mucus viscoelasticity of the novel mechano-acoustic frequencer<sup>TM</sup>”; accepted in *Respir. Med.*
- 2019 - N. A. Patience, F. Galli, M. G. Rigamonti, D. Schieppati, and D. C. Boffito; “Ultrasonic intensification to produce diester biolubricants”; *Ind. Eng. Chem. Res*[161]
- 2019 - H. Khan, M. G. Rigamonti, and D. C. Boffito; “Enhanced photocatalytic activity of Pt–TiO<sub>2</sub>/WO<sub>3</sub> hybrid material with energy storage ability”; *Appl. Catal. B Environ.*[145]
- 2018 - M.G. Rigamonti, F.G. Gatti and G.S. Patience; “Experimental Methods in Chemical Engineering: Nuclear Magnetic Resonance”; *Can. J. of Chem. Eng.*[160]
- 2018 - D. Carnevali, M. G. Rigamonti, T. Tabanelli, G. S. Patience, and F. Cavani; “Levulinic acid upgrade to succinic acid with hydrogen peroxide”; *Appl. Catal. A: General.*[10]
- 2018 - D. Carnevali, O. Guévremont, M. G. Rigamonti, M. Stucchi, F. Cavani, and G. S. Patience; “Gas-Phase Fructose Conversion to Furfural in a Microfluidized Bed Reactor”; *ACS Sustain. Chem. Eng.*[123]
- 2018 - H. Li, M. Rostamizadeh, K. Mameri, D. C. Boffito, N. Saadatkah, M. G. Rigamonti, and G. S. Patience; “Ultrasound assisted wet stirred media mill of high concentration LiFePO<sub>4</sub> and catalysts”; *Can. J. of Chem. Eng.*[86]
- 2018 - M. Stucchi, A. Elfiad, M. Rigamonti, H. Khan, and D. Boffito; “Water treatment: Mn–TiO<sub>2</sub> synthesized by ultrasound with increased aromatics adsorption”; *Ultrasonics Sonochemistry.*[138]

- 2017 - H. Khan, M. G. Rigamonti, G. S. Patience, and D. C. Boffito; “Spray Dried  $\text{TiO}_2/\text{WO}_3$  Heterostructure for Photocatalytic Applications with Residual Activity in the Dark”; *Appl. Catal. B.*[8]
- 2017 - M. G. Rigamonti, Y.-X. Song, H. Li, N. Saadatkah, P. Sauriol, and G. S. Patience; “Influence of atomization conditions on spray drying Lithium Iron Phosphate nanoparticle suspensions”; *Can. J. of Chem. Eng.*[84]
- 2017 - G.S. Patience; “Experimental Methods and Instrumentation for Chemical Engineers - 2nd Edition”; *Elsevier*, contributor for the chapters "analysis of solids and powders" and "spectroscopy".[9]
- 2016 - N. Saadatkah, M. G. Rigamonti, D. C. Boffito, H. Li, and G. S. Patience; “Spray dried  $\text{SiO}_2 \text{WO}_3/\text{TiO}_2$  and  $\text{SiO}_2$  vanadium pyrophosphate core-shell catalysts”; *Powder Tech. J.*[7]

#### CONFERENCES PRESENTATIONS:

- 2018 - XXIX Interamerican Congress, 68<sup>th</sup> Canadian Chemical Engineering conference, (Toronto, Canada)
- 2018 - 25<sup>th</sup> Canadian Symposium on Catalysis, (Saskatoon, Canada)
- 2018 - McGill’s Chemical Engineering Research Day (Montreal, Canada)
- 2017 - 8<sup>th</sup> World Congress on Oxidation Catalysis conference (Krakow, Poland)
- 2017 - Organic Chemistry 2017 conference (Chicago, USA)
- 2016 - 66<sup>th</sup> Canadian Chemical Engineering conference (Quebec City, Canada)
- 2016 - International Fluidization XV conference (Montebello, Canada)

#### PROFESSIONAL GROWTH AND ACHIEVEMENTS:

- Since 2017, editor of the “*Journal of Chemistry: Education Research and Practice.*”
- HeroX 1 M\$ challenge with The Coca-Cola Company: invention proposal for a novel sweetener.
- 2017 - Moderator honor at “Organic chemistry 2017” conference.



- 2017 - Certificate of Outstanding Contribution in Reviewing, *Powder Technology Journal*.
- 2019 - “Experimental Methods in Chemical Engineering: Nuclear Magnetic Resonance” chosen as issue highlight for the month of March.
- Teaching Assistant: Méthodes expérimentales et instrumentation.
- Teaching Assistant: Calcul des réacteurs chimiques.
- Teaching Assistant: Chimie organique.
- Research supervisor: three undergraduate students, one graduate.
- Resurrect, revamp, calibrate and operate the attrition jet mill.
- Being able to operate independently: Yamato spray dryer, GEA spray dryer, Netzsch micronizer, Attrition jet mill, SEM, EDS, XRD, PSD, N<sub>2</sub> physisorption, Hg porosimetry, rheometer.
- Establishing as a professional in N<sub>2</sub> physisorption porosimetry analysis and rheology, execute analysis for other researchers and discuss the results.